Harnessing Spatial Dispersion in Wire Media to Control the Shape of Electromagnetic Fields

William Taylor Boyd

Lancaster University

Department of Physics
University of Lancaster
United Kingdom
September 2019

Abstract

We have detailed the development of our method for field profile shaping of longitudinal electric fields by exploiting the spatial dispersion of wire media. The development of this method involved a theoretical analysis of the problem where we derived the required variation in the electromagnetic properties of a medium that can be described by a 1D spatially dispersive model. Integrating this with information on how the wire radius affects the electromagnetic properties of our structures, taken from numerical simulations, we were able to develop our field profiling method. This method allows us to generate a function for the radius variation of our wires that should produce the desired profile. These profiles come from the solutions of Mathieu's equation. We have validated our method for a variety of realisations of wire media, comprising metal and dielectric wires, in eigenmode simulations, with work also undertaken in the time domain.

Declarations

I hereby declare that I am the sole author of this thesis and that this work has not been submitted in substantially the same form for the award of a higher degree elsewhere.

The following segments of this thesis contain work previously published by ourselves in [1]: Chapter 4, Chapter 5, Chapter 6 Sections I-V, Chapter 6 Section VIII, Chapter 7 Section I and Chapter 7 Section IV. The following segments contain work previously published by ourselves in [2]: Chapter 7 Sections V-VII.

The research underpinning this thesis was undertaken with the help and guidance of my supervisors Dr Jonathan Gratus and Dr Rosa Letizia, as well as Dr Paul Kinsler. Our research was also helped greatly by the advice of Professor Rebecca Seviour.

I grant the institutional repository any permissions and conditions that are necessary with respect to the online access to my work. Where subsidiary material owned by third party copyright holders has been included permission has been sought.

Acknowledgements

Contents

List of Figures

13

14

16

17

18

List of Tables

Chapter 1

Thesis outline

In this thesis, we present the work we have undertaken in the development and testing of our method for field profile shaping using wire media. To thoroughly detail this process, an extensive number of investigations are detailed in the following chapters. Below we summarize the content of these chapters to aid navigation to relevant information.

Chapter 2 provides an overview of the work that we have done. We describe how we developed our method for mode profile shaping by a mixture of theoretical analysis based on the models detailed in Chapter 3 and numerical simulations which provided us with vital information on how to control the electromagnetic properties of our wire medium. We also set out the steps taken to test our method and to extend it to more realistic and varied realisations of wire media.

Chapter 3 contains an exploration of the background knowledge upon which we built our work. Primarily this chapter focuses on a discussion of wire media, spatial dispersion and methods for field profile shaping. We have attempted to provide an introduction to these topics while explaining how they relate to our work.

Chapter 4 presents the theoretical analysis of wire media that we have carried out. Building upon the previously predicted existence of plasma-like longitudinal modes, we show that with a one-dimensional spatially dispersive model we can predict the required longitudinal variation in the cut-off frequency to produce our desired field profile. As an aside, these desired field profiles are taken from Mathieu's equation, which arises naturally from our theoretical analysis.

Chapter 5 covers our initial simulations of dielectric wire media, which are realised as an infinite lattice of dielectric rods. The rods used in this section have an extremely high permittivity, $\varepsilon_r = 1600$, and small radii, $r = 0.3\,\text{mm}$. We believed that these choices would help us find our desired longitudinal modes, but we later found these modes for a wide variety of material parameters. Despite this, these simulations did allow us to confirm the existence of longitudinal electric fields with a plasma-like dispersion relation in our chosen wire medium. We also examined the effect of different choices for the mesh on these results. We found that

an increase in mesh size caused no apparent increase in the quality of results. In this chapter we have confirmed the prediction of plasma-like longitudinal modes, which was essential as it validated the use of our chosen theoretical framework.

Chapter 6 sets forth the development and initial testing of our field profiling method. Carrying on from the work and structures in Chapter 5, we investigated the effect of the wire radius on the dispersion of our longitudinal modes and, hence, their cut-off frequency in section I. Using the data from Section I, we found an extremely successful way of describing the relationship between the wire radius and cut-off frequency. This took the form of an exponential decay function as detailed in Section II. With an analytic function that described this relationship well, it was then possible to use our theoretical analysis to solve for a function of the wire radius that should support our desired field profile as detailed in Section III.

Before attempting to use our method, we gave some consideration to the fixing of free parameters and how to make sensible choices for these parameters in Section IV. After considering these choices, it was necessary to test our ability to produce the desired field profiles in our simulations using these solutions. To realise the required radius variation, we employed a structure made from a series of segments, conical frustums, with varying radii. This led to a discrete variation in the radius of our wires. Despite this, we had a great deal of success replicating our desired profile across a whole range of frequencies, structure lengths and differing radius variations in Section V. We also investigated the effect of the chosen number of segments on our field profiling success; finding that our success remained remarkably robust for even small numbers of segments as shown in Section VI. Another critical factor to consider is the quality of the mesh, where we found that an increase in mesh cells per wavelength did lead to a convergence in the mesh frequency but erratic changes in the success of the field profile shaping. Both coarse and relatively sparse meshes showed successful profile shaping, while for some intermediate meshes the mode profile shaping was quite poor. It seemed that it was more important to allow CST to run its mesh refinement than specify a large amount of cells per wavelength as discussed in Section VII.

These initial successful results were all based on the replication of the same field profile, a profile resembling a flattened sinusoidal curve. One of the strengths of our method is that it is not limited in its support of field profiles. All the solutions to Mathieu's equation can be easily replicated by solving for the wire radius function after choosing the appropriate Mathieu parameters q and a, covered more in Chapter 3. We carried out simulations that showed that our method remained remarkably successful when tested for a variety of different profiles as detailed in Section VIII.

Chapter 7 focuses on the extension of our field profiling method to a variety of realisations of wire media and other steps taken to increase our confidence of the viability of our method in real world scenarios. This work was motivated by the fact that our initial results in Chapters 5 and 6 were solely eigenmode

results achieved using infinite wire media formed from high permittivity rods. This raised the prospect that our results would be restricted to a narrow class of high permittivity wire media.

We were able to show that the results we have obtained can be replicated in wire media with permittivities as low as $\varepsilon_r = 3$ in our infinite structures in Section I. We analysed the effect of changing lattice parameters on our longitudinal modes. We showed that these modes are still supported but with a shifted frequency. This raises the possibility of extending our results to different frequency ranges by changing the lattice parameters as discussed in Section II.

The introduction of various forms of disorder into our infinite structures was also studied. Our field profiling success proved to be fairly robust to both systematic and random errors in the wire radius. Although, as we would expect for extremely large variations in the wire radius (0.2 mm) the field profiling did break down as shown in Section III. As a possible means to aid fabrication of our dielectric rods, we also examined the effect of introducing a sheath of lower permittivity material around the varying wires in our infinite lattice. The results showed no significant decrease in the quality of the results produced as shown in Section IV.

Moving to finite structures is a significant step in our aim to move towards more realistic wire media. As an intermediary step, we were able to extend our results to partially finite wire media. By this, we mean that we were able to achieve successful field profiling in a simulation of a two by two lattice of infinitely long wires. The transverse boundaries of these simulations were the standard distance from the nearest rod but had metallic boundary conditions, as shown in Section V. The extension of our results from a partially finite structure to a completely finite structure proved to be straightforward. By taking the same structures used to successfully show field profiling for the partially finite case and applying metallic boundaries to the longitudinal dimension we were able to achieve field profiling in a completely finite structure as detailed in Section VI. Having shown that our method was applicable to finite two by two lattices, we also realised field profile shaping in a four by four lattice to show that we are not limited in our choice of lattice size as confirmed in Section VII.

With successful finite structures tested, it was then possible to investigate the sensitivity of these structures to a variety of different disorders. These included random errors in the wire radius, and both random and coordinated shifts in the wire positions. We have laid out the effects we have observed after the introduction of each of these disorders in Section VIII.

An important aspect of any successful experimental realisation of our method will be the ability to excite our longitudinal modes. To examine this possibility, we have performed a series of time domain simulations of modifications of successful finite structures. We were able to show that we can observe field profiling in our wire media. Although, despite seeing signs of field profile shaping, our analysis was incomplete as we have yet to confirm the ease with which these fields can be transmitted and supported in our wire medium, as covered in Section IX.

Chapter 8 details the development of our method for achieving field profiling in metallic wire media. Our first steps in this area were taken with an idealised infinite lattice of perfectly electrically conducting wires. These structures were shown to be capable of achieving field profile shaping in Section I. At this stage, we then switched our attentions to wire media made of copper wires. With copper wires we were able to replicate all the results achieved with dielectric rods, including the realisation of field profile shaping in finite structures and the exploration of the excitation of a structure, as detailed in sections II, III and IV.

In Chapter 9 we explore some of the ways in which our work could be extended. We then provide a conclusion of our work in Chapter 10, which summarises the results which we have detailed in this thesis.

Chapter 2

Introduction

This thesis focuses on our study of wire media and exploitation of their spatially dispersive nature to form a method for field profile shaping. Here we use the term "field profile shaping" to mean controlling the spatial variation of typically sinusoidal electromagnetic fields. Our work on field profile shaping has proved to be successful, with the developed method shown to reproduce a range of desired profiles within various realisations of wire media.

We have developed our field profile shaping method around the longitudinal electric fields that are natively supported by wire media. This is advantageous as it opens up the possibility of using our shaped fields in applications where the field interacts with particles, such as in particle acceleration.

The ability to control the spatial variation of a field could be useful in a variety of scenarios beyond particle acceleration: enhancing ionization in high harmonic generation, the reduction of non-linearity and improving the resolution of signals in signal processing. Previous techniques to achieve this control have been limited by their need for iterative design, i.e. the crab cavity. Our aim when developing our method for field profile shaping was to create a flexible, prescriptive method. This prescriptive nature would allow for the realisation of our desired profile directly without the need for iterative design. Whereas the flexibility of being able to produce a range of field profiles increases the range of potential applications. We have focused on the use of Mathieu functions as profiles, but this is just a choice we have made for reasons of convenience and familiarity.

The theoretical underpinning of our work is centred around the phenomena of spatial dispersion. Spatial dispersion can be defined for plane waves as the dependence of the permittivity and other constitutive relations on the wavevector. Accordingly, the electric displacement field at a point does not just depend on the electric field at that point but the electric field at other points in the neighbourhood of the examined point.

Spatial dispersion has been studied for decades since its discovery when considering excitons in crystals. Since then, it has been known that spatially dispersive media should support longitudinal electric fields with a plasma-like disper-

sion relation. Our theoretical analysis builds upon this knowledge to show that introducing an inhomogeneity into the plasma frequency can allow us to manipulate the behaviour of the medium to support the desired profile. The medium will then have a dependence on both position and wavevector. The dependence of a structure on conjugate Fourier variables has been explored in the literature [3]. We treat the resulting permittivity relation as a differential equation in our work.

Wire media are a well-studied set of metamaterial structures consisting of a lattice of parallel wires where the wire radius is small compared to the lattice constants. Here we understand a metamaterial to mean an artificial material made of inclusions with dimensions such that the structure is experienced as a homogenised material by electromagnetic waves in the considered frequency range. One of the interesting properties of wire media is that their homogenised effective properties are significantly spatially dispersive along the direction of their wires. Usually, when modelling structures, spatial dispersion effects are treated as negligible. Ignoring spatial dispersion while modelling wire media compromises the model's predictive power. Therefore, wire media are an ideal choice for a spatially dispersive medium into which we can attempt to introduce an inhomogeneity to produce our desired field profiles.

Using dielectric wire media as our starting point, we established the existence of longitudinal modes with a plasma-like dispersion relation in numerical simulations with CST microwave studio. Our work mainly utilised the eigenmode solver of CST. Using our investigation of the effect of the wire radius on the plasma frequency, we developed a scheme for controlling the plasma frequency; aided by the discovery that the relationship between these two parameters is remarkably well described by an exponential decay function. We can use this control to satisfy the conditions for the support of our desired field profile.

With some careful consideration, we were able to develop a method that given a desired profile and choice of parameters, typically the field frequency and a central radius, produces a function for the radius which if implemented in our wire media should replicate the chosen profile. We tested this method and showed in numerical simulations that a variety of desired profiles could be replicated accurately with a variety of chosen parameters.
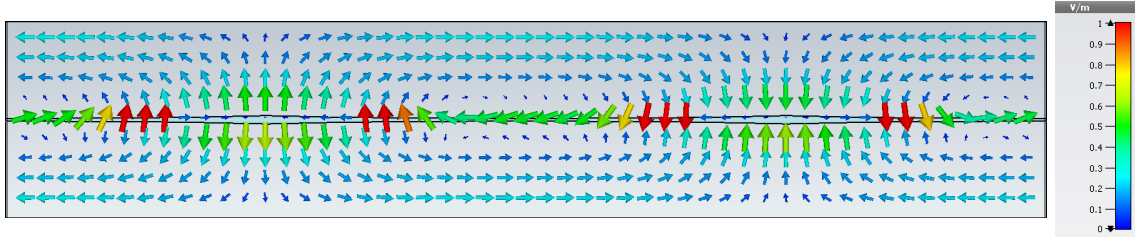
Figure 2.1: An image showing the resulting longitudinal mode after the implementation of the calculated radius function for a flattened profile (given by a solution to Mathieu's equation characterised by the Mathieu parameter $q = 0.8$) in an infinite dielectric wire medium ($\varepsilon_r = 1600$, $a_x = 13.06$ mm and $a_y = 15.00$ mm). The field is represented using arrow plots where the arrow direction represents field direction and colour represents the magnitude of the field strength.

We had therefore successfully demonstrated our method, but this was qualified by the fact that the structure used was an infinite wire medium of extremely high permittivity wires. Although these permittivity values are achievable using barium-strontium-titanate (BST), they do limit the scope of the validity of our result. Given this, we then worked to extend these successful results to a broader variety of representations of wire media.

This extension of our work proved to be fruitful; we demonstrated that our results held for a variety of different dielectric permittivities, as low as $\varepsilon_r = 3$. We achieved field profiling in finite wire media, and we made some progress in exhibiting field profiling in time domain simulations when excited by a waveguide port. We also extended our method to include the use of metallic wire media. This work alleviated concerns that our field profile shaping method was limited to a narrow and difficult to achieve set of wire media.

An example of the electric field supported in one of our dielectric wire media structures with a varying wire radius designed to produce a flattened profile is shown in Fig. 2.1.
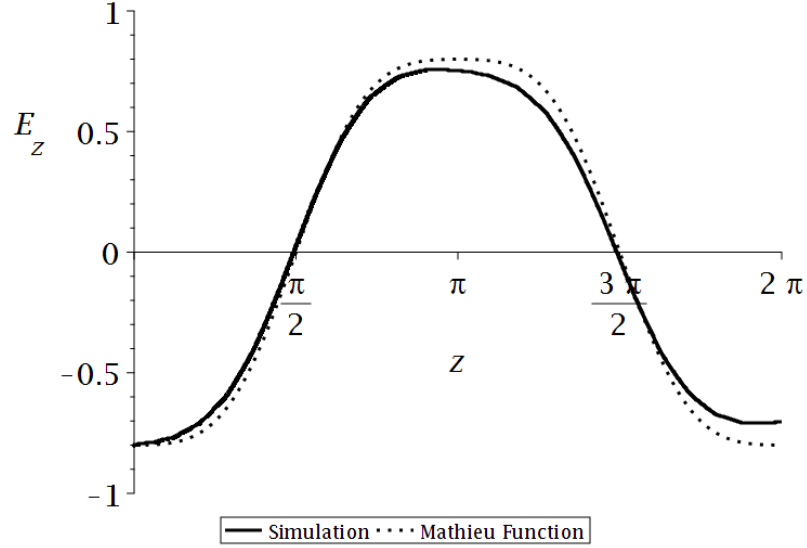
Figure 2.2: A plot of the field profile (longitudinal, z, spatial variation of the electric field strength, E_z) of a longitudinal mode in an infinite dielectric wire medium ($\varepsilon_r = 1600$, $a_x = 13.06$ mm and $a_y = 15.00$ mm) for our attempt to produce a flattened profile (which is a Mathieu function defined by parameter $q = 0.8$). The plot includes the field profile observed in our numerical simulation (solid black) and the desired profile (dotted black).

The profile of this mode is shown in Fig. 2.2 along with a comparison with the desired profile. This comparison clearly shows the success of our method. We have replicated our desired profile in our structure, using design parameters generated directly from the choice of profile, with a high degree of accuracy. In order to aid comparison the field profile from our simulation and the z coordinate have been scaled. As with all other plots of this type, the z coordinate has been scaled by $\frac{2\pi}{L}$ where L is the length of the unit cell and the E_z values have been scaled so that at $z = 0$ the field is equal to the Mathieu function value.

In total, we have developed and tested in numerical simulations a successful field profile shaping method that has proven to be incredibly flexible. We have demonstrated field profile shaping for a wide variety of different realisations of wire media for a variety of different profiles.

Chapter 3

Background

Our work touches upon a variety of areas of research that may be unfamiliar, such as wire media, spatial dispersion and methods for field profile shaping. In this section, we will endeavour to provide a suitable background to these areas and an understanding of how they factor into our work.

I. SPATIAL DISPERSION

The existence of spatial dispersion in wire media leads to interesting electromagnetic properties that we exploit in our field profile shaping method. As such, it is important to provide an overview of the phenomena of spatial dispersion.

I.1 History and definition of spatial dispersion

We can describe spatial dispersion with a comparison to temporal dispersion. Temporal dispersion is the well-known phenomena exhibited in media with a constitutive relation of the form shown in equation 3.1.

$$\hat{\mathbf{D}}(\mathbf{r}, \omega) = \hat{\varepsilon}(\omega)\hat{\mathbf{E}}(\mathbf{r}, \omega) \tag{3.1}$$

Here $\hat{\mathbf{D}}(\mathbf{r}, \omega)$ is the electric displacement field in position-frequency space, $\hat{\mathbf{E}}(\mathbf{r}, \omega)$ is the electric field in position-frequency space, $\mathbf{r}$ is the position vector, ω is the angular frequency and $\hat{\varepsilon}(\omega)$ is the position-frequency space permittivity. This representation of the electric field is related to the position-time representation, $\mathbf{E}(\mathbf{r}, t)$, by a Fourier transform as illustrated in equation 3.2.

$$\hat{\mathbf{E}}(\mathbf{r}, \omega) = \int_{-\infty}^{\infty} \mathbf{E}(\mathbf{r}, t)e^{i\omega t}dt \tag{3.2}$$

Using the same principle, we can find the expression for the position-time representation of the displacement field in a temporally dispersive media by applying the inverse Fourier transform to equation 3.1. This gives, using the convolution theorem, equation 3.3.

$$\mathbf{D}(\mathbf{r}, t) = \int_{-\infty}^{\infty} \varepsilon(t - t')\mathbf{E}(\mathbf{r}, t')dt' \tag{3.3}$$

Here $\varepsilon(t)$ is the permittivity in position-time space, the Fourier transform of $\hat{\varepsilon}(\omega)$ and is required by causality to equal zero for $t < 0$; and t' is a dummy variable used in the integration. The relationship between $\mathbf{D}$ and $\mathbf{E}$ in equation 3.3 is described as being local in the spatial argument and nonlocal in the temporal argument. Here the concept of locality refers to whether the relationship for a field at a coordinate depends on other coordinates and is closely tied with spatial dispersion. In the case of equation 3.3, for a given position $\mathbf{D}$ only depends on $\mathbf{E}$ at that point, whereas $\mathbf{D}$ at a given time depends on $\mathbf{E}$ at that time and earlier times. This leads to the phenomena of the dispersal of a wave packet travelling through a temporally dispersive medium.

As mentioned, spatial dispersion is related to non-locality. This is because in spatially dispersive materials the relation between $\hat{\mathbf{D}}$ and $\hat{\mathbf{E}}$ is non-local in the spatial argument. This is shown in the constitutive relation in equation 3.4.

$$\hat{\mathbf{D}}(\mathbf{r}, \omega) = \iiint_{-\infty}^{\infty} \hat{\varepsilon}(\mathbf{r} - \mathbf{r}', \omega)\hat{\mathbf{E}}(\mathbf{r}', \omega)d^3\mathbf{r}' \tag{3.4}$$

We can clearly see from equation 3.4 that with spatial dispersion $\hat{\mathbf{D}}$ at a point will not only depend on the $\hat{\mathbf{E}}$ field at that point but also on the $\hat{\mathbf{E}}$ field at other points in the neighbourhood of our examined point. A Fourier transform of the $\hat{\mathbf{D}}(\mathbf{r}, \omega)$ field relating it to $\tilde{\mathbf{D}}(\mathbf{k}, \omega)$ can be defined, as shown in equation 3.5 where $\mathbf{k}$ is the wavevector. $\hat{\mathbf{D}}(\mathbf{r}, \omega)$ is the function for the $\mathbf{D}$ field in position-frequency space, whereas $\tilde{\mathbf{D}}(\mathbf{k}, \omega)$ is the function for the $\mathbf{D}$ field in wavevector-frequency space.

$$\tilde{\mathbf{D}}(\mathbf{k}, \omega) = \iiint_{-\infty}^{\infty} \hat{\mathbf{D}}(\mathbf{r}, \omega)e^{-i\mathbf{k}\cdot\mathbf{r}}d^3\mathbf{r} \tag{3.5}$$

We can use the Fourier transform defined in equation 3.5 along with the constitutive relation in 3.4 to give a different representation of the spatially dispersive constitutive relation. This is shown in equation 3.6.

$$\tilde{\mathbf{D}}(\mathbf{k}, \omega) = \tilde{\varepsilon}(\mathbf{k}, \omega)\tilde{\mathbf{E}}(\mathbf{k}, \omega) \tag{3.6}$$

We will most commonly refer to a medium as spatially dispersive when its permittivity and constitutive relation depends on $\mathbf{k}$. The series of steps above is a commonly used description of spatial dispersion, as previously laid out in [4].

Spatial dispersion was first described decades ago when considering excitons in crystals. This analysis by Pekar found that the relationship between the polarization field, $\mathbf{P}$, and electric field, $\mathbf{E}$, was not described by a simple direct proportionality, but instead by a differential equation. This had the consequence of making Maxwell's equations higher order and leading to new, more complicated solutions. The discovery of spatial dispersion led to the prediction of the existence of longitudinal waves or fields in these crystals [5]. Our field profile

30

shaping method is built around these predicted longitudinal fields as laid out in Chapter 4.

The theoretical description of spatial dispersion was followed with experimental verification. Reflection spectra in crystals made of CdS and ZnTe could not be explained using classical approaches and required the use of a spatially dispersive model [6]. Experiments such as this established spatial dispersion as a real phenomenon that should be considered and could potentially be exploited.

I.2   Weak and strong spatial dispersion

In the literature, there is a distinction made between media with weak and strong spatial dispersion. This distinction goes beyond the relative magnitudes of the effects involved. According to [7], the presence of strong spatial dispersion in a structure destroys the continuity in its effective medium representation, while the presence of weak spatial dispersion does not.

In this thesis, the structures we consider exhibit strong spatial dispersion. The wavelengths considered are on the order of the lattice spacings, and the permittivity functions include higher orders of $\mathbf{k}$ [8]. It should, therefore, be understood that mentions of spatial dispersion in descriptions of our work refer to strong spatial dispersion.

I.3   Work in the area of spatial dispersion

Our interest in spatial dispersion is focused on its existence in wire media and our attempts to exploit it to achieve field profile shaping. There has been a significant amount of interest in the phenomena outside these areas. We will give a brief overview of some other areas of interest in spatial dispersion in this section.

One area of interest which followed straight from the initial description of spatial dispersion by Pekar is the need for additional boundary conditions (ABCs) [5]. As previously mentioned, the presence of spatial dispersion in a medium makes Maxwell's equations higher order and leads to the existence of new solutions. This is not a problem when considering the bulk of a medium or an unbounded medium, but complications do occur at boundaries and interfaces. The classical boundary conditions are not sufficient to uniquely describe the problem. This has major implications when trying to study reflection and transmission in spatially dispersive media and can be solved by introducing ABCs. The development and choice of these ABCs was a source of controversy as there is no single method for their development and different ABCs can be derived for the same structure. This has caused a significant amount of interest and literature on the subject [4, 9–20], including the consideration of boundaries in media with weak spatial dispersion [21].

A large amount of the early work on spatial dispersion continued to consider insulating crystals [6,22–25]. Pekar extended his description to a cubic crystal [22],

whereas others focused on experimental observation of the reflectance of crystals of CdS, ZnTe and GaAs [6] [24]. Thought was also given to how spatial dispersion would manifest itself in dielectrics that were finite or semi-finite [4, 12, 26, 27]. It should be noted that often the effects of spatial dispersion are analysed in terms of their effect on optical properties, such as reflection or absorption [9, 10, 12, 13, 26, 28–34].

Spatial dispersion was discovered in the context of excitons [5] and excitons continued to be a significant area of interest for the study of spatial dispersion for many years [23, 30, 35–38]. The interest in excitations continued with the study of polaritons in the context of spatially dispersive media [9–12, 14, 29, 39].

The work on spatial dispersion has not just focused on dielectric materials; spatial dispersion has also been considered in the description of plasmas [40, 41]. Nonlocal approaches have also been used in the theoretical study of metallic films [28, 42]. It has been shown that in a spatially dispersive dielectric the energy flux cannot be described using only the Poynting vector; it requires another term that describes the energy transported by excitons [37]. A generalized Poynting vector that accounts for nonlocal interactions has also been derived [43]. Spatial dispersion has also been linked to other research areas and phenomena: negative refraction [44], chirality [45, 46], transformation optics [47, 48] and the study of graphene [34].

A major area of research in the study of spatial dispersion in recent years is its effect in the developing field of artificial materials. Spatial dispersion has been considered in nanostructures [31, 32, 49, 50] and metamaterials [33, 51–56]. For our work, the most important development in this area was the demonstration of strong spatial dispersion in wire media [8], which form the foundation of our field profile shaping method. An illustration of such a wire medium is shown in Fig. 3.1. The work that has been laid out in this thesis was built upon the proposal in [20]. This paper was concerned with the theoretical analysis of inhomogeneous spatially dispersive media, which requires the dependence of ε on fourier conjugate variables k and z (in 1D) [3]. The possibility of controlling the field profile of usually sinusoidal fields was considered and wire media were suggested as a suitable medium [20].
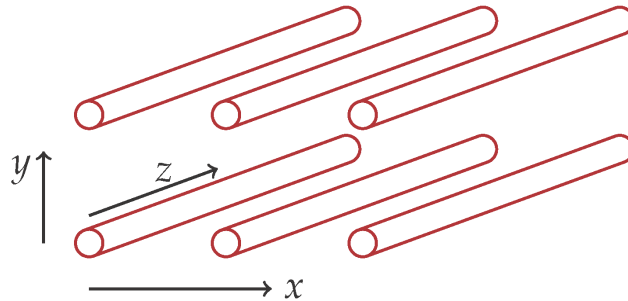
Figure 3.1: An illustration of a uniaxial wire medium oriented along the z axis.

II. Metallic wire media

Our method for field profile shaping is based on exploiting the spatial dispersion of wire media, which should provide longitudinal electric fields with a dispersion relation that we could manipulate. Wire media consist of a lattice of parallel wires, as shown in Fig. 3.1. Despite the fact that we first demonstrated field profile shaping in dielectric wire media, metallic wire media have traditionally been considered more frequently and have been shown to be strongly spatially dispersive [8].

Therefore, we will focus on the literature surrounding metallic wire media first. As a brief introduction, metallic wire media are a well-studied set of structures consisting of a lattice of parallel conducting wires where the wire radius is small compared to the lattice constants. Other configurations of wire media exist with wires spanning across multiple axes.

II.1 Original interest

Metal wire media have been studied for decades. In early papers, metallic wire media were commonly studied as an example of an artificial dielectric and referred to as a rodded medium [57–62]. Artificial dielectrics were defined as an array of conducting elements that achieves the behaviour that the phase velocity of light inside the medium differed from the free space phase velocity [57]. Artificial dielectrics should, therefore, enable the refraction of electromagnetic waves [58]. Rodded media were considered to be capable of achieving refractive indices of less than one [57]. Later work also considered rodded media to be capable of acting as an artificial plasma [62].

II.2 Metamaterials and homogenisation

Metallic wire media are now often classified as metamaterials or components of metamaterials [8]. As before, we understand a metamaterial to be an artificial material made of inclusions with dimensions such that the structure is experienced as a homogenised material by electromagnetic waves in the considered frequency range. Metamaterials are artificial structures that are formed from a collection of objects whose spacing and size are much smaller than the electromagnetic wavelength considered. Crucially these small length scales mean that the metamaterial can be considered a homogeneous medium characterised by an effective permittivity and permeability. This is analogous to the description of glass interacting with light as a homogeneous medium where we ignore the atomic detail of glass because the atomic scale is far smaller than the wavelength of light [63]. Our control over the elements making up the metamaterial gives us the ability to tune their properties and achieve properties not usually available in natural materials [64]. The field of metamaterials has attracted significant interest due to the possibility

of achieving negative refraction [63,65–67], sub-diffraction imaging [65,68–70] and perfect absorbers [71,72].
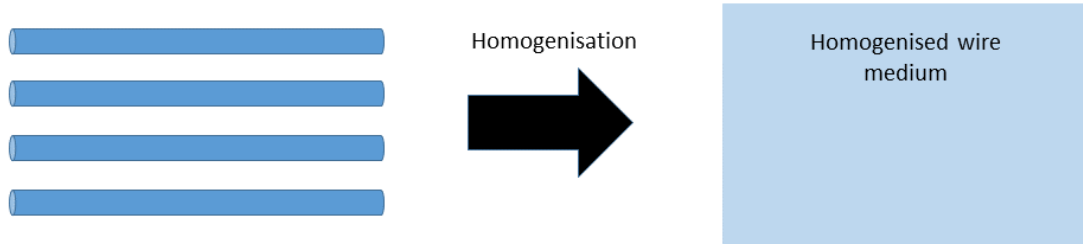
Figure 3.2: An illustration of the representation of a wire medium structure as a homogenised wire medium.

The process of describing a complex structure as a homogenous effective medium is called homogenisation, as illustrated in Fig. 3.2. Clearly, homogenisation plays a vital role in the characterization of metamaterials [73–77]. Homogenisation allows for the description of the metallic wire medium, which we use for field profile shaping, as a 1D medium with a non-local permittivity [8]. The approach taken in [8] is the one adopted in our work, but further work on the homogenisation of other realisations of wire media has been carried out by others [78–82].

II.3   Modern interest in metallic wire media

As we have mentioned, modern interest in metallic wire media structures has mainly been driven by their use as metamaterials. Here we will try to give an overview of the work done in this area and some of the possible applications of wire media. Our work has focused on uniaxial wire media that contain one lattice of parallel wires directed along a single axis [8]. Interest in wire media extends to other wire media geometries: two-dimensional [83], three-dimensional [84–87], crossed wires [88–96], mushroom type [97–101] and composite structures [102,103]. A number of different wire media geometries are shown in Fig. 3.3. A more comprehensive review of the field of metal wire media structures up until 2012 is given in [104].
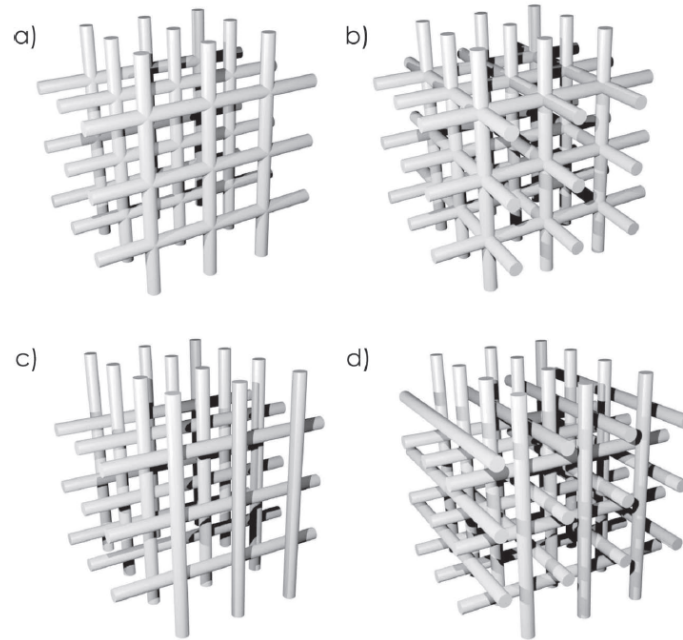
Figure 3.3: An illustration of a variety of different wire media geometries. (a) is a double connected wire media, (b) is a triple connected wire media, (c) is a double disconnected wire media and (d) is a triple disconnected wire media. This illustration initially appeared in [104].

The resurgence in the study of metallic wire media was partly due to a renewal in the interest of the plasmonic properties of wire media [85, 105–109]. Along with this, metallic wires were part of composite metamaterial structures involved with the exploration of left handed media and negative refraction [83, 102, 103]. Subsequently, there have been a large number of studies and homogenisations of various metallic wire media geometries [84, 86, 87, 100, 110–120]

One of the possible applications of metallic wire media that has been explored is the use of wire media as lenses with unique imaging properties [69, 89, 90, 93, 95, 96, 101, 121–136]. Some of these applications focus on subwavelength imaging of the near field [69, 94, 95, 123, 125, 129, 134, 135], whereas others focus on the transport of the near field, using a canalization regime, over several wavelengths [93, 122, 128, 132, 136]. An illustration of a subwavelength imaging scheme using wire media is shown in Fig. 3.4.
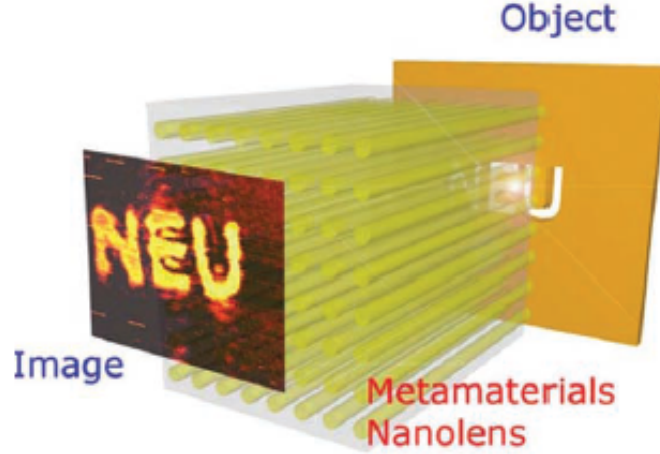
Figure 3.4: An illustration of a subwavelength imaging scheme using wire media [78].

Metallic wire media have also found applications in a large number of other areas. They have been shown to exhibit unique properties such as negative refraction [92, 99, 137–141], partial focusing [96, 142], extremely high refractive indices [88, 89] and anomalous dispersion [91]. Metallic wire media have also been studied in the realisation of antenna [143, 144], impedance surfaces [97, 98, 145], electromagnetic absorbers [146], periscope-like endoscopes [147] and image splitters [148]. There has also been some interest in their use in accelerator applications [149].

II.4 Spatial dispersion in metallic wire media

The most important area of research involving metallic wire media, for our purposes, is the exploration of their spatially dispersive properties. The work in [8] established the presence of strong spatial dispersion in uniaxial wire media, lattices of wire aligned along one axis, and provided a nonlocal model for the permittivity of the structure along the spatially dispersive axis. Based on an analysis of the polarization of the fields they establish a dyadic, or tensor, shown in equation 3.7 to describe the anisotropic nature of the permittivity of the structure.

$$\bar{\varepsilon} = \varepsilon \underline{u}_z \underline{u}_z + \varepsilon_0 (\underline{u}_x \underline{u}_x + \underline{u}_y \underline{u}_y) \tag{3.7}$$

Here ε is the axial permittivity and $\underline{u}_{x,y,z}$ are the base vectors of the coordinate system. From this dyadic, with reference to [150], they establish that the medium will have the dispersion relation given in equation 3.8 for an extraordinary plane wave ($E_z \neq 0$) with $\underline{k} = (k_x, k_y, k_z)$ and $\underline{E} = (E_x, E_y, E_z)$.

$$\varepsilon_0 \beta^2 c^2 (k_x^2 + k_y^2) = \varepsilon(\omega^2 - \omega_0^2 - \beta^2 c^2 k_z^2) \tag{3.8}$$

Here βc is the polariton velocity and ω_0 is the polariton resonance frequency. Polaritons are quasiparticles relating the the coupling of electromagnetic waves with excitations which are related to spatial dispersion. In the paper they note the use of the local model given in equation 3.9 for the permittivity along the wire axis [62, 111].

$$\varepsilon = \varepsilon_0 \left(1 - \frac{4\pi^2 f_p^2}{\omega^2 - \omega_0^2} \right) \tag{3.9}$$

Here $4\pi^2 f_p^2$ is the plasma frequency.

As Helmholtz's equation should also apply to the extraordinary plane waves they derive another condition for the wave. It is shown that equation 3.9 is incompatible with this new condition. This is solved in the paper by introducing a new non-local model for the axial permittivity, ε, in equation 3.10. The rigorous derivation of equation 3.10 is based on the work in [112].

$$\varepsilon(\omega, k_z) = \varepsilon_0 \left(1 - \frac{4\pi^2 f_p^2}{\omega^2 - \omega_0^2 - \beta^2 c^2 k_z^2} \right) \tag{3.10}$$

This permittivity is consistent with the condition from Helmholtz's equation and when substituted into equation 3.8 gives the dispersion relation in equation 3.11.

$$\beta^2 c^2 k^2 = \omega^2 - \omega_0^2 - 4\pi^2 f_p^2 \tag{3.11}$$

The use of these two different models leads to significantly different descriptions of the behaviour of metallic wire media. The non-local model predicts a stop band for extraordinary waves, at $4\pi^2 f_p^2$, that does not exist when using the local model. This established strong spatial dispersion as a significant effect in uniaxial metallic wire media and provided a model for their nonlocal permittivity [8].

After the discovery of the spatially dispersive properties of metallic wire media more work followed, including the realisation that all geometries of metallic wire media exhibit spatial dispersion to some degree [16, 80]. As with the discovery of spatial dispersion in crystals this led to an interest in the reflection properties of metallic wire media and the need for additional boundary conditions [16–19, 151–154], as well as other studies of the spatial dispersion in metallic wire media geometries [74, 78, 81, 83, 97, 98, 119, 120, 145, 155–160].

The spatial dispersion in metallic wire media has proved useful in some cases. It has allowed for the development of subwavelength imaging schemes [69, 122–125, 136], impedance surfaces [16, 17, 97, 145] and the exploration of epsilon-near-zero materials [144, 161]. The spatial dispersion in a crossed wire mesh has led to possible applications in the realisation of extreme refractive indices [88], subwavelength waveguides [88, 89], superlensing [90], negative refraction [92] and anomalous dispersion [91]. However, spatial dispersion is not always welcome with some making efforts to suppress the spatial dispersion in metallic wire media [108, 162].

Of the work following the demonstration of spatial dispersion in metallic wire media, one of the most relevant to this thesis is the work in [163]. In this paper the general outline of our field profile shaping method was first proposed. Spatial dispersion in wire media is considered and the possibility of modifying the radius of the wires, as shown in Fig. 3.5, to give a desired profile is suggested. The work in [163] does not attempt to demonstrate the field profile shaping effect but does propose it.
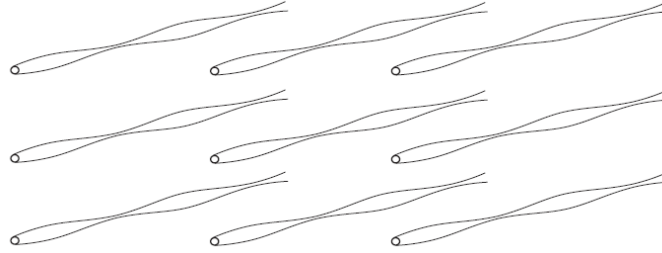
Figure 3.5: An illustration of a wire medium where the radius of the wires varies longitudinally [163].

III. Dielectric wire media

The wires in the structures we have considered have been metallic or dielectric. In the case of dielectric wire media, it may be more appropriate to refer to dielectric rods populating the lattice as the use of the word wire may suggest conductivity. These dielectric structures do not have as extensive a body of literature as their metal counterparts.

In the case of dielectric wire media, which was the starting point for the development of our field profile shaping method, the regime of its behaviour is dependent on the particular structural configuration. One scheme for the distinction of these regimes is that when a dielectric wire medium consists of tightly spaced rods with low permittivity or sparsely spaced rods with high permittivity the wire medium will behave as a metamaterial. Otherwise, they will behave as a photonic crystal. In the case when they act as metamaterials, this is due to the Bragg scattering length being less than the Mie scattering wavelength [164]. This concept is illustrated well in Fig. 3.6.
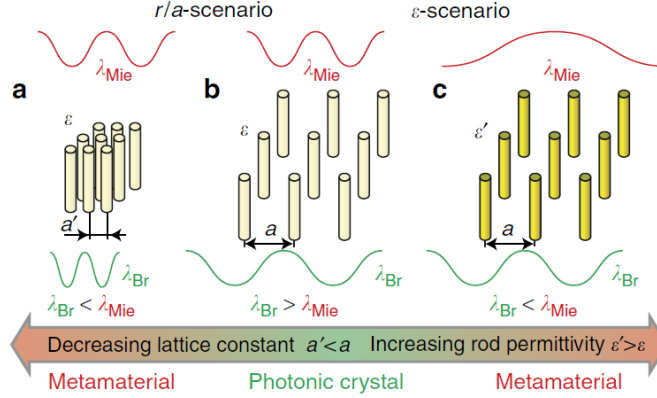
Figure 3.6: An illustration of the transition between different dielectric wire media regimes where the structures either act as metamaterials or photonic crystals [164].

Interest in dielectric wire media, or rodded media, has grown in recent years with attempts to realise metamaterial structures in the optical frequency range [164,165]. High permittivity dielectrics can be used to avoid the losses and saturation effects that occur in metals at this frequency range [166]. The high permittivity is also motivated by the desire to ensure these materials can be considered as effective media [165,167]. It should be noted that the presence of Mie resonances is critical to the electromagnetic behaviour of these structures [168].

These structures have been shown to exhibit interesting properties such as negative permeabilities, negative refractive indices and left-handed behaviour [165, 167,169–174]. This is not the only interest in artificial media made from dielectric wire lattices [175–181]. A review of the field of dielectric metamaterials up until 2018 is available in [182].

As far as we are aware, there is not an extensive body of literature of spatial dispersion in dielectric wire media. Although, in [165] it is demonstrated that strong spatial dispersion is a factor in dielectric wire media even in the long wavelength regime. This fits well with our experience of metallic wire media [8].

IV. FIELD PROFILE SHAPING

The realisation of field profile shaping is the aim of the design of our structures. By field profile shaping we mean the support of fields, in our case longitudinal electric fields, where the variation in field strength is given by a function chosen by ourselves rather than the usual sinusoidal variation. The spatial variation in the strength of a field is the field profile.

The attempt to control the electromagnetic properties of fields is an area of significant interest. Photonic crystals are used to control properties such as the transmission and the band gap [183–185]. In the emerging field of metaphotonics a greater level of control could enable zero electromagnetic response, chirality control and cloaking [186]. In the case of the field profile shaping method that

we have developed, a desired field profile can be generated directly using design parameters which result from the choice of profile. This direct method avoids the need for an iterative design of our structures and can be applied to a large variety of profiles [1, 2, 187].

This degree of control over the profile of an electromagnetic field could lend itself to a number of applications. In the case of accelerator application, crab cavities are currently used to tailor field profiles for the control of the particle bunch [188]. "Nose cone" profiles are used to concentrate the electric field, but these structures require an iterative design process not necessary for our profiling [189, 190]. This could lead to an interest in accelerator applications such as the shaping of electron bunches or use in plasma ionisation in laser wakefield accelerators [191, 192]. An illustration of a possible use of wire media in controlling the electric fields used in acceleration is shown in Fig. 3.7. Accelerator applications are complicated by the fact that we have little control over the temporal profile of the field experienced by particles. Other potential applications are the enhancing of ionisation in high harmonic generation [193–198]. It could also be imagined that flattened profiles with high gradients but minimised peak field values could be useful in applications where non-linearity is harmful. A field with a pronounced peak could also find use in signal processing where it could increase resolution [1, 2].
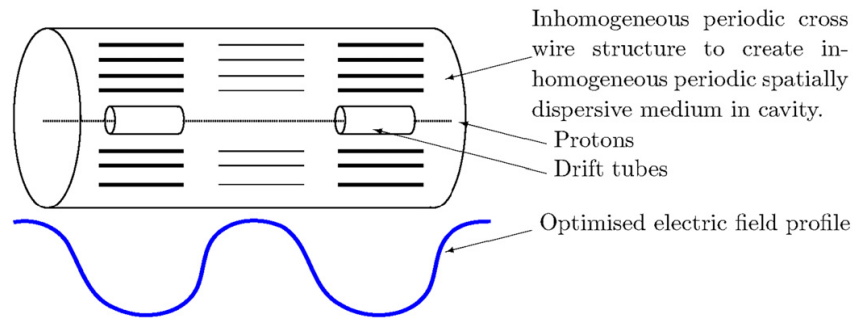
Figure 3.7: An illustration of the use of wire media to optimise electric fields in a particle acceleration setting [163].

The use of wire media to achieve field profile shaping is a unique approach, as far as the authors are aware. Although, it is interesting to note that there has been some interest in the study of electromagnetic fields resulting from charges travelling through spatially dispersive metallic wire media [199–207]. These papers have comprised studies of Cherenkov radiation in the structures with possible uses in diagnostics [199–202], studies of the radiation in planar and other geometries [203–206], and a proposal of a theoretical approach for describing the radiation associated with bunches travelling in wire media structures [207]. There has also been work on the effect of sinusoidally varying permittivities in photonic structures, but without considering the effect on the field profiles supported [208].

Other methods for achieving some level of control over the field profile do

exist. As already mentioned, the use of crab cavities and "nose-cones" is common in accelerators [188–190]. Sometimes radio-frequency quadrupoles are used that can give some degree of field profile control by the iterative design of their vane modulation [209–213]. The replication of a field profile has also been achieved using harmonic synthesis [214, 215]. A similarly prescriptive method for field profile shaping has been demonstrated that is limited to the control of transverse field profiles using blocks of different permittivities [216].

The method we have developed involves the use of spatially dispersive wire media. Based on the prediction of plasma-like longitudinal modes, we showed how an appropriate variation in the plasma frequency could give a desired profile. This desired profile is given by a solution to Mathieu's equation,

$$\frac{d^2y}{d\sigma^2} + (a - 2q\cos(2\sigma))\,y(\sigma) = 0 \tag{3.12}$$

which is a differential equation with a well-known set of solutions characterised by the choice of a and q. Here, y corresponds to the z component of the electric field and sigma to the z coordinate.

After confirming the existence of these modes in numerical simulations and exploring the effect of the wire radius, we were able to develop our method linking a desired profile with a required radius function. We have explored this work in some detail for dielectric wire media in [1, 2]. This thesis will expand on our previous publications, including the use of metal wire media and other developments.

V. Finite Element Analysis

The work carried out in this thesis largely centres on the use of CST microwave studio to simulate wire media structures [217]. This is an electromagnetic modelling software that utilises finite element analysis. It has several solvers available, but we have mainly used the eigenmode solver supplemented with some results from the time domain solver. In this section, we will give a brief overview of finite element analysis and the operation of these solvers.

Finite element analysis is a tool for studying systems that can be described by differential equations. The technique can be applied to a range of problems such as heat flow, structural analysis and, in our case, electromagnetism. What this method has in common for all these applications is that the model being analysed is first broken into small cells, on which the applicable governing equation is solved. In our simulations, this is Maxwell's equations. This set of discrete cells which make up the model is known as the mesh [218].

We have used tetrahedral meshing for our eigenmode simulations, where the model is broken up into tetrahedrons, and hexahedral meshing in our time domain simulations, where the model is broken up into hexahedrons. In the case of the tetrahedral mesh, CST first meshes the edges and faces of the elements in the

structure before then meshing the volume of the elements. This ensures that the mesh produced is consistent between different elements [219]. When modelling a structure with a hexahedral mesh, the mesh will not necessarily conform to material jumps. This is taken care of by the use of the finite integration technique and the Perfect Boundary Approximation. These techniques allow for a single cell to represent different materials, so avoiding the issues usually associated with 'staircase' approximation where a cell is filled with just one material causing problems when encountering curved surfaces [220].

Now that we have discussed the meshing of our structure, we will move onto the solvers used. The eigenmode solver, which was used for the bulk of our work, allows us to calculate the frequencies and field patterns of the modes supported in our structure. It does this by solving the eigenvalue equation, shown in equation 3.13, on our tetrahedral mesh.

$$\nabla \times [\underline{v}(\nabla \times \underline{E})] = \underline{\omega}^2 \underline{\varepsilon} \underline{E} \tag{3.13}$$

In equation 3.13 $\underline{\varepsilon}$ is the complex permittivity, $\underline{v}$ is the complex reluctivity and $\underline{\omega}$ is the complex angular frequency. These quantities are defined further below in equations 3.14-3.16.

$$\underline{\varepsilon} = \varepsilon'(\omega_0) - i\varepsilon''(\omega_0) \tag{3.14}$$

$$\underline{v} = v'(\omega_0) - iv''(\omega_0) \tag{3.15}$$

$$\underline{\omega} = \omega\left(1 + i\frac{1}{2Q}\right) \tag{3.16}$$

Where ω_0 is the evaluation frequency at which the permittivity and reluctivity are evaluated, x' is the real part of the complex quantities, x'' is the imaginary part of the complex quantities, and Q is the Q-factor, which is the ratio of stored energy and dissipated energy at the resonance frequency [219, 221].

As we have mentioned, the time domain solver utilises the finite integration technique on a hexagonal mesh. We have used the time domain solver to find field patterns at specific frequencies and for some limited analysis of the scattering parameters for our structures. In the time domain solver, as well as setting up our structure it is also necessary to define an excitation signal and ports for the entry of this signal. The solver solves a discretised version of integral Maxwell's equation on the mesh, to calculate the fields through time [219].

Chapter 4

Theory of spatial dispersion and profile shaping

Our aim is to develop a method for controlling the field profile of longitudinal electric modes, $E_z(z)$, by making changes to the geometry of our structure. We should mention that although our calculations are based on purely longitudinal electric modes, the modes in our simulation are largely longitudinal with some transverse components. This small perturbation from our theory has not proved to be a problem. We believed that we could achieve this for the modes defined in equations 4.1-4.4 in a direct manner using wire media.

$$\underline{E} = E(t,z)\underline{e_z} \tag{4.1}$$
$$\underline{P} = P(t,z)\underline{e_z} \tag{4.2}$$
$$\underline{B} = 0 \tag{4.3}$$
$$\underline{H} = 0 \tag{4.4}$$

Given the fields defined in equations 4.1-4.4, we can now consider the source free version of Maxwell's equations.

$$\nabla \cdot \underline{D} = 0 \tag{4.5}$$
$$\nabla \cdot \underline{H} = 0 \tag{4.6}$$
$$\nabla \times \underline{E} = -\frac{\partial \underline{B}}{\partial t} \tag{4.7}$$
$$\nabla \times \underline{H} = \frac{\partial \underline{D}}{\partial t} \tag{4.8}$$

Our definition of the fields mean equations 4.6 and 4.7 are automatically satisfied. The other two equations, 4.5 and 4.8, can be reduced to the following:

43

$$\frac{\partial \underline{D}}{\partial t} = 0 \tag{4.9}$$

$$\frac{\partial \underline{D}}{\partial x} = 0 \tag{4.10}$$

These conditions can be satisfied if $\underline{D} = 0$. Alternatively, the condition for this solution can be written in terms of $\underline{E}$ and $\underline{P}$ by using the conventional definition of $\underline{D}$, shown below in equation 4.11.

$$\underline{D} = \varepsilon \underline{E} = \varepsilon_0 \underline{E} + \underline{P} = 0 \tag{4.11}$$

Equation 4.11 is the condition for the existence of longitudinal electric modes, which we want to build our method around. To explore whether we can observe these modes in our wire medium, we must introduce a theoretical model for the electromagnetic response. We have taken this model from the literature [8]. Our chosen model describes a wire medium as a one dimensional spatially dispersive medium. It also describes them as an epsilon-near-zero material for certain values of frequency. All this information is encoded into the constitutive relation shown in equation 4.12.

$$\underline{\hat{P}}(\omega, k) = \frac{-4\pi^2 f_p^2 \varepsilon_0}{\omega^2 - \omega_0^2 - \beta^2 c^2 k^2} \underline{\hat{E}}(\omega, k) \tag{4.12}$$

Where f_p is the plasma frequency of the medium, ω_0 is the angular polariton frequency and $c\beta$ is the polariton velocity. Comparing equation 4.12 with equation 4.11, we can see that the condition for the existence of longitudinal modes is satisfied for a mode with the following dispersion relation:

$$4\pi^2 f_p^2 = \omega^2 - \omega_0^2 - \beta^2 c^2 k^2 \tag{4.13}$$

As we will be simulating our wire media in CST, where mode frequency is not given in terms of the angular frequency, it is helpful for us to rewrite equation 4.13. We can do this by introducing $f = \frac{\omega}{2\pi}$, $f_0 = \frac{\omega_0}{2\pi}$ and $\kappa = \frac{k}{2\pi}$.

$$f_p^2 = f^2 - f_0^2 - \beta^2 c^2 \kappa^2 \tag{4.14}$$

Equation 4.14 is the predicted dispersion relation for longitudinal electric modes in a wire medium, as derived from our one dimensional spatially dispersive model.

Before we can develop a method for mode profile shaping, we need to choose our profiles. We want our choice to give us a large variety of profiles which are all mathematically defined in as simple a manner as possible. Given this we chose to use the solution to Mathieu's equation, shown in equation 4.15.

$$\frac{d^2 y}{d\sigma^2} + (a - 2q \cos(2\sigma)) y(\sigma) = 0 \tag{4.15}$$

We can find a differential equation describing fields which have solutions of Mathieu's equation as their profile by making a change of variables and, to make things clearer, relabelling the function y. Changing y to P and introducing the change $\sigma = \frac{2\pi z}{L}$, with differential $\frac{dz}{d\sigma} = \frac{L}{2\pi}$ where L is a characteristic length scale of the system, gives:

$$\frac{L^2}{4\pi^2} \frac{\partial^2 P}{\partial z^2} + \left(a - 2q \cos\left(\frac{4\pi z}{L} \right) \right) P = 0 \tag{4.16}$$

Similarly, we can find a differential equation describing the behaviour of fields in wire media by Fourier transforming equation 4.12. With a little rearrangement this gives:

$$c^2 \beta^2 \frac{\partial^2 P}{\partial z^2} + 4\pi^2 \left(f^2 - \lambda^2 \right) P = 0 \tag{4.17}$$

Where $\lambda^2 = f_0^2 + f_p^2$ and corresponds to the cut-off frequency of the structure. We can now see the similarity between the Fourier transformed Constitutive relation and this form of Mathieu's equation that was a key reason for using Mathieu's equation as a source of profiles. If we compare equations 4.16 and 4.17 then we find the following relation for their agreement:

$$f^2 - \lambda^2 = \frac{c^2 \beta^2}{L^2} \left(a - 2q \cos\left(\frac{4\pi z}{L} \right) \right) \tag{4.18}$$

When looking at equation 4.18, we can see that the right hand side varies with z, whereas the left hand side is constant. In order to solve this, we can introduce a varying cut-off frequency, $\Lambda(z)$.

$$f^2 - \Lambda^2(z) = \frac{c^2 \beta^2}{L^2} \left(a - 2q \cos\left(\frac{4\pi z}{L} \right) \right) \tag{4.19}$$

Introducing the appropriate function $\Lambda(z)$ will satisfy this equation and will enable the support of our desired mode profiles in our wire media structure.

Equation 4.18 represents the culmination of our theoretical analysis of wire media. Using our simple one-dimensional model for wire media, we have derived a condition which if satisfied, will support field profiling. In other words, given a chosen Mathieu solution as a profile and after choosing fixed values for the free parameters, we can find a function for the plasma frequency that should support our desired field profile.

This theoretical analysis represents one half of the development of our field profiling method, as can be seen in Fig. 4.1. Knowing the plasma frequency variation required is not enough without knowing how to achieve the required values in our wire medium. This information can be gained from our numerical simulations of three-dimensional wire media structures. In these simulations, we expect to find these longitudinal modes with a dispersion relation as shown in equation 4.20.
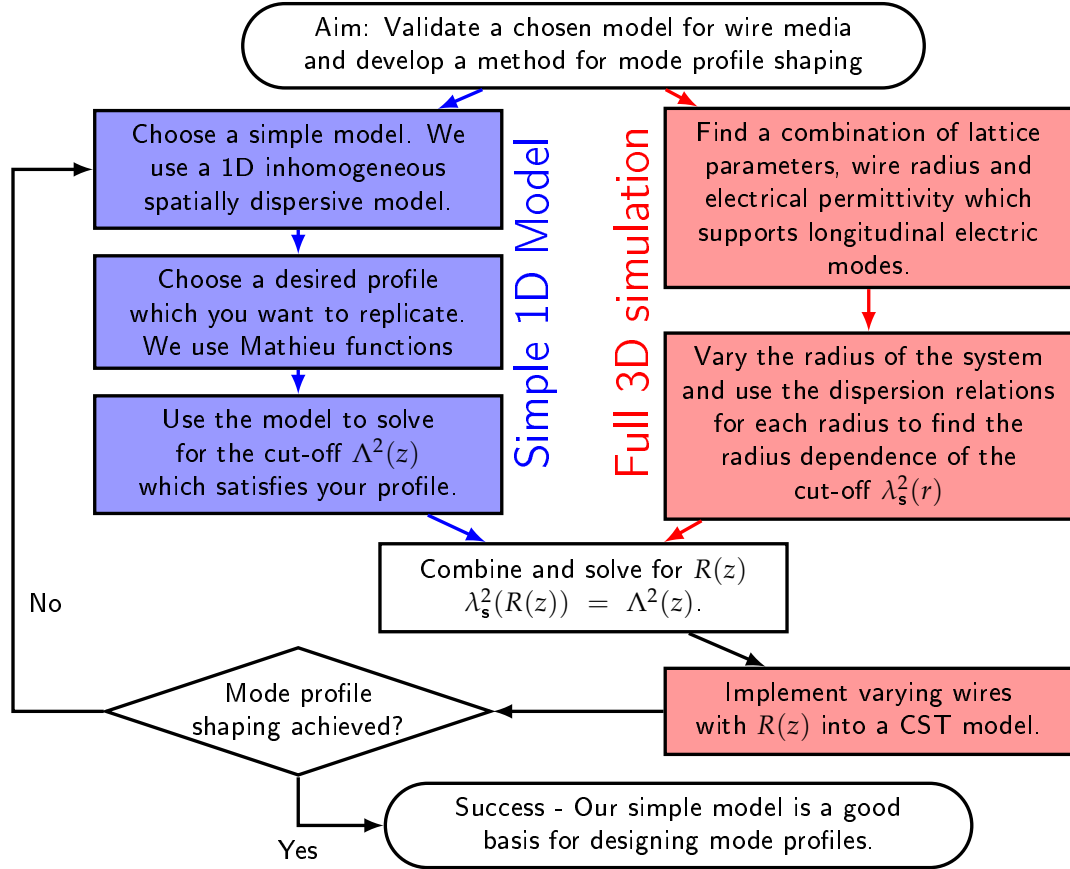
Figure 4.1: The steps used for generating and then validating our field profiling model.

$$\beta^2 c^2 \kappa^2 = f^2 - \lambda_s^2 \tag{4.20}$$

If we make the reasonable assumption, which we will attempt to verify in our simulations, that the simulation cut-off frequency, λ_s, has a radius dependency then we have a route to satisfy equation 4.19. With an analytic function for this relationship, $\lambda_s(r)$, we can find a radius function, $R(z)$, that will satisfy equation 4.19 by solving equation 4.21. These steps for developing a mode field profile shaping method are illustrated in a flowchart in Fig. 4.1.

$$\lambda_s^2(R(z)) = \Lambda^2(z) \tag{4.21}$$

Chapter 5

Confirming the existence of longitudinal electric modes

In Chapter 4, the prediction of the existence of longitudinal electric fields in wire media was detailed. This prediction was based on the use of a one-dimensional inhomogeneous spatially dispersive model of wire media. It was important to test this prediction was true for dielectric wire media, especially as the work this prediction was based on considered metallic wire media. In order to verify these predictions, we simulated our structure in the electromagnetic simulation software CST microwave studio.

A convenient starting point for these simulations was provided by the case of a single dielectric wire—or rod—in a system with periodic boundary conditions. Given such a set-up, we were effectively simulating an infinite lattice of dielectric wires. This is simple from a design and computational point of view, while also resembling the work providing the theoretical underpinning of our predictions.
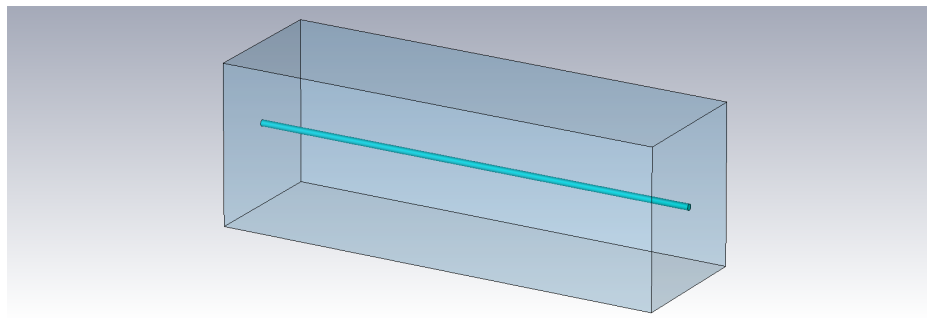
Figure 5.1: A typical representation of wire media in CST, consisting of a section of dielectric wire in a unit cell with periodic boundary conditions. This effectively represents an infinite dielectric wire medium.

There are a number of parameters we can vary when looking for our predicted longitudinal modes: the relative permittivity of the dielectric wires ε_r, the radius of the wires r, the wire spacings of the structure a_x and a_y, and the length L of our

unit cell. For an infinite periodic system, the length L of the unit cell should have no material effect on the results found.

An image from CST of a typical uniform radius wire medium structure, shown in Fig. 5.1, illustrates how simple these initial structure are to construct in CST. Eigenmode simulations show that the majority of the modes in such a structure are transverse modes, such as the one shown in Fig. 5.2. We should note that these simulations were carried out with a mesh generated based on the choice of four mesh cells per wavelength. After trying several combinations of parameter values, we were able to confirm the existence of longitudinal electric modes in our structure. It is worth noting that these modes were originally found with structural parameters $\varepsilon_r = 1600$, $r = 0.3$ mm and with zero loss tangent. These material values are achievable using ceramics such as barium-strontium-titanate (BST), but we will later show that we are not confined to this choice of material.

(a)

(b)
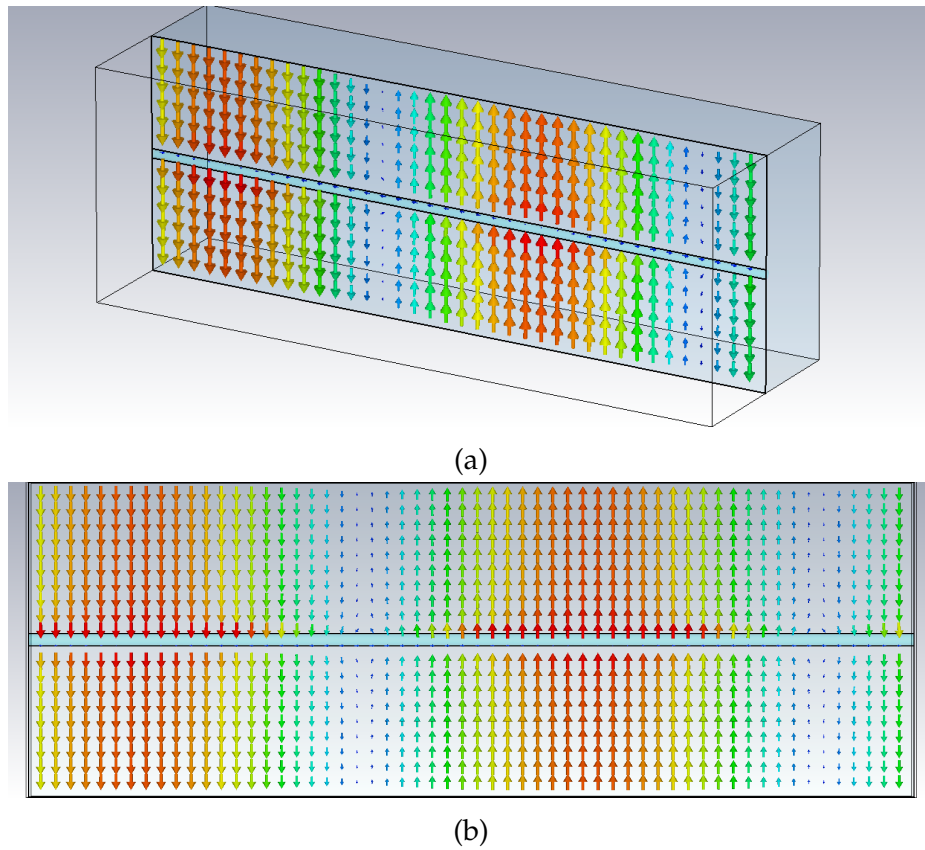
Figure 5.2: Numerical results showing a transverse electric mode, with a frequency of 6.85 GHz, in a representation of an infinite array of dielectric wires of relative permittivity 1600, radius 0.3mm, and wire spacings $a_x = 13.06$mm and $a_y = 15.00$mm. The electric field is represented using a vector plot where the arrow direction represents field direction and colour represents the magnitude of the field strength. (a) shows a perspective view of a y-z slice of the unit cell and (b) a view from the side of the same slice.

By looking at the longitudinal mode shown in Fig. 5.3, we can identify a few key features of the modes beyond its defining longitudinal nature. Firstly, they have a significant longitudinal component outside the wire in the region of free space. Also, comparing the field outside the wire with the field inside the wire we can see that they are anti-parallel, which is made clearer by Fig. 5.3b. In other words, the field inside the wire is oriented in the opposite direction to the field outside the wire.

(a)

(b)

(c)

(d)
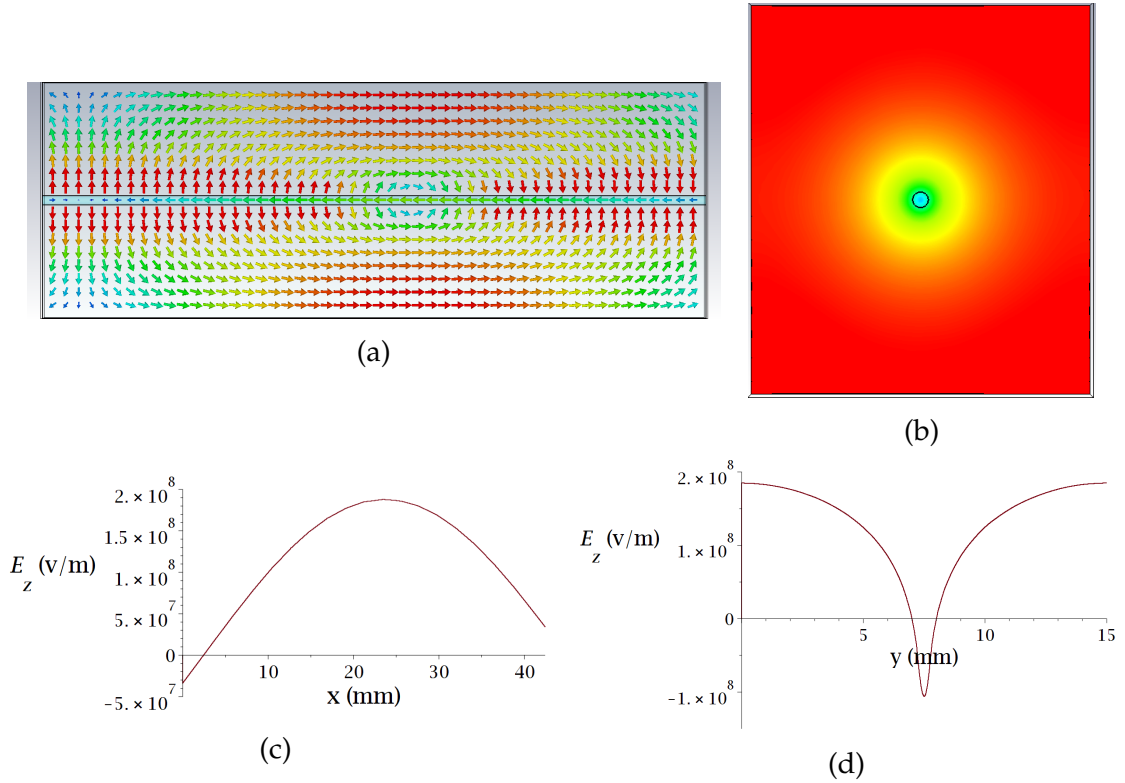
Figure 5.3: A series of images illustrating the characteristics of the longitudinal electric mode, with simulation frequency $f = 6.03$ GHz, we have found in our eigenmode simulation of an infinite dielectric wire medium ($\varepsilon_r = 1600$, $r = 0.3$ mm, $a_x = 13.06$mm and $a_y = 15.00$mm). (a) is an arrow plot of the field on a y-z slice of the structure where the electric field is represented using a vector plot where the arrow direction represents field direction and colour represents the magnitude of the field strength. (b) shows a colour plot of the longitudinal field on an x-y slice of the structure where the direction and magnitude of the field is represented by colour. (c) is a plot of the electric field strength along a line at the top of the structure directed along the axis of the wire, showing the profile of the mode. (d) is a plot of the electric field strength along a line from the bottom to the top of the structure passing through the dielectric rod.

Having confirmed the existence of longitudinal modes in our structure, we then needed to confirm that these longitudinal modes had the plasma-like disper-

sion relation that was predicted. This required varying the longitudinal phase set in our simulations and, hence, simulating the structure for different κ values. By doing this, we built up a plot of f against κ, shown in Fig. 5.4a.
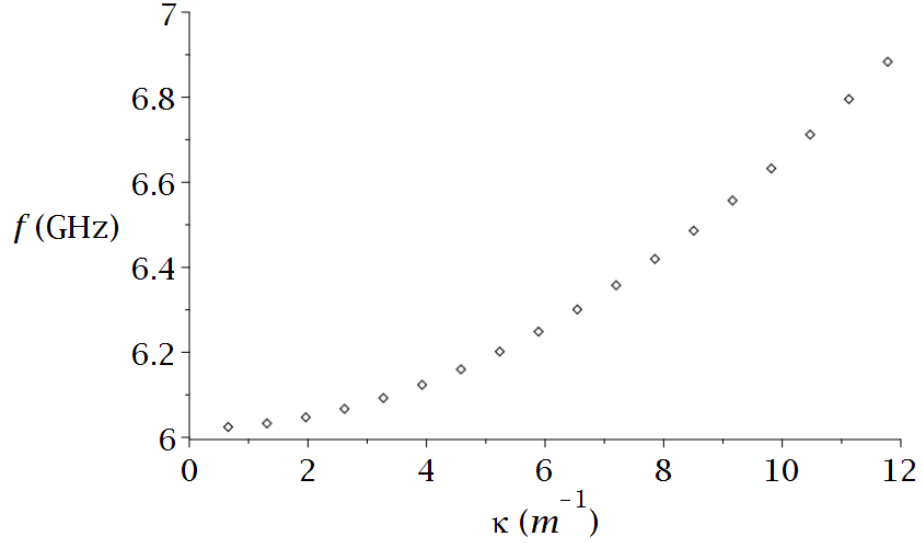
(a)
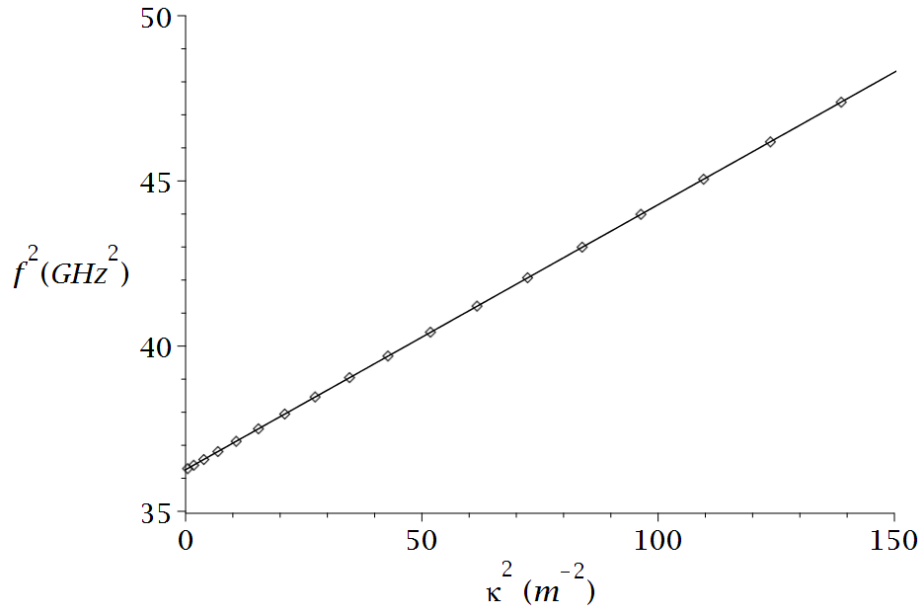
(b)

Figure 5.4: Plots of the dispersion relation of the longitudinal mode found in an infinite dielectric wire medium ($\varepsilon_r = 1600$, $r = 0.3$ mm, $a_x = 13.06$mm and $a_y = 15.00$mm) that demonstrate the mode's plasma-like dispersion relation. (a) is a plot of the frequency, f, against our wavenumber, κ, and (b) is a plot of f^2 against κ^2 along with a straight line fit which helps to demonstrate the plasma-like nature of the dispersion relation.
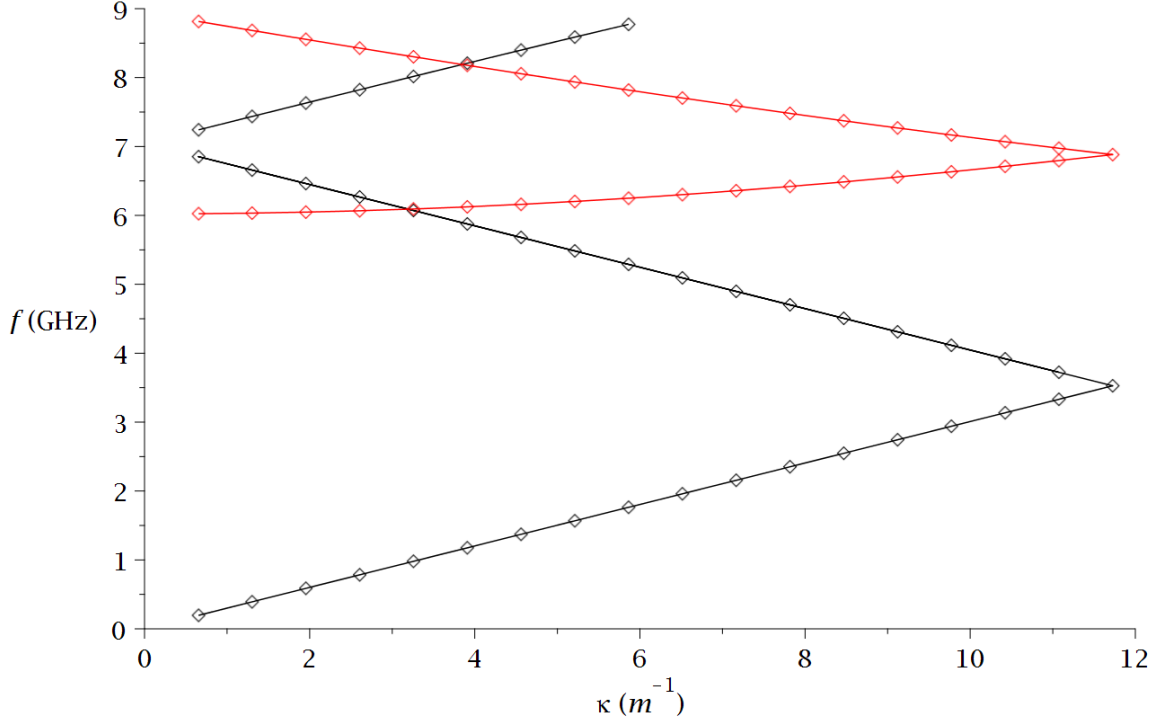
Figure 5.5: A band plot showing the dispersion curves of both transverse (black) and longitudinal (red) electric modes in an infinite dielectric wire medium ($\varepsilon_r = 1600$, $r = 0.3$ mm, $a_x = 13.06$ mm and $a_y = 15.00$ mm).

In order to confirm that the dispersion relation was correct we plotted f^2 against κ^2, as the curve should then obey the classic straight line formula—$y = mx + c$. We can see that this is true by looking at the predicted dispersion relation in equation 4.20. If we set f^2 as y and κ^2 as x then we will retrieve the straight line equation with $m = \beta^2 c^2$ and $C = \lambda_s^2$. Fig. 5.4b clearly shows that the relationship between f^2 and κ^2 is a straight line and, therefore, the dispersion relation for the simulated longitudinal modes is plasma-like. From this plot we can also find the plasma frequency, $\lambda_s = 6.02$ GHz, and phase velocity, $\beta = 0.94$, from the y intercept, C, and slope, m, of the line.

As well as finding the dispersion relation of the longitudinal modes, we ran simulations to observe the entire band structure of our structure, shown in Fig. 5.5. This was complicated by CST not being able to differentiate between different modes; modes are numbered in order of their frequency, so two modes can swap mode numbers as their frequencies cross with increasing κ. It is, therefore, necessary to adjust the plots manually to unpick the mode crossings. We can also see from Fig. 5.5 that the bands fold back on each other as a result of the periodic boundary conditions and the effect of the Brillouin zone.

One important factor to consider is the effect of the mesh on our results. Therefore, we have done a mesh analysis of our structure. Using our 0.3 mm radius

Mesh cells/wavelength	m_N	f (GHz)
4	34657	6.0247
5	47076	6.0237
6	58535	6.0240
7	72675	6.0245
8	91384	6.02425
9	110014	6.0237

Table 5.1: Table showing the cells per wavelength setting, total number of mesh cells (m_N) and the resulting frequency of the longitudinal mode found in an infinite dielectric wire medium ($\varepsilon_r = 1600$, $r = 0.3$ mm, $a_x = 13.06$mm and $a_y = 15.00$mm).

structures, we have ran repeated simulations while varying the mesh cells per wavelength setting in CST. The cells per wavelength examined, the resulting total number of mesh cells, m_N, and the resulting mode frequency of our longitudinal modes are shown in Table 5.1.
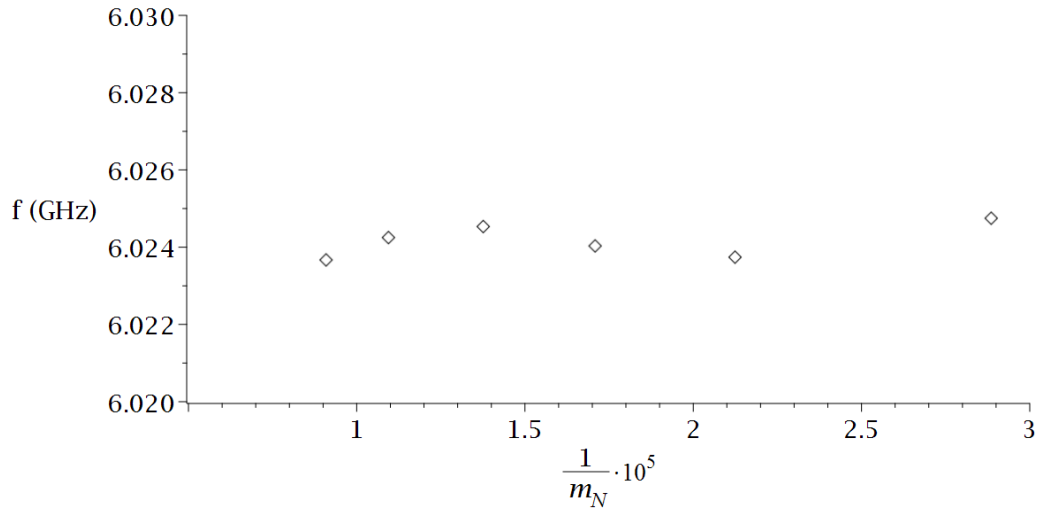
Figure 5.6: A plot of the frequency, f, of the longitudinal modes found in an infinite dielectric wire medium ($\varepsilon_r = 1600$, $r = 0.3$ mm, $a_x = 13.06$mm and $a_y = 15.00$mm) against the inverse of the total number of mesh cells, which has been scaled for ease of display.

As shown in Table 5.1, the frequency of our longitudinal mode does not vary significantly or with any discernible pattern. We can see this even more clearly in Fig. 5.6, which shows a plot of the longitudinal mode frequency against the reciprocal of the total number of mesh cells. As the reciprocal goes to zero, representing an infinite mesh, we would expect the frequency to converge on a value. What we observe is the frequency seemingly randomly varying in small degrees

around 6.024 GHz. This suggests that the meshes studied are already working well enough to give us an accurate result for our longitudinal mesh frequency. We have concluded that we can be satisfied with the mesh we are currently using (4 mesh cells per wavelength) and its ability to accurately model our system.

This work was a critical first step as it not only confirmed the existence of the modes that form the basis of our method, but it also validated our chosen theoretical model and its ability to predict the behaviour of our structure accurately.

Chapter 6

Mode profile shaping in infinite dielectric wire media

I. INVESTIGATING THE RADIUS DEPENDENCE OF OUR LONGITUDINAL MODES

In Chapter 5, we confirmed the existence of the longitudinal electric modes described in Chapter 4. We believed these modes and their properties could provide a route to mode profile shaping because their plasma frequency, a parameter present in our theoretical model, can be determined from our simulations and it is reasonable to think that it would be structurally dependent. This would provide a link between our theoretical model, which we can easily manipulate in order to find a condition for the support of our desired mode profiles, and the 3D simulated structure we are designing.

The structural parameter we chose to focus on was the radius of the dielectric wires. Therefore, it was necessary to confirm that the plasma frequency of our wire media does depend on wire radius. To do this, we ran simulations of our structures with different radii, keeping all other parameters constant. In Fig. 6.1 we can see the longitudinal modes found for several wire radii. It is clear that the key features of these modes are unchanged by the varying of the radius; there is a strong longitudinal component in the wire and between the wires, and the fields in these regions are anti-parallel. One observation we can make from these images is that the field in the wires seems to be stronger for smaller radii. This is clearer in Fig. 6.2 where the longitudinal field strength of the modes for each radii is plotted along a line from the top to the bottom of the structure.
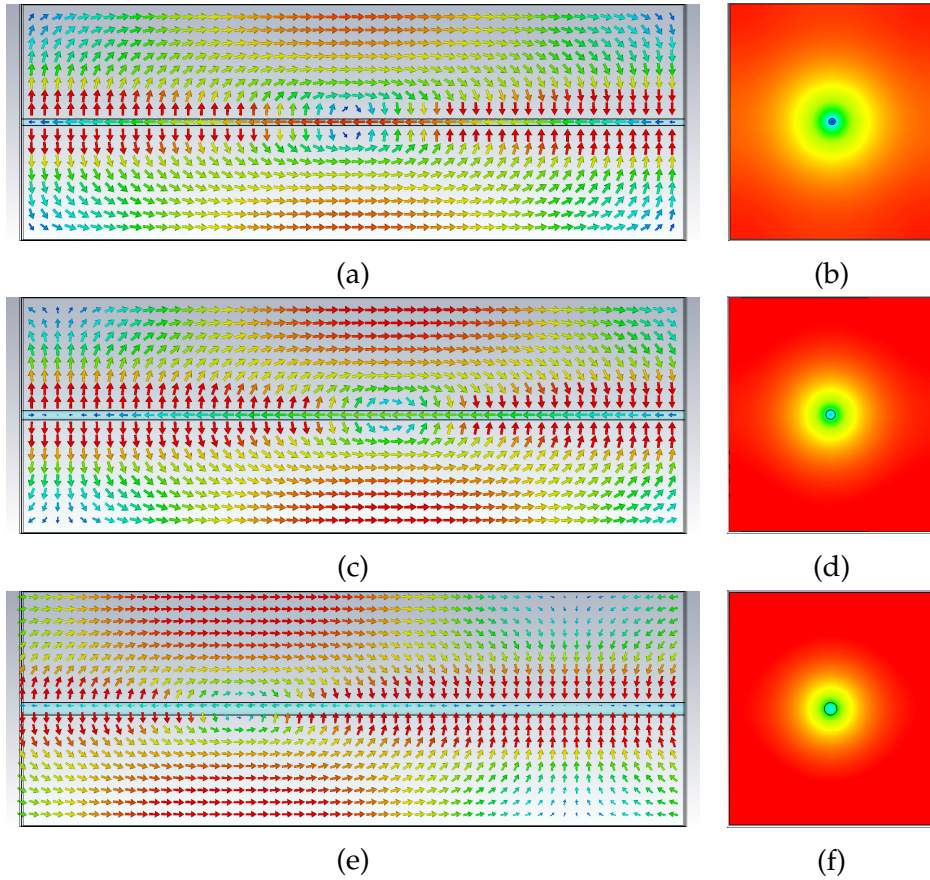
Figure 6.1: A series of images from numerical simulations in CST showing the longitudinal modes found in infinite dielectric wire media ($\varepsilon_r = 1600$, $a_x = 13.06$ mm and $a_y = 15.00$ mm) with a variety of radii. The fields are either represented using arrow plots where the arrow direction represents field direction and colour represents the magnitude of the field strength, or colour plots where the direction and magnitude of the longitudinal field is represented by colour. (a) and (b) show a longitudinal mode ($f = 6.60$ GHz) in a wire medium with $r = 0.2$ mm, with (a) showing a y-z slice and (b) an x-y slice. (c) and (d) show a longitudinal mode ($f = 6.02$ GHz) in a wire medium with $r = 0.3$ mm, with (c) showing a y-z slice and (d) an x-y slice. (e) and (f) show a longitudinal mode ($f = 5.89$ GHz) in a wire medium with $r = 0.4$ mm, with (e) showing a y-z slice and (f) an x-y slice.
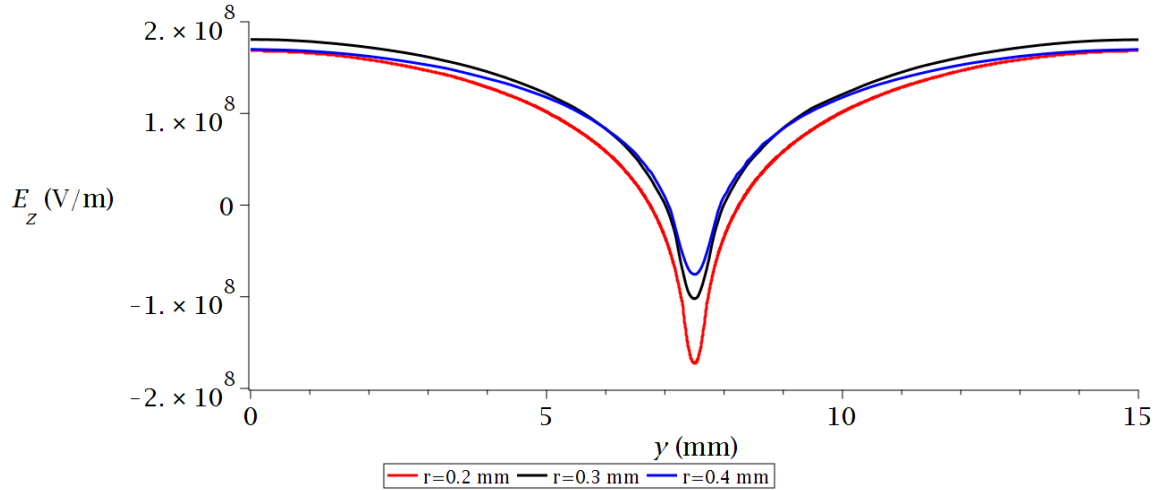
Figure 6.2: A plot of the variation of the electric field strength of the longitudinal modes found in infinite dielectric wire media ($\varepsilon_r = 1600$, $a_x = 13.06$ mm and $a_y = 15.00$mm), with a variety of radii, against the position, y, along a line from the top to the bottom of the structure, which passes through the dielectric rod. The radii are 0.2 mm (red), 0.3 mm (black) and 0.4 mm (blue).
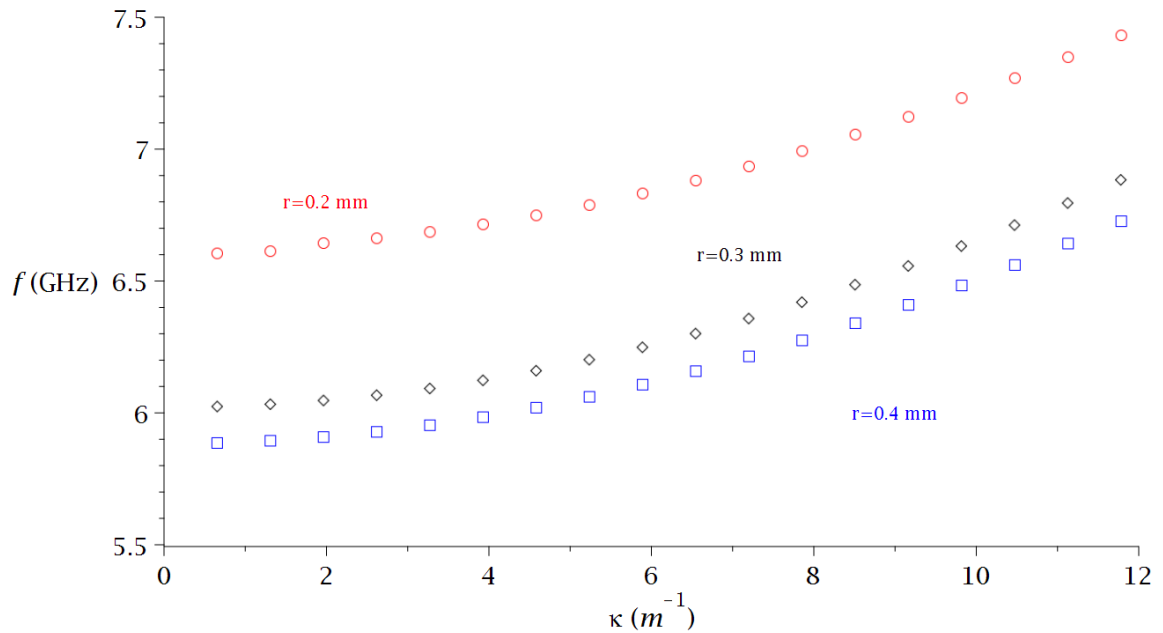
Figure 6.3: The dispersion plots, frequency (f) against wavenumber (κ), of the longitudinal modes in infinite dielectric wire media ($\varepsilon_r = 1600$, $a_x = 13.06$ mm and $a_y = 15.00$ mm) with a variety of radii. The radii are 0.2 mm (red), 0.3 mm (black) and 0.4 mm (blue).
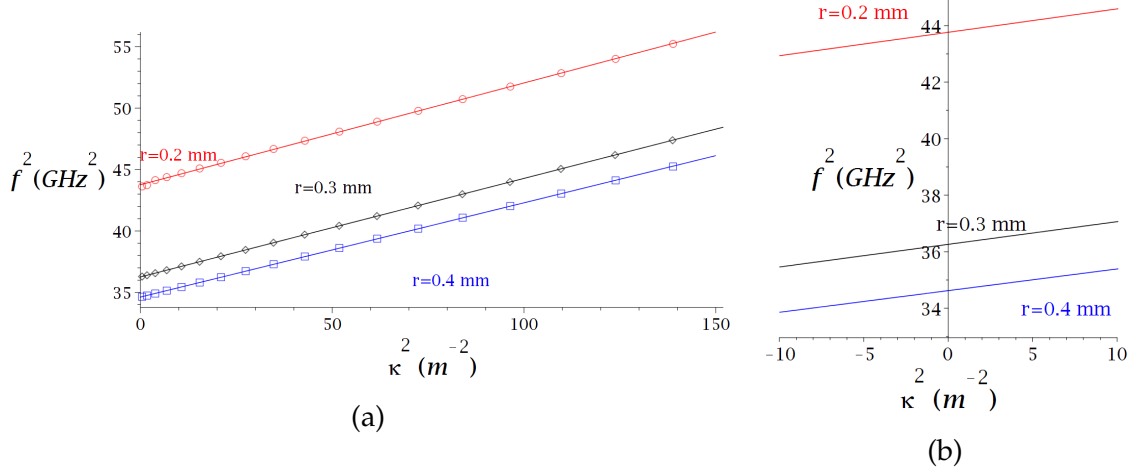
Figure 6.4: Plots of frequency squared, f^2, against wavenumber squared, κ^2, for the longitudinal modes in infinite dielectric wire media ($\varepsilon_r = 1600$, $a_x = 13.06$ mm and $a_y = 15.00$ mm) with a variety of radii. Straight line fitting curves have been included for each radii. The radii shown are 0.2 mm (red), 0.3 mm (black) and 0.4 mm (blue). (a) shows the plots and the fitting curves, whereas (b) shows only the fitting curves as they cross the y-axis to emphasise their different intercept values.

Having found these longitudinal modes for a variety of radii, we then plotted their dispersion relation. It is clear from Fig. 6.3 that the radius of the wires affects the dispersion relation of the longitudinal modes. We then repeated the method established in Chapter 5 of plotting κ^2 against f^2, the results of which are shown in Fig. 6.4. The agreement between this data and their straight line fitting curves can be quantified by looking at the R^2 value for these comparisons. R^2 values closer to 1 mean a greater agreement between the data and the fitting curve. The R^2 values for the 0.2 mm, 0.3 mm and 0.4 mm plots are 0.9997, 0.9999, 0.9999 respectively.

The definition of the R^2 value, which quantifies the agreement between a data set and a fitting function, we have used in this thesis is set out below:

$$R^2 = 1 - \frac{SS_{reg}}{SS_{tot}} \tag{6.1}$$

$$y_{av} = \frac{1}{N} \sum_{i=1}^{N} y_i \tag{6.2}$$

$$SS_{tot} = \sum_{i=1}^{N} (y_i - y_{av})^2 \tag{6.3}$$

$$SS_{reg} = \sum_{i=1}^{N} (f(x_i) - y_{av})^2 \tag{6.4}$$

Where SS_{reg} is the regression sum of squares, SS_{tot} is the total sum of squares, N is the number of data points, x_i is the x coordinate of the ith data point, y_i is the

57

y coordinate of the ith data point, y_{av} is the average value of the y coordinates of the data and $f(x)$ is the fitting function evaluated.

By looking at Fig. 6.4b, we can see the effect of varying the wire radius on the y-intercept and, hence, the cut-off frequency, λ_s. We have shown that changing the radius does affect λ_s. More importantly, this allows us to build up a set of data relating the plasma frequency of infinite dielectric wire media and the wire radius, as shown in Fig. 6.5.
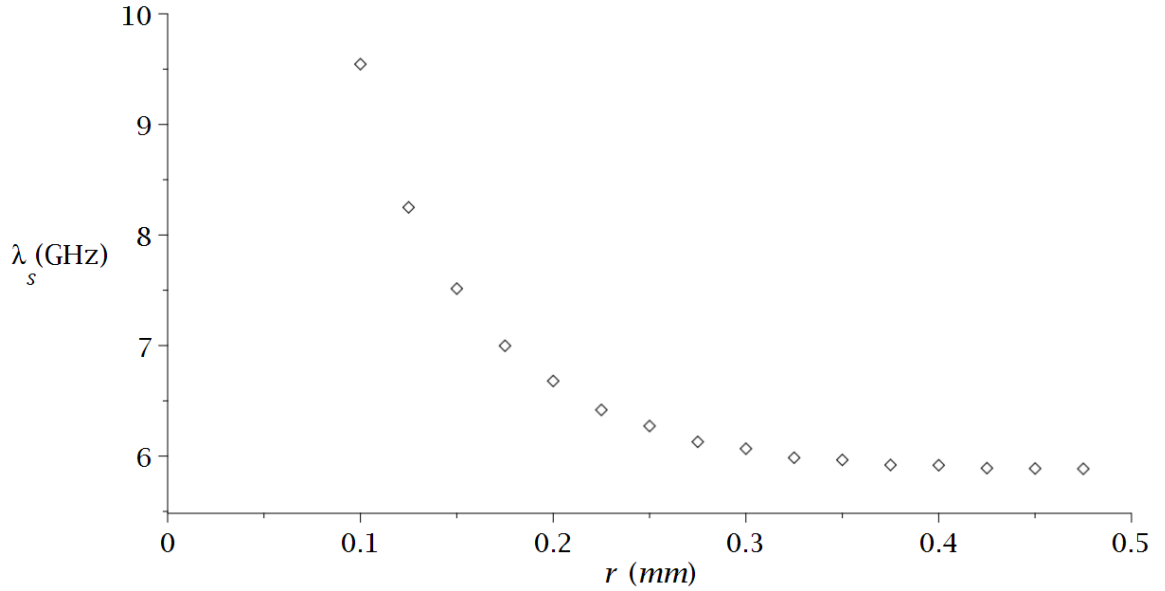
Figure 6.5: A plot of the plasma frequency, λ_s, of infinite dielectric wire media ($\varepsilon_r = 1600$, $a_x = 13.06$ mm and $a_y = 15.00$ mm) against wire radius, r.

As covered in Chapter 4, our method for mode profile shaping relies on us finding an analytic relationship between the plasma frequency and wire radius. As plasma frequency appears in our calculations as a squared quantity, the relationship we are most interested in is λ_s^2 vs. r. We can easily take the data from Fig. 6.5 and produce the required data, which is shown in Fig. 6.6.
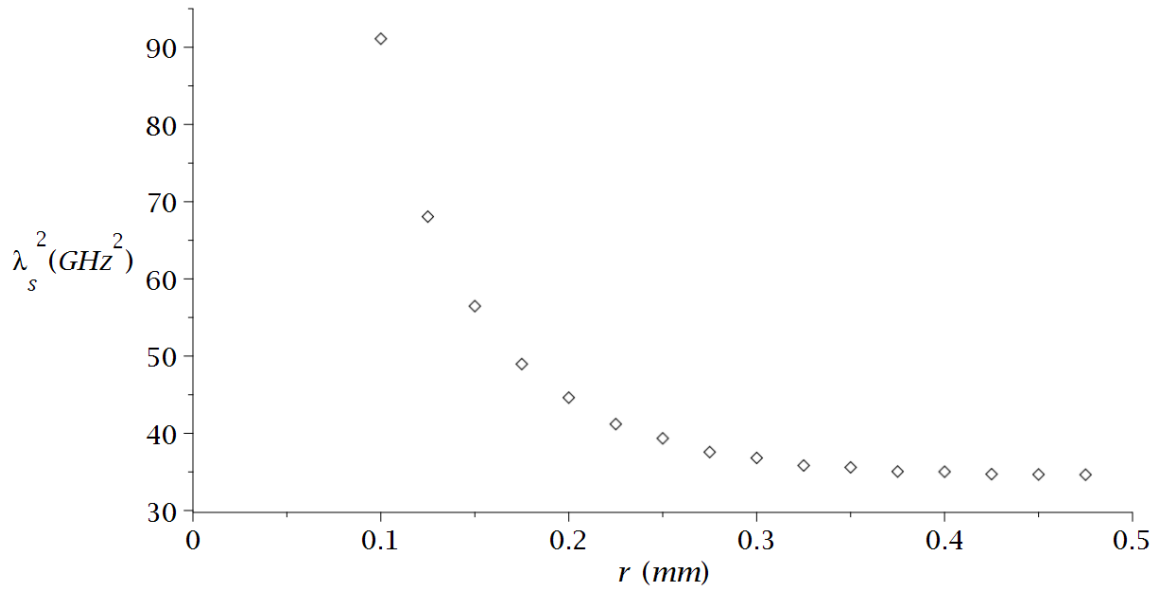
Figure 6.6: A plot of the plasma frequency squared, λ_s^2, of infinite dielectric wire media ($\varepsilon_r = 1600$, $a_x = 13.06$ mm and $a_y = 15.00$ mm) against wire radius, r.
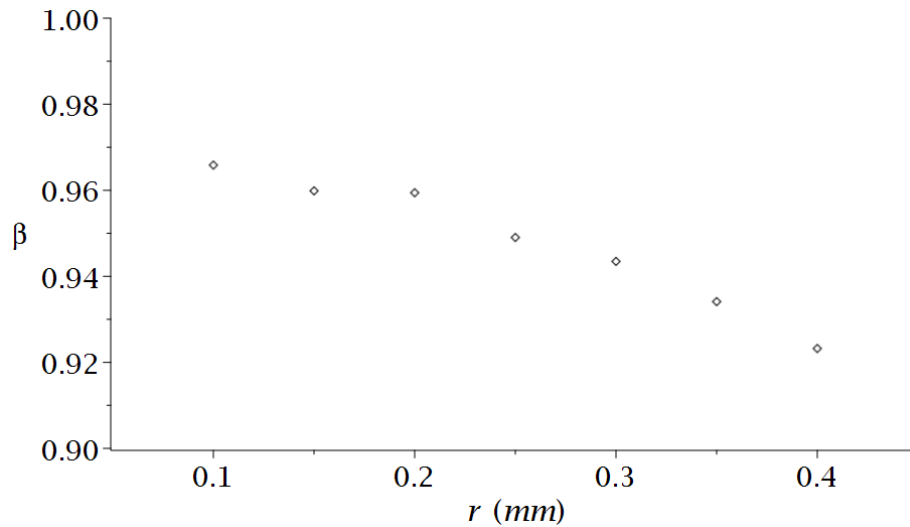
Figure 6.7: A plot of the phase velocity, β, of infinite dielectric wire media ($\varepsilon_r = 1600$, $a_x = 13.06$ mm and $a_y = 15.00$ mm) against wire radius, r.

As well as obtaining the plasma frequency for each radius, we can also find the β value. β is the polariton velocity which appears in the dispersion relation of our longitudinal modes. As mentioned in Chapter 4, our method for achieving mode profile shaping assumes a constant β value. We can see from Fig. 6.7 that this is a simplification. The actual relationship between β and r is an irregular but steady decline as r increases. In the range of data examined β decreases from 0.966 to 0.923, a percentage decrease of 4.5 %. Despite this not insignificant decrease in

β across our examined range, we have assumed a constant β value of 0.96. Our results in later chapters show this simplification does not cause any significant hindrance to our method.

II. Finding an accurate analytic relationship to describe the radius dependency

To find the required analytic relationship between the plasma frequency and wire radius of dielectric wire media, we needed to find an accurate fit for the data shown in Fig. 6.6. Our initial idea was to fit the data with a second order polynomial, shown in equation 6.5 where a_i are the fitting parameters. Fig. 6.8 shows an attempt to use a second order polynomial to fit the data shown in Fig. 6.6. It is clear from looking at Fig. 6.8 that a second order polynomial is a weak fit to the data.

$$\lambda_s^2(r) \approx a_0 + a_1 r + a_2 r^2 \tag{6.5}$$
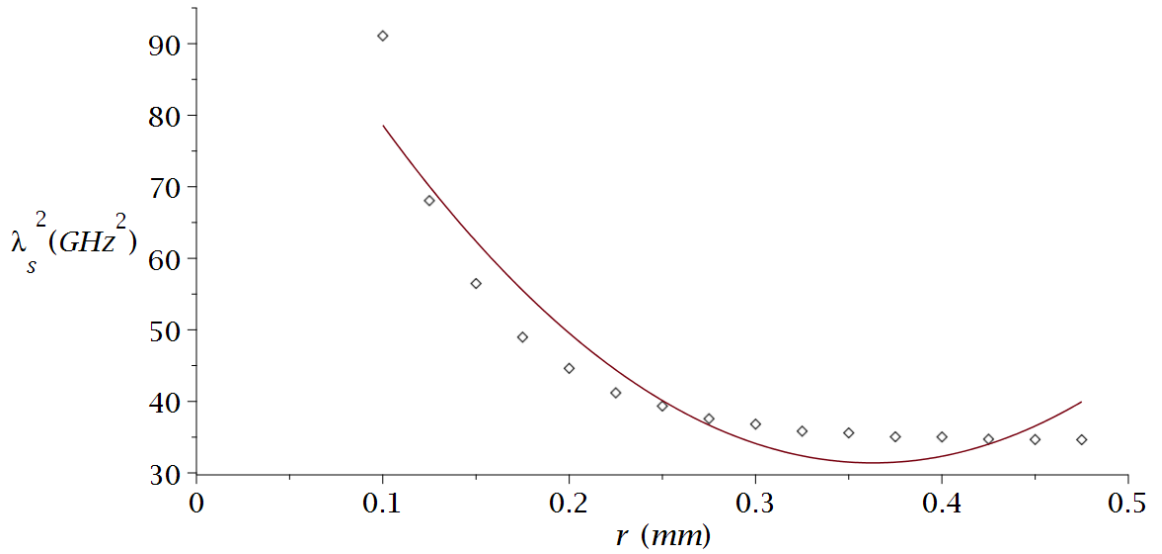
Figure 6.8: A plot of the plasma frequency squared, λ_s^2, of infinite dielectric wire media ($\varepsilon_r = 1600$, $a_x = 13.06$ mm and $a_y = 15.00$ mm) against wire radius, r, with a polynomial fitting curve.

After some initial efforts to use the second order polynomial fit, a first order exponential decay curve, of the form shown in equation 6.6, was attempted as a fitting curve. The results of this attempt are shown in Fig. 6.9 and it is clear even from a qualitative standpoint that this a far more successful method of fitting the data.

$$\lambda_s^2(r) \approx \delta + \sigma \exp\left(-\frac{r}{\rho}\right) \tag{6.6}$$

Our initial impression of the relative merits of the two fitting curves is only emphasised by looking at quantitative measures of their accuracy. Table 6.1 shows a series of figures of merit for the two fitting curves: χ^2, or the residual sum of squares, is an indicator of how tight the curve fits the data, with a small value being a tighter fit; $\mathfrak{R}^2$ is a measure of how well the fitting curve explains the variation of the data, with values closer to 1 being most accurate; and the RMSE, root mean square error, is a measure of how well the curve predicts the behaviour of the data, with values closer to 0 being better. Looking at the figures of merit in Table 6.1 confirms that the exponential decay curve is a vastly superior fitting curve. Also, looking purely at the figures of merit for the exponential decay curve, we can see that it is an accurate fit for the data. This degree of accuracy suggests that there is an underlying physical reason for this relationship between λ_s^2 and r.
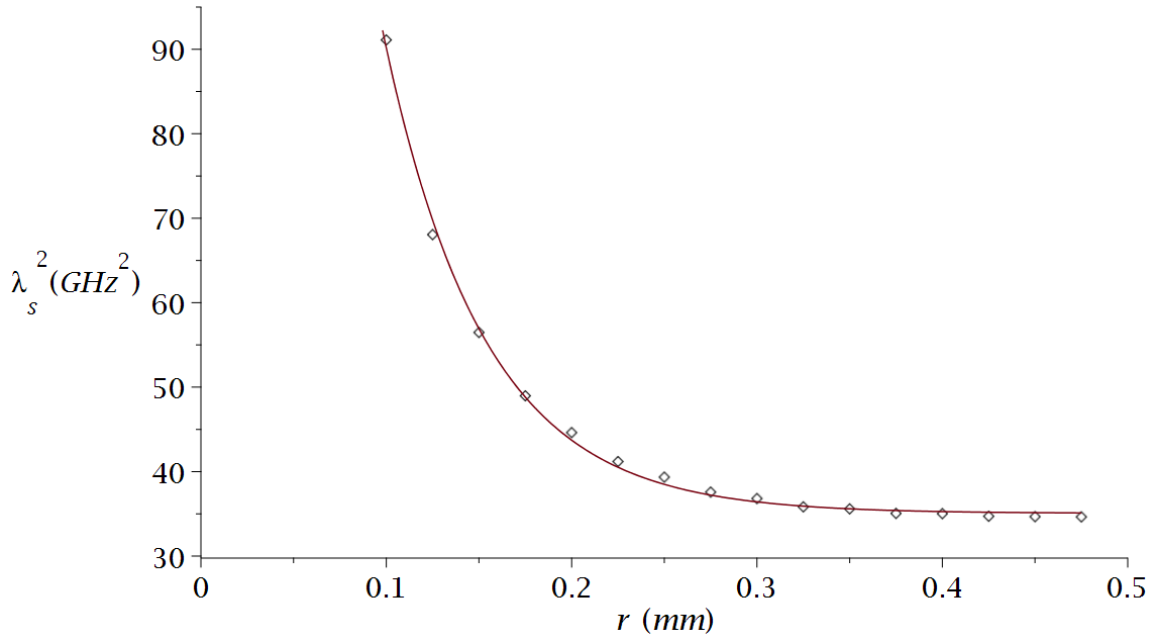
Figure 6.9: A plot of the plasma frequency squared, λ_s^2, of infinite dielectric wire media ($\varepsilon_r = 1600$, $a_x = 13.06$ mm and $a_y = 15.00$ mm) against wire radius, r, with an exponential decay fitting curve.

Fitting Curve	χ^2	$\mathfrak{R}^2$	RMSE
Polynomial	362	0.901	5.27
Exponential Decay	7.12	0.998	0.740

Table 6.1: A comparison of figures of merits for polynomial and exponential decay fitting curves for the λ_s^2 vs. r data for infinite dielectric wire media ($\varepsilon_r = 1600$, $a_x = 13.06$ mm and $a_y = 15.00$ mm).

III. Developing a method for mode profile shaping

With an analytic expression that relates the plasma frequency and radius accurately, we were able to develop our method for controlling the field profile of our longitudinal modes. As covered in more detail in Chapter 4, we have shown that the longitudinal profile of these modes will be given by the solutions of Mathieu's equation, if equation 4.21 is satisfied. This condition has been reproduced in equations 6.7 and 6.8, below, for convenience.

$$\Lambda^2(z) = f^2 - \frac{\beta^2 c^2}{L^2}\left[a - 2q\cos\left(\frac{4\pi z}{L}\right)\right] \tag{6.7}$$

$$\lambda_s^2(R(z)) = \Lambda^2(z) \tag{6.8}$$

Introducing the approximate, but highly accurate, function for the radius dependency of λ_s^2, shown in equation 6.6, into equations 6.7 and 6.8 gives:

$$\delta + \sigma \exp\left(-\frac{R(z)}{\rho}\right) = f^2 - \frac{\beta^2 c^2}{L^2}\left[a - 2q\cos\left(\frac{4\pi z}{L}\right)\right] \tag{6.9}$$

We can solve equation 6.9 to give an $R(z)$ function that if satisfied will give our desired profile, as specified by our choice of the Mathieu parameters a and q. The resulting $R(z)$ function is shown in equation 6.10.

$$R(z) = -\rho \ln\left(\frac{f^2 - \delta}{\sigma} - \frac{\beta^2 c^2}{L^2 \sigma}\left[a - 2q\cos\left(\frac{4\pi z}{L}\right)\right]\right) \tag{6.10}$$

This can be written more simply, to emphasise the form of the $R(z)$ solution, as:

$$R(z) = -\Gamma_1 \ln\left(\Gamma_2 + \Gamma_3 \cos(\Gamma_4 z)\right) \tag{6.11}$$

$$\Gamma_1 = \rho \tag{6.12}$$

$$\Gamma_2 = \frac{f^2 L^2 - \delta L^2 - \beta^2 c^2 a}{L^2 \sigma} \tag{6.13}$$

$$\Gamma_3 = \frac{2\beta^2 c^2 q}{L^2 \sigma} \tag{6.14}$$

$$\Gamma_4 = \frac{4\pi}{L} \tag{6.15}$$

IV. Fixing the parameters of our mode profiling condition

Before it is possible to use equation 6.10, we need to fix some of the free parameters. The chosen solution to Mathieu's equation specifies the parameters a and q. In our calculations, we have treated the phase velocity, β, as a constant with the value 0.96.

With a, q and β fixed, we only have to specify the design frequency f_d and the unit cell length L. It helps us to choose sensible values for these parameters if we look at the minimum and maximum required values of $\Lambda^2(z)$, found by taking the minimum and maximum values of the cosine function in equation 6.7.

$$\Lambda_+^2 = f_\mathrm{d}^2 - \frac{\beta^2 c^2}{L^2}[a - 2q] \tag{6.16}$$

$$\Lambda_-^2 = f_\mathrm{d}^2 - \frac{\beta^2 c^2}{L^2}[a + 2q] \tag{6.17}$$

Equations 6.16 and 6.17 become especially important when you consider that the range of values for λ_s^2 is limited. As can be seen from Fig. 6.9 our function for λ_s^2 has a lower bound where the function reaches an asymptote, $\lambda_s^2 = C$, and an upper bound at $r = 0$, $\lambda_s^2 = C + A$. Therefore, if we were to naively choose f and L values without any consideration for these bounds, it is possible that the required minimum and maximum values of the plasma frequency would fall outside of the possible range. This would result in the need for imaginary radii and would make the solution useless.

We can avoid these problems by fixing Λ_+^2 and Λ_-^2 with values which fall in the allowed range given by the expression for the plasma frequency in equation 6.6:

$$C < \Lambda_+^2 < C + A \tag{6.18}$$

$$C < \Lambda_-^2 < C + A \tag{6.19}$$

We can take the sum and difference of equations 6.16 and 6.17 to find equations 6.20 and 6.21 that specify f_d and L, which are now guaranteed to give a solution for $R(z)$ with purely real values.

$$L^2 = \frac{4\beta^2 c^2 q}{\Lambda_+^2 - \Lambda_-^2} \tag{6.20}$$

$$f_\mathrm{d}^2 = \frac{\Lambda_+^2 + \Lambda_-^2}{2} + \frac{\left(\Lambda_+^2 - \Lambda_-^2\right) a}{4q} \tag{6.21}$$

It is also possible to fix any two other free variables in equations 6.16 and 6.17. Choosing a different set of variables requires reworking the conditions set out in equations 6.18 and 6.18, and finding a new set of equations, 6.20 and 6.21, for specifying the remaining two variables. It is also possible to create new variables that we would prefer to use.

$$\lambda_C^2 = \frac{\Lambda_+^2 + \Lambda_-^2}{2} \tag{6.22}$$

$$\lambda_W^2 = \Lambda_+^2 - \Lambda_-^2 \tag{6.23}$$

In particular, the actual method we have implemented in our work involves the introduction of new variables defined in equations 6.22 and 6.23. λ_C^2 represents a central value for the range of λ_s^2 values, whereas λ_W^2 is the width of the range. As the relationship between λ_s^2 and r is monotonically decreasing, λ_C^2 can also be related to a central radius R_C with $\lambda_s^2(R_C) = \lambda_C^2$. We chose to make f_d and λ_C^2 our independent variables, as we prefer to work with less abstract quantities. f_d is the design frequency for the shaped mode and λ_C^2, as has been mentioned, can be chosen by picking a central radius R_C.

With our new variables and choice of independent variables, the conditions in equations 6.18 and 6.19 become:

$$C < \lambda_C^2 + \frac{2q}{a}(f_d^2 - \lambda_C^2) < C + A \tag{6.24}$$

$$C < \lambda_C^2 - \frac{2q}{a}(f_d^2 - \lambda_C^2) < C + A \tag{6.25}$$

This choice of variables lead to the following equation for fixing the other parameters:

$$L^2 = \frac{\beta^2 c^2 a}{f_d^2 - \lambda_C^2} \tag{6.26}$$

$$\lambda_W^2 = \frac{4q}{a}(f_d^2 - \lambda_C^2) \tag{6.27}$$

This approach is based on an exponential decay relation taken from a fit of a limited range of radius values. It is, therefore, good practice to only rely on solutions which require radii in this range as we cannot be sure the relationship will hold outside of this range. As our model is based on wire media with small radii compared to the lattice constants, we would not expect it to be valid for much larger radii.
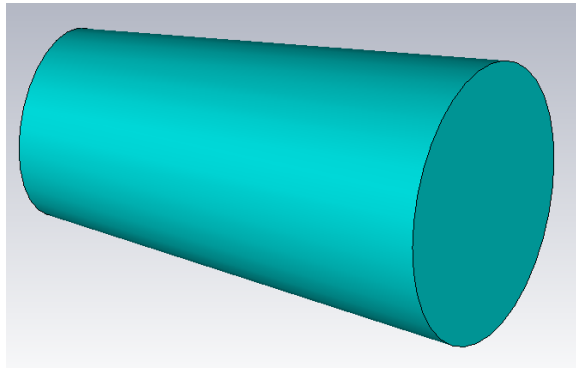
Figure 6.10: An image from CST showing a conical frustum shape, which we use as the building blocks for our varying radius dielectric rods.
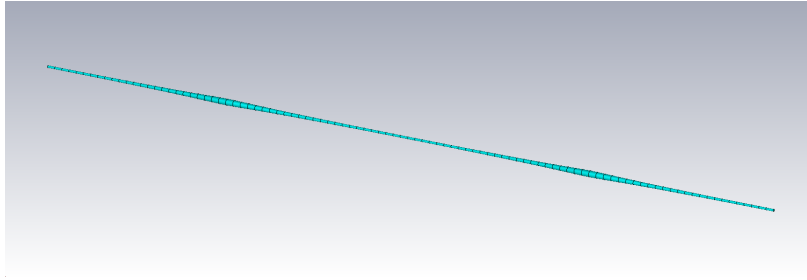
Figure 6.11: An example of a dielectric rod with a varying radius that has been formed from a series of conical frustums.

V. TESTING THE MODE PROFILE SHAPING METHOD

Now that we have a method for relating a chosen profile to a radius function, $R(z)$, for infinite dielectric wire media, it was necessary to test its effectiveness. In our CST simulations, the continuous variation of our $R(z)$ solution was approximated by a dielectric rod made up of a collection of conical frustums, shown in Fig. 6.10. A conical frustum is essentially a truncated cone where two circular faces of differing radii are linearly connected. The resulting wire with a varying radius is shown in Fig. 6.11. Usually, a hundred of these segments are used to form our varying radius wires; the effect of the number of segments is considered in Section VI.
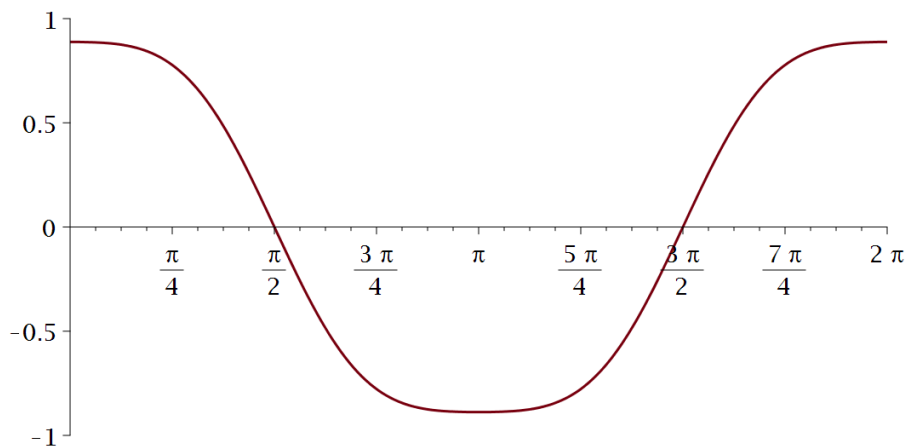
Figure 6.12: A solution to Mathieu's equations (distinguished by the choice of Mathieu parameters $q = 0.8$, $a = 1.711853605$) that can be loosely described as a flattened sinusoidal curve.

Our initial attempts at mode profile shaping were aimed at replicating a flat profile ($q = 0.8$, $a = 1.711853605$), with the desired profile shown in Fig. 6.12; the dielectric rods had a relative permittivity $\epsilon = 1600$, and the lattice spacings were $a_x = 15$ mm and $a_y = 13.06$ mm. The fitting parameters for this permittivity

f_d (GHz)	R_C (mm)	λ_C (GHz)	Γ_1 (μm)	Γ_2	Γ_3	Γ_4 (mm^{-1})	L (mm)
8.90	0.150	7.54	54.1	$6.24 \cdot 10^{-2}$	$5.94 \cdot 10^{-2}$	0.157	79.8
7.70	0.150	7.54	54.1	$6.24 \cdot 10^{-2}$	$6.33 \cdot 10^{-2}$	0.0514	244
7.70	0.180	6.90	54.1	$3.58 \cdot 10^{-2}$	$3.12 \cdot 10^{-2}$	0.114	110
6.10	0.300	6.03	54.1	$0.389 \cdot 10^{-2}$	$0.211 \cdot 10^{-2}$	0.0297	423
6.14	0.300	6.03	54.1	$0.389 \cdot 10^{-2}$	$0.342 \cdot 10^{-2}$	0.0378	333
6.14	0.270	6.12	54.1	$0.678 \cdot 10^{-2}$	$0.720 \cdot 10^{-2}$	0.0173	725

Table 6.2: A table summarising some of the key parameters related to the implemented radius functions for a flattened profile ($q = 0.8$) in infinite dielectric wire media ($\varepsilon_r = 1600$, $a_x = 13.06$ mm and $a_y = 15.00$ mm). The first set of parameters listed are design parameters we chose: design frequency (f_d), central radius (R_C) and the corresponding central plasma frequency (λ_c). The rest are the resulting structural parameters: the parameters specifying the corresponding radius function (Γ_{1-4}) and the length of our unit cell (L).

are as follows: $\delta = 35.1$ (GHz^2), $\sigma = 350$ (GHz^2) and $\rho = 0.0541$ (mm^{-1}). The parameters Γ_i of the $R(z)$ solutions we tested are shown in Table 6.2 for a variety of values for our chosen independent values f_d and λ_c.

Our first attempt at mode profiling had a design frequency, f_d, of 8.9 GHz; central radius, R_c, of 0.15 mm; and, therefore, a central cut-off frequency, λ_C, of 7.54 GHz. The parameters for the corresponding $R(z)$ function are listed in Table 6.2 as well as the resulting length of the unit cell, 79.8 mm. The corresponding $R(z)$ function is plotted in Fig. 6.13.
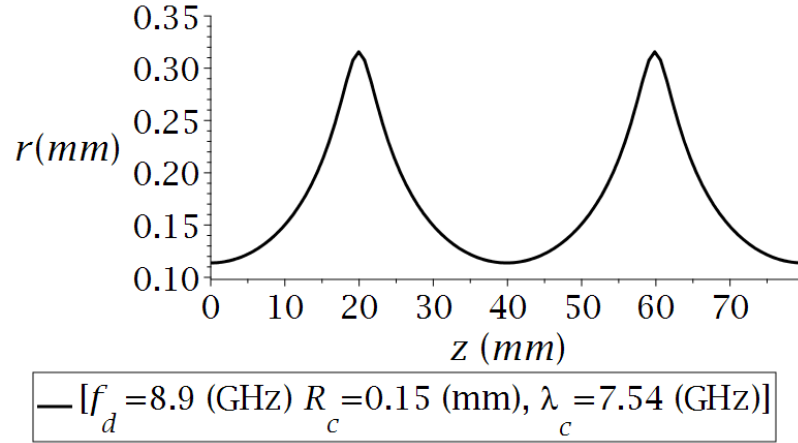
Figure 6.13: The radius function calculated for a flattened profile ($q = 0.8$) in an infinite dielectric wire medium ($\varepsilon_r = 1600$, $a_x = 13.06$ mm and $a_y = 15.00$ mm) for the parameter choice of $f_d = 8.9$ GHz, $R_c = 0.15$ mm and $\lambda_C = 7.54$ GHz.

Having the wire radius in our CST simulations vary according to this $R(z)$ function should result in the field profile we desired. As previously discussed, we can achieve an approximately equal variation by using a wire made up of a series

of conical frustum segments. Unless otherwise stated 100 frustum segments have been used to approximate the required radius variation. The mode found in this structure are shown in Fig. 6.14.

(a)

(b)   (c)   (d)
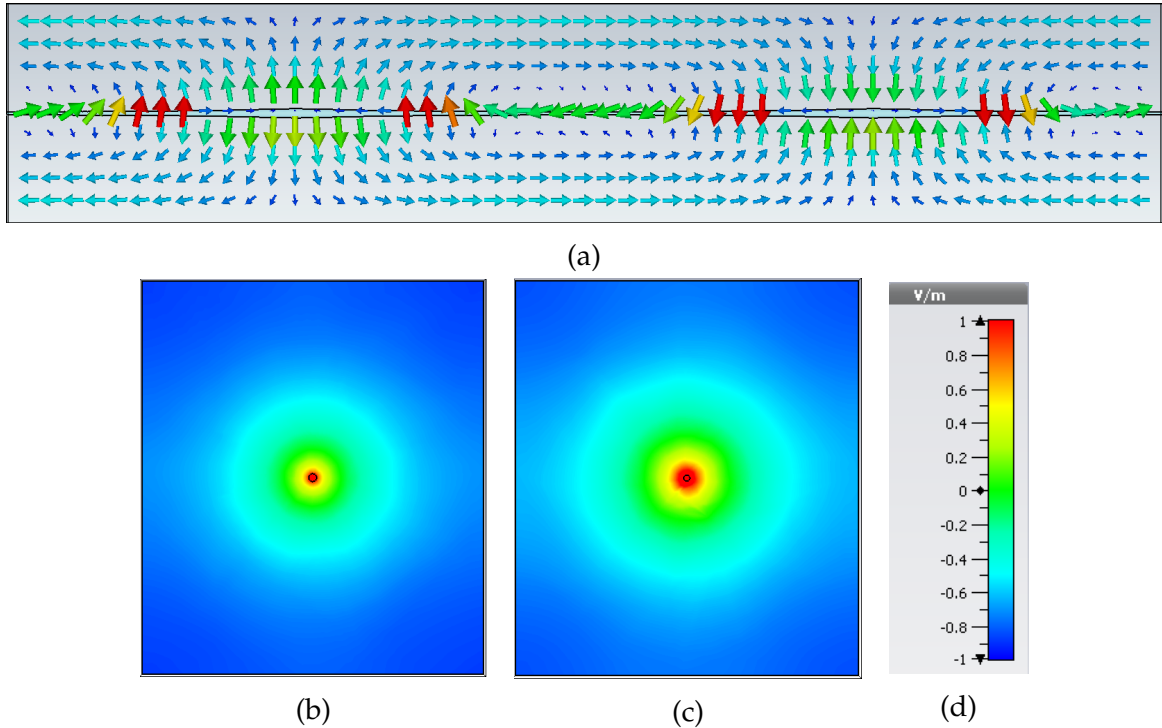
Figure 6.14: Images showing the resulting longitudinal mode (simulation frequency $f = 8.74$ GHz) after the implementation of the calculated radius function for a flattened profile ($q = 0.8$) in an infinite dielectric wire medium ($\varepsilon_r = 1600$, $a_x = 13.06$ mm and $a_y = 15.00$ mm) for the parameter choice of $f_d = 8.9$ GHz, $R_c = 0.15$ mm and $\lambda_C = 7.54$ GHz. The fields are either represented using arrow plots where the arrow direction represents field direction and colour represents the magnitude of the field strength, or colour plots where the direction and magnitude of the longitudinal field is represented by colour. (a) shows the field on a y-z slice of the structure, whereas (b) and (c) show the field at two different x-y slices. The z coordinate of these slices are $z = 30$ mm and $z = 40$ mm respectively, where $z = 0$ mm is at the edge of the box. (d) is a colour key for the electric field colour plots (b) and (c), where red is a strongly positive electric field and blue a strongly negative electric field.

The images in Fig. 6.14 are of limited value. It is promising that we have found a longitudinal mode with the expected characteristics around our design frequency $f_d = 8.9$ GHz as opposed to the mode frequency of $f = 8.74$ GHz. A 0.16 GHz, or 1.83 %, difference is acceptable for our first attempt at profiling. The closeness between our design frequency and the mode frequency is in itself a validation of our chosen model and the method we have developed. Also, from

Fig. 6.14b and 6.14c, we can see that the varying radius along the longitudinal direction does seem to affect the field profile. Ultimately, we aimed to control the longitudinal profile—how the longitudinal field strength, E_z, along the longitudinal direction, z, changes—and, in particular, to gain a degree of control that allows us to specify a specific profile shape. We cannot determine whether these aims have been met by looking at the images in Fig. 6.14.
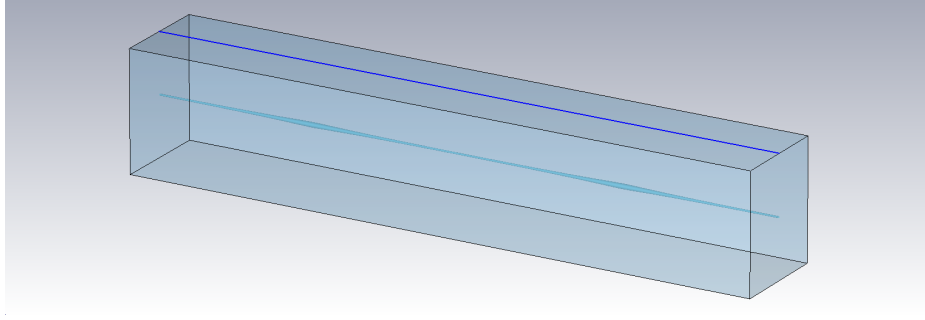
Figure 6.15: A unit cell of a varying radius wire in a representation of an infinite dielectric wire medium ($\varepsilon_r = 1600$, $a_x = 13.06$ mm and $a_y = 15.00$ mm). A blue line has been introduced into the unit cell along which the field strength of our longitudinal field will be evaluated in order to better determine the field profile of a longitudinal mode.

Previously, in Fig. 5.3c, we have represented the longitudinal profile of a mode by a line plot, which more clearly illustrated the simple sinusoidal shape of our original unmodified longitudinal modes. We can use the same technique to represent the profile of the modes in Fig. 6.14. To produce these graphs, we introduce a line into our CST models, as shown in Fig. 6.15. By plotting the field strength on this line, we can produce plots such as Fig. 5.3c. Using this technique for the modes shown in Fig. 6.14, we were able to produce the plot in Fig. 6.16.

Fig. 6.16 is extremely useful in determining the success of our attempts at mode profiling. From a qualitative standpoint, we can see by comparing the simulation results and the desired Mathieu function that there has been considerable success in shaping the mode profile. This is especially true if we consider the mode profile of a longitudinal mode for a uniform wire medium, which is generally sinusoidal, as shown in Fig. 5.3c. It is also possible to gain a quantitative measure of our mode profiling success by calculating the $\mathfrak{R}^2$ value, discussed previously in II, of our simulation results compared to the desired Mathieu function. For the case of the mode profile in Fig. 6.16 the $\mathfrak{R}^2$ value is 0.9907. Profiles with $\mathfrak{R}^2$ values closer to 1 are most similar to the desired profile, so this represents a close similarity between the profiles. This reinforces the success of our first attempt at mode profiling.
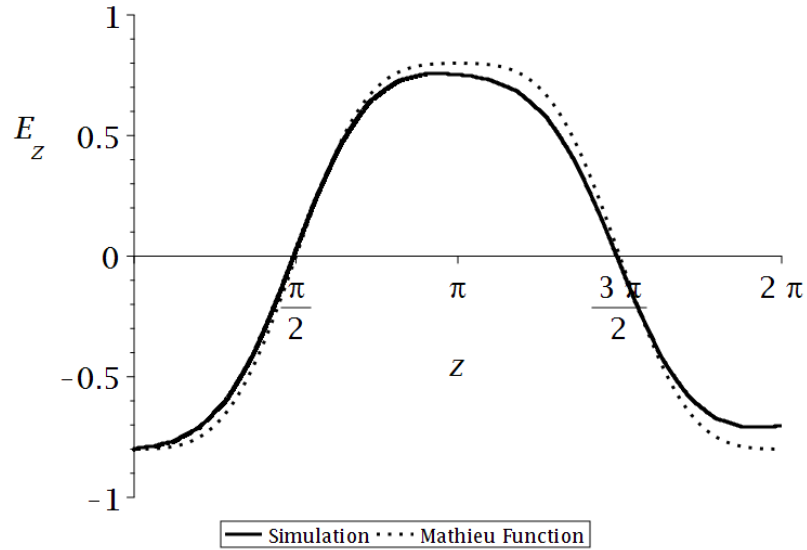
Figure 6.16: A plot of the field profile (longitudinal, z, spatial variation of the electric field strength, E_z) of the longitudinal mode ($f = 8.74$ GHz) in an infinite dielectric wire medium ($\varepsilon_r = 1600$, $a_x = 13.06$ mm and $a_y = 15.00$ mm) for our attempt to produce a flattened profile ($q = 0.8$) with a radius function based on the parameter choice of $f_d = 8.9$ GHz, $R_c = 0.15$ mm and $\lambda_C = 7.54$ GHz. The plot includes the field profile observed in our numerical simulation (solid black) and the desired profile (dotted black). In order to aid comparison the field profile from our simulation and the z coordinate have been normalised.
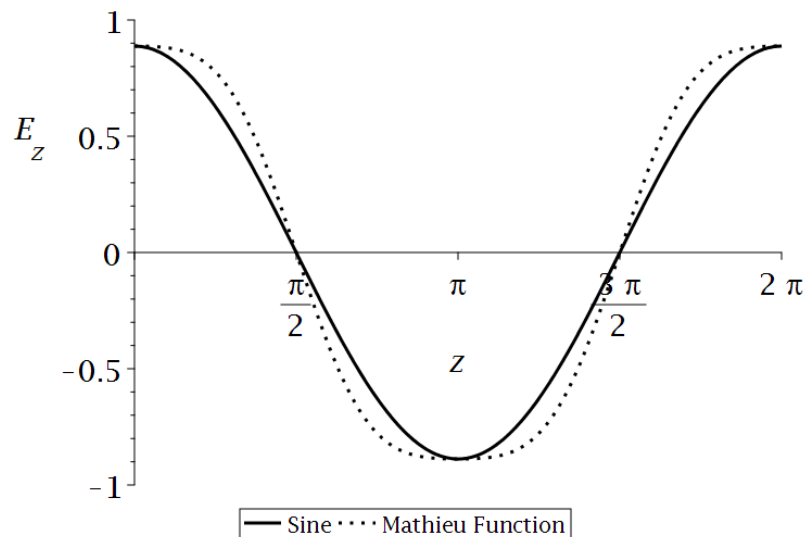
Figure 6.17: A comparison of the flattened Mathieu profile (dotted black), $q = 0.8$, with a sinusoidal curve with an identical peak value (solid black).

We can put the success of this mode profiling into context by comparing the

desired profile with a sinusoidal curve. This comparison is shown in Fig. 6.17. The comparison has an $\mathfrak{R}^2$ value of 0.9712. Our simulation profile is, therefore, closer to our desired profile than a sinusoidal curve.
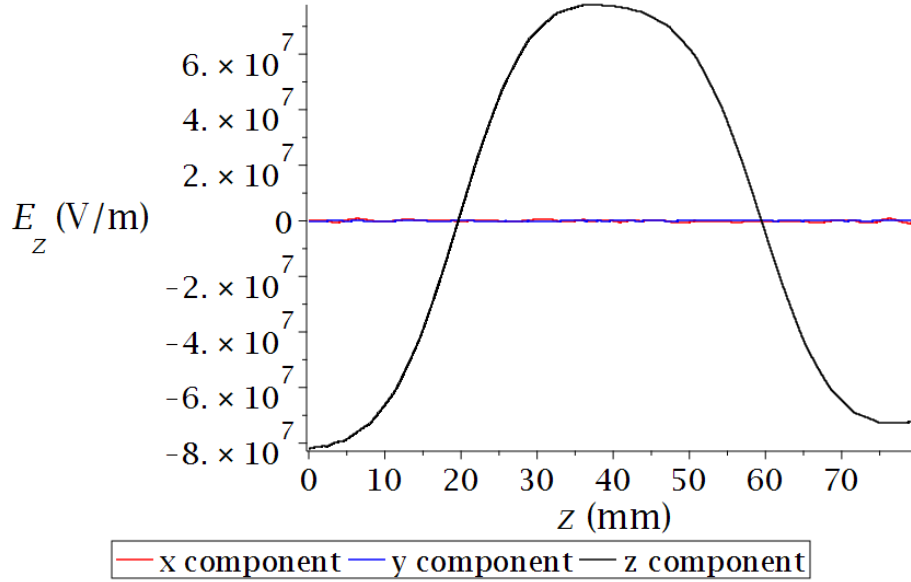
Figure 6.18: A plot of the variation of the different components of the electric field strength of a longitudinal mode found in infinite dielectric wire media ($\varepsilon_r = 1600$, $a_x = 13.06$ mm and $a_y = 15.00$mm) for our attempt to produce a flattened profile ($q = 0.8$) with a radius function based on the parameter choice of $f_d = 8.9$ GHz, $R_c = 0.15$ mm and $\lambda_C = 7.54$ GHz.

We also considered how longitudinal our field is at this position at the top of the unit cell. A plot of the different component of the electric field at this position are shown in Fig. 6.18. We can see that the field is dominated by the z component of the electric field as we would hope.

As covered previously, for every desired profile we have a choice of free parameters. We have had great success with one choice of parameters. It seems sensible to now explore the parameter space to confirm the flexibility in our choice of parameters and to observe any obvious effects these different parameters may have on the results. As listed in rows 2 and 3 of Table 6.2, we started exploring in the area around our initial choice of parameters. Row 2 represents a shift in the choice of design frequency while keeping the R_c value constant. Whereas row 3 represents, in comparison to row 2, a small shift of the R_c value, while the design frequency is kept constant. The resulting radius functions are shown in Figs. 6.19 and 6.20, along with the original radius function of row 1 for comparison.

(a)

(b)

(c)
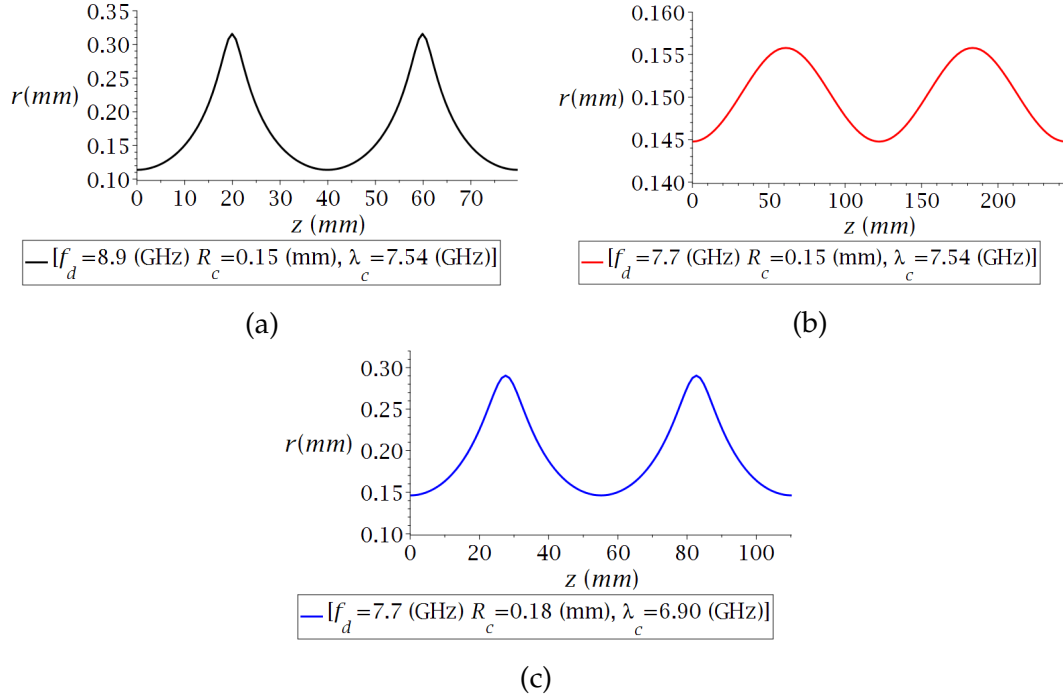
Figure 6.19: A series of plots of radius functions calculated for a flattened profile ($q = 0.8$) in infinite dielectric wire media ($\varepsilon_r = 1600$, $a_x = 13.06$ mm and $a_y = 15.00$ mm) for a variety of parameter choices. (a) shows the radius function for a choice of $f_d = 8.9$ GHz, $R_c = 0.15$ mm and $\lambda_C = 7.54$ GHz (black); (b), for a choice of $f_d = 7.7$ GHz, $R_c = 0.15$ mm and $\lambda_C = 7.54$ GHz (red); and (c), for a choice of $f_d = 7.7$ GHz, $R_c = 0.18$ mm and $\lambda_C = 6.90$ GHz (blue).
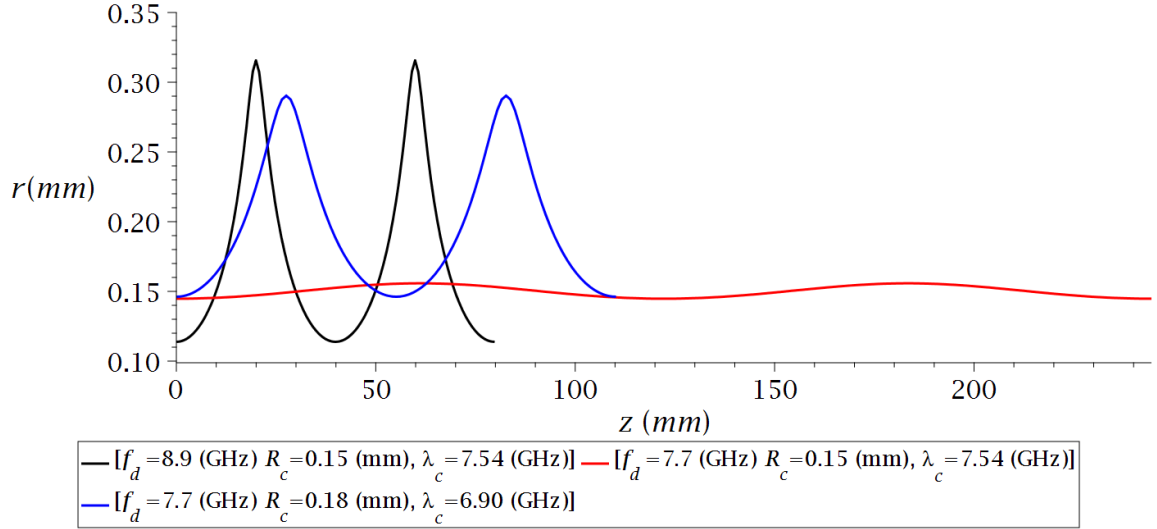
Figure 6.20: A plot of some of the radius functions calculated for a flattened profile ($q = 0.8$) in infinite dielectric wire media ($\varepsilon_r = 1600$, $a_x = 13.06$ mm and $a_y = 15.00$ mm) for a variety of parameter choices. The radius functions shown are based on a choice of $f_d = 8.9$ GHz, $R_c = 0.15$ mm and $\lambda_C = 7.54$ GHz (black); $f_d = 7.7$ GHz, $R_c = 0.15$ mm and $\lambda_C = 7.54$ GHz (red); and $f_d = 7.7$ GHz, $R_c = 0.18$ mm and $\lambda_C = 6.90$ GHz (blue).

We can see from Fig. 6.19 that these different radius functions do have some similar traits, as we would expect. They are all roughly centred around their R_C value, and the $R(z)$ functions in Figs. 6.19a and 6.19c have very similar shapes, with Fig. 6.19b showing a more rounded function. The difference between these functions is more clearly shown in Fig. 6.20 where the differing lengths over which the radius functions are defined is more clearly shown. This variety of shapes and length scales could be an asset for our method as it gives the user greater choice.

Having produced these alternate radius functions, we then tested them. We implemented them into CST simulations using our established method. The modes found are shown in Fig. 6.21. As we would hope, Fig. 6.21 shows that the modes all have the expected traits and have been found near our design frequency.

(a)

(b)
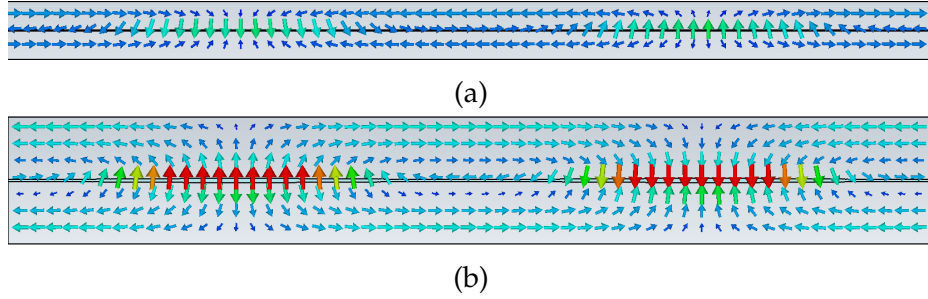
Figure 6.21: Images showing the resulting longitudinal modes after the implementation of two different calculated radius function for a flattened profile ($q = 0.8$) in infinite dielectric wire media ($\varepsilon_r = 1600$, $a_x = 13.06$ mm and $a_y = 15.00$ mm) based on different parameter choices. The fields are represented using arrow plots on a y-z slice of the structure where the arrow direction represents field direction and colour represents the magnitude of the field strength. (a) shows the resulting longitudinal mode ($f = 7.63$ GHz) for implementation of the radius function based on a choice of $f_d = 7.7$ GHz, $R_c = 0.15$ mm and $\lambda_C = 7.54$ GHz; and (b), the resulting longitudinal mode ($f = 7.59$ GHz) for the implementation of the radius function based on a choice of $f_d = 7.7$ GHz, $R_c = 0.18$ mm and $\lambda_C = 6.90$ GHz.

Having found the longitudinal modes for our new radius functions, we checked their mode profiles. Repeating the method we have previously outlined, we can produce the mode profile plots in Fig. 6.22. We can see from looking at Fig. 6.22 that the simulations of both radius functions have shown great success in achieving mode profiling success. In particular, in comparison with Fig. 6.16 the simulation results seem to be an even closer fit to the desired Mathieu function. It should be noted that despite showing the same shape the two profiles in Fig. 6.16 show a phase shift between each other. This difference in phase has no physical significance and the phase found in the simulation is arbitrary. This is confirmed by looking at our quantitative measure of the mode profiling accuracy; the $\mathfrak{R}^2$ values for Fig. 6.22a and 6.22b are 0.9991 and 0.9987 respectively.
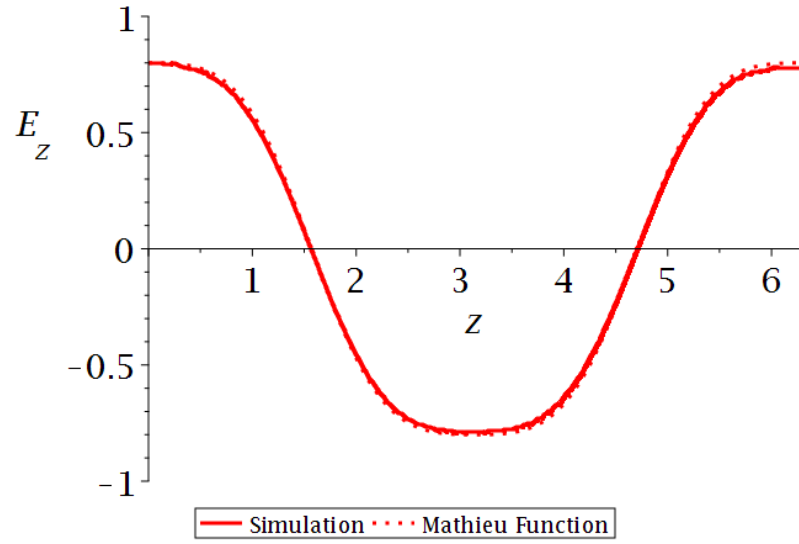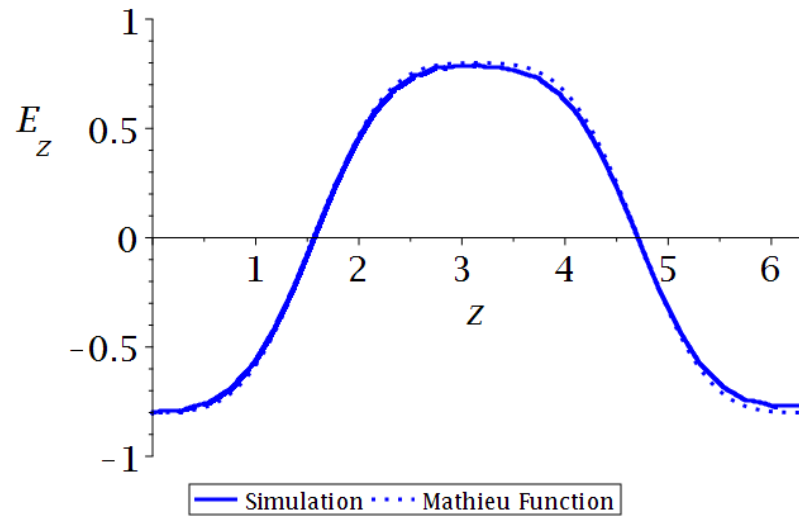
Figure 6.22: Two plots of the field profiles (longitudinal, z, spatial variation of the electric field strength, E_z) of longitudinal modes in infinite dielectric wire media ($\varepsilon_r = 1600$, $a_x = 13.06$ mm and $a_y = 15.00$ mm) for our attempts to produce a flattened profile ($q = 0.8$) with two different radius functions. The plots include the field profile observed in our numerical simulation (solid) and the desired profile (dotted). In order to compare these the field profile and z coordinate have been normalised. (a) shows the field profile of the longitudinal mode ($f = 7.63$ GHz) resulting from the implementation of the radius function based on a choice of $f_d = 7.7$ GHz, $R_c = 0.15$ mm and $\lambda_C = 7.54$ GHz (red); and (b), the field profile of the longitudinal mode ($f = 7.59$ GHz) resulting from the implementation of the radius function based on a choice of $f_d = 7.7$ GHz, $R_c = 0.18$ mm and $\lambda_C = 6.90$ GHz (blue).

(a)

(b)

(c)
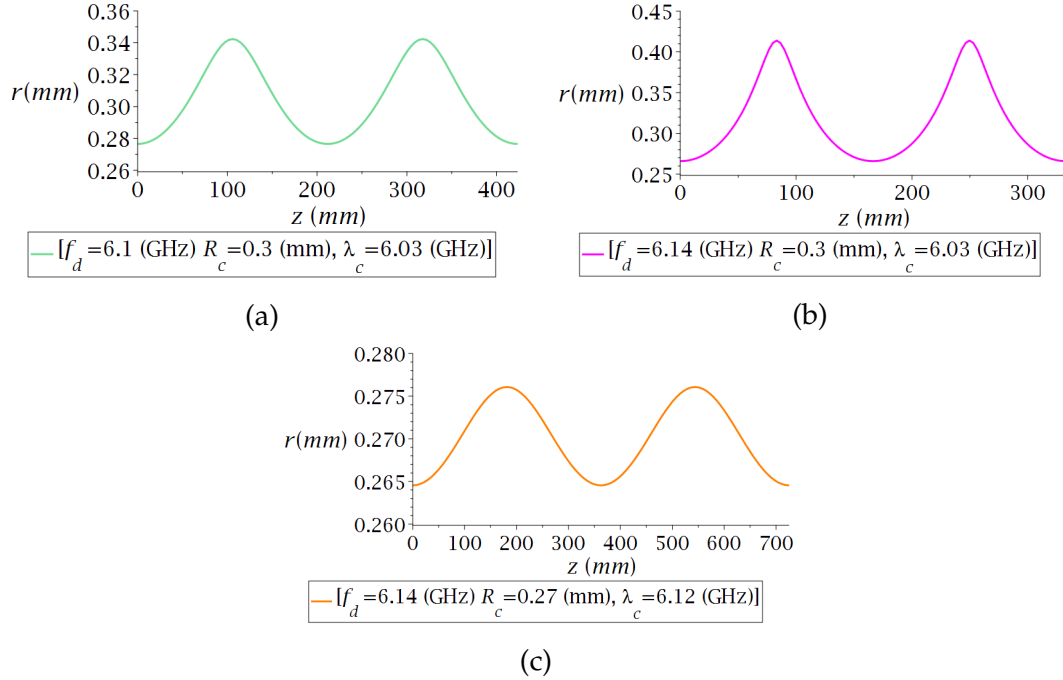
Figure 6.23: A series of plots of radius functions calculated for a flattened profile ($q = 0.8$) in infinite dielectric wire media ($\varepsilon_r = 1600$, $a_x = 13.06$ mm and $a_y = 15.00$ mm) for a variety of parameter choices. (a) shows the radius function for a choice of $f_d = 6.1$ GHz, $R_c = 0.3$ mm and $\lambda_C = 6.03$ GHz (green); (b), for a choice of $f_d = 6.14$ GHz, $R_c = 0.3$ mm and $\lambda_C = 6.03$ GHz (magenta); and (c), for a choice of $f_d = 6.14$ GHz, $R_c = 0.27$ mm and $\lambda_C = 6.12$ GHz (orange).
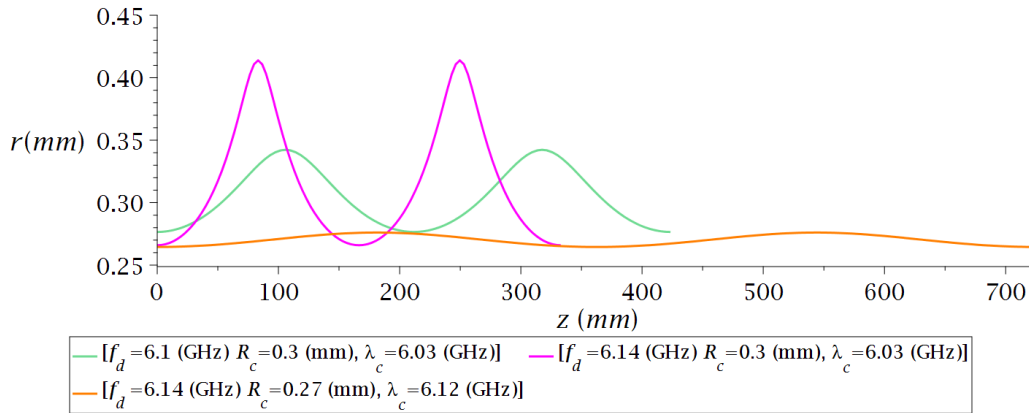
Figure 6.24: A plot of some of the radius functions calculated for a flattened profile ($q = 0.8$) in infinite dielectric wire media ($\varepsilon_r = 1600$, $a_x = 13.06$ mm and $a_y = 15.00$ mm) for a variety of parameter choices. The radius functions shown are based on a choice of $f_d = 6.1$ GHz, $R_c = 0.3$ mm and $\lambda_C = 6.03$ GHz (green); $f_d = 6.14$ GHz, $R_c = 0.3$ mm and $\lambda_C = 6.03$ GHz (magenta); and $f_d = 6.14$ GHz, $R_c = 0.27$ mm and $\lambda_C = 6.12$ GHz (orange).

So far, our examination of the parameter space in which we can produce valid $R(z)$ functions has been very successful, but we have only examined a small region of the parameter space, as we have produced our new radius functions by introducing small shifts in our original chosen parameters. To more fully explore the parameter space, we should explore parameters far removed from our original choice.
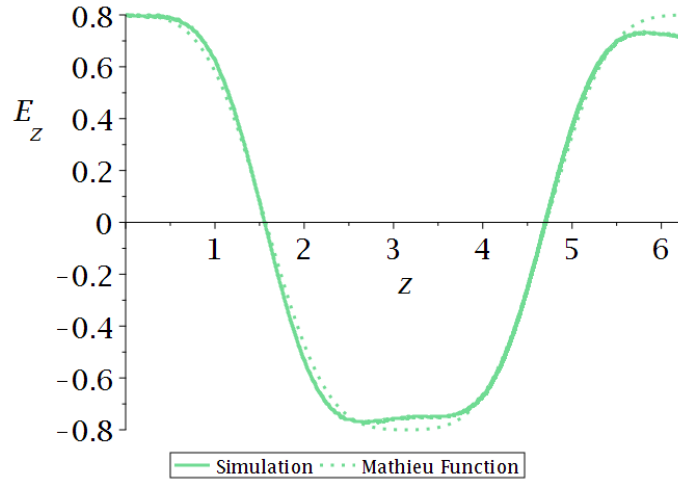
(a)
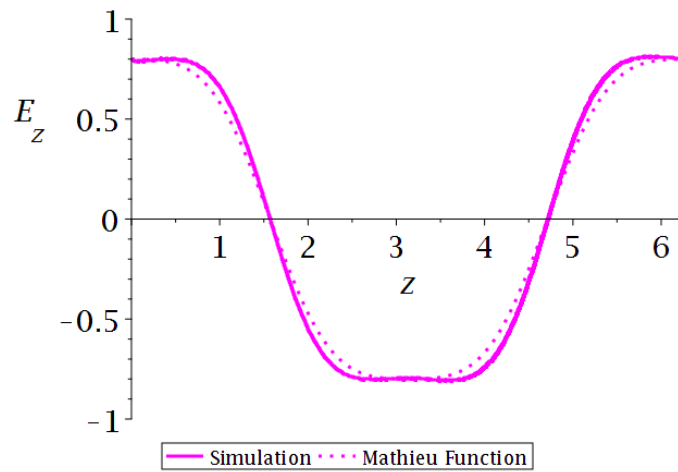
(b)
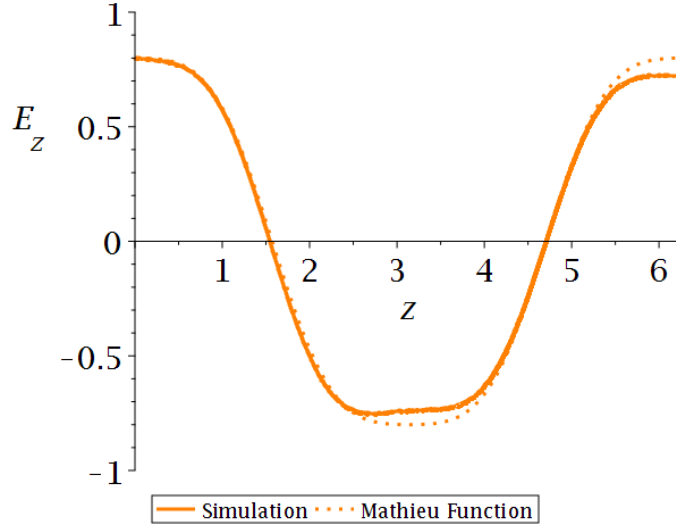
(c)

Figure 6.25: A series of plots of the field profiles (longitudinal, z, spatial variation of the electric field strength, E_z) of the longitudinal modes in infinite dielectric wire media ($\varepsilon_r = 1600$, $a_x = 13.06$ mm and $a_y = 15.00$ mm) for our attempt to produce a flattened profile ($q = 0.8$) with a variety of different radius functions. The plots include the field profile observed in our numerical simulation (solid) and the desired profile (dotted). In order to compare these the field profile and z coordinate have been normalised. (a) shows the field profile of the longitudinal mode ($f = 6.09$ GHz) resulting from the implementation of the radius function based on a choice of $f_d = 6.10$ GHz, $R_c = 0.3$ mm and $\lambda_C = 6.03$ GHz (green); (b), the field profile of the longitudinal mode ($f = 6.12$ GHz) resulting from the implementation of the radius function based on a choice of $f_d = 6.14$ GHz, $R_c = 0.3$ mm and $\lambda_C = 6.03$ GHz (magenta); and (c), the field profile of the longitudinal mode ($f = 6.14$ GHz) resulting from the implementation of the radius function based on a choice of $f_d = 6.14$ GHz, $R_c = 0.27$ mm and $\lambda_C = 6.12$ GHz (orange).

If we look at the parameters chosen for our tested radius functions, we can see that the parameters have stayed in a region corresponding to radius values on the steeper part of the curve in Fig. 6.9. It makes sense to now explore parameters corresponding to the flatter region of the curve. This is what motivated the choice of parameters shown in row 4 of Table 6.2, with the R_C value being shifted significantly towards the flatter region of the λ_s^2 curve. From this choice we shifted the frequency, though not by a large degree due to restrictions associated with the narrow range of allowed frequencies for the given R_C, to produce row 5. Similarly, by shifting the R_C value of row 5 we obtained the values in row 6 of Table 6.2.

The resulting radius function from the choice of parameters are plotted individually in Fig. 6.23 and plotted together in Fig. 6.24. These plots are as we would expect. They are similar in shape to previous radius functions we have examined

while their range of radius values has been shifted by the large shift in R_C values compared to our original radius functions.

As before, we can implement these radius function into CST using a series of conical frustums. Our eigenmode simulations found longitudinal modes with the expected characteristics around the design frequencies for all three radius functions. Further details on the mode frequencies can be found in Table 6.3, which is a summary of the simulation results and measures of success for all six simulated radius functions. The mode profiles for the resulting radius function are plotted individually in Fig. 6.25. Once again, we can see that our mode profiling attempts have been very successful. The quantitative measures of their success are listed in Table 6.3.
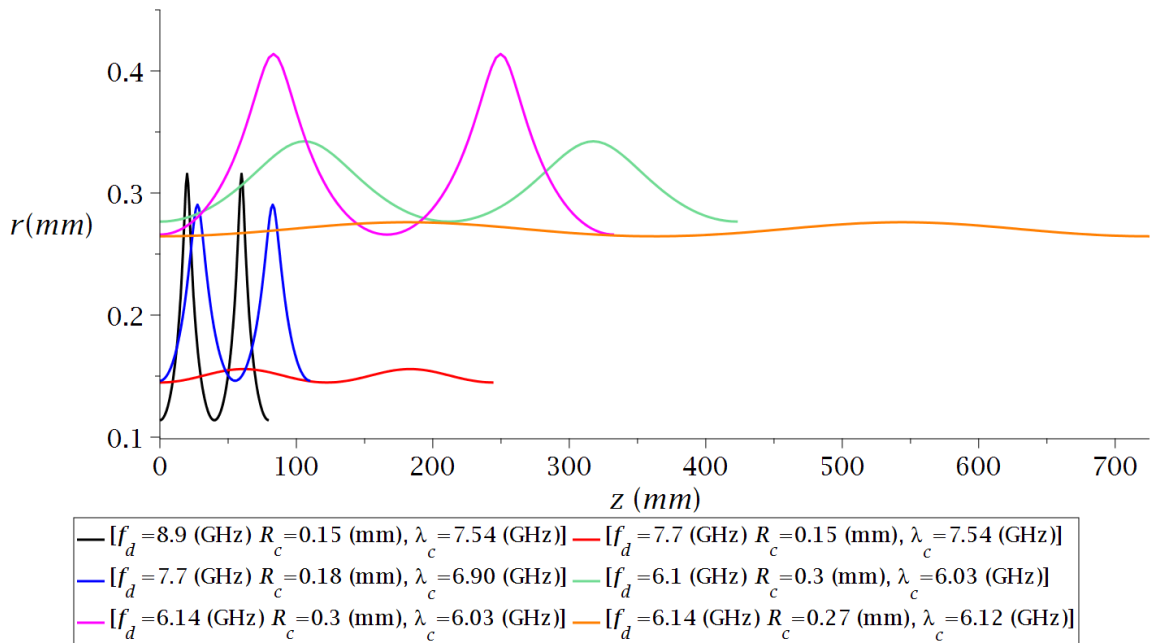
Figure 6.26: A plot of all of the radius functions calculated for a flattened profile ($q = 0.8$) in infinite dielectric wire media ($\varepsilon_r = 1600$, $a_x = 13.06$ mm and $a_y = 15.00$ mm) for a variety of parameter choices. The radius functions shown are based on a choice of $f_d = 8.9$ GHz, $R_c = 0.15$ mm and $\lambda_C = 7.54$ GHz (black); $f_d = 7.7$ GHz, $R_c = 0.15$ mm and $\lambda_C = 7.54$ GHz (red); $f_d = 7.7$ GHz, $R_c = 0.18$ mm and $\lambda_C = 6.90$ GHz (blue); $f_d = 6.1$ GHz, $R_c = 0.3$ mm and $\lambda_C = 6.03$ GHz (green); $f_d = 6.14$ GHz, $R_c = 0.3$ mm and $\lambda_C = 6.03$ GHz (magenta); and $f_d = 6.14$ GHz, $R_c = 0.27$ mm and $\lambda_C = 6.12$ GHz (orange).

We have demonstrated success in achieving mode profiling with our method, confirming this success by qualitative and quantitative steps. We have also tested the robustness of our method for a variety of different parameter choices. These differing parameters choices have also shown the wide range of radius variations that can be used to achieve the same mode profile, as illustrated in Fig. 6.26.

#	f_d (GHz)	λ_C (GHz)	L (mm)	f (GHz)	$\mathfrak{R}^2$
1	8.90	7.54	79.8	8.74	0.9907
2	7.70	7.54	244	7.63	0.9991
3	7.70	6.90	110	7.59	0.9987
4	6.10	6.03	423	6.09	0.9968
5	6.14	6.03	333	6.12	0.9943
6	6.14	6.12	725	6.14(3)	0.9963

Table 6.3: A table summarising some of the key parameters related to the results of our implemented radius functions for a flattened profile ($q = 0.8$) in infinite dielectric wire media ($\varepsilon_r = 1600$, $a_x = 13.06$ mm and $a_y = 15.00$ mm). The parameters listed are attempt number, design frequency (f_d), central plasma frequency (λ_c), length of our unit cell (L), longitudinal mode frequency (f) and a figure of merit for the agreement between our field profile and the desired profile ($\mathfrak{R}^2$).

Table 6.3 shows the parameters for the radius functions previously listed in Table 6.2 along with measures of the success of the mode profiling achieved through their implementation. This underscores the fact that we have demonstrated remarkable accuracy in our mode profiling method for a variety of radius functions, with even the worst-performing functions still doing very well in absolute terms. It would be tempting to attempt to use Table 6.3 to determine some area of the parameter space where our method is particularly accurate, but there is no clear pattern to my eyes, and it is too small a sample size to draw any definitive conclusions. This sort of analysis would require a more rigorous and methodical probing of the parameter space, which is made difficult by the manual nature of much of the work involved in producing a profile and the problem of untangling the effect of differing mesh qualities in the simulations. Given these problems, this is not an analysis that we have attempted.

VI. STUDYING THE EFFECT OF THE NUMBER OF FRUSTUMS

Our method for field profiling produces a required radius function, which if realised in our wire media should produce the desired profile for the chosen parameters. These radius functions describe wires with continuously varying radii. An example radius function is shown in Fig. 6.27 that is designed to produce a flattened profile with the parameters $f_\mathrm{d} = 6.14$ GHz and $R_c = 0.3$ mm.
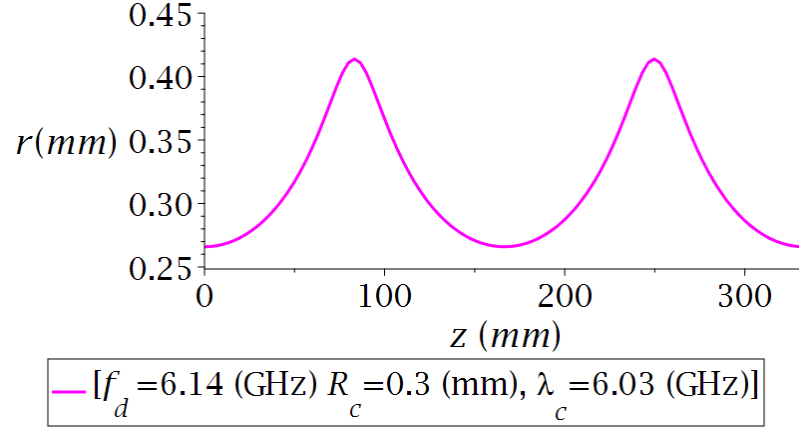
Figure 6.27: A radius function calculated for a flattened profile ($q = 0.8$) in an infinite dielectric wire medium ($\varepsilon_r = 1600$, $a_x = 15.00$mm and $a_y = 13.06$mm) for the parameter choice of $f_d = 6.14$ GHz, $R_c = 0.3$ mm and $\lambda_C = 6.03$ GHz. This is the radius function for our control case in our analysis of the number of conical frustums used to approximate our required radius function.

As we have previously discussed, we do not implement these functions in our simulations exactly, but instead, we approximate the variation with a series of conical frustums. We have already shown the results of implementing our example radius function with 100 conical frustums. The results of these simulations exhibited successful mode profiling at a frequency within 0.4% of the design frequency. Despite this success, it is reasonable to consider the effect of the number of frustums used on our results.

In this section, we will examine the effect of the number of conical frustums used by implementing the same radius function with different numbers of conical frustum segments. We have simulated the following values $N = (10, 50, 90, 100, 110, 150, 200)$, where N is the number of conical frustum segments used to approximate the required radius function. We have again simulated the case of $N = 100$ in an attempt to keep all the simulation comparable by using the same mesh settings in CST.
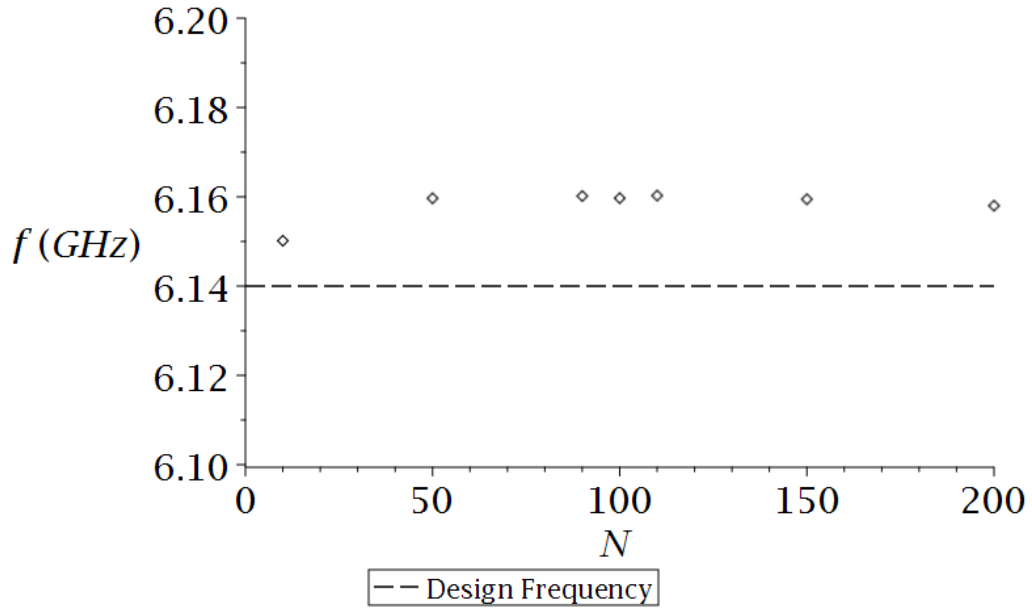
Figure 6.28: A plot of the frequency of the longitudinal modes (f) found in our attempts to achieve a flattened profile ($q = 0.8$) in an infinite dielectric wire medium ($\varepsilon_r = 1600$, $a_x = 13.06$ mm and $a_y = 15.00$ mm) against the number of conical frustums used to approximate the required radius function. The required radius function was based on the parameter choice of $f_d = 6.14$ GHz, $R_c = 0.3$ mm and $\lambda_C = 6.03$ GHz. A black dashed line has been included to indicate the design frequency (f_d).
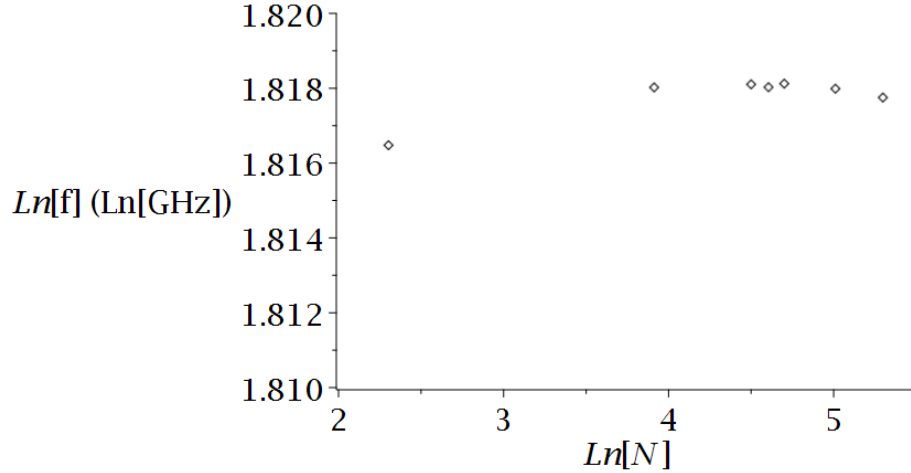
Figure 6.29: A log-log plot of the frequency of the longitudinal modes ($Ln(f)$) found in our attempts to achieve a flattened profile ($q = 0.8$) in an infinite dielectric wire medium ($\varepsilon_r = 1600$, $a_x = 13.06$ mm and $a_y = 15.00$ mm) against the number of conical frustums used to approximate the required radius function. The required radius function was based on the parameter choice of $f_d = 6.14$ GHz, $R_c = 0.3$ mm and $\lambda_C = 6.03$ GHz.

The frequency of the longitudinal modes found are plotted against N in Fig. 6.28. We can see that that the number of frustums seems to have little difference on the frequency of the modes with most found around 6.16 GHz, while for $N = 10$ the mode is found at the slightly lower frequency of 6.15 GHz. All these frequencies are very close to the design frequency of 6.14 GHz. We also examined a log-log plot of this relationship, as shown in Fig. 6.29, but it also showed no clear trend in the data. The field profiles for the cases of $N = 10, 100, 200$ are shown in Fig. 6.30.
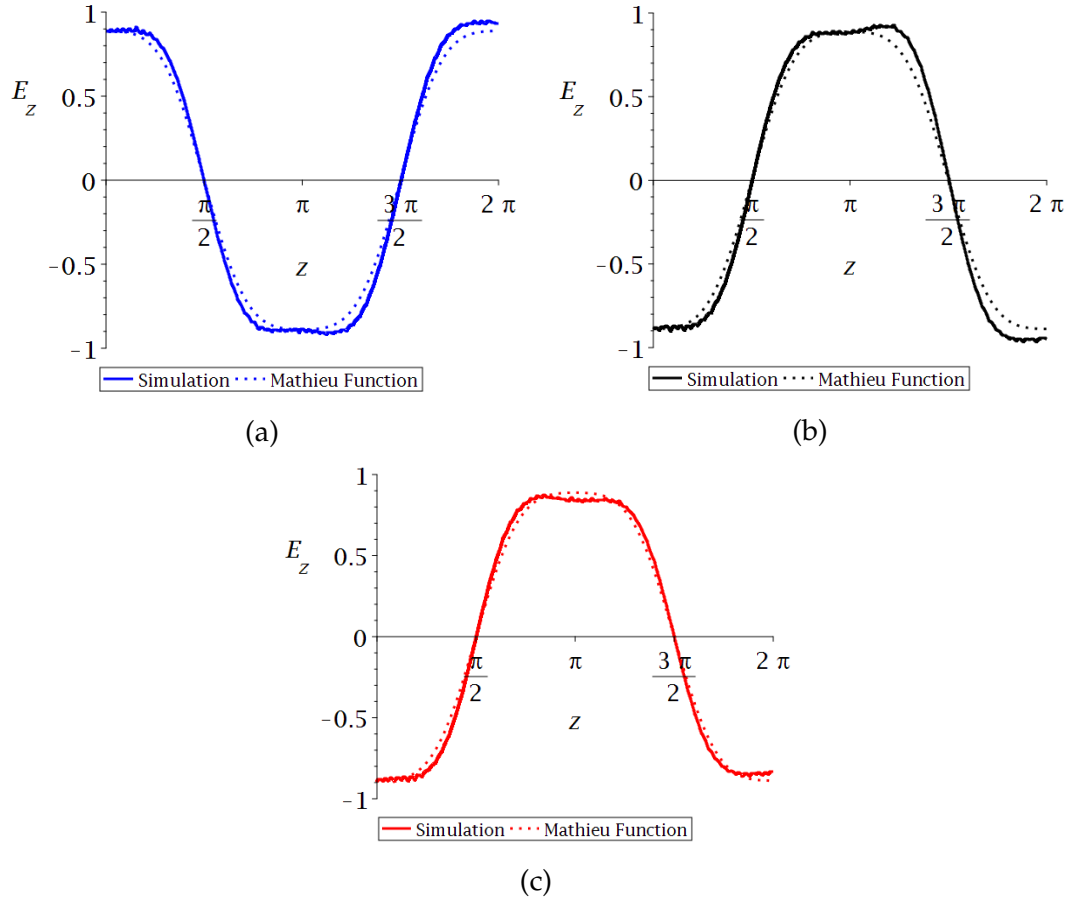
Figure 6.30: A series of plots of the field profiles (longitudinal, z, spatial variation of the electric field strength, E_z) of the longitudinal modes in an infinite dielectric wire medium ($\varepsilon_r = 1600$, $a_x = 13.06$ mm and $a_y = 15.00$ mm) for our attempt to produce a flattened profile ($q = 0.8$) with a radius function based on the parameter choice of $f_d = 8.9$ GHz, $R_c = 0.15$ mm and $\lambda_C = 7.54$ GHz. The plots include the field profile observed in our numerical simulations (solid) and the desired profile (dotted). In order to compare these the field profile and z coordinate have been normalised. The difference between these plots is the number of conical frustums used to approximate the required radius function. (a) is the profile of the longitudinal mode ($f = 6.15$ GHz) for a dielectric rod formed by 10 conical frustums (blue), (b) is the profile of the longitudinal mode ($f = 6.16$ GHz) for a dielectric rod formed by 100 conical frustums (black) and (c) is the profile of the longitudinal mode ($f = 6.16$ GHz) for a dielectric rod formed by 200 conical frustums.

The profiles in Fig. 6.30 clearly show that even at the extreme ends of the range examined, the frustum number does not seem to impact the general shape of the profile produced. The $\mathfrak{R}^2$ value for these profiles and the profiles for all cases considered are plotted in Fig. 6.31 along with a dashed line representing the sinusoidal benchmark value. Fig. 6.31 shows that for all N the profiles are

very close to the desired profile and are an improvement on the comparison with a sinusoidal curve. There are no clear patterns in the data, although there is a small dip around $N = 100$. There is no apparent reason why 100 segments should produce worse results than 90 or 150. It seems safe to assume this is not a significant trend and that it most probably arose from an unpredictable decrease in the quality of the mesh for these cases. Moving forward, this analysis suggests that the use of 100 frustums to approximate the required radius function should be adequate.
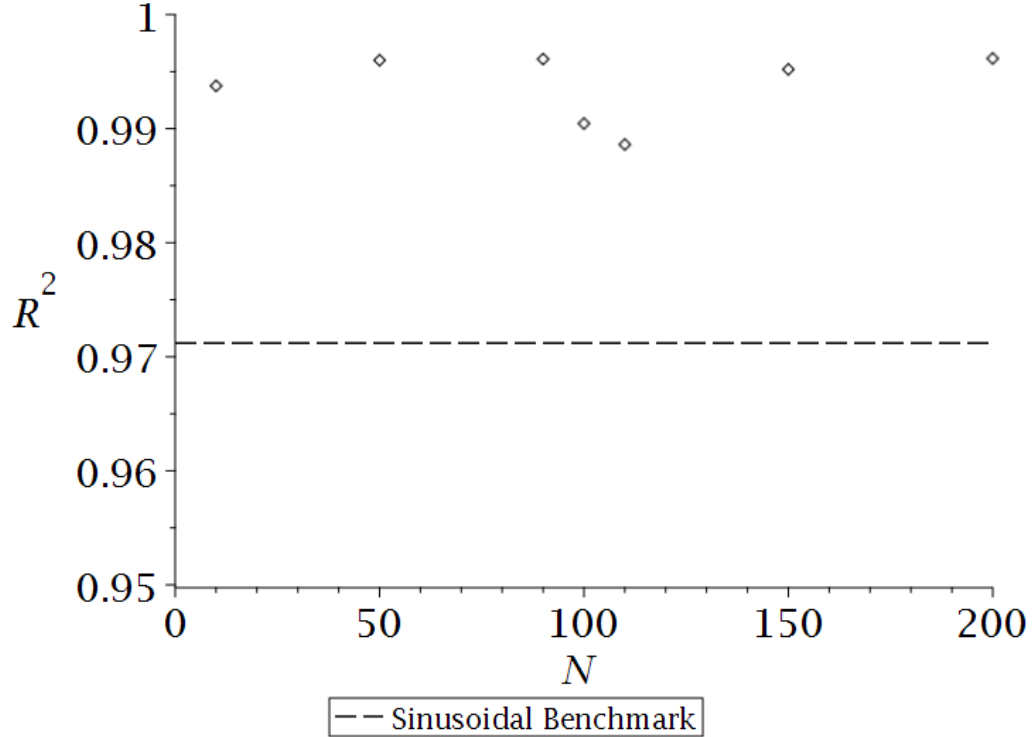
Figure 6.31: A plot of a figure of merit for the comparison between our field profile and our desired profile ($\Re^2$) in our attempts to achieve a flattened profile ($q = 0.8$) in an infinite dielectric wire medium ($\varepsilon_r = 1600$, $a_x = 13.06$ mm and $a_y = 15.00$ mm) against the number of conical frustums used to approximate the required radius function. The required radius function was based on the parameter choice of $f_\mathrm{d} = 6.14$ GHz, $R_c = 0.3$ mm and $\lambda_C = 6.03$ GHz. A black dashed line has been included to indicate the benchmark $\Re^2$ value of the comparison between a sinusoidal curve and our desired profile.

VII. Mesh analysis

It was important to investigate the effect of the mesh used on our field profiling results. We simulated one of our previous varying radius structures multiple times while varying the mesh cells per wavelength setting in CST. The structure

Mesh cells per wavelength	m_N	f (GHz)	$\mathfrak{R}^2$
5	59134	8.7360	0.9981
6	80832	8.7133	0.9187
7	117252	8.6982	0.9944
8	147274	8.6887	0.7888
9	177007	8.6855	0.1754
10	205721	8.6842	0.4717
11	247151	8.6797	0.9829
12	291936	8.6803	0.9960

Table 6.4: A table summarising the result of our mesh analysis of an infinite dielectric wire medium ($\varepsilon_r = 1600$, $a_x = 13.06$ mm and $a_y = 15.00$ mm) for our attempt to produce a flattened profile ($q = 0.8$) with a radius function based on the parameter choice of $f_d = 8.9$ GHz, $R_c = 0.15$ mm and $\lambda_C = 7.54$ GHz. The parameters listed are the number of mesh cells per wavelength, the total number of mesh cells (m_N), the frequency of the longitudinal mode (f) and a figure of merit for the comparison between our field profile and the desired profile ($\mathfrak{R}^2$).

we chose to simulate was based on the choice of parameters $R_c = 0.15$ mm and $f_d = 8.9$ GHz. The relevant parameters and results from our mesh analysis are summarised in Table 6.4. Also, following on from the conclusion of Section VI we are using 100 frustums to approximate the required variation, as we will for all following simulations.

We can see from Table 6.4 that as the mesh increases in size we do see a convergence around a longitudinal mode frequency of 8.68 GHz. Although the difference between this converged value and the mode frequency at 5 mesh cells per wavelength is only ≈ 0.05 GHz. The development of the $\mathfrak{R}^2$ values for the field profiles is more complex. The agreement is actually very successful for 5 cells per wavelength and is significantly worse for some of the more dense meshes. We are unsure of the reasons for the poor performance for 8, 9 and 10 mesh cells per wavelength, but assume this is due to an increase in numerical error and may be related to problems involving stiff equations, where there are complications associated with introducing a reduced spatial step.

(a)

(b)

(c)
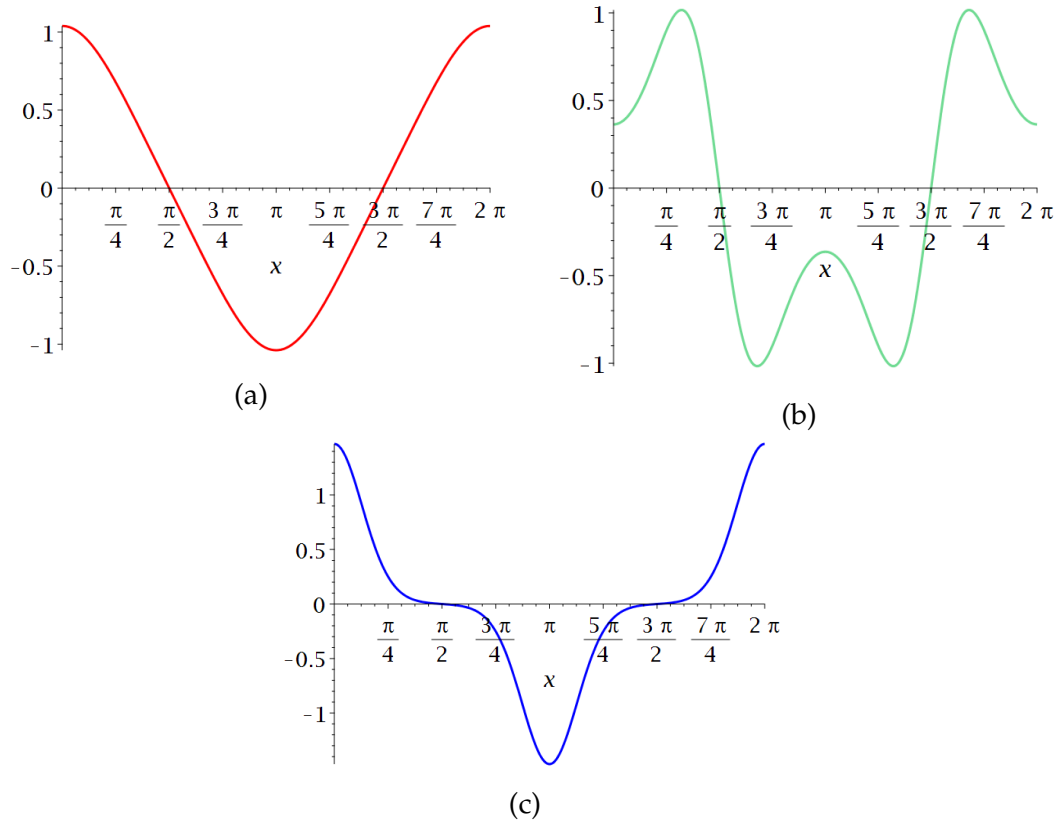
Figure 6.32: A series of plots of different Mathieu functions that we have attempted to replicate using our field shaping method with infinite dielectric wire media. (a) is a triangular profile where $q = -0.329$ and $a = 0.6580176262$ (red), (b) is a profile with multiple turning points where $q = 4.0$ and $a = 2.318008170$ (green) and (c) is a profile with a pronounced peak where $q = -10.0$ and $a = -13.93655248$ (blue).

One of the advantages of using Mathieu's equation as a source of mode profiles is that it has a large set of known solutions providing a large number of possible profiles. After confirming the success of mode profile shaping for a flat profile, we then wanted to attempt to replicate other profiles. Fig. 6.32 shows the solutions to Mathieu's equation that we attempted to replicate. These solutions are a triangular profile, a profile with multiple turning points and a profile with a pronounced peak. Table 6.5 shows our choice of design parameters for these profiles and the resulting parameters for the required radius functions. These radius functions have been plotted in Fig. 6.33.

q	f_d (GHz)	R_C (mm)	λ_C (GHz)	Γ_1 (μm)	$\Gamma_2 \cdot 10^{-3}$	$\Gamma_3 \cdot 10^{-3}$	Γ_4 (m^{-1})	L (m)
-0.329	6.80	0.2	6.61	54.1	24.7	-7.18	85.3	0.147
4	7.70	0.15	7.54	54.1	62.4	23.4	44.2	0.284
-10	6.50	0.2	6.61	54.1	24.7	-6.04	14.2	0.885

Table 6.5: A table summarising some of the key parameters related to the implemented radius functions for a variety of profiles in infinite dielectric wire media ($\varepsilon_r = 1600$, $a_x = 13.06$ mm and $a_y = 15.00$ mm). The first set of parameters listed are design parameters we chose: the Mathieu parameter characterising the profile (q), design frequency (f_d), central radius (R_C) and the corresponding central plasma frequency (λ_c). The rest are the resulting structural parameters: the parameters specifying the corresponding radius function (Γ_{1-4}) and the length of our unit cell (L). The profiles considered are a triangular profile ($q = -0.329$), a profile with multiple turning points ($q = 4.0$) and a profile with a pronounced peak ($q = -10.0$).

(a)

(b)

(c)

Figure 6.33: A series of plots of radius functions calculated for a variety of desired profiles in infinite dielectric wire media ($\varepsilon_r = 1600$, $a_x = 13.06$ mm and $a_y = 15.00$ mm). (a) shows the radius function for a triangular profile with a parameter choice of $f_d = 6.8$ GHz, $R_c = 0.2$ mm and $\lambda_C = 6.61$ GHz (red); (b), for a profile with multiple turning points with a parameter choice of $f_d = 7.7$ GHz, $R_c = 0.15$ mm and $\lambda_C = 7.54$ GHz (green); and (c), for a profile with a pronounced peak with a parameter choice of $f_d = 6.5$ GHz, $R_c = 0.2$ mm and $\lambda_C = 6.61$ GHz (blue).

In Fig. 6.34 we can see the longitudinal modes resulting from our calculated

radius functions for the attempts to replicate a triangular profile and a profile with multiple turning points. The mode profiles for these modes are shown in Fig. 6.35. It can be seen that, once again, our method has proved to be very successful. This is underscored by the $\mathfrak{R}^2$ values of 0.9730 and 0.9814 for the profiles in Figs. 6.35a and 6.35b respectively. Although the $\mathfrak{R}^2$ value for Fig. 6.35b is good, we can see some substructure to the plot in the form of a bumpy pattern. In our experience with other profiles, when we experience this sort of substructure it is related to the mesh. In these cases, the substructure disappears when refining the mesh, but we do not run mesh refinements on all our results as it is time consuming.
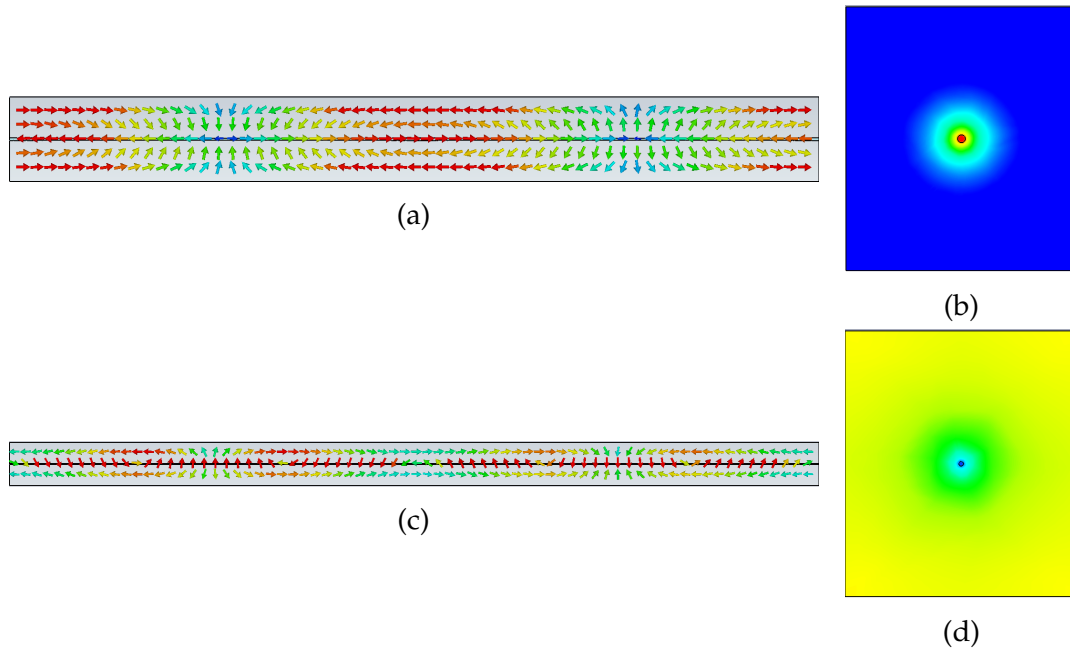
Figure 6.34: Images showing the resulting longitudinal modes after the implementation of the calculated radius functions for a triangular profile ($q = -0.329$) and a profile with multiple turning points ($q = 4.0$) in infinite dielectric wire media ($\varepsilon_r = 1600$, $a_x = 13.06$ mm and $a_y = 15.00$ mm). The fields are represented using arrow plots on an x-z slice of the structure where the arrow direction represents field direction and colour represents the magnitude of the field strength, and colour plots on an x-y slice where the strength and magnitude of the longitudinal field is represented by colour. (a) and (b) shows the resulting longitudinal mode ($f = 6.81$ GHz) for the attempt to demonstrate a triangular profile by the implementation of a radius function based on the choice of $f_d = 6.8$ GHz, $R_c = 0.2$ mm and $\lambda_C = 6.61$ GHz; and (c) and (d), the resulting longitudinal mode ($f = 7.72$ GHz) for the attempt to achieve a profile with multiple turning points by the implementation of a radius function based on the choice of $f_d = 7.7$ GHz, $R_c = 0.15$ mm and $\lambda_C = 7.54$ GHz.

We can put the mode profiling success we have had in some context by com-
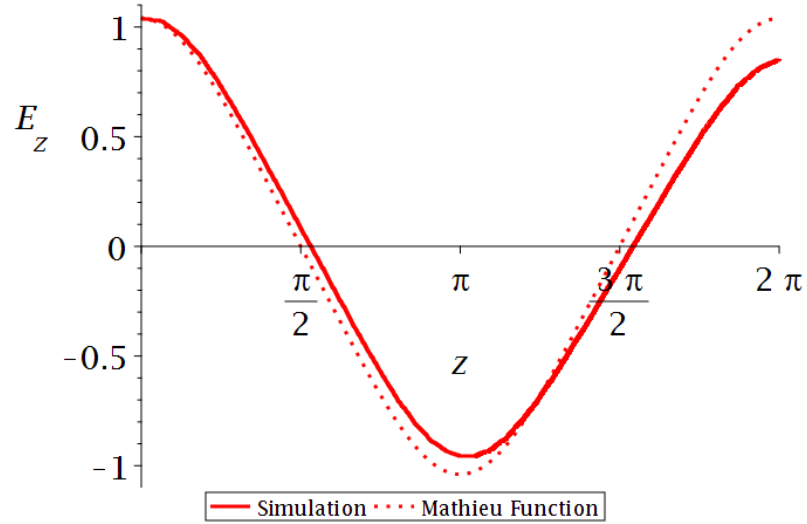
(a)
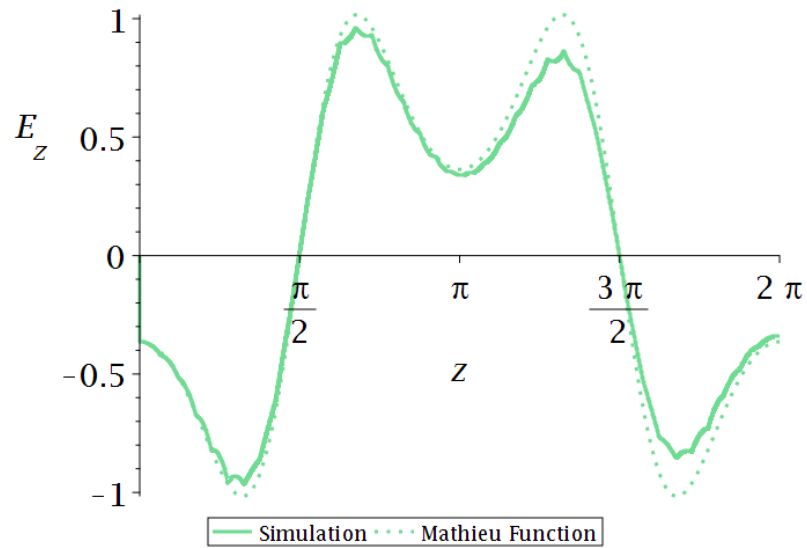
(b)

Figure 6.35: Plots of the field profiles (longitudinal, z, spatial variation of the electric field strength, E_z) of the longitudinal modes in infinite dielectric wire media ($\varepsilon_r = 1600$, $a_x = 13.06$ mm and $a_y = 15.00$ mm) for our attempts to produce a triangular profile ($q = -0.329$) and a profile with multiple turning points ($q = 4.0$). The plots include the field profile observed in our numerical simulation (solid) and the desired profile (dotted). In order to compare these the field profile and z coordinate have been normalised. (a) shows the field profile of the longitudinal mode ($f = 6.81$ GHz) for the attempt to demonstrate a triangular profile by the implementation of a radius function based on the choice of $f_d = 6.8$ GHz, $R_c = 0.2$ mm and $\lambda_C = 6.61$ GHz (red); and (b), the field profile of the longitudinal mode ($f = 7.72$ GHz) for the attempt to achieve a profile with multiple turning points by the implementation of a radius function based on the choice of $f_d = 7.7$ GHz, $R_c = 0.15$ mm and $\lambda_C = 7.54$ GHz (green).

paring our desired profiles with a sinusoidal curve. These comparisons for the triangular profile and the profile with more turning points are shown in Fig. 6.36. The $\mathfrak{R}^2$ values for these comparisons are 0.9971 for the triangular profile and 0.6001 for the profile with more turning points. The extreme similarity between the sine curve and the triangular profile does make it hard to judge for these profiles whether the profiling has made a significant change. Although even getting close to such a high $\mathfrak{R}^2$ value is a success, especially as a normal sinusoidal mode would not have a perfect sine curve profile like our comparison curve. The excellent $\mathfrak{R}^2$ value of our multiple turning point simulation profile is especially impressive considering how poor the comparison is between the desired profile and a sine curve. Although, we should mention that in this result and future results for the turning point profile the peaks are slightly shallower than expected. We are unsure why this occurs.
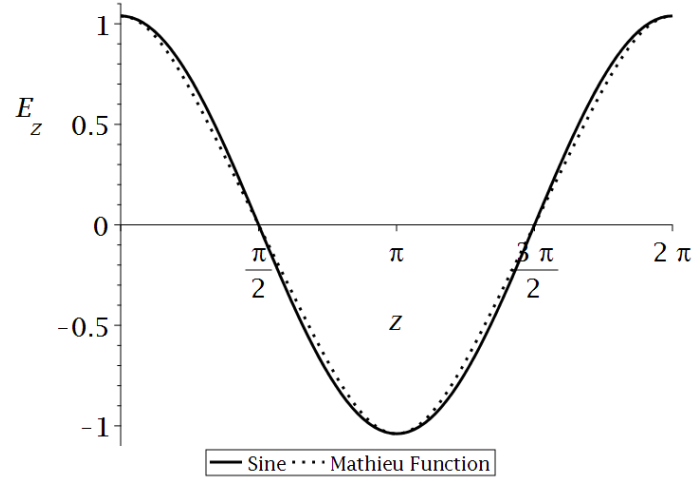
(a)
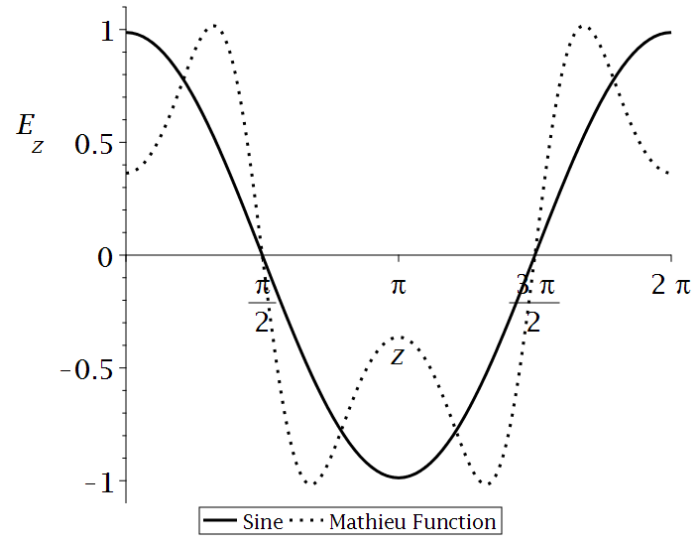
(b)

Figure 6.36: (a) shows a comparison of the triangular Mathieu profile, $q = -0.329$, (dotted black) with a sinusoidal curve with an identical peak value (solid black), and (b) shows a comparison of the Mathieu profile with multiple turning points, $q = 4.0$, (dotted black) with a sinusoidal curve with an identical peak value (solid black).

Our attempt to achieve a profile with a pronounced peak suffered from complications. We find that in the range around the design frequency where we expect to find our longitudinal mode, we find two longitudinal modes with very similar frequencies. These longitudinal modes occur at 6.5060 and 6.5064 GHz, a difference of 0.0004 GHz or, equivalently, a percentage difference of 0.00615 % from the second mode's frequency to the first's. These modes are unusual in only having a significant electric field in certain regions of the structure. The profiles of these modes are shown in Fig. 6.37.

(a)

(b)
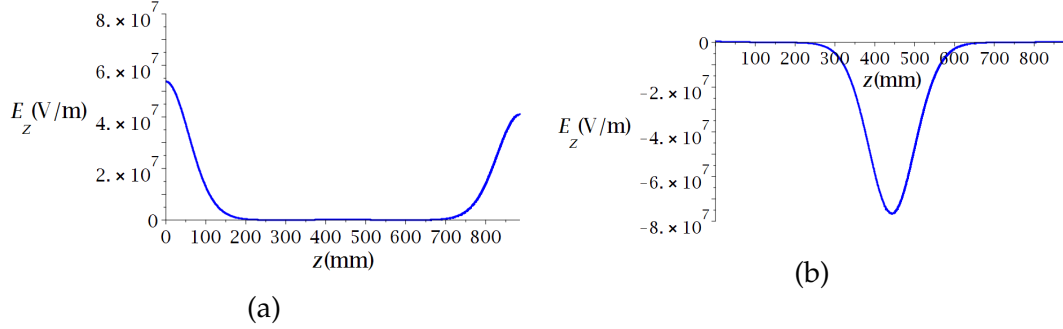
Figure 6.37: Plots of the field profiles (longitudinal, z, spatial variation of the electric field strength, E_z) of the longitudinal modes in an infinite dielectric wire medium ($\varepsilon_r = 1600$, $a_x = 13.06$ mm and $a_y = 15.00$ mm) for our attempts to produce a profile with a pronounced peak ($q = -10.0$) with the parameter choice of $f_d = 6.5$ GHz, $R_c = 0.2$ mm and $\lambda_C = 6.61$ GHz. (a) shows the field profile of one of the longitudinal modes ($f = 6.5060$ GHz); and (b), the field profile of the other longitudinal mode ($f = 6.5064$ GHz).

From Fig. 6.37 it can be seen that taken together these modes would give us something close to the expected behaviour. We have concluded that CST has recognised one mode as two partly due to issues that arise for high negative q Mathieu solutions. If we linearly superimpose with no weighting the profiles of the two modes, we can compare it to our desired profiles as usual, as shown in Fig. 6.38. Looking at Fig. 6.38 we can see that there is good agreement between our combined profile and the desired Mathieu solution, underlined by the calculated $\mathfrak{R}^2$ value of 0.9266.
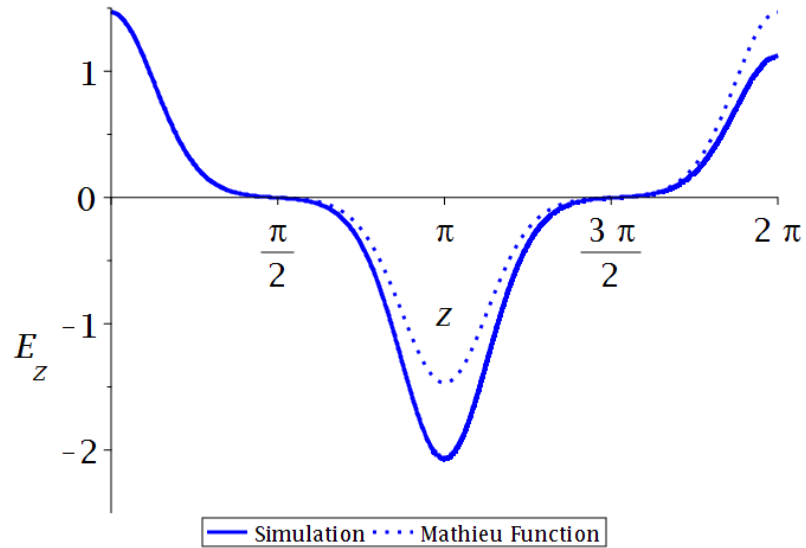
Figure 6.38: A plot of the combined field profile (longitudinal, z, spatial variation of the electric field strength, E_z) of the two longitudinal modes ($f = 6.5060$ GHz and $f = 6.5064$ GHz) in an infinite dielectric wire medium ($\varepsilon_r = 1600$, $a_x = 13.06$ mm and $a_y = 15.00$ mm) for our attempts to produce a profile with a pronounced peak ($q = -10.0$) with the parameter choice of $f_d = 6.5$ GHz, $R_c = 0.2$ mm and $\lambda_C = 6.61$ GHz.

The comparison between our desired profile with a pronounced peak and a sine curve is shown in Fig. 6.39. The $\mathfrak{R}^2$ value for this comparison is 0.7536. This makes the $\mathfrak{R}^2$ valued achieved by our simulation profile even more impressive.
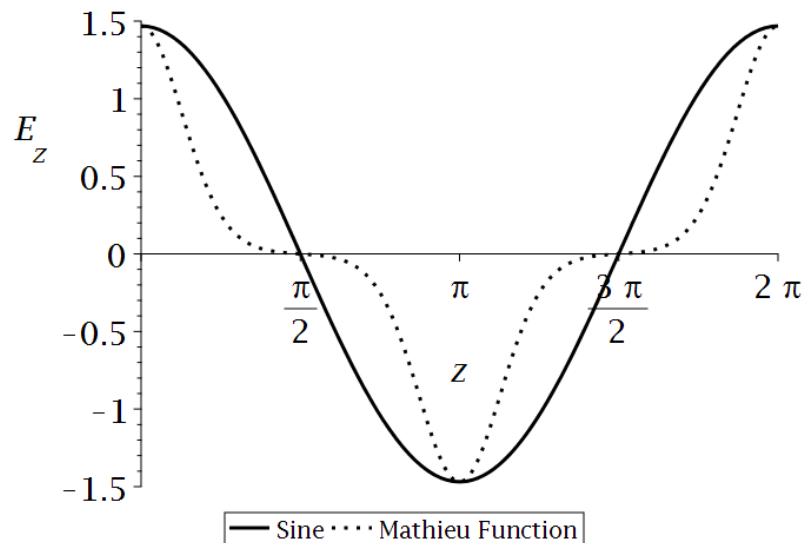
Figure 6.39: A comparison of the Mathieu function with a pronounced peak (dotted black), $q = -10.0$, with a sinusoidal curve with an identical peak value (solid black).

93

IX. Conclusions

In this chapter, we have presented the development and initial testing of our mode profile shaping method with infinite dielectric wire media. We have shown that the wire radius has an effect on the plasma frequency and quantified this effect with an exponential decay relationship for $\varepsilon_r = 1600$ wires. We have related this to our previous theoretical analysis to find a function for the required radius variation to support a desired field profile in our wire media. After setting forth considerations taken in fixing our free parameters, we have tested the method for a variety of different parameter choices in simulations. The results of these simulations were successful, as we have confirmed via qualitative and quantitative means. We have shown that these results are stable with regards to changes in the mesh and the number of segments which form our varying dielectric wire. Having tested our method for a flattened profile initially, we then tested it for a variety of profile with similar success.

Chapter 7

Method verification in practical dielectric wire media

The results described in Chapter 6 were promising. They provided strong validation of our theoretical model, as it had successfully predicted the existence of our longitudinal modes, the dispersion relation of those modes and how these fields could be controlled with a varying plasma frequency. This success was qualified by the fact that these were simulations of idealised structures that would require specific material parameters.

All the results listed in Chapter 6 were achieved in simulations of an infinite lattice. This consisted of a unit cell with periodic boundary conditions and containing a thin dielectric wire that had an extremely large value for the relative permittivity. This raised the prospect of two possible problems for the potential realisation of our mode profiling method: these results would no longer hold in a realistic structure that would necessarily be finite, or that the results would be prohibitively difficult to replicate due to the extreme values of radius and permittivity required. This necessitated simulations of more easily fabricated realisations of wire media.

I. REPLICATING RESULTS WITH DIFFERENT PERMITTIVITY VALUES

Our first step in this process was to see if we could replicate our results for different values of the relative permittivity of our dielectric rods. It was reasonable to expect that if the radius and lattice parameters affect the electromagnetic behaviour of our structure, so should the permittivity. Therefore, we assumed we could not just use the data taken for $\varepsilon_r = 1600$ and apply it to structures with wires that have different permittivities. As such, we started from the beginning of the process detailed in Chapter 6.

We ran simulations to find longitudinal modes for these new structures. In Fig. 7.1 there are images of the longitudinal modes found in dielectric wire media with a variety of different permittivity values, where otherwise the wire radius

and lattice parameters are identical. The permittivity values shown are $\varepsilon_r = 1600$, $\varepsilon_r = 400$ and $\varepsilon_r = 100$. Fig. 7.1 shows that for each permittivity, we can find our desired longitudinal mode, although they are found at different frequencies.
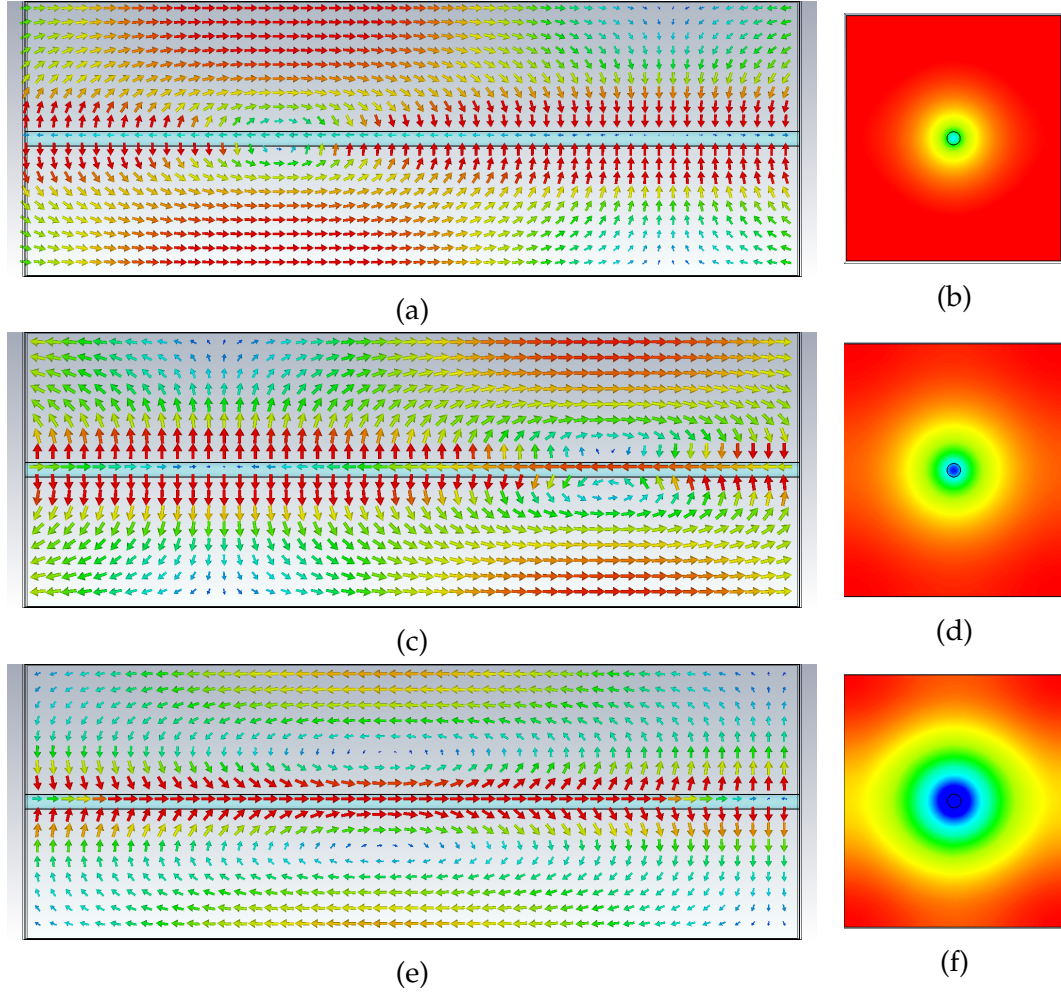
Figure 7.1: A series of images from numerical simulations in CST showing the longitudinal modes found in infinite dielectric wire media ($r = 0.4$ mm, $a_x = 13.06$ mm and $a_y = 15.00$ mm) for a variety of dielectric permittivities. The fields are either represented using arrow plots where the arrow direction represents field direction and colour represents the magnitude of the field strength, or colour plots where the direction and magnitude of the longitudinal field is represented by colour. (a) and (b) show a longitudinal mode ($f = 6.72$ GHz) in a wire medium with $\varepsilon_r = 1600$, with (a) showing a y-z slice and (b) an x-y slice. (c) and (d) show a longitudinal mode ($f = 8.11$ GHz) in a wire medium with $\varepsilon_r = 400$, with (c) showing a y-z slice and (d) an x-y slice. (e) and (f) show a longitudinal mode ($f = 11.7$ GHz) in a wire medium with $\varepsilon_r = 100$, with (e) showing a y-z slice and (f) an x-y slice.

We then plotted the dispersion relation of these longitudinal modes to confirm

they had the predicted plasma-like dispersion relation. These dispersion relations are shown in Fig. 7.2; it is fairly clear that these relations are plasma-like, but, as we have done previously, we plotted f^2 vs k^2 graphs for these modes to confirm our judgement. Fig. 7.2 clearly shows that changing the permittivity of the wires in our wire medium has the effect of shifting the dispersion relations of our longitudinal modes. This will influence the plasma frequencies of these modes and the radius values required for a given profile, justifying the need to repeat the method laid out in Chapter 6 for each permittivity.
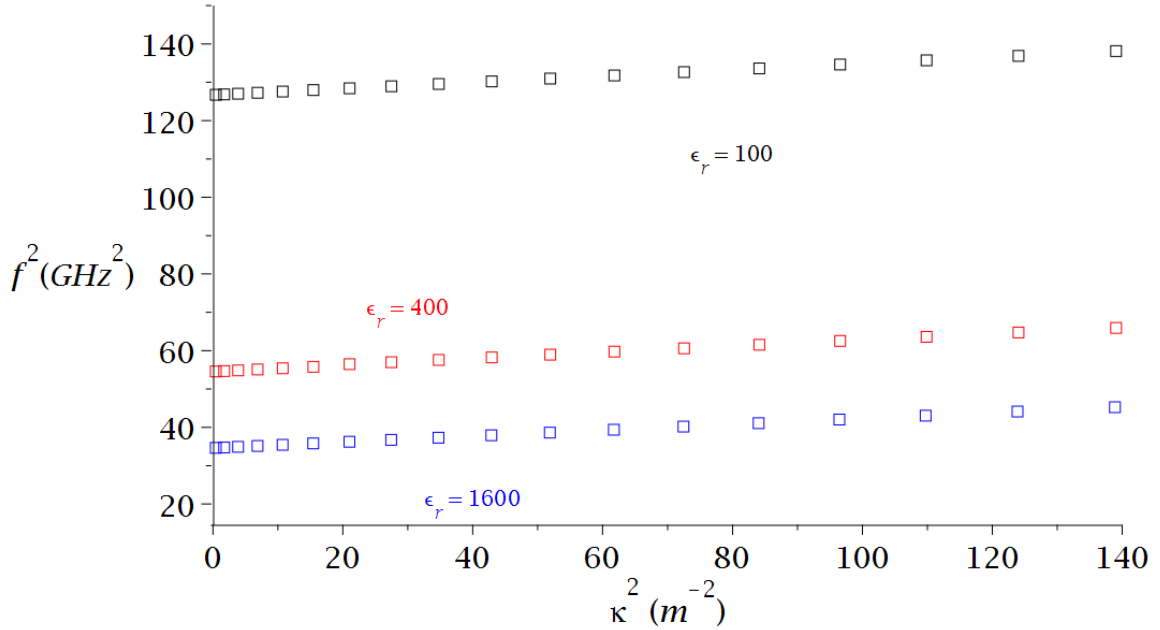
Figure 7.2: The squared dispersion plots, frequency (f^2) against wavenumber (κ^2), of the longitudinal modes in infinite dielectric wire media ($r = 0.4$ mm, $a_x = 13.06$ mm and $a_y = 15.00$ mm) for a variety of dielectric permittivities. These permittivities are $\varepsilon_r = 1600$ (blue), $\varepsilon_r = 400$ (red) and $\varepsilon_r = 100$ (black).

As for the original case of $\varepsilon_r = 1600$, we explored the relationship between plasma frequency and radius for these new structures. A plot of the relationship between plasma frequency and wire radius for a variety of different permittivity values, $\varepsilon_r = (1600, 400, 100, 50, 5, 3)$, is shown in Fig. 7.3. One important aspect of Fig. 7.3 to note is that the relationship for all the permittivity values can still be well described by an exponential decay curve, as shown by the inclusion of our fitting curves for each set of data. This means we do not need to change our method for calculating the radius function required; instead, we can input the new fitting parameters for a given permittivity into the existing method. These new fitting parameters for the different permittivity values are shown in Table 7.1, along with the original fitting parameters for $\varepsilon_r = 1600$.
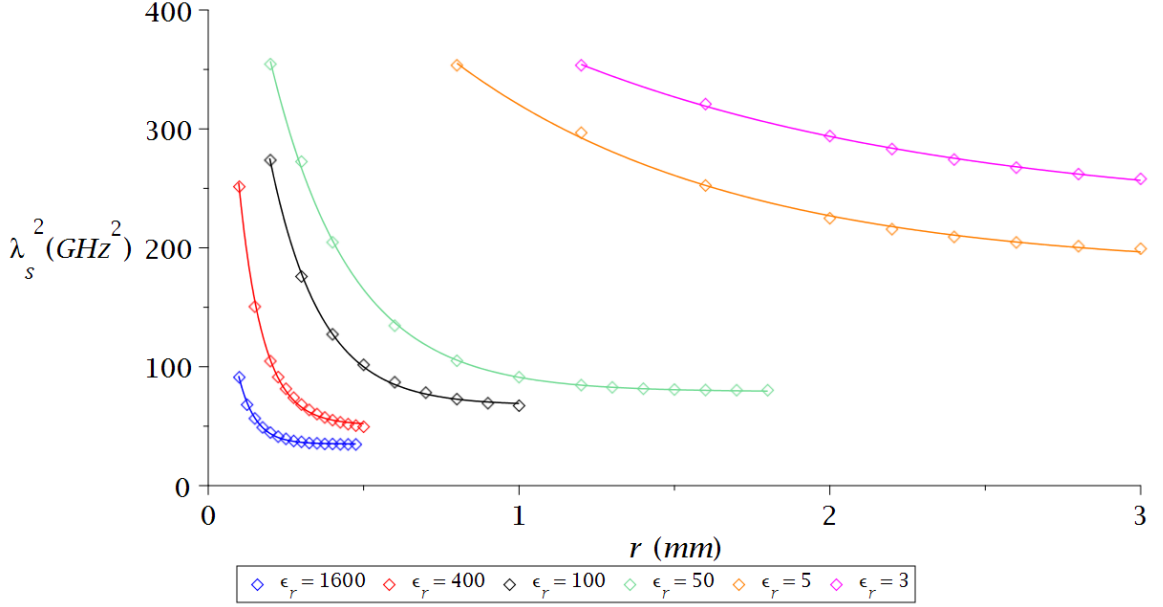
Figure 7.3: Plots of the plasma frequency squared, λ_s^2, of infinite dielectric wire media ($a_x = 13.06$ mm and $a_y = 15.00$ mm) against wire radius, r, for a variety of dielectric permittivities. These permittivities are $\varepsilon_r = 1600$ (blue), $\varepsilon_r = 400$ (red), $\varepsilon_r = 100$ (black), $\varepsilon_r = 50$ (green), $\varepsilon_r = 5$ (orange) and $\varepsilon_r = 3$ (magenta).

We were then able to test our mode profiling method for these new permittivity values. For our test case of each permittivity, we attempted to replicate a flattened mode profile (Mathieu parameter $q = 0.8$), which is shown in Fig. 7.4. We have listed the parameters used for our mode profiling attempts for each permittivity value in Table 7.2.

ε_r	δ (GHz^2)	σ (GHz^2)	ρ (mm^{-1})	$\mathfrak{R}^2$
1600	35.1	350	0.0541	0.9981
400	50.9	721	0.0776	0.9985
100	67.6	703	0.162	0.9995
50	78.9	608	0.256	0.9995
5	182	426	0.890	0.9982
3	227	335	1.24	0.9990

Table 7.1: A table summarising some of the key parameters related to the exponential decay fit $\left(\delta + \sigma \exp\left(-\frac{r}{\rho}\right)\right)$ for the plasma frequency against radius data of infinite dielectric wire media ($a_x = 13.06$ mm and $a_y = 15.00$ mm) with a variety of dielectric permittivities. The parameters listed are: the dielectric permittivity (ε_r), the exponential decay function parameters (δ, σ and ρ) and a figure of merit for the agreement between our exponential decay fit and the data ($\mathfrak{R}^2$).

ε_r	f_d (GHz)	R_C (mm)	λ_C (GHz)	Γ_1 (μm)	$\Gamma_2 \cdot 10^{-2}$	$\Gamma_3 \cdot 10^{-2}$	Γ_4 (m^{-1})	L (mm)
400	9.0	0.3	8.13	77.6	2.09	1.94	129	97.3
100	11	0.5	10.0	162	4.59	2.80	153	82.1
50	12.5	0.6	11.7	256	9.56	2.94	146	86.1
5	14	2.0	13.1	890	10.6	5.36	165	76.2
3	18	2.3	16.7	1410	19.7	13.2	221	56.7

Table 7.2: A table summarising some of the key parameters related to the implemented radius functions for a flattened profile ($q = 0.8$) in infinite dielectric wire media ($a_x = 13.06$ mm and $a_y = 15.00$ mm) for a variety of dielectric permittivities. The first set of parameters listed are design parameters we chose: the dielectric permittivity (ε_r), design frequency (f_d), central radius (R_C) and the corresponding central plasma frequency (λ_c). The rest are the resulting structural parameters: the parameters specifying the corresponding radius function (Γ_{1-4}) and the length of our unit cell (L).
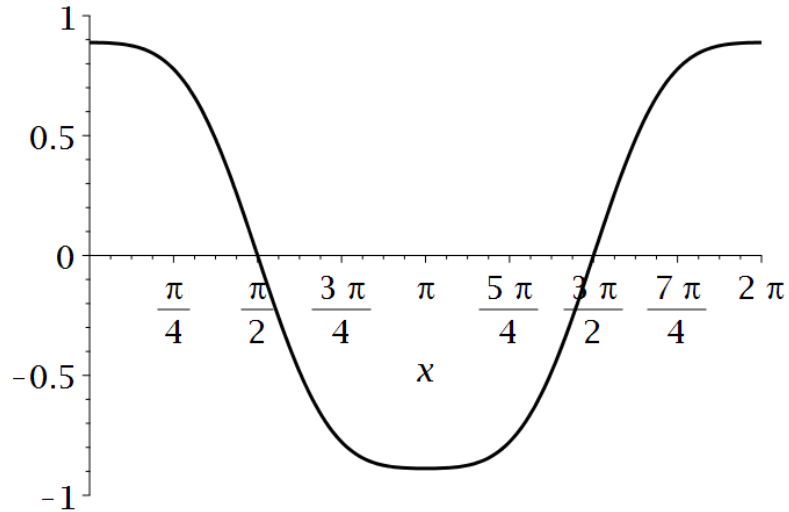
Figure 7.4: A solution to Mathieu's equations ($q = 0.8$) that can be loosely described as a flattened sinusoidal curve.

The radius functions for the mode profiling attempts detailed in Table 7.2 are plotted in Fig. 7.5.
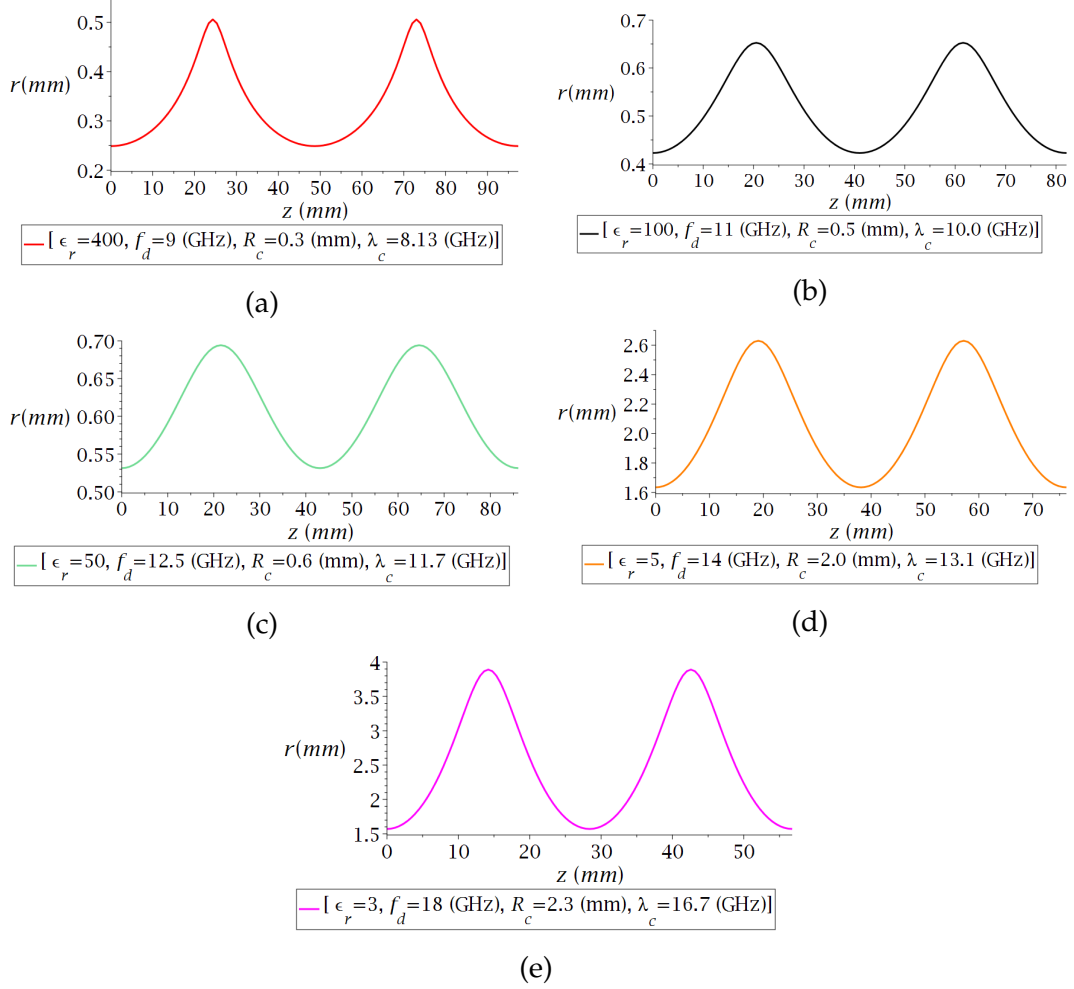
Figure 7.5: A series of plots of radius functions calculated for a flattened profile ($q = 0.8$) in infinite dielectric wire media ($a_x = 13.06$ mm and $a_y = 15.00$ mm) for a variety of dielectric permittivities. (a) shows the radius function for a choice of $\varepsilon_r = 400$, $f_d = 9$ GHz, $R_c = 0.3$ mm and $\lambda_C = 8.13$ GHz (red); (b), for a choice of $\varepsilon_r = 100$, $f_d = 11$ GHz, $R_c = 0.5$ mm and $\lambda_C = 10.0$ GHz (black); (c), for a choice of $\varepsilon_r = 50$, $f_d = 12.5$ GHz, $R_c = 0.6$ mm and $\lambda_C = 11.7$ GHz (green); (d), for a choice of $\varepsilon_r = 5$, $f_d = 14$ GHz, $R_c = 2$ mm and $\lambda_C = 13.1$ GHz (orange); and (e), for a choice of $\varepsilon_r = 3$, $f_d = 18$ GHz, $R_c = 2.3$ mm and $\lambda_C = 16.7$ GHz (magenta).

We implemented these radius functions in CST and the modes found are shown in Fig. 7.6. The profiles of these longitudinal modes are plotted in Fig. 7.7, and the results of these simulations are summarised in Table 7.3, where it can be seen that the field profile shaping has been successful for all permittivities attempted. We have shown that we can use our method for a variety of permittivity values as low as $\varepsilon_r = 3$. As well as this, it can be seen that as we start using lower permittivity wires, the radius required increases. This is useful as the small radii required for $\varepsilon_r = 1600$ would have caused difficulties with fabrication.
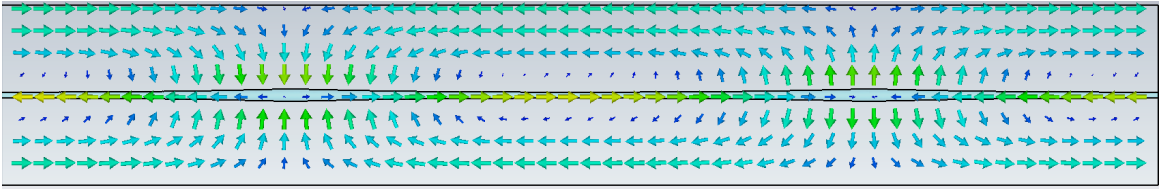
(a)
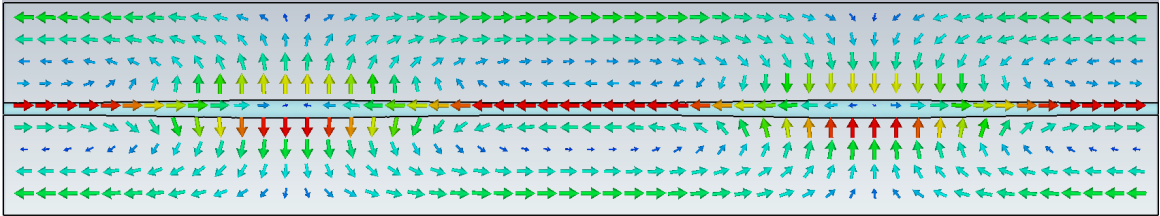
(b)
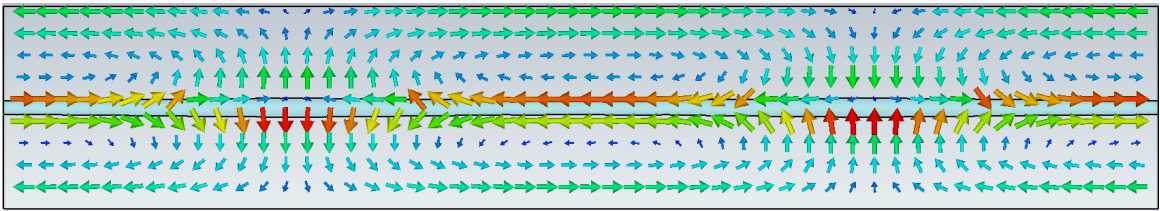
(c)
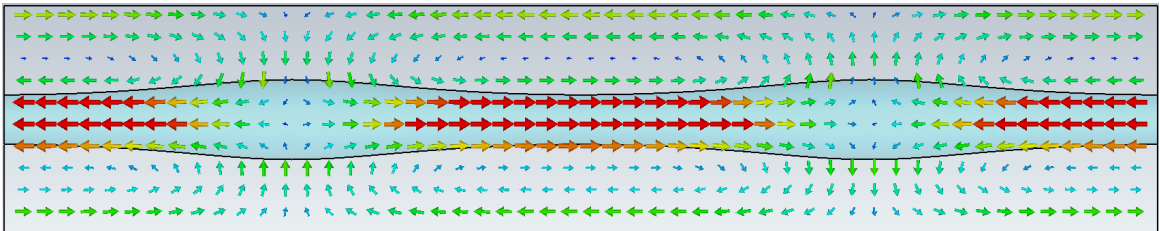
(d)
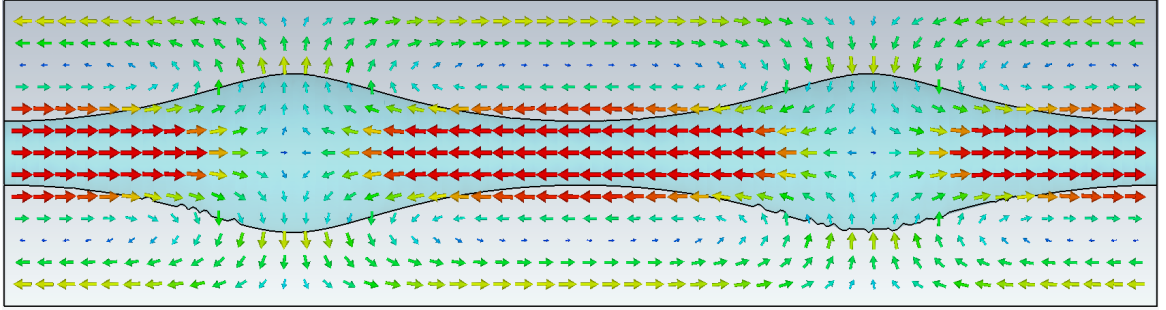
(e)

Figure 7.6: Images showing the resulting longitudinal modes after the implementation of the calculated radius functions for a flattened profile ($q = 0.8$) in infinite dielectric wire media ($a_x = 13.06$ mm and $a_y = 15.00$ mm) for a variety of dielectric permittivities. The fields are represented using arrow plots on a y-z slice of the structure where the arrow direction represents field direction and colour represents the magnitude of the field strength. (a) shows the resulting longitudinal mode ($f = 8.99$ GHz) for the attempt to demonstrate a flattened profile by the implementation of a radius function based on the choice of $\varepsilon_r = 400$, $f_d = 9$ GHz, $R_c = 0.3$ mm and $\lambda_C = 8.13$ GHz; (b) shows the resulting longitudinal mode ($f = 10.96$ GHz) for the attempt to demonstrate a flattened profile by the implementation of a radius function based on the choice of $\varepsilon_r = 100$, $f_d = 11$ GHz, $R_c = 0.5$ mm and $\lambda_C = 10.0$ GHz; (c) shows the resulting longitudinal mode ($f = 12.34$ GHz) for the attempt to demonstrate a flattened profile by the implementation of a radius function based on the choice of $\varepsilon_r = 50$, $f_d = 12.5$ GHz, $R_c = 0.6$ mm and $\lambda_C = 11.7$ GHz; (d) shows the resulting longitudinal mode ($f = 15.71$ GHz) for the attempt to demonstrate a flattened profile by the implementation of a radius function based on the choice of $\varepsilon_r = 5$, $f_d = 14$ GHz, $R_c = 2$ mm and $\lambda_C = 13.1$ GHz; and (e) shows the resulting longitudinal mode ($f = 17.84$ GHz) for the attempt to demonstrate a flattened profile by the implementation of a radius function based on the choice of $\varepsilon_r = 3$, $f_d = 18$ GHz, $R_c = 2.3$ mm and $\lambda_C = 16.7$ GHz.

(a)

(b)

(c)

(d)

104
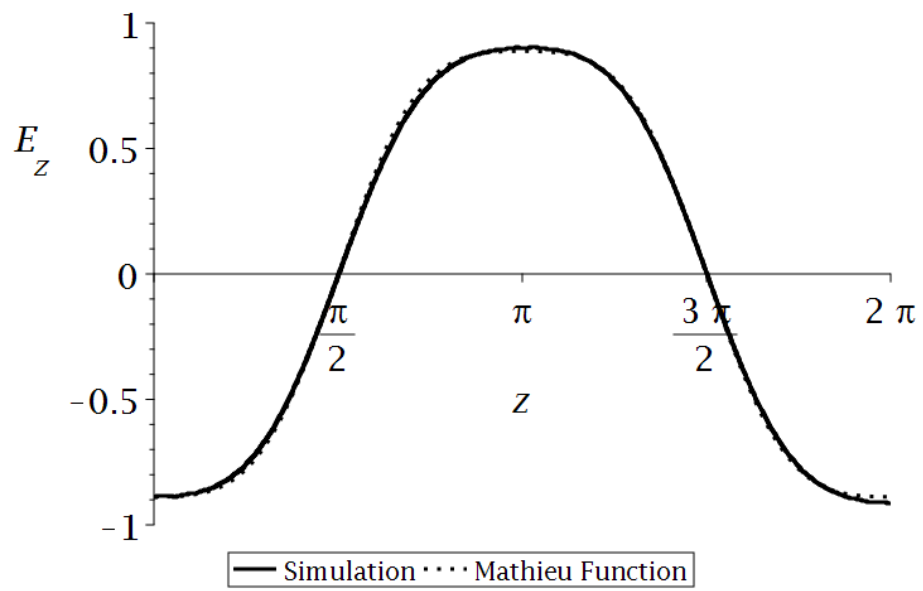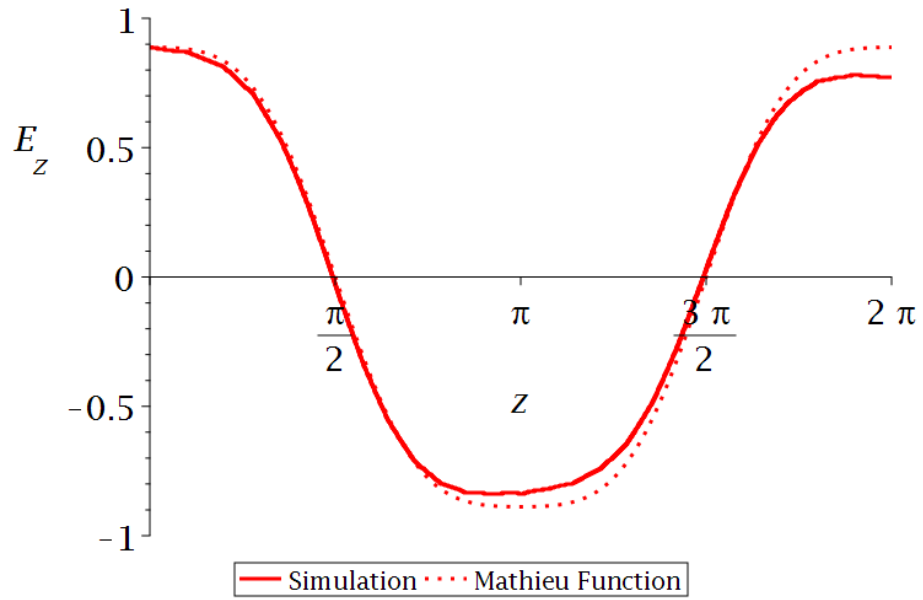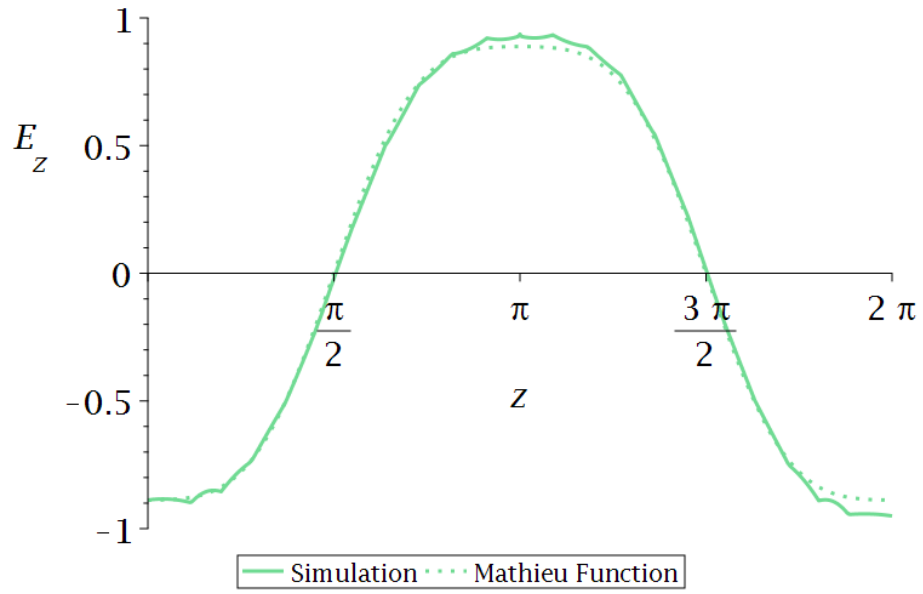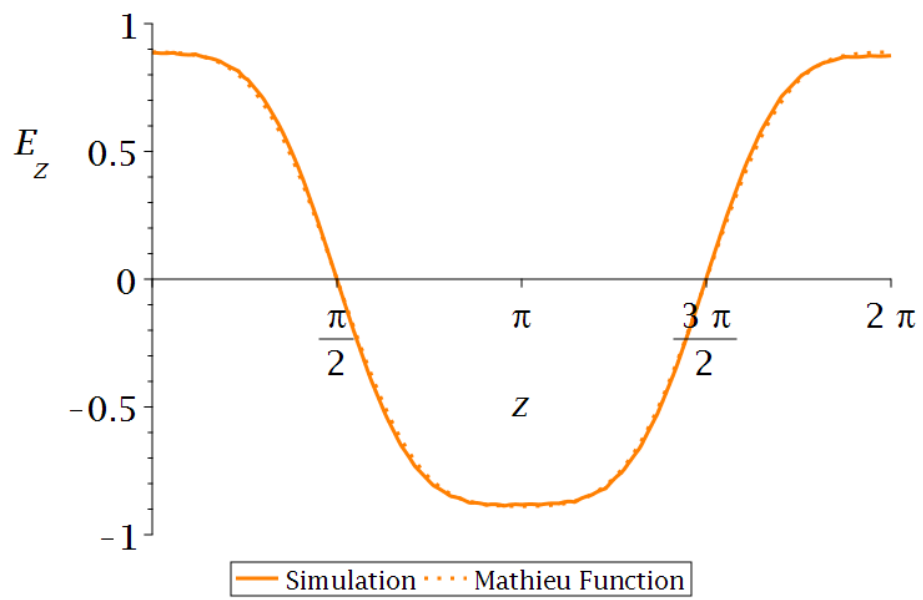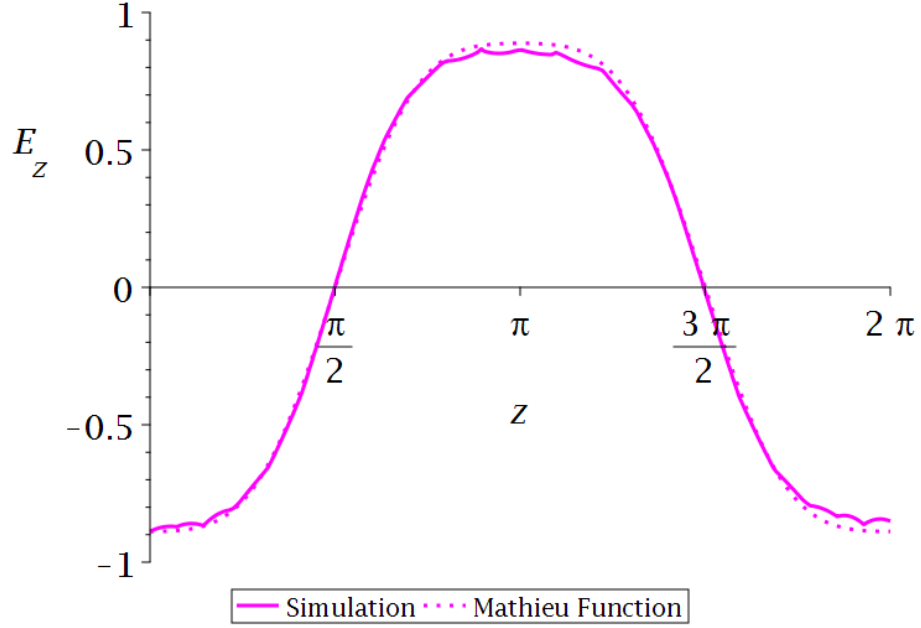
(e)

Figure 7.7: Plots showing the field profiles of the longitudinal modes after the implementation of the calculated radius functions for a flattened profile ($q = 0.8$) in infinite dielectric wire media ($a_x = 13.06$ mm and $a_y = 15.00$ mm) for a variety of dielectric permittivities. The plots include the field profile observed in our numerical simulation (solid) and the desired profile (dotted). In order to compare these the field profile and z coordinate have been normalised. (a) shows the field profile of the resulting longitudinal mode ($f = 8.99$ GHz) for the attempt to demonstrate a flattened profile by the implementation of a radius function based on the choice of $\varepsilon_r = 400$, $f_d = 9$ GHz, $R_c = 0.3$ mm and $\lambda_C = 8.13$ GHz; (b) shows the field profile of resulting longitudinal mode ($f = 10.96$ GHz) for the attempt to demonstrate a flattened profile by the implementation of a radius function based on the choice of $\varepsilon_r = 100$, $f_d = 11$ GHz, $R_c = 0.5$ mm and $\lambda_C = 10.0$ GHz; (c) shows the field profile of resulting longitudinal mode ($f = 12.34$ GHz) for the attempt to demonstrate a flattened profile by the implementation of a radius function based on the choice of $\varepsilon_r = 50$, $f_d = 12.5$ GHz, $R_c = 0.6$ mm and $\lambda_C = 11.7$ GHz; (d) shows the field profile of resulting longitudinal mode ($f = 15.71$ GHz) for the attempt to demonstrate a flattened profile by the implementation of a radius function based on the choice of $\varepsilon_r = 5$, $f_d = 14$ GHz, $R_c = 2$ mm and $\lambda_C = 13.1$ GHz; and (e) shows the field profile of resulting longitudinal mode ($f = 17.84$ GHz) for the attempt to demonstrate a flattened profile by the implementation of a radius function based on the choice of $\varepsilon_r = 3$, $f_d = 18$ GHz, $R_c = 2.3$ mm and $\lambda_C = 16.7$ GHz.

ε_r	f_d (GHz)	λ_C (GHz)	L (mm)	f (GHz)	$\mathfrak{R}^2$
400	9	8.13	97.3	8.99	0.9935
100	11	10.0	82.1	11.0	0.9996
50	12.5	11.7	86.1	12.3	0.9986
5	14	13.1	76.2	15.7	0.9997
3	18	16.7	56.7	17.8	0.9988

Table 7.3: A table summarising some of the key parameters related to the results of the implemented radius functions for a flattened profile ($q = 0.8$) in infinite dielectric wire media ($a_x = 13.06$ mm and $a_y = 15.00$ mm) for a variety of dielectric permittivities. The parameters listed are: the dielectric permittivity (ε_r), design frequency (f_d), central plasma frequency (λ_c), the length of our unit cell (L), longitudinal mode frequency (f) and a figure of merit for the agreement between our field profile and the desired profile ($\mathfrak{R}^2$).

II.   EXAMINING THE EFFECT OF THE LATTICE CONSTANTS

Our method for mode profile shaping relies on the effect of the wire radius on the properties of our longitudinal electric modes. It was natural to expect that other structural parameters, such as the lattice spacing, could affect these modes. With this in mind, simulations were run to probe the dependence of our longitudinal modes on the lattice spacing. These simulations all involve the previously explored set-up of a unit cell with periodic boundary conditions applied to all boundaries, effectively representing an infinite lattice of dielectric wires.
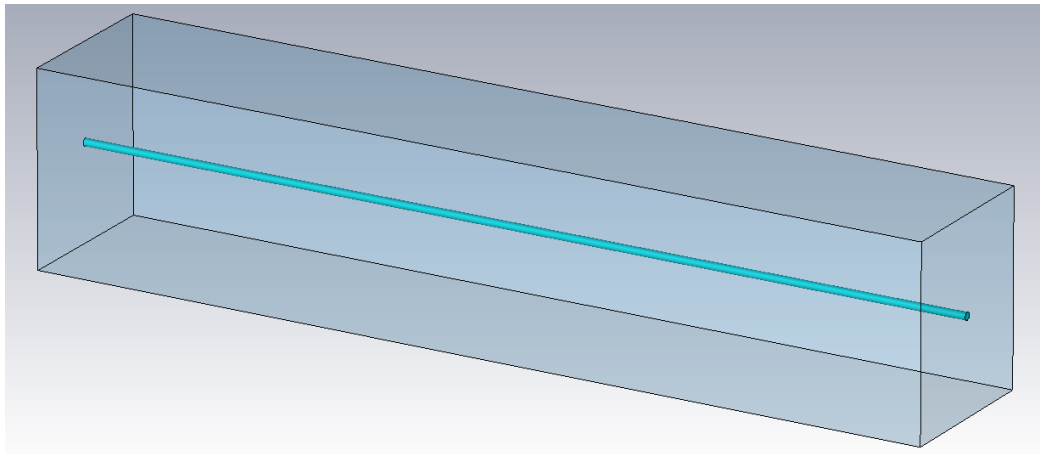
Figure 7.8: A typical representation of wire media in CST, consisting of a section of dielectric wire in a unit cell with periodic boundary conditions ($a_x = 13.06$ mm and $a_y = 15.00$ mm). The dielectric wire has a radius (r) of 0.3 mm and a relative permittivity (ε_r) of 400. This is our control structure for our lattice constant analysis.

It makes sense to compare our results when varying the lattice parameters to a familiar set of results. Therefore, we used as our comparison case the simulations involving our commonly used values for the lattice parameters (a_x = 13.06 mm and a_y = 15.00 mm). Our comparison unit cell contains a uniform dielectric wire of radius 0.3 mm and a relative permittivity of 400. This structure is shown in Fig. 7.8. The longitudinal mode supported by this structure is shown in Fig. 7.9, with a frequency of 8.21 GHz.

(a)

(b)
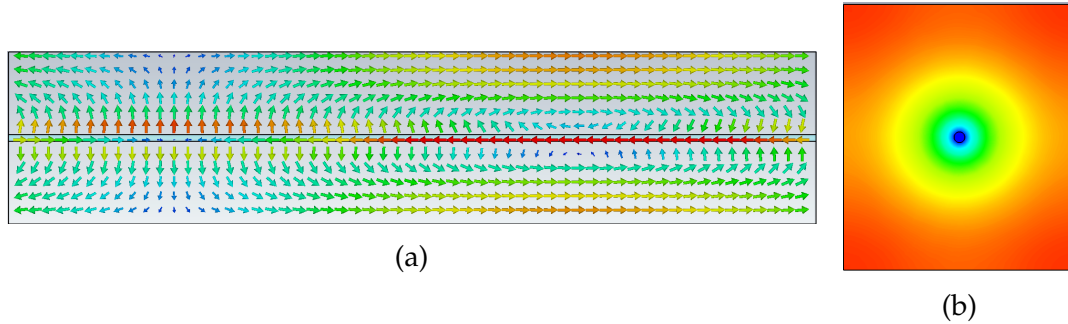
Figure 7.9: Images from numerical simulations in CST showing the longitudinal mode (f = 8.21 GHz) found in an infinite dielectric wire medium (ε_r = 400, r = 0.3 mm, a_x = 13.06 mm and a_y = 15.00 mm). The fields are either represented using arrow plots where the arrow direction represents field direction and colour represents the magnitude of the field strength, or colour plots where the direction and magnitude of the longitudinal field is represented by colour. (a) shows a y-z slice of the structure and (b) an x-y slice. This is the longitudinal mode found in our control structure.

We then ran simulations where one lattice constant was kept constant (a_x = 13.06 mm) while the other was varied. The other lattice constant, a_y, was varied from 2 mm to 24 mm. Images of the structures at the extremes of this range are shown in Fig. 7.10.

(a)

(b)
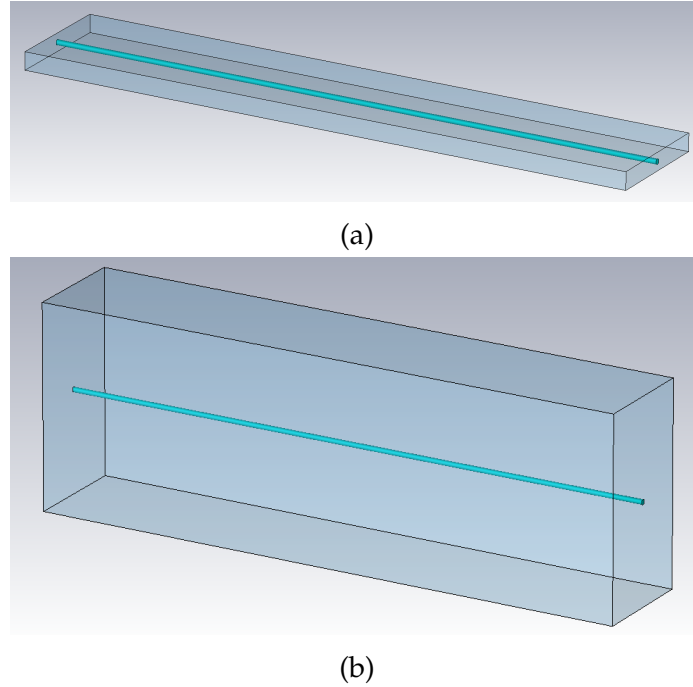
Figure 7.10: Two different representations of infinite dielectric wire media in CST ($\varepsilon_r = 400$, $r = 0.3$ mm, and $a_x = 13.06$mm). (a) shows a wire medium with $a_y = 2$ mm and (b) shows a wire medium with $a_y = 24$ mm. These two structures represent the edge cases in our analysis of varying one lattice parameter.

The longitudinal modes supported by these structures at the extremes of our range are shown in Fig. 7.11. These modes were found at 12.1 GHz, for $a_y = 2$ mm, and 7.04 GHz, for $a_y = 24$ mm.

Altering the lattice constant a_y does not stop the support of our longitudinal modes, but it does alter their frequency. This is illustrated in Fig. 7.12 where the frequency of our longitudinal mode is plotted against the value of a_y. This relationship can be fitted with an exponential decay curve, as represented by the black fitting curve. This fit has an $\mathfrak{R}^2$ value of 0.9992.

As well as varying one lattice constant value, we also changed both lattice constants by scaling their value by the scaling factor ζ. The new lattice constants are therefore $\zeta 13.06$ mm and $\zeta 15$ mm. We did this for a variety of ζ values, ranging from 0.4 to 2.1. The structures corresponding to the extremes of these scaling factors are shown in Fig. 7.13.

(a)

(b)

(c)

(d)

(e)

(f)
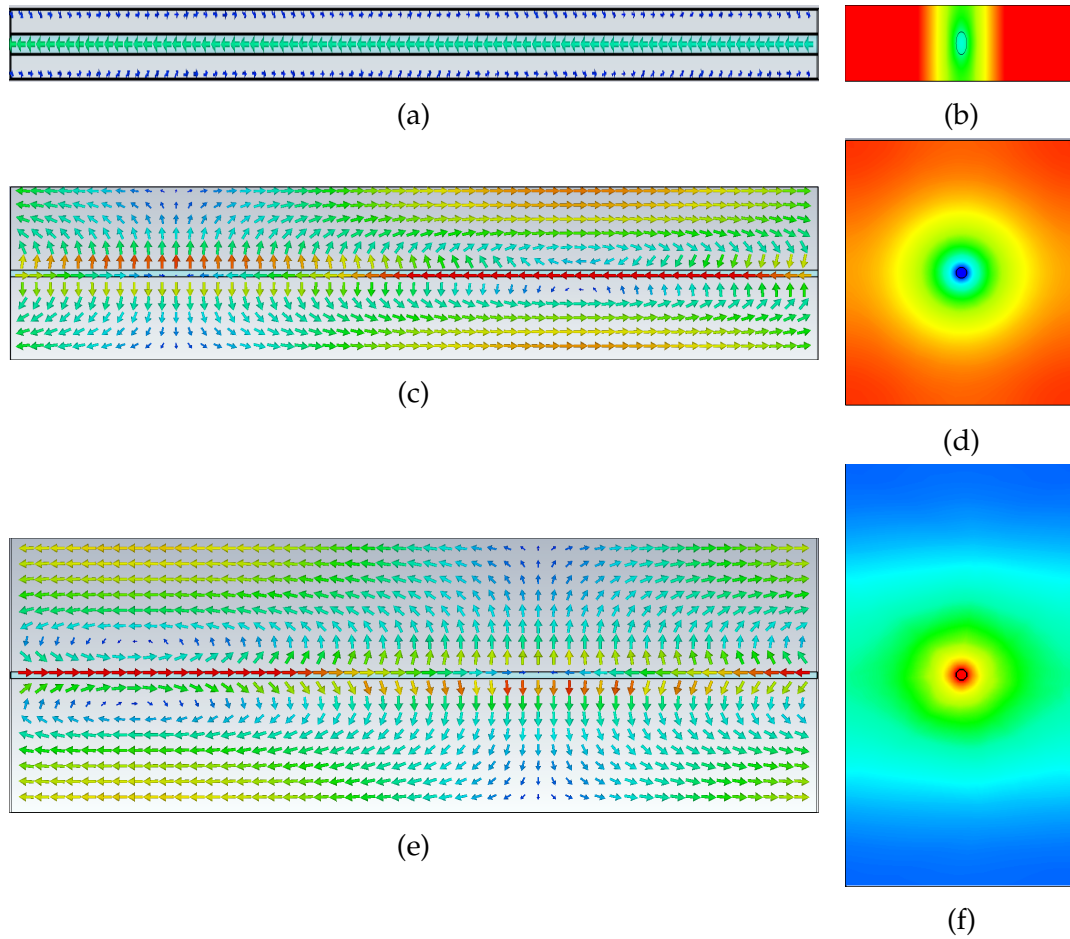
Figure 7.11: A series of images from numerical simulations in CST showing the longitudinal modes found in infinite dielectric wire media ($\varepsilon_r = 400$, $r = 0.3$ mm and $a_x = 13.06$ mm) for a variety of lattice constants a_y. The fields are either represented using arrow plots where the arrow direction represents field direction and colour represents the magnitude of the field strength, or colour plots where the direction and magnitude of the longitudinal field is represented by colour. (a) and (b) show a longitudinal mode ($f = 12.1$ GHz) in a wire medium with $a_y = 2$ mm, with (a) showing a y-z slice and (b) an x-y slice. (c) and (d) show a longitudinal mode ($f = 8.21$ GHz) in a wire medium with $a_y = 15$ mm, with (c) showing a y-z slice and (d) an x-y slice. (e) and (f) show a longitudinal mode ($f = 7.04$ GHz) in a wire medium with $a_y = 24$ mm, with (e) showing a y-z slice and (f) an x-y slice.
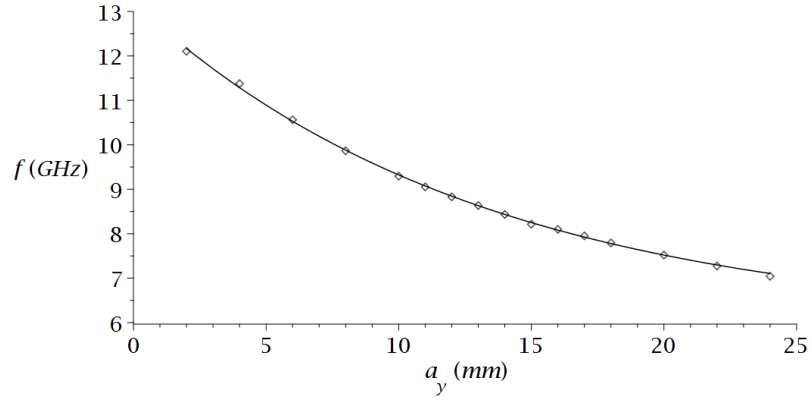
Figure 7.12: A plot of the frequency, f, of the longitudinal modes found in infinite dielectric wire media ($\varepsilon_r = 400$, $r = 0.3$ mm, and $a_x = 13.06$mm) against the lattice constant a_y. An exponential fitting curve has been included that describes the data well (black).
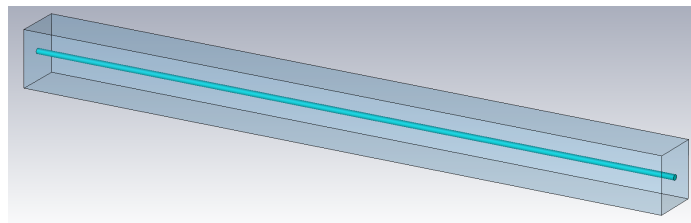
(a)
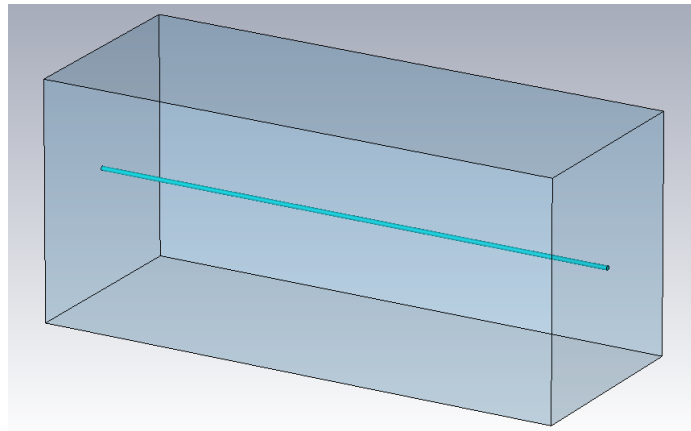
(b)

Figure 7.13: Two different representations of infinite dielectric wire media in CST ($\varepsilon_r = 400$ and $r = 0.3$ mm). (a) shows a wire media structure with $\zeta = 0.4$, $a_x = \zeta 13.06$ mm and $a_y = \zeta 15.00$ mm; and (b) shows a wire media structure with $\zeta = 2.1$, $a_x = \zeta 13.06$ mm and $a_y = \zeta 15.00$ mm. These two structure represent the edge cases in our analysis of scaling both lattice parameters of a wire medium.

The longitudinal modes supported by the structures shown in Fig. 7.13 are

shown in Fig. 7.14. These longitudinal modes were found at 17 GHz, for $\zeta = 0.4$, and 6 GHz, for $\zeta = 2.1$.
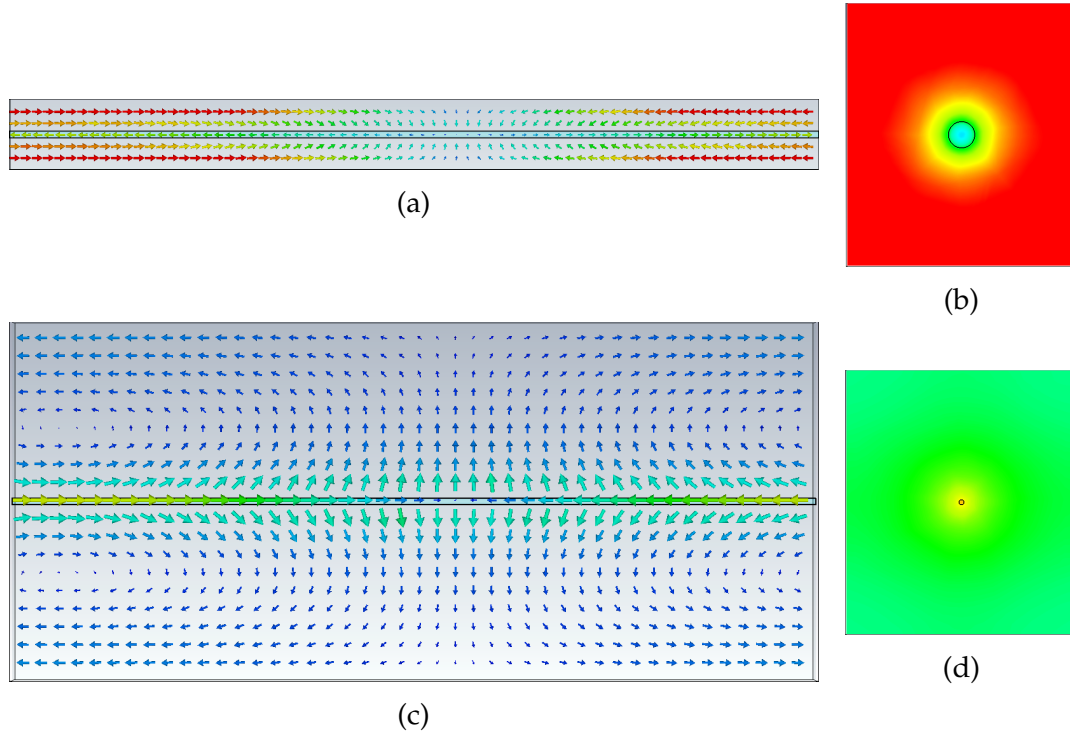
Figure 7.14: A series of images from numerical simulations in CST showing the longitudinal modes found in infinite dielectric wire media ($\varepsilon_r = 400$, $r = 0.3$ mm, $a_x = \zeta 13.06$ mm and $a_y = \zeta 15.00$ mm) for a variety of scaling constants ζ. The fields are either represented using arrow plots where the arrow direction represents field direction and colour represents the magnitude of the field strength, or colour plots where the direction and magnitude of the longitudinal field is represented by colour. (a) and (b) show a longitudinal mode ($f = 17.0$ GHz) in a wire medium with $\zeta = 0.4$, with (a) showing a y-z slice and (b) an x-y slice. (c) and (d) show a longitudinal mode ($f = 6.00$ GHz) in a wire medium with $\zeta = 2.1$, with (c) showing a y-z slice and (d) an x-y slice.

Again, we see an effect on the frequency of the longitudinal modes supported by our structures when varying ζ. This effect is shown in Fig. 7.15, where the frequency at which our longitudinal modes are supported is plotted against the scaling factor ζ. This relationship can also be fitted with an exponential decay curve. The $\mathfrak{R}^2$ value for this fit is 0.9951. Although, we can see that there seems to be a small systematic shift between the data and the fitting curve.
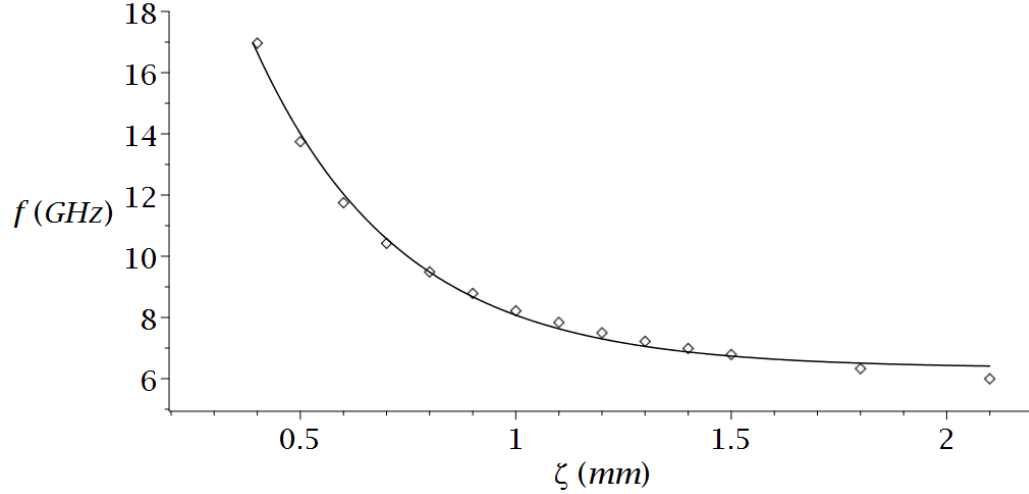
Figure 7.15: A plot of the frequency, f, of the longitudinal modes found in infinite dielectric wire media ($\varepsilon_r = 400$, $r = 0.3$ mm, $a_x = \zeta 13.06$ mm and $a_y = \zeta 15.00$ mm) against the scaling factor ζ. An exponential fitting curve has been included that describes the data accurately (black).

These results clearly show the importance of the choice of lattice parameters. We cannot take our analysis of the plasma frequency of a structure with one set of lattice parameters and apply it to another. It is necessary to analyse the specific structure you want to use. These simulations also present a possible route for tuning the frequencies supported by our wire medium. For example, if we have a structure which supports longitudinal modes, but we want to operate in a different frequency regime, it seems possible to scale our system to achieve this.

III.   Introducing disorder into our infinite wire media

III.1   Random error in the radii

In this section, we will overview our attempts to explore how resilient our mode profile shaping results are to the introduction of the disorder. By disorder, we mean deviations in our structures from our prescribed structural design. This is to be expected in any physical realisation of our structure as fabrication will introduce minor variations in structural parameters. In particular, we are looking at the effect of minor differences in the wire radius from our specified radius values. This will give us an idea of acceptable engineering tolerances for our wires.
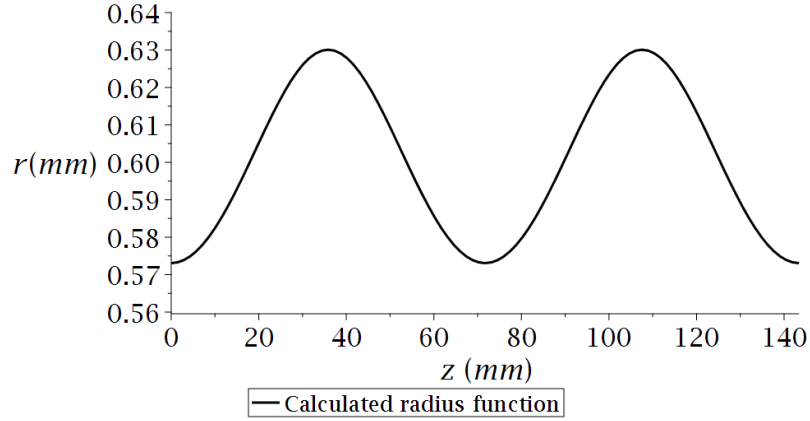
Figure 7.16: Radius function calculated for a flattened profile ($q = 0.8$) in an infinite dielectric wire medium ($\varepsilon_r = 50$, $a_x = 13.06$ mm and $a_y = 15.00$ mm) for the parameter choice of $f_d = 12$ GHz, $R_c = 0.6$ mm and $\lambda_C = 11.7$ GHz. This is the radius function of our control case.
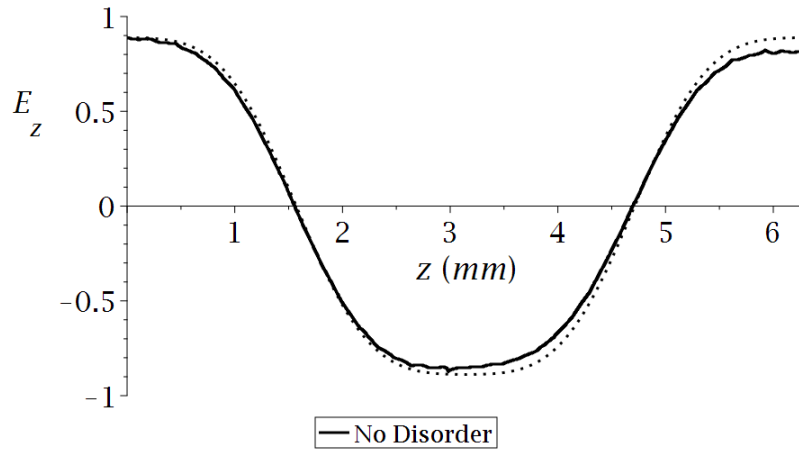
Figure 7.17: A plot of the field profile (longitudinal, z, spatial variation of the electric field strength, E_z) of the longitudinal mode ($f = 11.86$ GHz) in an infinite dielectric wire medium ($\varepsilon_r = 50$, $a_x = 13.06$ mm and $a_y = 15.00$ mm) for our attempt to produce a flattened profile ($q = 0.8$) with a radius function based on the parameter choice of $f_d = 12$ GHz, $R_c = 0.6$ mm and $\lambda_C = 11.7$ GHz. The plot includes the field profile observed in our numerical simulation (solid black) and the desired profile (dotted black). In order to aid comparison the field profile from our simulation and the z coordinate have been normalised. This the field profile of our control case.

One way to introduce disorder is to add a random variation to each of the desired radius values we calculate. This can be done simply in Maple, the software we use for our calculations, by using a random number generator. It is reason-

able to believe that any fabrication errors might manifest as seemingly random variations in the wire radius.

Our control case against which we will compare our disordered results is the case of a lattice of dielectric wires, with $\varepsilon_r = 50$, with a variation designed to produce a flat profile ($q = 0.8$) with lattice parameters $a_x = 15$ mm and $a_y = 13.1$ mm. In our simulations, this is represented by a unit cell with a length encompassing two periods of the radius variation, $L = 143$ mm, with periodic boundary conditions for all dimensions. With this choice of lattice properties and profile, we then chose the following values for our free parameters: $R_C = 0.6$ mm and $f_d = 12$ GHz. This choice of parameters results in a necessary radius function that is shown in Fig. 7.16. Implementing this radius function into CST, with no variations from the calculated radius values, gives the field profile shown in Fig. 7.17. It is clear from looking at Fig. 7.17 that our mode profile shaping efforts have been successful, which is affirmed by calculating the $\mathfrak{R}^2$ value of 0.9958. As previously defined in Chapter 6, the $\mathfrak{R}^2$ value is a measure of how well a function, in this case our chosen Mathieu function, fits a set of data, the simulation data, with values closer to 1 signifying better fits. It is possible for $\mathfrak{R}^2$ be negative; this means the chosen function is a worse fit than a horizontal line $y = C$ where the constant C is the average of the y values of the data set.
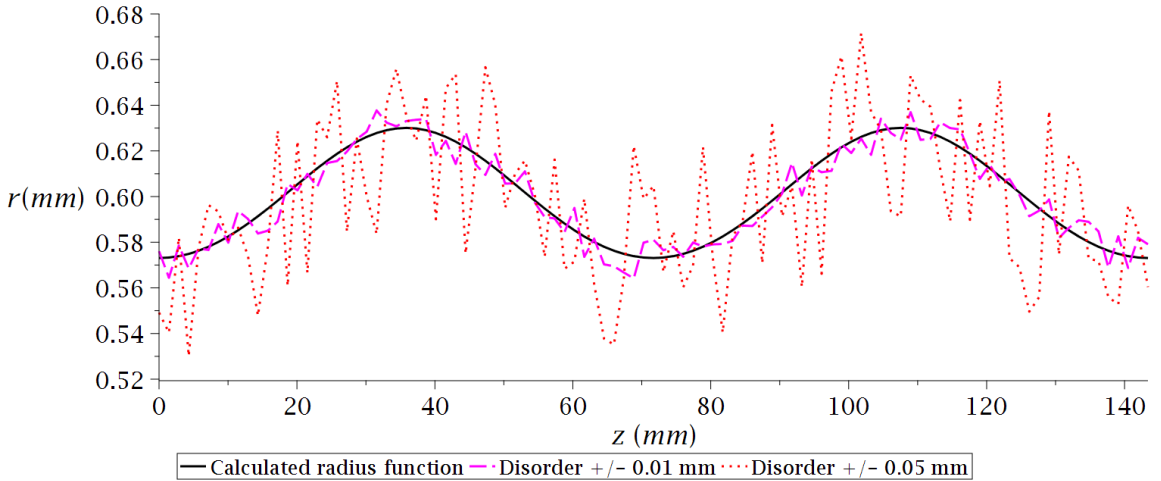
Figure 7.18: A plot of the resulting radius functions when different levels of disorder are introduced into our control radius function calculated for a flattened profile ($q = 0.8$) in an infinite dielectric wire medium ($\varepsilon_r = 50$, $a_x = 13.06$ mm and $a_y = 15.00$ mm) for the parameter choice of $f_d = 12$ GHz, $R_c = 0.6$ mm and $\lambda_C = 11.7$ GHz (black). The levels of disorder shown are ± 0.01 mm (dashed magenta) and ± 0.05 mm (dotted red).

When introducing our random disorder we used four levels of disorder: errors in the range of ± 0.01 mm; errors, of ± 0.05 mm; errors, of ± 0.1 mm; and errors, of ± 0.2 mm. As the radius values are centred around a value of 0.6 mm these

represent significant variations. The resulting radius functions have been plotted in Figs. 7.18, 7.19 and 7.20 with the control radius function.
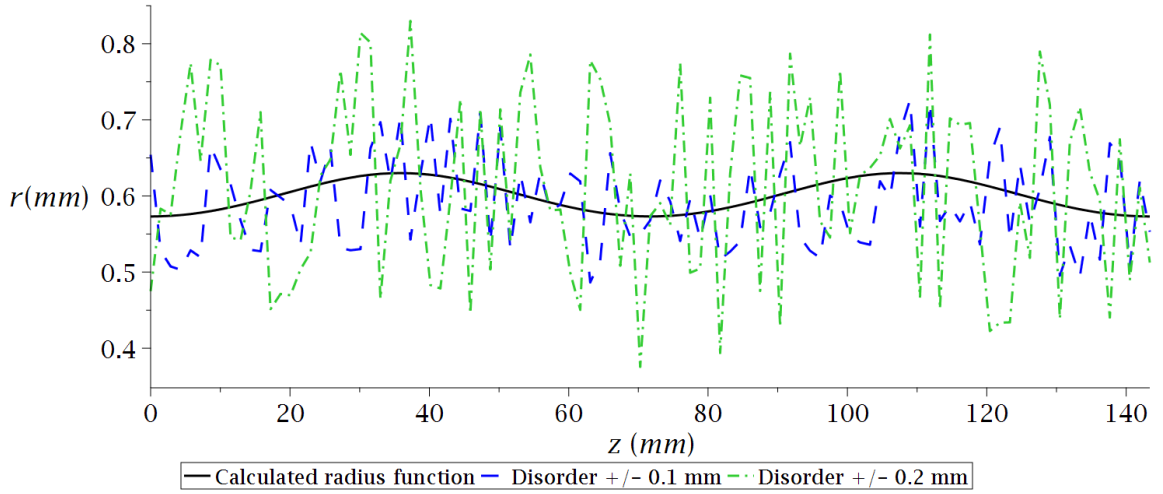
Figure 7.19: A plot of the resulting radius functions when different levels of disorder are introduced into our control radius function calculated for a flattened profile ($q = 0.8$) in an infinite dielectric wire medium ($\varepsilon_r = 50$, $a_x = 13.06$ mm and $a_y = 15.00$ mm) for the parameter choice of $f_d = 12$ GHz, $R_c = 0.6$ mm and $\lambda_C = 11.7$ GHz (black). The levels of disorder shown are ± 0.1 mm (dashed blue) and ± 0.2 mm (dash-dot green).

We can implement the radius functions shown in Fig. 7.20 in CST in the usual way by using a series of wire segments which approximate the desired radius variation. Fig. 7.21 is a CST image of a segment of the resulting wire after the implementation of the radius function with ± 0.05 mm disorder, which shows the effect this disorder has on the shape of the wire.

The modes profiles resulting from the inclusion of these levels of disorder are shown in Figs. 7.22 and 7.23. It can be seen that while mode profiling continues to perform well with a variation of the order ± 0.05 mm, Fig. 7.22b, there is significant deterioration for ± 0.1 mm, Fig. 7.23a, and profiling completely fails for ± 0.2 mm, Fig. 7.23b. This analysis is reinforced by the $\mathfrak{R}^2$ values for these attempts, as shown in Table 7.4 along with the frequency of the longitudinal modes associated with the different levels of disorder.
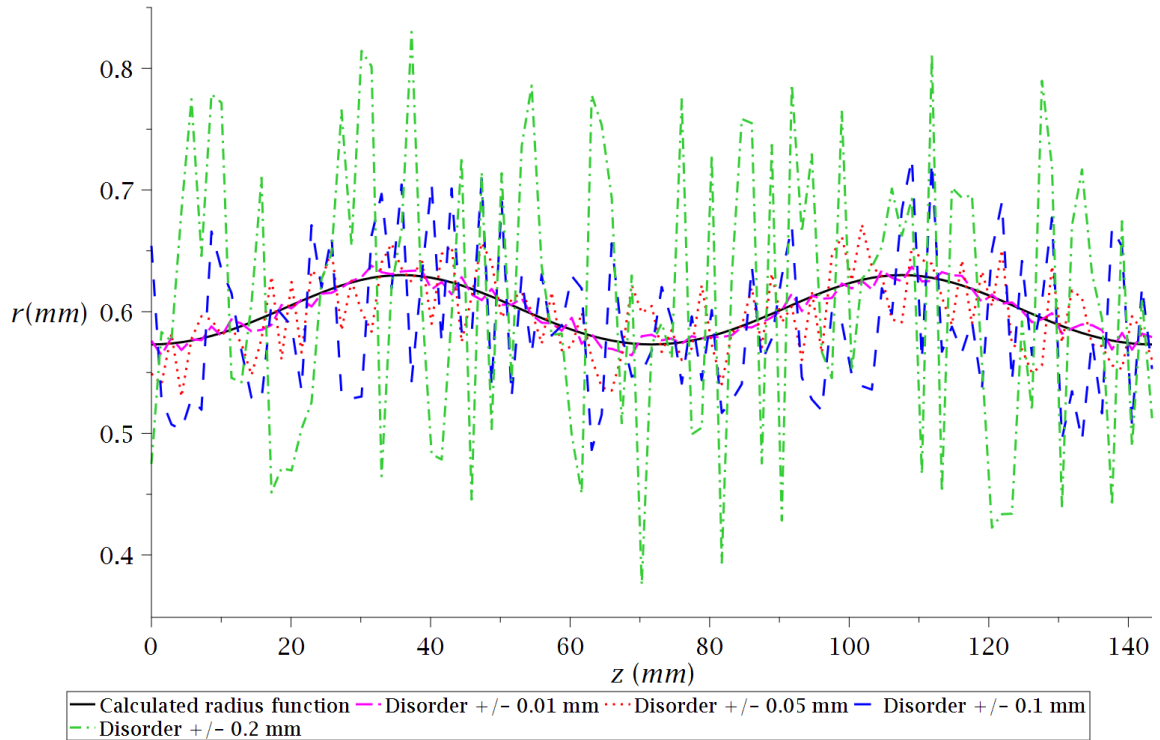
Figure 7.20: A plot of the resulting radius functions when different levels of disorder are introduced into our control radius function calculated for a flattened profile ($q = 0.8$) in an infinite dielectric wire medium ($\varepsilon_r = 50$, $a_x = 13.06$ mm and $a_y = 15.00$ mm) for the parameter choice of $f_d = 12$ GHz, $R_c = 0.6$ mm and $\lambda_C = 11.7$ GHz (black). The levels of disorder shown are ± 0.01 mm (dashed magenta) and ± 0.05 mm (dotted red), ± 0.1 mm (dashed blue) and ± 0.2 mm (dash-dot green).
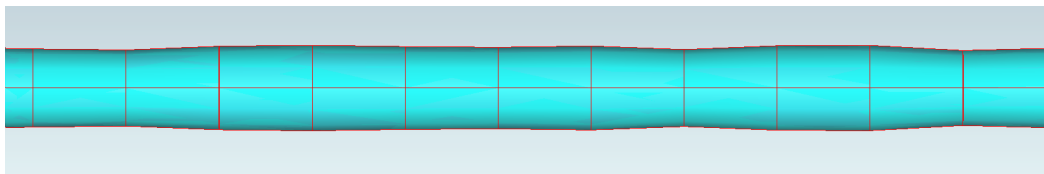
Figure 7.21: A segment of the resulting dielectric wire for the inclusion of ± 0.05 mm disorder into the radius function calculated for a flattened profile ($q = 0.8$) in an infinite dielectric wire medium ($\varepsilon_r = 50$, $a_x = 13.06$ mm and $a_y = 15.00$ mm) for the parameter choice of $f_d = 12$ GHz, $R_c = 0.6$ mm and $\lambda_C = 11.7$ GHz.

Given the results of this analysis, it would be sensible to aim to ensure fabrication errors are at most on the order of ± 0.05 mm. This seems like a reasonable level of accuracy to aim for, although the requirement for materials with certain permittivity values could be a complicating factor.

116

Disorder	f (GHz)	$\mathfrak{R}^2$
None	11.86	0.9958
± 0.01 mm	11.86	0.9980
± 0.05 mm	11.89	0.9945
± 0.1 mm	12.00	0.8937
± 0.2 mm	11.92	-0.1716

Table 7.4: Table summarising the results of the implementation of radius functions when different levels of disorder are introduced into our control radius function calculated for a flattened profile ($q = 0.8$) in an infinite dielectric wire medium ($\varepsilon_r = 50$, $a_x = 13.06$ mm and $a_y = 15.00$ mm) for the parameter choice of $f_\mathrm{d} = 12$ GHz, $R_c = 0.6$ mm and $\lambda_C = 11.7$ GHz. The parameters listed are: the level of disorder introduced, longitudinal mode frequency (f), and a figure of merit for the agreement between our field profile and the desired profile ($\mathfrak{R}^2$).
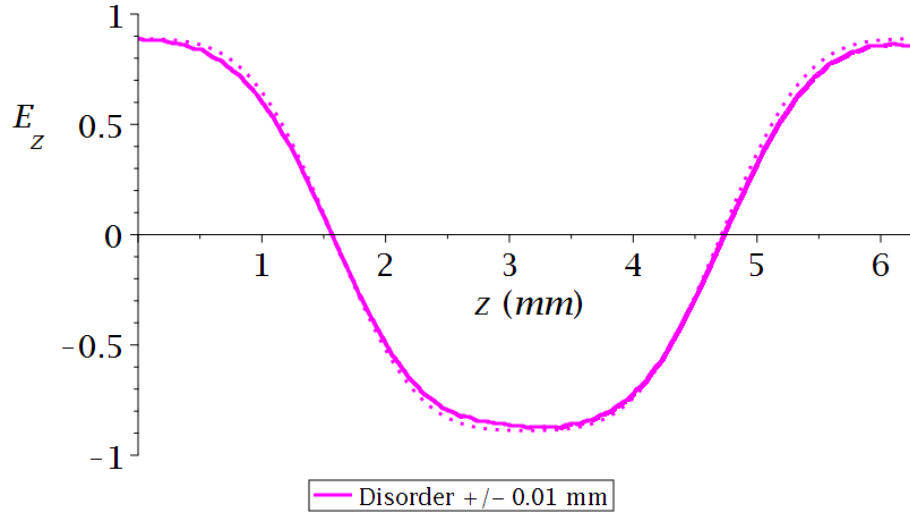
(a)
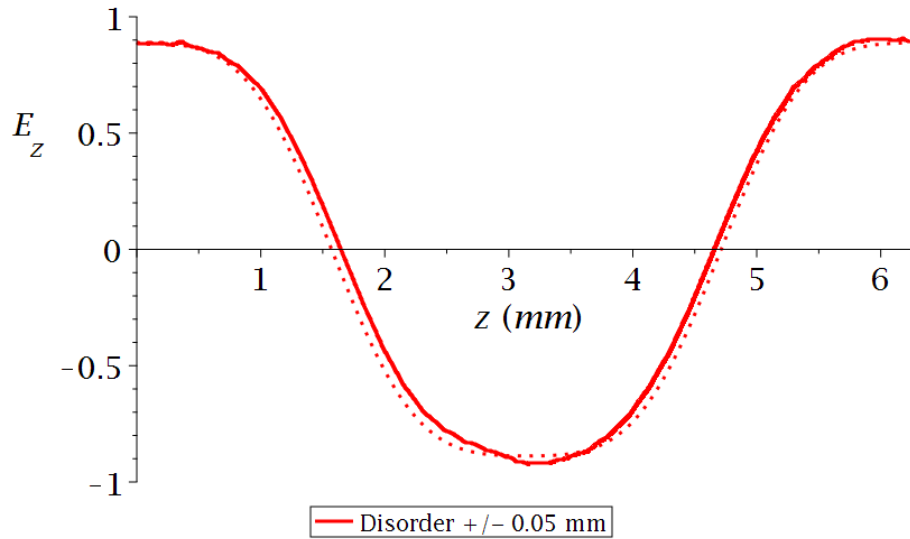
(b)

Figure 7.22: Plots showing the field profiles of the longitudinal modes when different levels of disorder are introduced into our control radius function for a flattened profile ($q = 0.8$) in infinite dielectric wire media ($\varepsilon_r = 50$, $a_x = 13.06$ mm and $a_y = 15.00$ mm) for the choice of $f_d = 12$ GHz, $R_c = 0.6$ mm and $\lambda_C = 11.7$ GHz, with a number of different levels of disorder. The plots include the field profile observed in our numerical simulation (solid) and the desired profile (dotted). In order to compare these the field profile and z coordinate have been normalised. (a) shows the field profile of the resulting longitudinal mode ($f = 11.86$ GHz) for a disorder of ± 0.01 mm and (b) shows the field profile of the resulting longitudinal mode ($f = 11.89$ GHz) for a disorder of ± 0.05 mm.
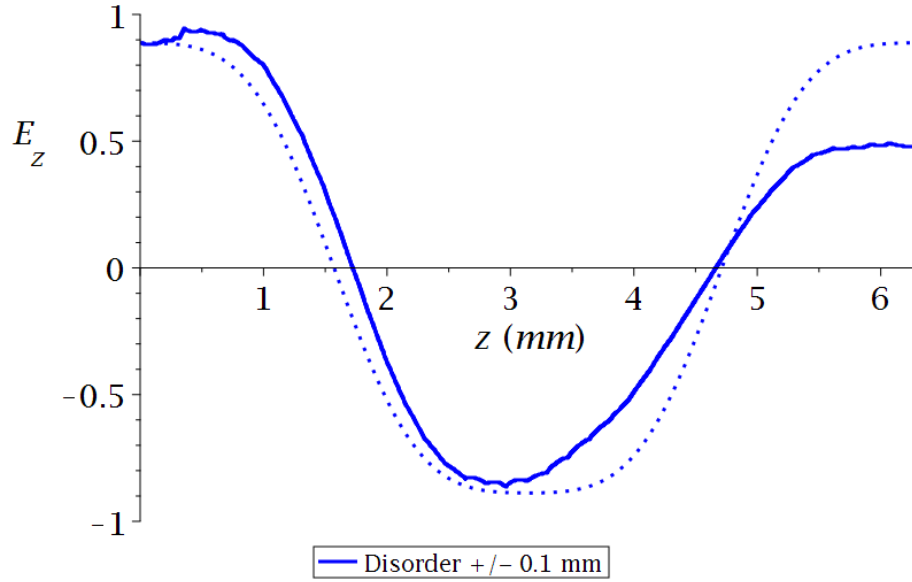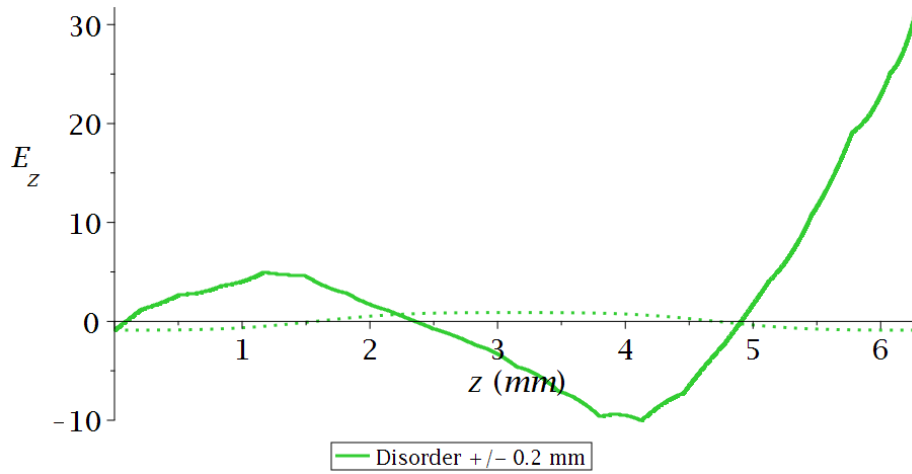
Figure 7.23: Plots showing the field profiles of the longitudinal modes when different levels of disorder are introduced into our control radius function for a flattened profile ($q = 0.8$) in infinite dielectric wire media ($\varepsilon_r = 50$, $a_x = 13.06$ mm and $a_y = 15.00$ mm) for the choice of $f_d = 12$ GHz, $R_c = 0.6$ mm and $\lambda_C = 11.7$ GHz, with a number of different levels of disorder. The plots include the field profile observed in our numerical simulation (solid) and the desired profile (dotted). In order to compare these the field profile and z coordinate have been normalised. (a) shows the field profile of the resulting longitudinal mode ($f = 12.00$ GHz) for a disorder of ± 0.1 mm and (b) shows the field profile of the resulting longitudinal mode ($f = 11.92$ GHz) for a disorder of ± 0.2 mm.

III.2 Systematic errors in the radii
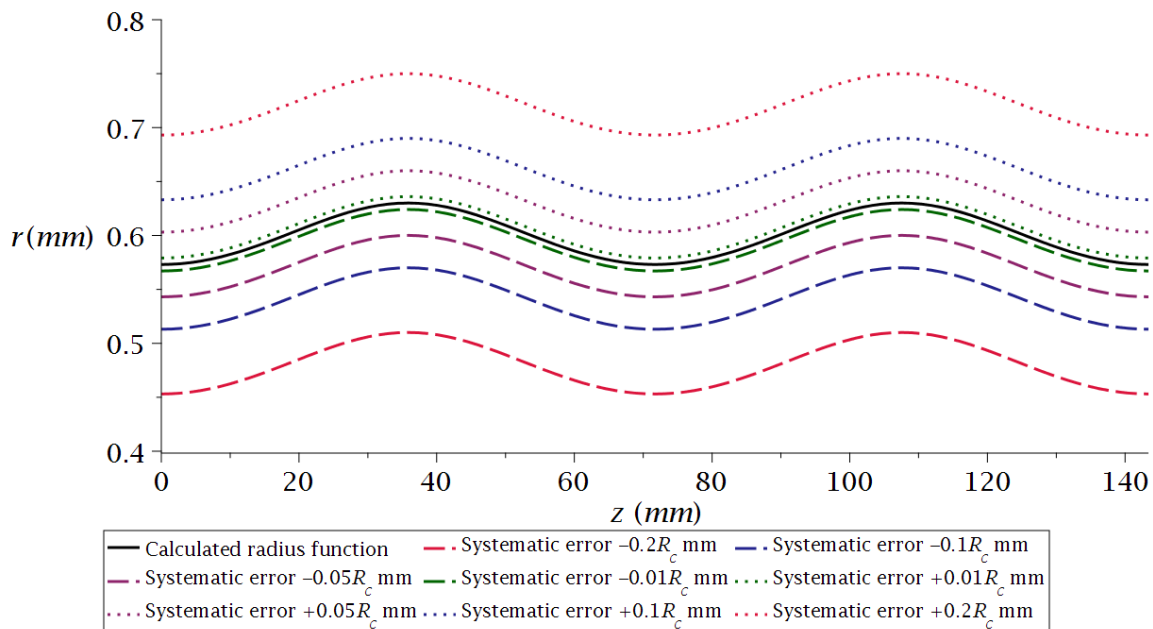
Figure 7.24: A plot of the resulting radius functions when different levels of systematic error are introduced into our control radius function calculated for a flattened profile ($q = 0.8$) in an infinite dielectric wire medium ($\varepsilon_r = 50$, $a_x = 13.06$ mm and $a_y = 15.00$ mm) for the parameter choice of $f_\mathrm{d} = 12$ GHz, $R_c = 0.6$ mm and $\lambda_C = 11.7$ GHz (black). The levels of systematic error are $-0.2R_c$ mm (dashed crimson), $-0.1R_c$ mm (dashed dark blue), $-0.05R_c$ mm (dashed magenta), $-0.01R_c$ mm (dashed dark green), $+0.01R_c$ mm (dotted dark green), $+0.05R_c$ mm (dotted magenta), $+0.1R_c$ mm (dotted dark blue) and $+0.2R_c$ mm (dotted crimson).

Another type of disorder that we have studied is the introduction of systematic errors into the radius of our wires. Systematic errors could easily occur when fabricating our wires, making this a valuable scenario to study. We have introduced several levels of systematic error into a varying wire configuration, using the same control case as the previous analysis, that are defined in terms of the central radius parameter R_C: $+0.01R_C$, $+0.05R_C$, $+0.1R_C$, $+0.2R_C$, $-0.01R_C$, $-0.05R_C$, $-0.1R_C$ and $-0.2R_C$. We have plotted the resulting radius functions when the systematic error has been introduced for all cases in Fig. 7.24. It is important to note that as this analysis is based on a specific varying radius medium the exact results will not hold for all wire media, but we should be able to make some general observations.

The resulting mode profiles for these new radius functions are shown in Figs. 7.25- 7.32.
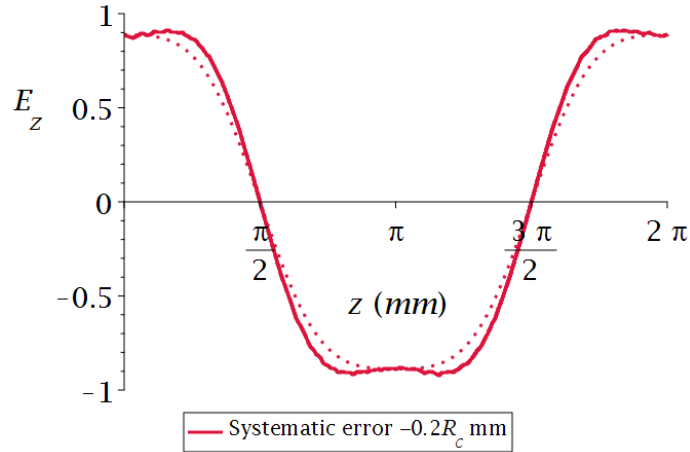
Figure 7.25: A plot of the field profile (longitudinal, z, spatial variation of the electric field strength, E_z) of the longitudinal mode ($f = 13.3$ GHz) in an infinite dielectric wire medium ($\varepsilon_r = 50$, $a_x = 13.06$ mm and $a_y = 15.00$ mm) for our attempt to produce a flattened profile ($q = 0.8$) with a radius function based on the parameter choice of $f_d = 12$ GHz, $R_c = 0.6$ mm and $\lambda_C = 11.7$ GHz, and a systematic error of $-0.2R_C$ (crimson). The plot includes the field profile observed in our numerical simulation (solid) and the desired profile (dotted). To aid comparison the field profile from our simulation and the z coordinate have been normalised.
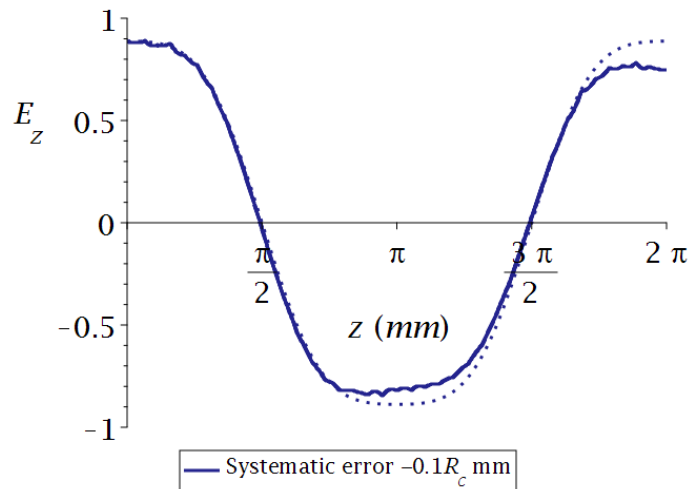
Figure 7.26: A plot of the field profile (longitudinal, z, spatial variation of the electric field strength, E_z) of the longitudinal mode ($f = 12.5$ GHz) in an infinite dielectric wire medium ($\varepsilon_r = 50$, $a_x = 13.06$ mm and $a_y = 15.00$ mm) for our attempt to produce a flattened profile ($q = 0.8$) with a radius function based on the parameter choice of $f_d = 12$ GHz, $R_c = 0.6$ mm and $\lambda_C = 11.7$ GHz, and a systematic error of $-0.1R_C$ (dark blue). The plot includes the field profile observed in our numerical simulation (solid) and the desired profile (dotted).
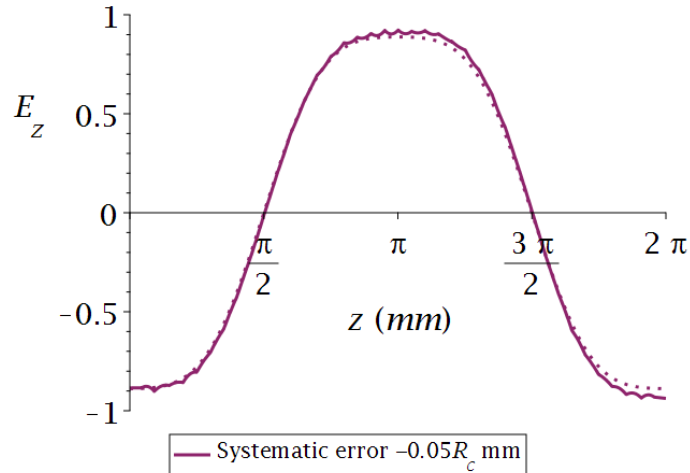
Figure 7.27: A plot of the field profile (longitudinal, z, spatial variation of the electric field strength, E_z) of the longitudinal mode ($f = 12.2$ GHz) in an infinite dielectric wire medium ($\varepsilon_r = 50$, $a_x = 13.06$ mm and $a_y = 15.00$ mm) for our attempt to produce a flattened profile ($q = 0.8$) with a radius function based on the parameter choice of $f_d = 12$ GHz, $R_c = 0.6$ mm and $\lambda_C = 11.7$ GHz, and a systematic error of $-0.05R_C$ (magenta). The plot includes the field profile observed in our numerical simulation (solid) and the desired profile (dotted).
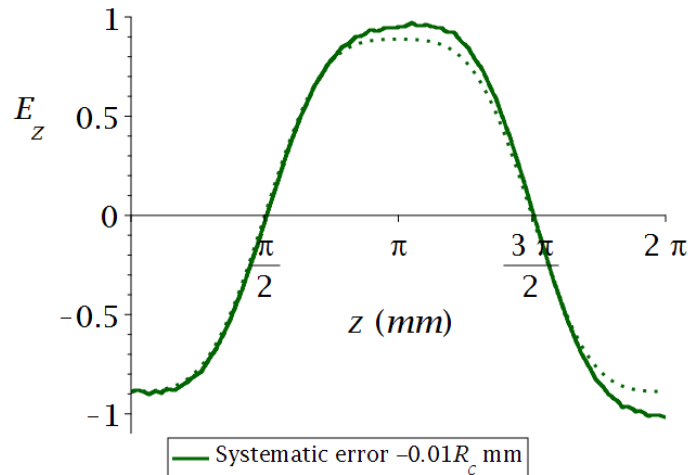
Figure 7.28: A plot of the field profile (longitudinal, z, spatial variation of the electric field strength, E_z) of the longitudinal mode ($f = 12$ GHz) in an infinite dielectric wire medium ($\varepsilon_r = 50$, $a_x = 13.06$ mm and $a_y = 15.00$ mm) for our attempt to produce a flattened profile ($q = 0.8$) with a radius function based on the parameter choice of $f_d = 12$ GHz, $R_c = 0.6$ mm and $\lambda_C = 11.7$ GHz, and a systematic error of $-0.01R_C$ (dark green). The plot includes the field profile observed in our numerical simulation (solid) and the desired profile (dotted).
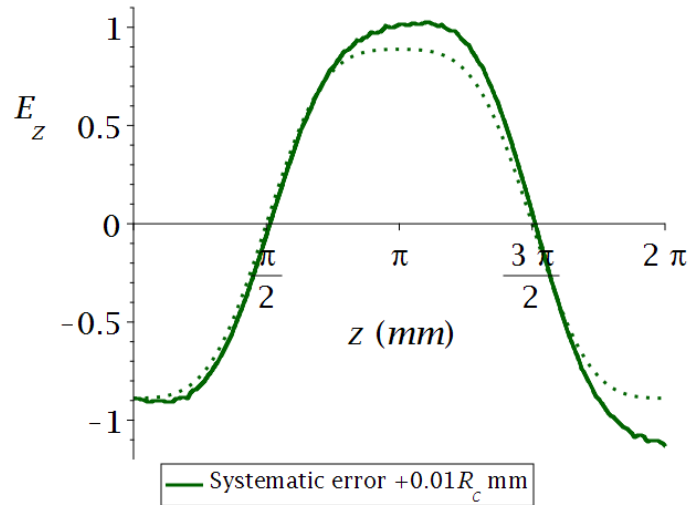
Figure 7.29: A plot of the field profile (longitudinal, z, spatial variation of the electric field strength, E_z) of the longitudinal mode ($f = 11.8$ GHz) in an infinite dielectric wire medium ($\varepsilon_r = 50$, $a_x = 13.06$ mm and $a_y = 15.00$ mm) for our attempt to produce a flattened profile ($q = 0.8$) with a radius function based on the parameter choice of $f_d = 12$ GHz, $R_c = 0.6$ mm and $\lambda_C = 11.7$ GHz, and a systematic error of $+0.01R_C$ (dark green). The plot includes the field profile observed in our numerical simulation (solid) and the desired profile (dotted).
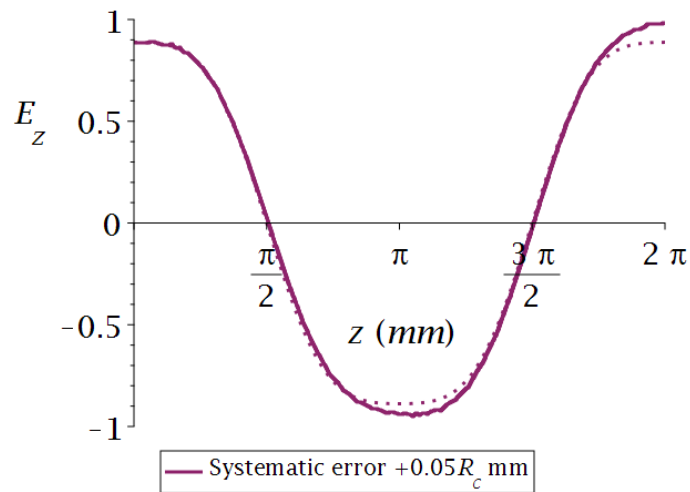
Figure 7.30: A plot of the field profile (longitudinal, z, spatial variation of the electric field strength, E_z) of the longitudinal mode ($f = 11.6$ GHz) in an infinite dielectric wire medium ($\varepsilon_r = 50$, $a_x = 13.06$ mm and $a_y = 15.00$ mm) for our attempt to produce a flattened profile ($q = 0.8$) with a radius function based on the parameter choice of $f_d = 12$ GHz, $R_c = 0.6$ mm and $\lambda_C = 11.7$ GHz, and a systematic error of $+0.05R_C$ (magenta). The plot includes the field profile observed in our numerical simulation (solid) and the desired profile (dotted).

123
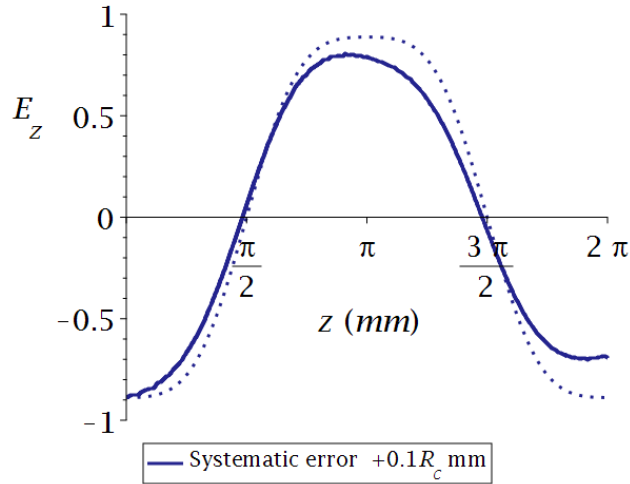
Figure 7.31: A plot of the field profile (longitudinal, z, spatial variation of the electric field strength, E_z) of the longitudinal mode ($f = 11.3$ GHz) in an infinite dielectric wire medium ($\varepsilon_r = 50$, $a_x = 13.06$ mm and $a_y = 15.00$ mm) for our attempt to produce a flattened profile ($q = 0.8$) with a radius function based on the parameter choice of $f_d = 12$ GHz, $R_c = 0.6$ mm and $\lambda_C = 11.7$ GHz, and a systematic error of $+0.1R_C$ (dark blue). The plot includes the field profile observed in our numerical simulation (solid) and the desired profile (dotted).
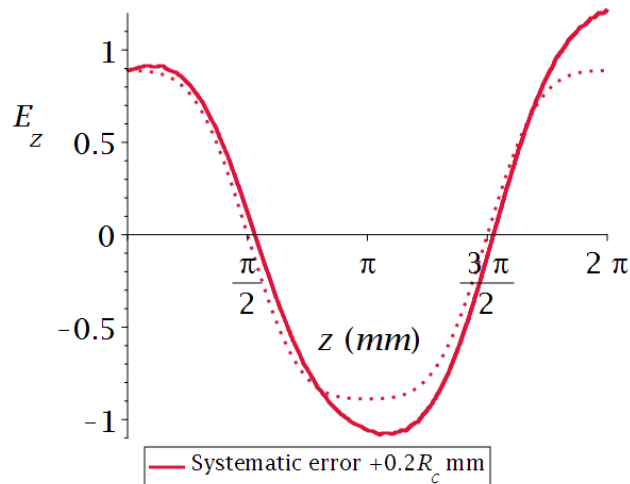
Figure 7.32: A plot of the field profile (longitudinal, z, spatial variation of the electric field strength, E_z) of the longitudinal mode ($f = 10.9$ GHz) in an infinite dielectric wire medium ($\varepsilon_r = 50$, $a_x = 13.06$ mm and $a_y = 15.00$ mm) for our attempt to produce a flattened profile ($q = 0.8$) with a radius function based on the parameter choice of $f_d = 12$ GHz, $R_c = 0.6$ mm and $\lambda_C = 11.7$ GHz, and a systematic error of $+0.2R_C$ (crimson). The plot includes the field profile observed in our numerical simulation (solid) and the desired profile (dotted).

The results of these simulations are summarised in Table 7.5. One conclusion we can make is that the introduction of a systematic error in the radius function affects the frequency of the resulting longitudinal mode. Modes resulting from wires that have had a decrease in radii have a larger frequency, whereas those with increased radii have a lower frequency. There is no clear pattern in the $\mathfrak{R}^2$ value of our profile plots. We can say that the mode profile shaping seems to have been very resilient to the introduction of disorder with the worst performance being a respectable $\mathfrak{R}^2$ value of 0.9607. The effect on the mode profiling also seems to be asymmetric with regards to the introduction of a systematic radius error. Systematic errors which decrease the radii have minimal impact on the $\mathfrak{R}^2$ values, whereas there is a more visible effect when the radii is increased. This may be because our method assumes a small wire radius as compared to the lattice constants of the wire medium.

Systematic error	f (GHz)	$\mathfrak{R}^2$
-0.2R_C	13.3	0.9918
-0.1R_C	12.5	0.9929
-0.05R_C	12.2	0.9989
-0.01R_C	12.0	0.9944
None	11.9	0.9958
0.01R_C	11.8	0.9836
0.05R_C	11.6	0.9975
0.1R_C	11.3	0.9607
0.2R_C	10.9	0.9718

Table 7.5: Table summarising the results of the implementation of radius functions when different levels of systematic error are introduced into our control radius function calculated for a flattened profile ($q = 0.8$) in an infinite dielectric wire medium ($\varepsilon_r = 50$, $a_x = 13.06$ mm and $a_y = 15.00$ mm) for the parameter choice of $f_d = 12$ GHz, $R_c = 0.6$ mm and $\lambda_C = 11.7$ GHz. The parameters listed are: the level of systematic error introduced, longitudinal mode frequency (f) and a figure of merit for the agreement between our field profile and the desired profile ($\mathfrak{R}^2$).

IV.   INCLUDING CLADDING AROUND OUR WIRES

Our previous simulations reassured us that we have flexibility in terms of the permittivity and radius values required for our wire media. Here we consider the possibility of introducing a low permittivity sheath to aid fabrication; possibly for use as a mould for our higher permittivity varying radius wire.

We assumed that the effect of the sheath would be negligible on the electromagnetic fields in our structure. Therefore, we added a sheath to structures that had already been shown to be successful with mode profile shaping. The structure chosen is shown in Fig. 7.33 and shows a unit cell with a dielectric wire, $\varepsilon_r = 50$,

that has a varying radius which has been designed to produce a flattened profile (Mathieu parameter $q = 0.8$). The radius function for this wire is shown in Fig. 7.34. This function results from fixing the parameters $R_c = 0.6$ mm and $f_d = 12.5$ GHz.
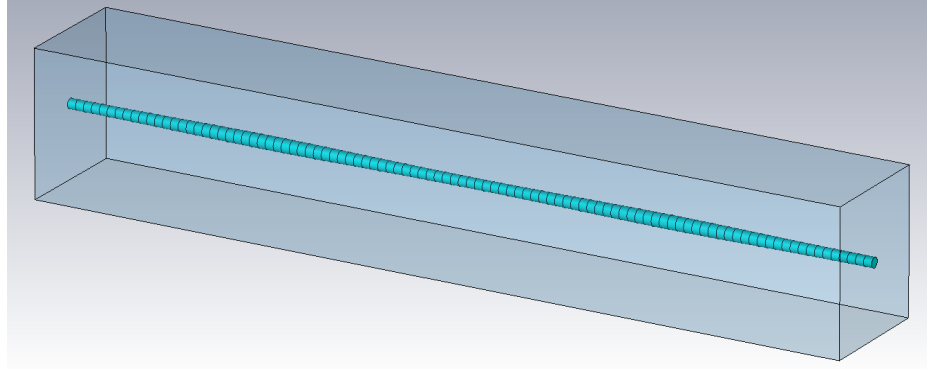
Figure 7.33: A typical representation of wire media in CST, consisting of a section of dielectric wire in a unit cell with periodic boundary conditions. The dielectric wire has a radius variation specified by a function calculated for a flattened profile ($q = 0.8$) in an infinite dielectric wire medium ($\varepsilon_r = 50$, $a_x = 13.06$ mm and $a_y = 15.00$ mm) for the parameter choice of $f_d = 12.5$ GHz, $R_c = 0.6$ mm and $\lambda_C = 11.7$ GHz. This is our control structure for our cladding analysis.
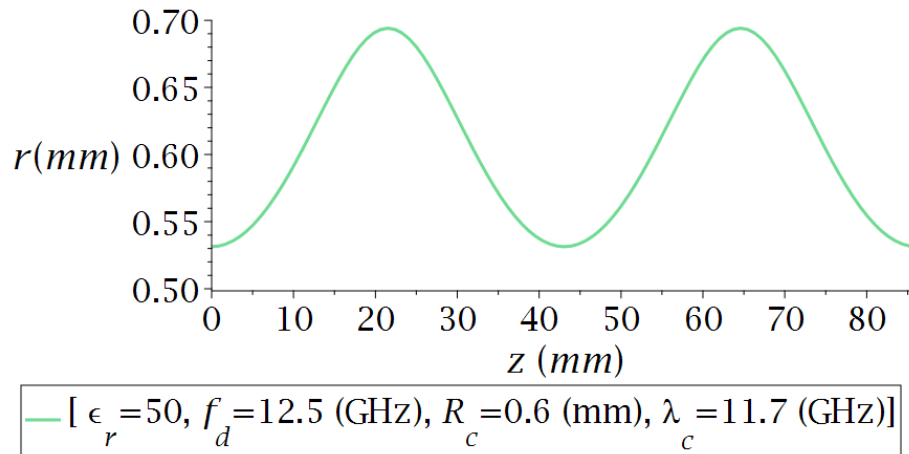
Figure 7.34: Radius function calculated for a flattened profile ($q = 0.8$) in an infinite dielectric wire medium ($\varepsilon_r = 50$, $a_x = 13.06$ mm and $a_y = 15.00$ mm) for the parameter choice of $f_d = 12.5$ GHz, $R_c = 0.6$ mm and $\lambda_C = 11.7$ GHz. This is the radius function of our control case.

The longitudinal mode supported by this structure is shown in Fig. 7.35, which was found at 12.34 GHz. The profile of this mode is shown in Fig. 7.36. This attempt at mode profiling has been very successful, with an $\mathfrak{R}^2$ value of 0.9986. These results represent our control case of a structure without any cladding.

126

(a)

(b)
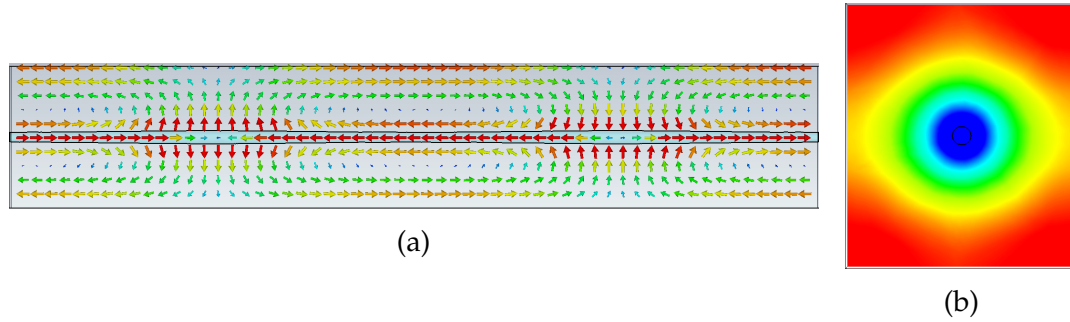
Figure 7.35: Images showing the resulting longitudinal mode (simulation frequency $f = 12.34$ GHz) after the implementation of the calculated radius function for a flattened profile ($q = 0.8$) in an infinite dielectric wire medium ($\varepsilon_r = 50$, $a_x = 13.06$ mm and $a_y = 15.00$ mm) for the parameter choice of $f_{\mathrm{d}} = 12.5$ GHz, $R_c = 0.6$ mm and $\lambda_C = 11.7$ GHz. The fields are either represented using arrow plots where the arrow direction represents field direction and colour represents the magnitude of the field strength, or colour plots where the direction and magnitude of the longitudinal field is represented by colour. (a) shows the field on an x-z slice of the structure, and (b) shows the field on an x-y slice. This is the longitudinal mode found in our control structure.

To have a limited effect on our modes; the cladding must have a relatively low permittivity. We have chosen for our cladding material a dielectric with $\varepsilon_r = 2$. This is an easily achievable permittivity value, with plastics such as polyethylene having a similar permittivity [222]. We also do not want the cladding to be too thick. As such, we have used a cladding that covers our varying dielectric wire and extends to an outer radius of 2 mm. The resulting structure with a clad wire is shown in Fig. 7.37.
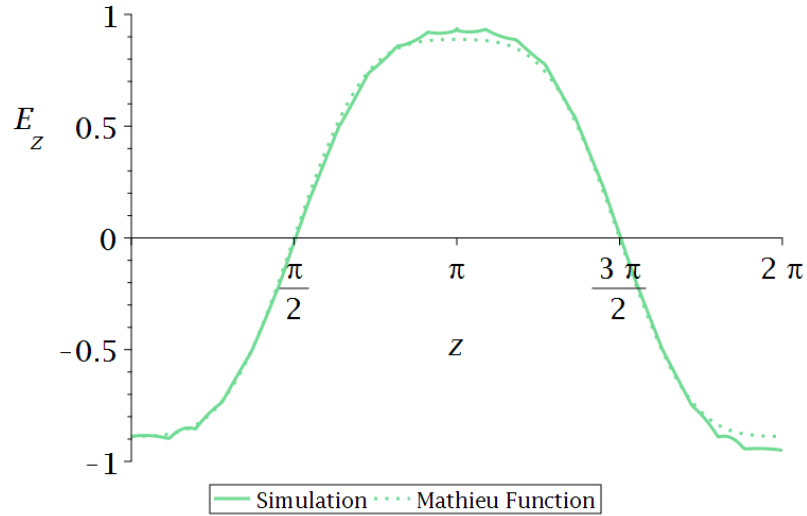
Figure 7.36: A plot of the field profile (longitudinal, z, spatial variation of the electric field strength, E_z) of the longitudinal mode ($f = 12.34$ GHz) in an infinite dielectric wire medium ($\varepsilon_r = 50$, $a_x = 13.06$ mm and $a_y = 15.00$ mm) for our attempt to produce a flattened profile ($q = 0.8$) with a radius function based on the parameter choice of $f_d = 12.5$ GHz, $R_c = 0.6$ mm and $\lambda_C = 11.7$ GHz (green). The plot includes the field profile observed in our numerical simulation (solid) and the desired profile (dotted). In order to aid comparison the field profile from our simulation and the z coordinate have been normalised. This is the field profile of the longitudinal mode found in our control structure.
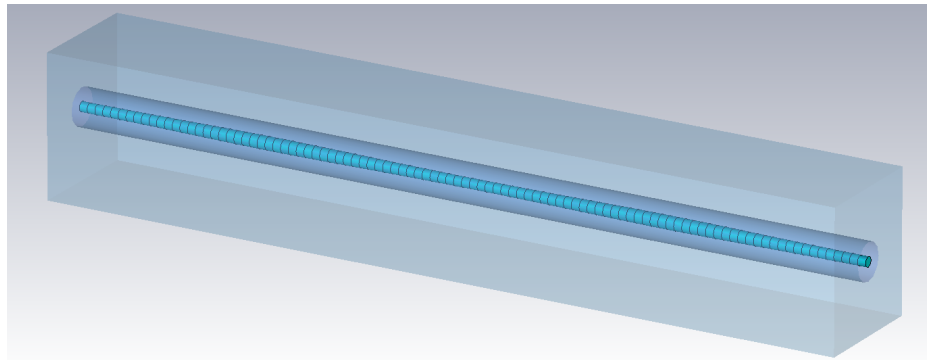
Figure 7.37: A representation of a clad wire medium in CST, consisting of a section of dielectric wire surrounded by a cladding material ($\varepsilon_r = 2$ and outer radius $r_O = 2$ mm) in a unit cell with periodic boundary conditions. The dielectric wire has a radius variation specified by a function calculated for a flattened profile ($q = 0.8$) in an infinite dielectric wire medium ($\varepsilon_r = 50$, $a_x = 13.06$ mm and $a_y = 15.00$ mm) for the parameter choice of $f_d = 12.5$ GHz, $R_c = 0.6$ mm and $\lambda_C = 11.7$ GHz.

The longitudinal modes found in our new structure with a clad wire are shown

in Fig. 7.38, along with images showing the longitudinal mode of the control case for comparison. The mode in our clad wire medium was found at a frequency of 12.05 GHz. The introduction of the cladding has had a significant effect on the frequency of our longitudinal mode, although it does still exhibit the features that characterise our mode.

(a)

(b)

(c)

(d)
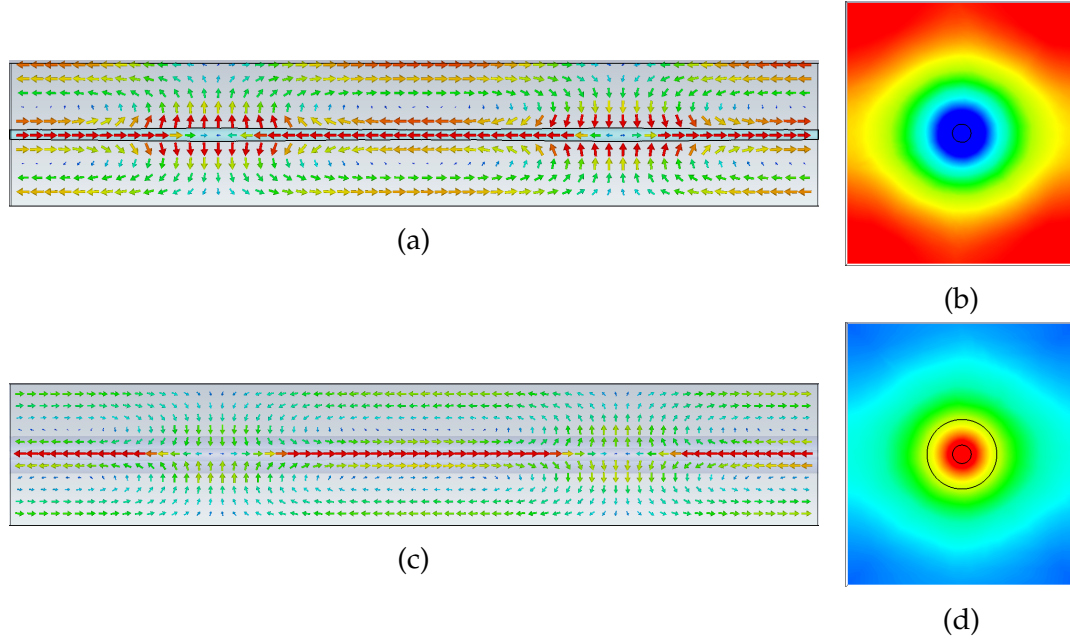
Figure 7.38: Images showing the resulting longitudinal modes after the implementation of the calculated radius function for a flattened profile ($q = 0.8$) in an infinite dielectric wire medium ($\varepsilon_r = 50$, $a_x = 13.06$ mm and $a_y = 15.00$ mm) for the parameter choice of $f_d = 12.5$ GHz, $R_c = 0.6$ mm and $\lambda_C = 11.7$ GHz with and without cladding. The fields are either represented using arrow plots on a y-z slice, where the arrow direction represents field direction and colour represents the magnitude of the field strength; or colour plots on an x-y slice, where the direction and magnitude of the longitudinal field is represented by colour. (a) and (b) show the resulting longitudinal mode ($f = 12.34$ GHz) for no cladding, and (c) and (d) show the resulting longitudinal mode ($f = 12.05$ GHz) when cladding ($\varepsilon_r = 2$ and $r_O = 2$ mm) is included.

The profile of the longitudinal mode in our clad structure is shown in Fig. 7.39. We can see from Fig. 7.39 that the success of our mode profiling efforts has continued, with an $\mathfrak{R}^2$ value of 0.9976.
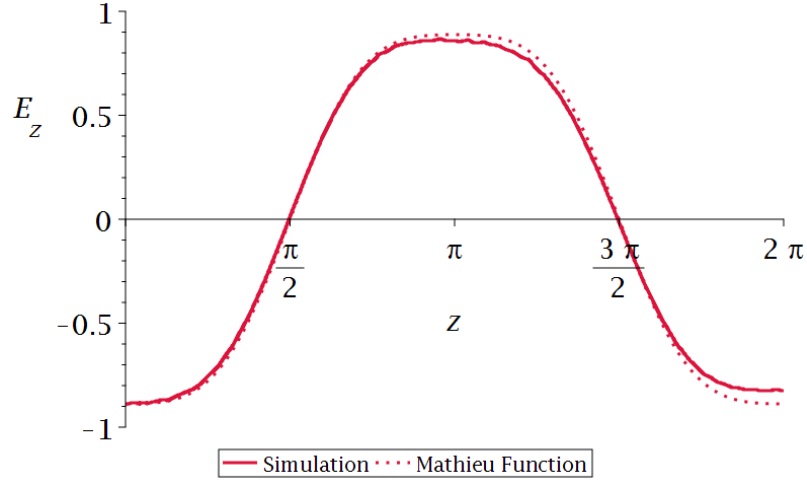
Figure 7.39: A plot of the field profile (longitudinal, z, spatial variation of the electric field strength, E_z) of the longitudinal mode ($f = 12.05$ GHz) in an infinite dielectric wire medium ($\varepsilon_r = 2$, $a_x = 13.06$ mm and $a_y = 15.00$ mm) with cladding ($\varepsilon_r = 50$ and $r_O = 2$ mm) for our attempt to produce a flattened profile ($q = 0.8$) with a radius function based on the parameter choice of $f_d = 12.5$ GHz, $R_c = 0.6$ mm and $\lambda_C = 11.7$ GHz (crimson). The plot includes the field profile observed in our numerical simulation (solid) and the desired profile (dotted). In order to aid comparison the field profile from our simulation and the z coordinate have been normalised.

The results of the comparison between an unclad and clad wire are shown in Table 7.6. We can see that the introduction of cladding does affect the mode frequency while leaving the mode profile largely unchanged. This result seems encouraging for the possibility of using cladding to aid fabrication. A shift in frequency can be accounted for if it can be anticipated, while the main aim of our method has still been achieved.

Cladding	f (GHz)	$\mathfrak{R}^2$
None	12.34	0.9986
$\varepsilon_r = 2$, $r_O = 2$ mm	12.5	0.9976

Table 7.6: Table summarising the results of the implementation of cladding ($\varepsilon_r = 50$ and $r_O = 2$ mm) around our varying wires based on a radius function calculated for a flattened profile ($q = 0.8$) in an infinite dielectric wire medium ($\varepsilon_r = 50$, $a_x = 13.06$ mm and $a_y = 15.00$ mm) for the parameter choice of $f_d = 12$ GHz, $R_c = 0.6$ mm and $\lambda_C = 11.7$ GHz. The parameters listed are: the presence of cladding, longitudinal mode frequency (f) and a figure of merit for the agreement between our field profile and the desired profile ($\mathfrak{R}^2$).

V. Extending our method to partially finite wire media

As already mentioned, it was important to confirm that our method was valid for finite structures. The first step towards this aim was to verify that our results could be extended to a partially finite structure. Our use of the term partially finite structure refers to a structure made up of a finite number of infinitely long wires. In this case, the transverse boundaries are now given metallic boundary conditions.

We would expect the existence of these metallic boundaries to affect the modes in the structure. We spent some time considering the placement of the boundaries as well as trying different placements in our simulations. The boundaries were eventually placed a quarter lattice parameter away from the nearest wire, as usual. Even with appropriately set boundaries, the effect of the introduction of these boundaries necessitated us starting our process, detailed in Chapter 6, from its start.

(a)   (b)
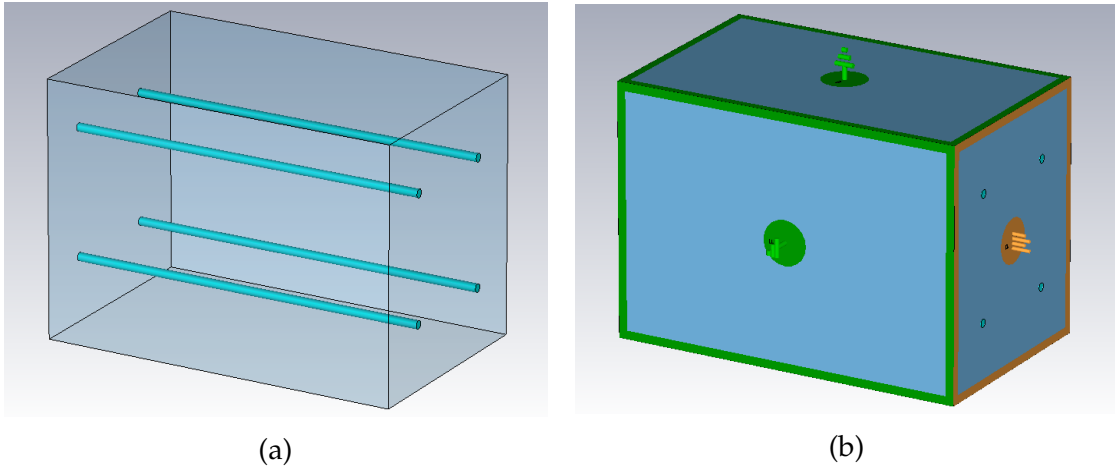
Figure 7.40: A representation of a partially finite wire medium in CST, consisting of a two by two lattice of dielectric wires in a unit cell with transverse metallic boundary conditions and longitudinal periodic boundary conditions ($a_x = 13.06$ mm and $a_y = 15.00$ mm). This is effectively a finite lattice of infinitely long wires in an infinite metallic waveguide. The dielectric wire has a radius (r) of 0.5 mm and a relative permittivity (ε_r) of 100. (a) shows the unit cell used in CST, and (b) shows the boundaries of the structure with green representing metallic boundaries and orange, periodic boundary conditions.

Before starting our simulations, we had to choose a lattice size. We started with the simplest finite lattice, a two by two grid, as this would be the least computationally challenging. The permittivity of the wires was set to $\varepsilon_r = 100$ as this struck a balance between the higher epsilon wires that require a higher mesh, which could potentially slow simulations down, and the low epsilon wires that we have found to be somewhat less reliable in terms of the frequency of the

simulation modes. The realisation of this structure in CST is shown in Fig. 7.40. Fig. 7.40b shows the different boundary conditions on the surfaces of our unit cell. The green outlines denote surfaces with metallic boundary conditions, and orange, periodic boundary conditions.
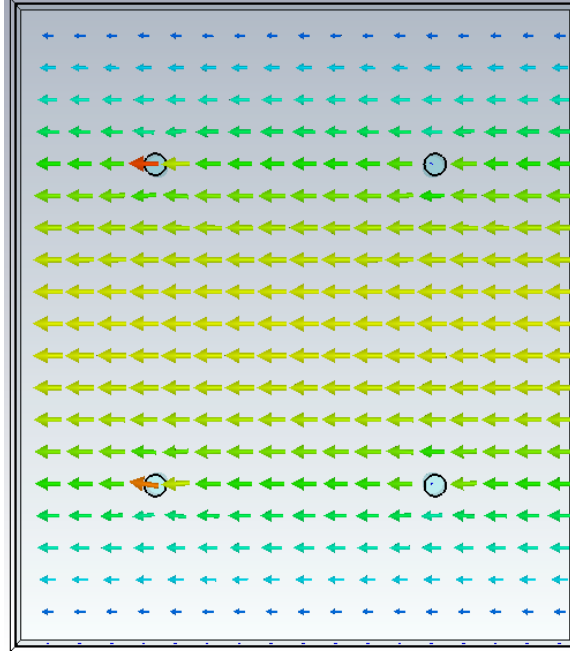
Figure 7.41: Numerical results showing a transverse electric mode, with a frequency of 4.98 GHz, in a representation of a partially finite two by two array of dielectric wires ($\varepsilon_r = 100$) of radius 0.5mm, and wire spacings $a_x = 13.06$ mm and $a_y = 15.00$ mm. The electric field is represented using a vector plot of an x-y slice of the structure where the arrow direction represents field direction and colour represents the magnitude of the field strength.

The first step in our study was examining the modes of this structure in order to find the longitudinal modes predicted. As usual, when running eigenmode simulations of our structure, we found a large number of transverse modes, such as the one shown in Fig. 7.41. The longitudinal modes found in a two by two array with a wire radius of 0.5 mm are shown in Fig. 7.42. We can see from Fig. 7.42 that these modes have the same characteristics as our previous longitudinal modes. We confirmed the dispersion relation of this mode was plasma-like, as shown in Fig. 7.43.

(a)

(b)

(c)
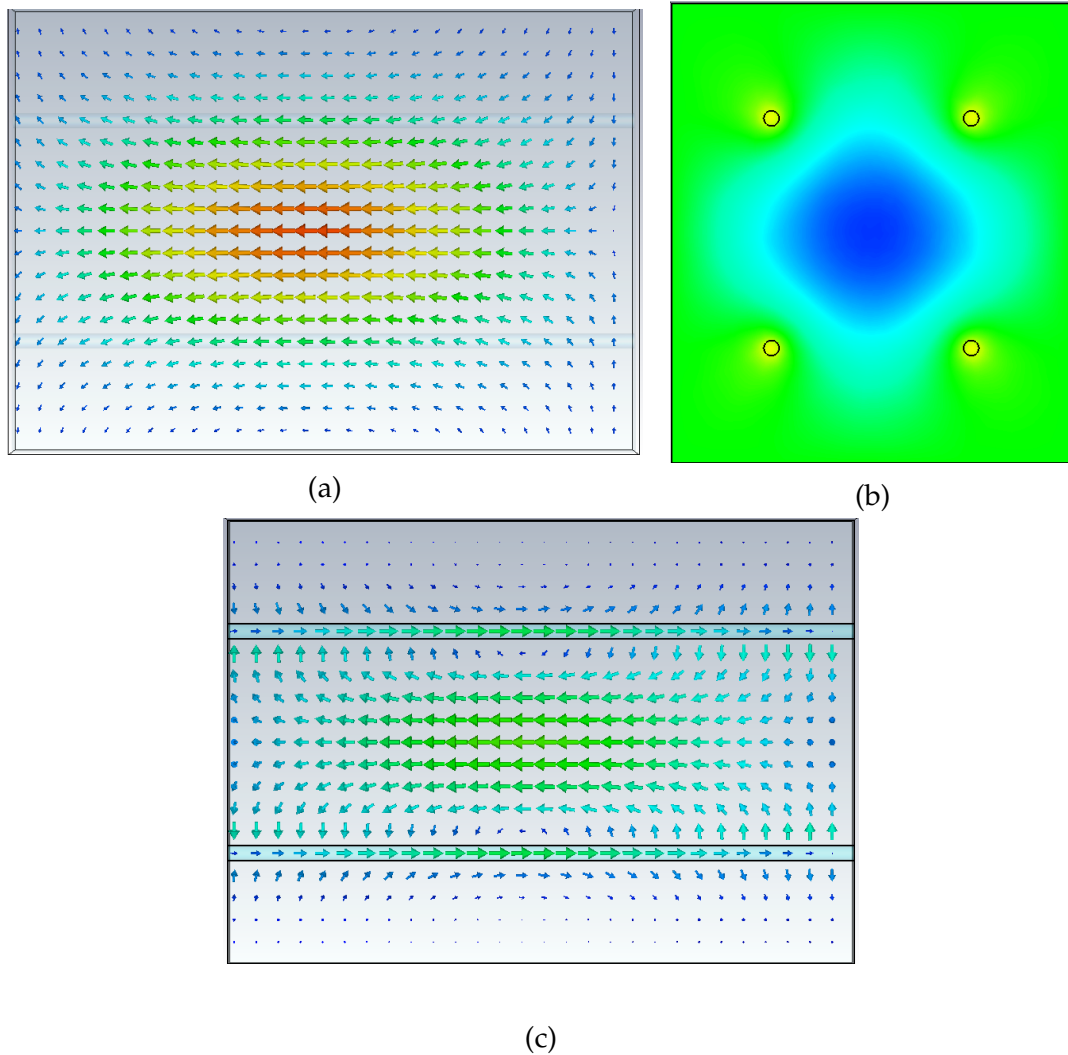
Figure 7.42: Images from numerical simulations in CST showing the longitudinal mode ($f = 11.24$ GHz) found in a partially finite dielectric wire medium (2×2, $\varepsilon_r = 100$, $r = 0.5$ mm, $a_x = 13.06$ mm and $a_y = 15.00$ mm). The fields are either represented using arrow plots where the arrow direction represents field direction and colour represents the magnitude of the field strength, or colour plots where the direction and magnitude of the longitudinal field is represented by colour. (a) shows a y-z slice through the centre of the structure, (b) an x-y slice and (c) a y-z slice through two of the wires.
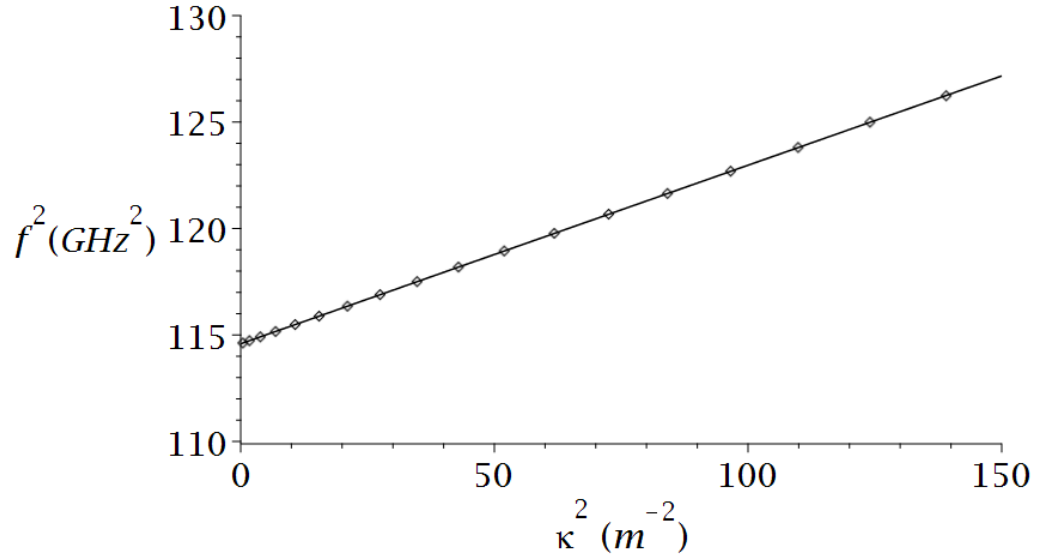
Figure 7.43: A plot of frequency squared (f^2) against the wavenumber squared (κ^2), of the longitudinal mode in a partially finite dielectric wire medium (2×2, $\varepsilon_r = 100$, $r = 0.5$ mm, $a_x = 13.06$ mm and $a_y = 15.00$ mm) along with a fitting curve that demonstrates the mode's plasma-like dispersion relation.

Once again, we investigate how the radius of the dielectric wires affects the longitudinal modes supported by our structure. Figs. 7.44 and 7.45 show the longitudinal modes for two more radii, 0.4 and 0.6 mm. These modes have the key characteristics we expect of our longitudinal modes while their frequencies clearly show the effect of the different wire radii. The squared dispersion relations for these modes, along with our original mode, are shown in Fig. 7.46.

(a)

(b)

(c)
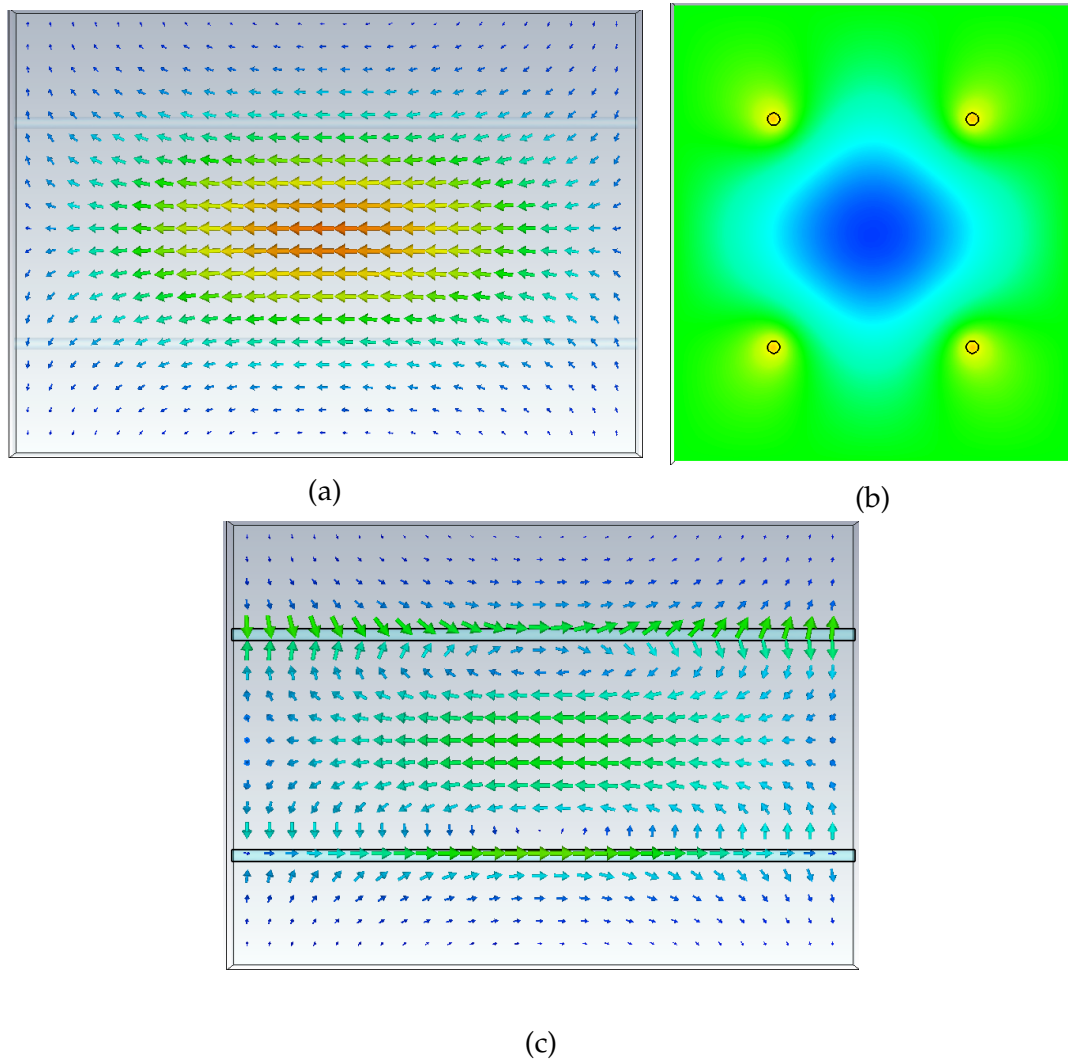
Figure 7.44: Images from numerical simulations in CST showing the longitudinal mode ($f = 11.90$ GHz) found in a partially finite dielectric wire medium (2×2, $\varepsilon_r = 100$, $r = 0.4$ mm, $a_x = 13.06$ mm and $a_y = 15.00$ mm). The fields are either represented using arrow plots where the arrow direction represents field direction and colour represents the magnitude of the field strength, or colour plots where the direction and magnitude of the longitudinal field is represented by colour. (a) shows a y-z slice through the centre of the structure, (b) an x-y slice and (c) a y-z slice through two of the wires.

(a)

(b)

(c)
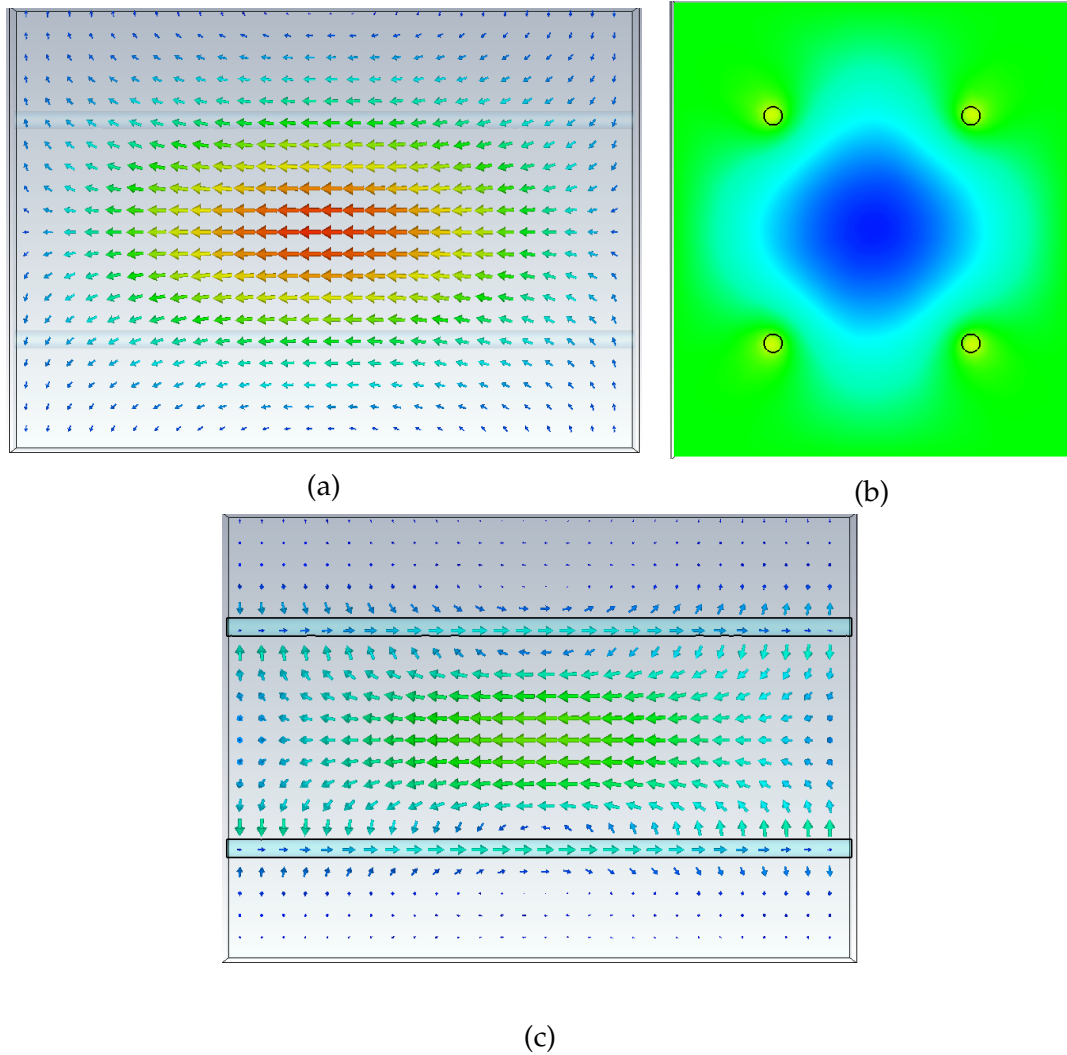
Figure 7.45: Images from numerical simulations in CST showing the longitudinal mode ($f = 10.89$ GHz) found in a partially finite dielectric wire medium (2×2, $\varepsilon_r = 100$, $r = 0.6$ mm, $a_x = 13.06$ mm and $a_y = 15.00$ mm). The fields are either represented using arrow plots where the arrow direction represents field direction and colour represents the magnitude of the field strength, or colour plots where the direction and magnitude of the longitudinal field is represented by colour. (a) shows a y-z slice through the centre of the structure, (b) an x-y slice and (c) a y-z slice through two of the wires.

Fig. 7.46 shows that the wire radius does affect the dispersion relation of our modes. The shift in the dispersion curves leads to a shift in the plasma frequency, which is related to the y-intercept of these plots. By extending our analysis to more wire radii values, we built up a set of data relating wire radius and plasma frequency squared. A plot of this data is shown in Fig. 7.47. Using this plot, we can see that the relationship between the wire radius and plasma frequency is well described by an exponential decay curve, which has been included in Fig.
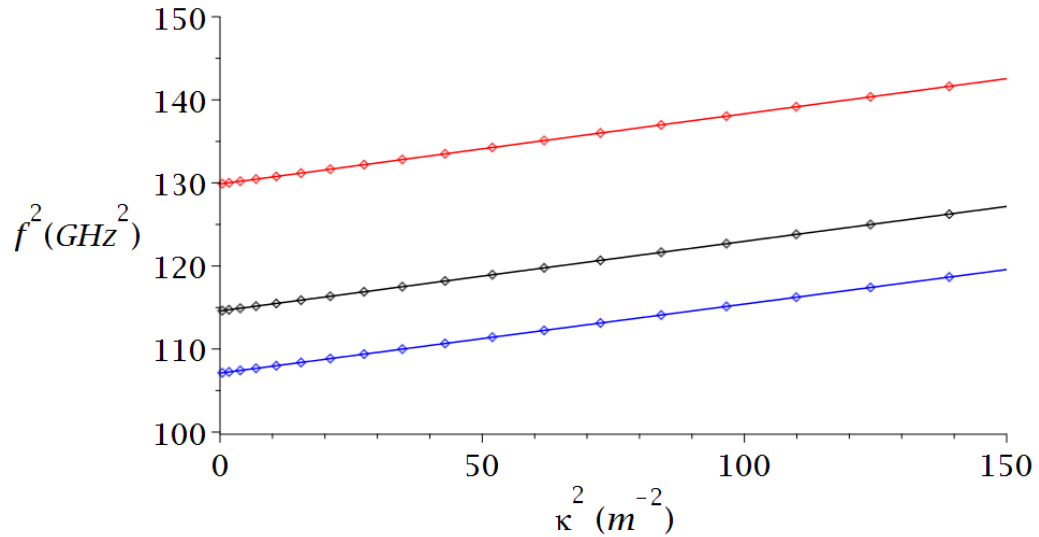
Figure 7.46: The squared dispersion plots, frequency squared (f^2) against wavenumber squared (κ^2), of the longitudinal modes in partially finite dielectric wire media (2×2, $\varepsilon_r = 100$, $a_x = 13.06$ mm and $a_y = 15.00$ mm) with a variety of radii along with fitting curves. The radii are 0.4 mm (red), 0.5 mm (black) and 0.6 mm (blue).

7.47. This is as we would hope, as our infinite case showed this same relationship. In this case, we can see the fit to the data is somewhat weaker for the final data point, $r = 1$ mm. In general, the curve does fit the data well with an $\mathfrak{R}^2$ value of 0.9973. The fitting parameters for this exponential decay curve are as follows: $\delta = 97.1$ (GHz^2), $\sigma = 462$(GHz^2) and $\rho = 0.153$ (mm^{-1}). With this information, we can apply our previous method for finding the required radius function to produce the desired mode profile.
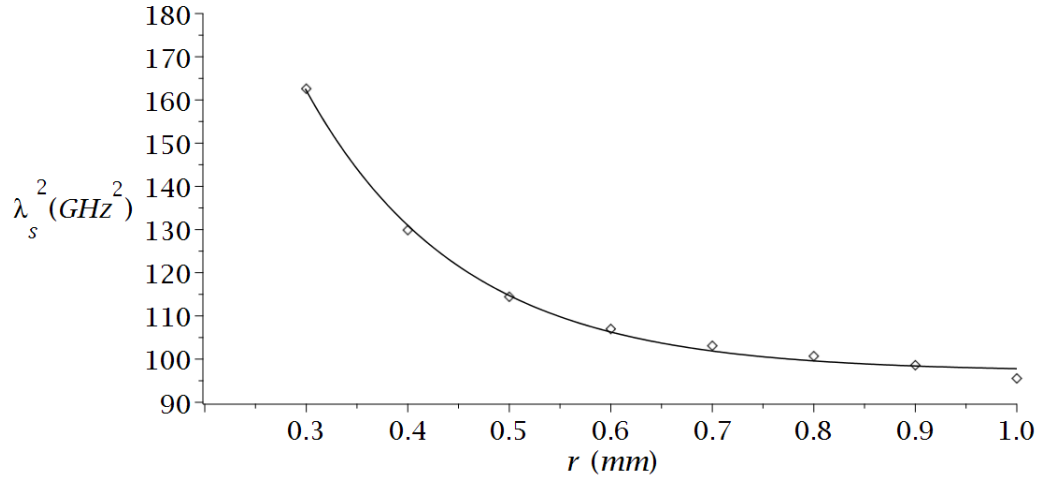
Figure 7.47: A plot of the plasma frequency squared, λ_s^2, of partially finite dielectric wire media (2×2, $\varepsilon_r = 100$, $a_x = 13.06$ mm and $a_y = 15.00$ mm) against wire radius, r, with an exponential decay fitting curve.
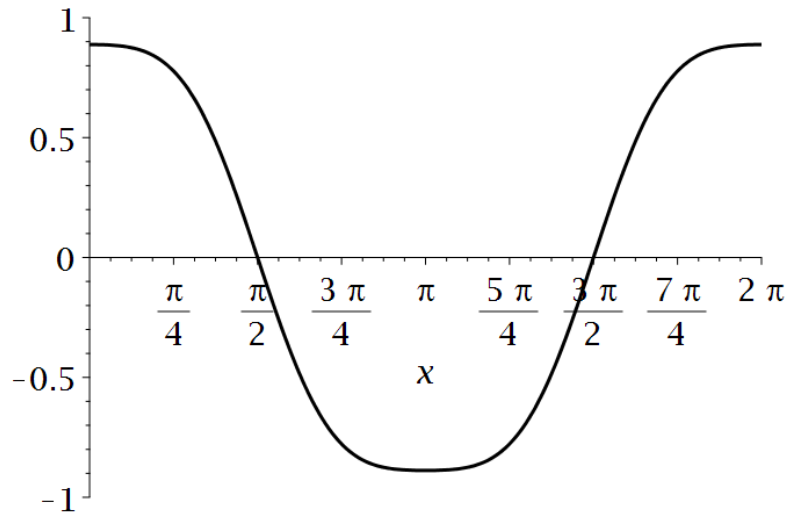
Figure 7.48: A solution to Mathieu's equations ($q = 0.8$) that can be loosely described as a flattened sinusoidal curve.

We followed the precedent we have previously set of first attempting to verify our structure's mode profiling capabilities by attempting to produce a flattened mode profile (Mathieu parameter $q = 0.8$). This desired profile is shown in Fig. 7.48. With our profile chosen, we then fixed the parameters of design frequency and central radius, $f_d = 11$ GHz and $R_C = 0.5$ mm. The corresponding radius function for this choice of parameters and profile is shown in Fig. 7.49. The parameters for this radius function are shown in Table 7.7.

138
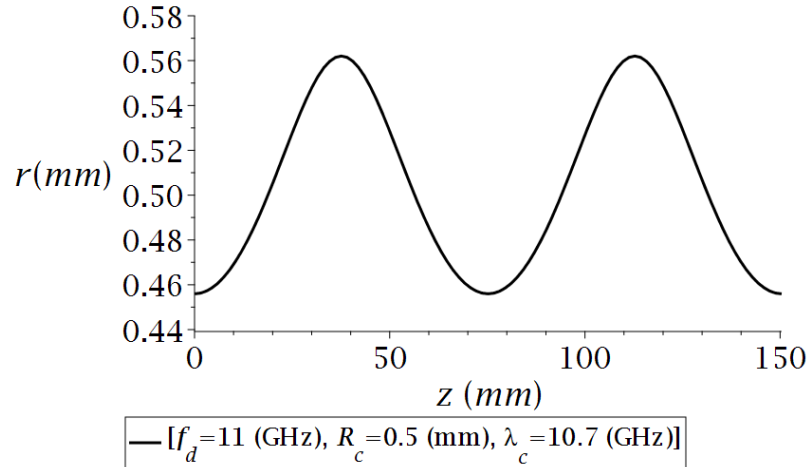
Figure 7.49: Radius function calculated for a flattened profile ($q = 0.8$) in a partially finite dielectric wire medium (2×2, $\varepsilon_r = 100$, $a_x = 13.06$ mm and $a_y = 15.00$ mm) for the parameter choice of $f_d = 11$ GHz, $R_c = 0.5$ mm and $\lambda_C = 10.7$ GHz.

Having calculated the required radius function for our desired flattened profile, we can implement this profile into our CST simulations in the same way as previously detailed. By doing this and running an eigenmode simulation, we can find our desired longitudinal mode. Fig. 7.50 shows images of this mode in CST, which has the characteristics we expect of our mode, although it is difficult to judge the success of our mode profiling efforts from these images.

(a)

(b)

(c)
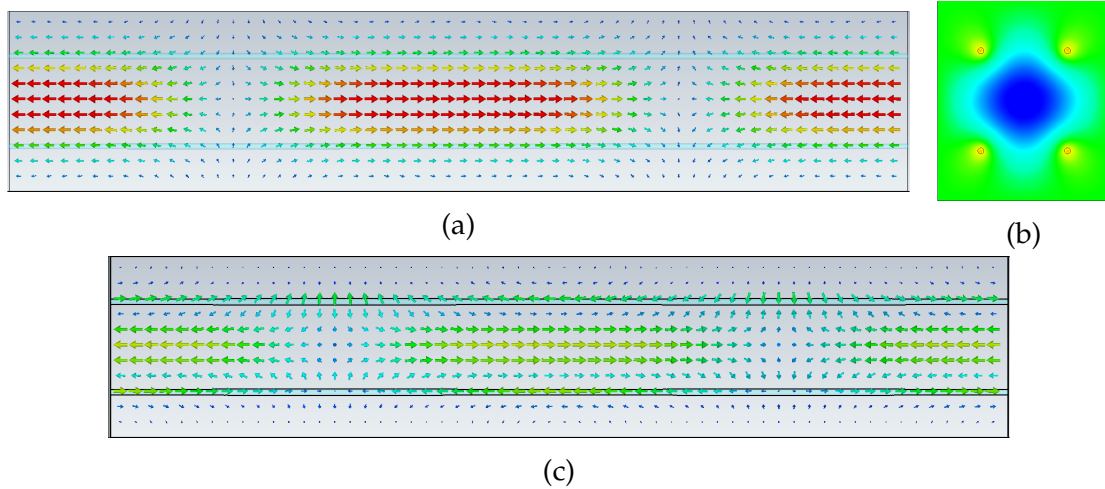
Figure 7.50: Images showing the resulting longitudinal mode ($f = 10.98$ GHz) after the implementation of the calculated radius function for a flattened profile ($q = 0.8$) in a partially finite dielectric wire medium (2×2, $\varepsilon_r = 100$, $a_x = 13.06$ mm and $a_y = 15.00$ mm) for the parameter choice of $f_d = 11$ GHz, $R_c = 0.5$ mm and $\lambda_C = 10.7$ GHz. The fields are either represented using arrow plots where the arrow direction represents field direction and colour represents the magnitude of the field strength, or colour plots where the direction and magnitude of the longitudinal field is represented by colour. (a) shows a y-z slice through the centre of the structure, (b) an x-y slice and (c) a y-z slice through two of the wires.

Our previous method for evaluating the success of our mode profiling method involved introducing a line into CST to plot the longitudinal component of the field along. This proved to be very useful in determining qualitatively the success of the profiling, as well as opening up the possibility of calculating a quantitative measure of our simulated profiles similarity to our desired profile by calculating the $\mathfrak{R}^2$ value for the two profiles. Previously, the line was placed at the top of the unit cell. This method worked well and can be adapted to our new partially finite structure, but we have to reconsider the placement of our line as the top of our unit cell is now a metallic boundary where the longitudinal component should be zero by definition.

We expect that both the metallic boundaries and dielectric wires will have a distorting effect on the longitudinal field around them. Therefore, it would be sensible not to place our evaluation line near either of these objects. We should especially avoid the corners of our structure where the field evaluated will be distorted by its close position to two metallic boundaries. Given this, we would expect a desirable position to place our line to be in the centre of the structure between the four wires, as shown in blue in Fig. 7.51.
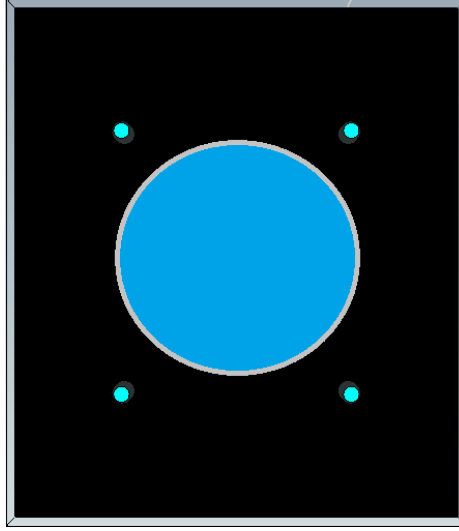
Figure 7.51: A representation of a partially finite wire medium in CST (2×2, $\varepsilon_r = 100$, $r = 0.5$ mm, $a_x = 13.06$ mm and $a_y = 15.00$ mm) shown from the end. The areas where we expect to observe good field profile shaping are shown in blue with the rest of the free space shaded black and the wires shown in cyan.

The position at which the field is evaluated has been explored for our simulation of a flattened mode. In Fig. 7.52b we show the field profile observed when a line spanning the length of the structure is placed at the coordinates $x = 1.5a_x$ and $y = 2a_y$, where a_x and a_y are the lattice constants. As shown in Fig. 7.52a, this line is in the usual position used, with it being directly above a varying wire at the extreme of the structure. We can see, even without comparison or any quantitative measure, that the profiling is not successful at this position, as we expected. Although, since we are evaluating the longitudinal component at the metal boundary, we would expect the field to be zero, but the field is a few magnitudes of order lower than our usual fields. We assume this is just numerical noise, possibly due to the mesh cells covering the boundary also covering some of the inner structure.

A line was also placed near the corner of the structure ($x = 1.75a_x$, $y = 1.55a_y$), as shown in Fig. 7.53a. We expect this position to be a particularly poor place to evaluate the field profile as it is close to two metallic boundaries. This was confirmed by the field profile shown in Fig. 7.53b, with an $\mathfrak{R}^2$ value of 0.7676.

Another line was placed with the same x-coordinate, $x = 1.75a_x$, but a smaller y-coordinate, $y = 1.25a_y$. This means that the evaluation line is further away from the metallic boundary at the top of the structure, as seen in Fig. 7.54a. As we had predicted, being near only one metallic boundary greatly improves the quality of the mode profile observed, which is shown in Fig. 7.54. The $\mathfrak{R}^2$ value at this position is 0.9965. Despite not being placed in the area we expect to be ideal, the mode profiling evaluated at this line is very successful.

A line was placed at the coordinates $x = a_x$ and $y = 1.9a_y$. This evaluation

(a)　　　　　　　　　　　　　(b)
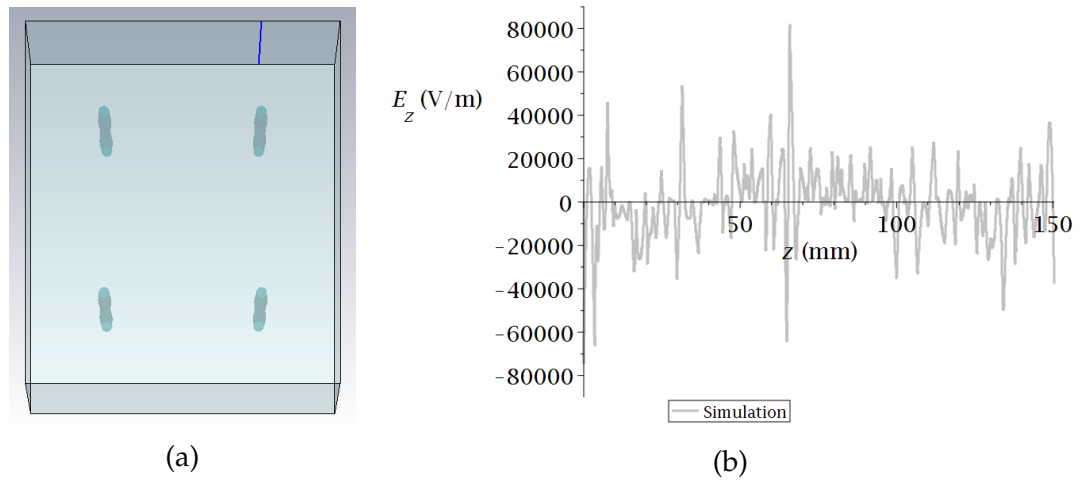
Figure 7.52: Images showing the position in the partially finite wire medium (2×2, $\varepsilon_r = 100$, $a_x = 13.06$ mm and $a_y = 15.00$ mm) at which the field profile of the longitudinal mode ($f = 10.98$ GHz), which results from the implementation of the calculated radius function for a flattened profile ($q = 0.8$) based on the parameter choice of $f_d = 11$ GHz, $R_c = 0.5$ mm and $\lambda_C = 10.7$ GHz, is examined and the resulting field profile. The coordinate system is centred at the bottom left of the structure as seen in (a) with the wires situated at the (x, y) positions of $(0.5a_x, 0.5a_y)$, $(0.5a_x, 1.5a_y)$, $(1.5a_x, 0.5a_y)$ and $(1.5a_x, 1.5a_y)$. (a) shows an evaluation position of $(1.5a_x, 2a_y)$, and (b) shows the resulting field profile (grey).

(a)

(b)
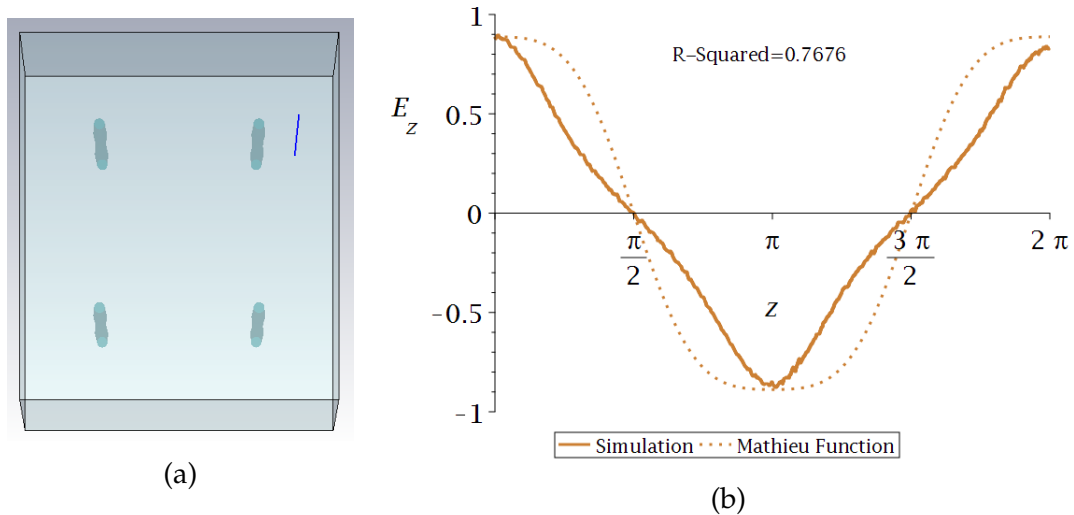
Figure 7.53: Images showing the position in the partially finite wire medium $(2 \times 2, \varepsilon_r = 100, a_x = 13.06$ mm and $a_y = 15.00$ mm) at which the field profile of the longitudinal mode $(f = 10.98$ GHz), which results from the implementation of the calculated radius function for a flattened profile $(q = 0.8)$ based on the parameter choice of $f_d = 11$ GHz, $R_c = 0.5$ mm and $\lambda_C = 10.7$ GHz, is examined and the resulting field profile. The coordinate system is centred at the bottom left of the structure as seen in (a) with the wires situated at the (x, y) positions of $(0.5a_x, 0.5a_y)$, $(0.5a_x, 1.5a_y)$, $(1.5a_x, 0.5a_y)$ and $(1.5a_x, 1.5a_y)$. (a) shows an evaluation position of $(1.75a_x, 1.55a_y)$, and (b) shows the resulting field profile scaled to compare with the desired profile along with the $\mathfrak{R}^2$ value of 0.7676 (brown).

(a)

(b)
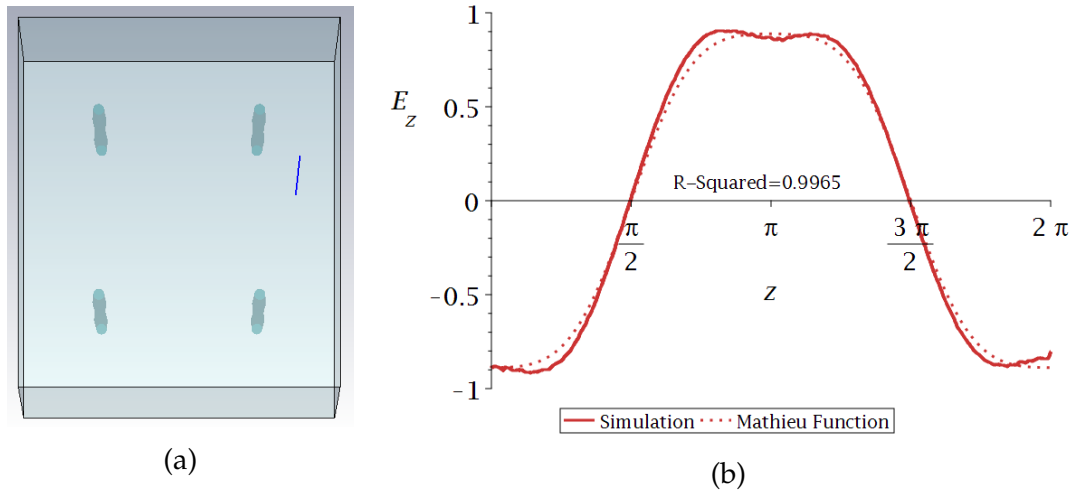
Figure 7.54: Images showing the position in the partially finite wire medium (2×2, $\varepsilon_r = 100$, $a_x = 13.06$ mm and $a_y = 15.00$ mm) at which the field profile of the longitudinal mode ($f = 10.98$ GHz), which results from the implementation of the calculated radius function for a flattened profile ($q = 0.8$) based on the parameter choice of $f_d = 11$ GHz, $R_c = 0.5$ mm and $\lambda_C = 10.7$ GHz, is examined and the resulting field profile. The coordinate system is centred at the bottom left of the structure as seen in (a) with the wires situated at the (x, y) positions of ($0.5a_x$, $0.5a_y$), ($0.5a_x$, $1.5a_y$), ($1.5a_x$, $0.5a_y$) and ($1.5a_x$, $1.5a_y$). (a) shows an evaluation position of ($1.75a_x$, $1.25a_y$), and (b) shows the resulting field profile scaled to compare with the desired profile along with the $\mathfrak{R}^2$ value of 0.9965 (brown).

(a)

(b)
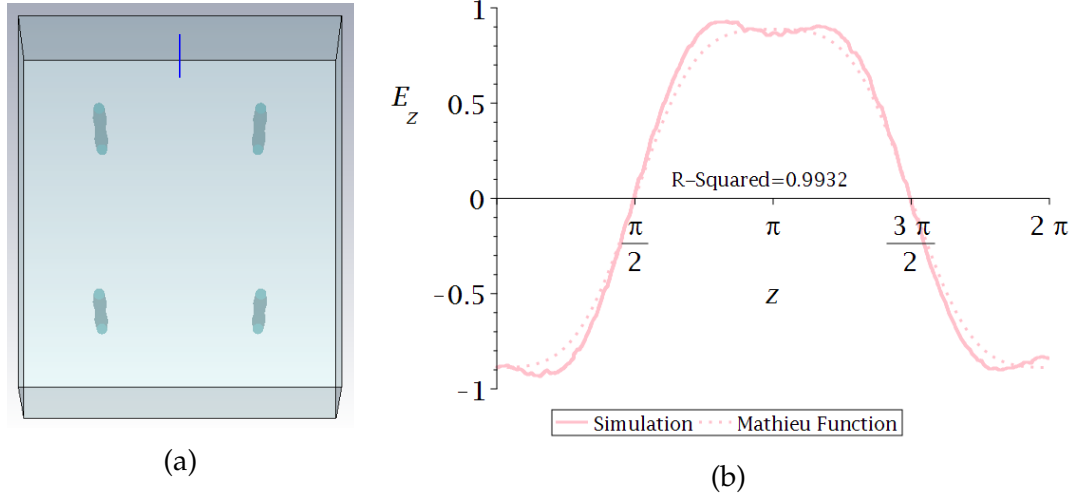
Figure 7.55: Images showing the position in the partially finite wire medium (2×2, $\varepsilon_r = 100$, $a_x = 13.06$ mm and $a_y = 15.00$ mm) at which the field profile of the longitudinal mode ($f = 10.98$ GHz), which results from the implementation of the calculated radius function for a flattened profile ($q = 0.8$) based on the parameter choice of $f_d = 11$ GHz, $R_c = 0.5$ mm and $\lambda_C = 10.7$ GHz, is examined and the resulting field profile. The coordinate system is centred at the bottom left of the structure as seen in (a) with the wires situated at the (x, y) positions of $(0.5a_x, 0.5a_y)$, $(0.5a_x, 1.5a_y)$, $(1.5a_x, 0.5a_y)$ and $(1.5a_x, 1.5a_y)$. (a) shows an evaluation position of $(a_x, 1.9a_y)$, and (b) shows the resulting field profile scaled to compare with the desired profile along with the $\mathfrak{R}^2$ value of 0.9932 (pink).

line is halfway between two of the metallic boundaries, as far away from each of them as possible and extremely close to the metallic boundary at the top of the structure. This is shown in Fig. 7.55a. Despite being very close to one metallic boundary the mode profiling observed at this position is still very good, with an $\mathfrak{R}^2$ value of 0.9932.

Two lines have been used to evaluate the field with the coordinates of $(1.5a_x, a_y)$ and $(a_x, 1.5a_y)$. These lines are similar to the lines used to evaluate our longitudinal fields in our analysis of infinite lattices. Each line is displaced by either a shift in the x and y coordinate by half of the corresponding lattice constant, $\frac{a_x}{2}$ or $\frac{a_y}{2}$. This is shown in Fig.7.56. Evaluating the field at these positions, we find the mode profiles shown in Fig. 7.56. The mode profiling at these positions is exceptionally successful, with $\mathfrak{R}^2$ values of 0.9989 and 0.9991.

Another of the line positions we tested was a line that is very close to the wires, with the coordinates $(1.45a_x, 1.45a_y)$. This line position is shown in Fig. 7.57a. As we had predicted, the mode profiling observed at this position is quite poor. This is shown in Fig. 7.57b, with the mode profile having an $\mathfrak{R}^2$ value of 0.5501.

Finally, we also introduced three lines in the region of the structure we had predicted to be the most suitable for evaluating the field, with the coordinates

(a)

(b)

(c)

(d)
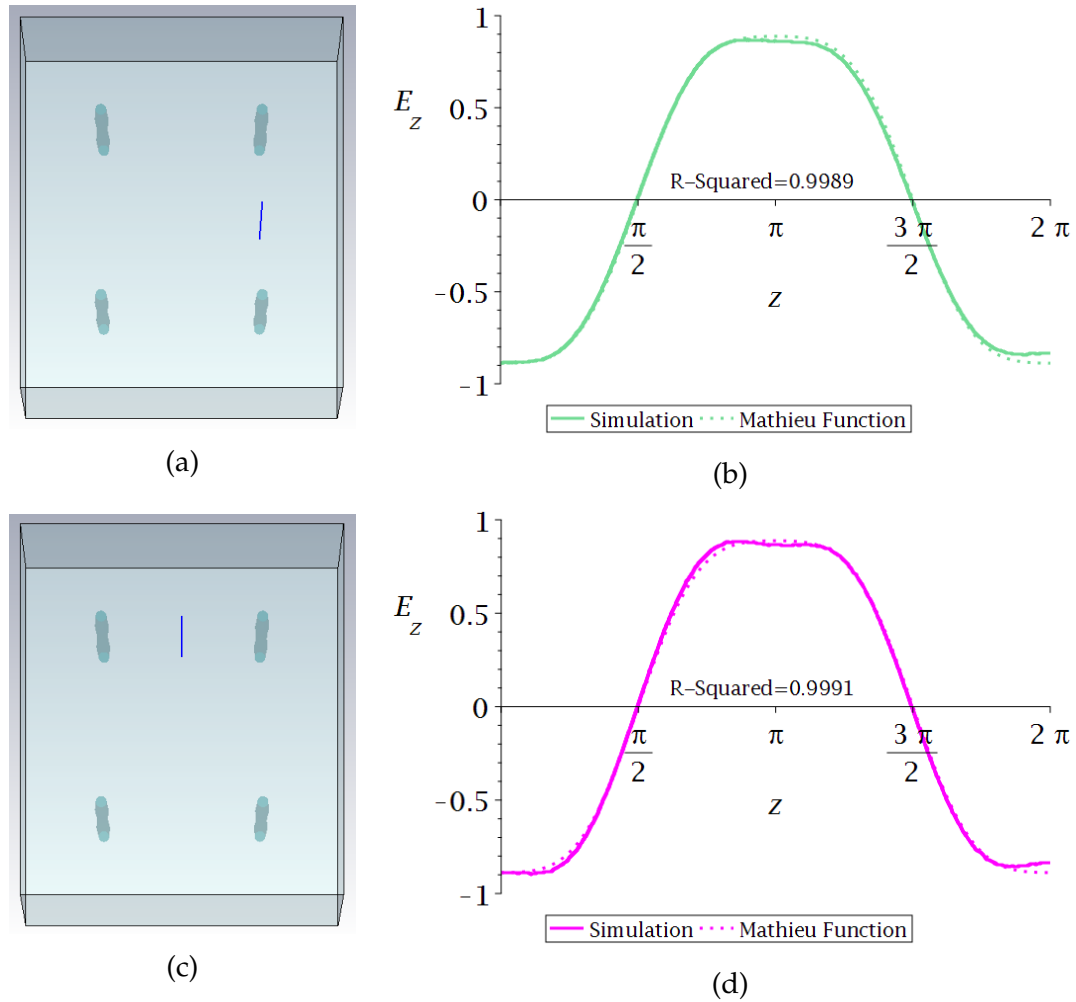
Figure 7.56: Images showing the positions in the partially finite wire medium (2×2, $\varepsilon_r = 100$, $a_x = 13.06$ mm and $a_y = 15.00$ mm) at which the field profile of the longitudinal mode ($f = 10.98$ GHz), which results from the implementation of the calculated radius function for a flattened profile ($q = 0.8$) based on the parameter choice of $f_d = 11$ GHz, $R_c = 0.5$ mm and $\lambda_C = 10.7$ GHz, is examined and the resulting field profiles. The coordinate system is centred at the bottom left of the structure as seen in (a) with the wires situated at the (x, y) positions of $(0.5a_x, 0.5a_y)$, $(0.5a_x, 1.5a_y)$, $(1.5a_x, 0.5a_y)$ and $(1.5a_x, 1.5a_y)$. (a) shows an evaluation position of $(1.5a_x, a_y)$, and (b) shows the resulting field profile scaled to compare with the desired profile along with the $\mathfrak{R}^2$ value of 0.9989 (green). (c) shows an evaluation position of $(a_x, 1.5a_y)$, and (d) shows the resulting field profile scaled to compare with the desired profile along with the $\mathfrak{R}^2$ value of 0.9991 (magenta).

(a)

(b)
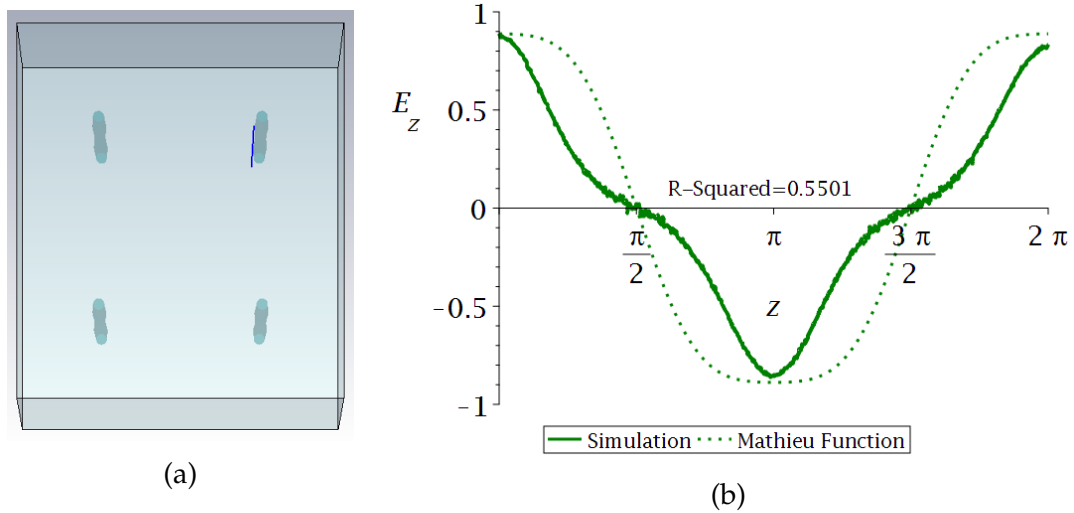
Figure 7.57: Images showing the position in the partially finite wire medium (2×2, $\varepsilon_r = 100$, $a_x = 13.06$ mm and $a_y = 15.00$ mm) at which the field profile of the longitudinal mode ($f = 10.98$ GHz), which results from the implementation of the calculated radius function for a flattened profile ($q = 0.8$) based on the parameter choice of $f_d = 11$ GHz, $R_c = 0.5$ mm and $\lambda_C = 10.7$ GHz, is examined and the resulting field profile. The coordinate system is centred at the bottom left of the structure as seen in (a) with the wires situated at the (x, y) positions of ($0.5a_x$, $0.5a_y$), ($0.5a_x$, $1.5a_y$), ($1.5a_x$, $0.5a_y$) and ($1.5a_x$, $1.5a_y$). (a) shows an evaluation position of ($1.45a_x$, $1.45a_y$), and (b) shows the resulting field profile scaled to compare with the desired profile along with the $\mathfrak{R}^2$ value of 0.5501 (dark green).
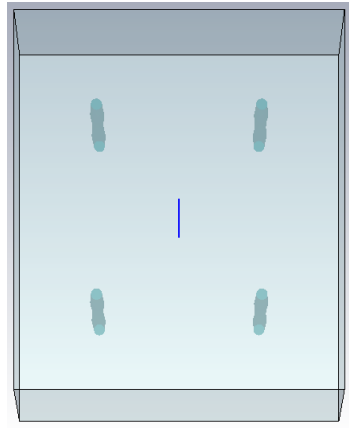
(a)
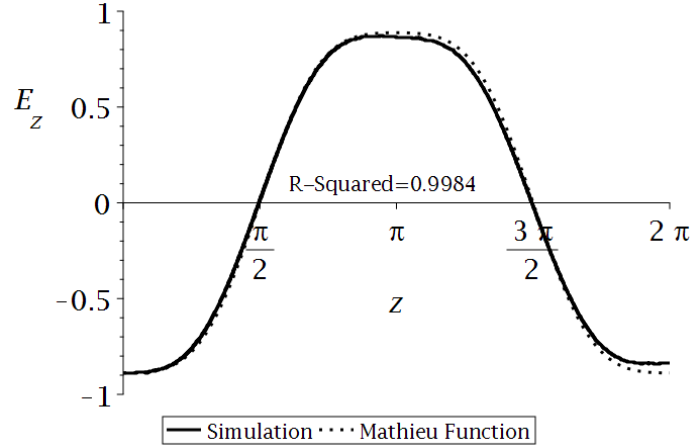
(b)
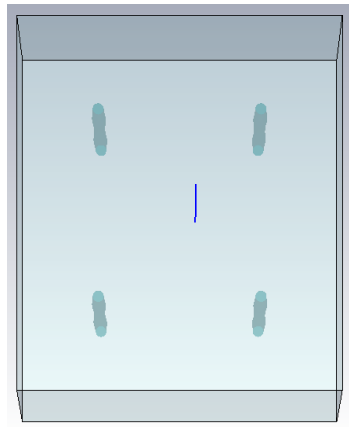
(c)
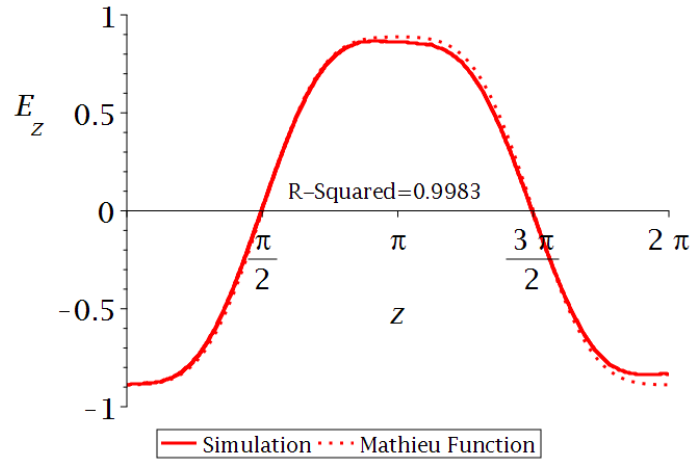
(d)

(a_x, a_y), $(1.1a_x, 1.1a_y)$ and $(1.2a_x, 1.2a_y)$. These lines are shown in Fig. 7.58. Fig. 7.58 show that the mode profiling observed at these positions is very successful. The $\mathfrak{R}^2$ values for the mode profiles at (a_x, a_y), $(1.1a_x, 1.1a_y)$ and $(1.2a_x, 1.2a_y)$ are 0.9984, 0.9983 and 0.9989 respectively.

One conclusion we can draw from this analysis is that our method for achieving mode profile shaping is exceptionally successful for our new scenario of a partially finite structure. The mode profile observed at several points in the structure, including in the central channel where we may want to interact with our field, was remarkably similar to our desired profile as confirmed by both qualitative and quantitative measures. We have also confirmed that near the dielectric wires and metal boundaries the mode profiling is poor, as even for this generally successful attempt the mode profile near these objects was not close to our desired profile. By evaluating the field profile at several points, we have shown that the quality of our mode profiling is very stable with regards to the evaluation position. We had expected the most accurate field profiles to be found in the central

148

(e)

(f)
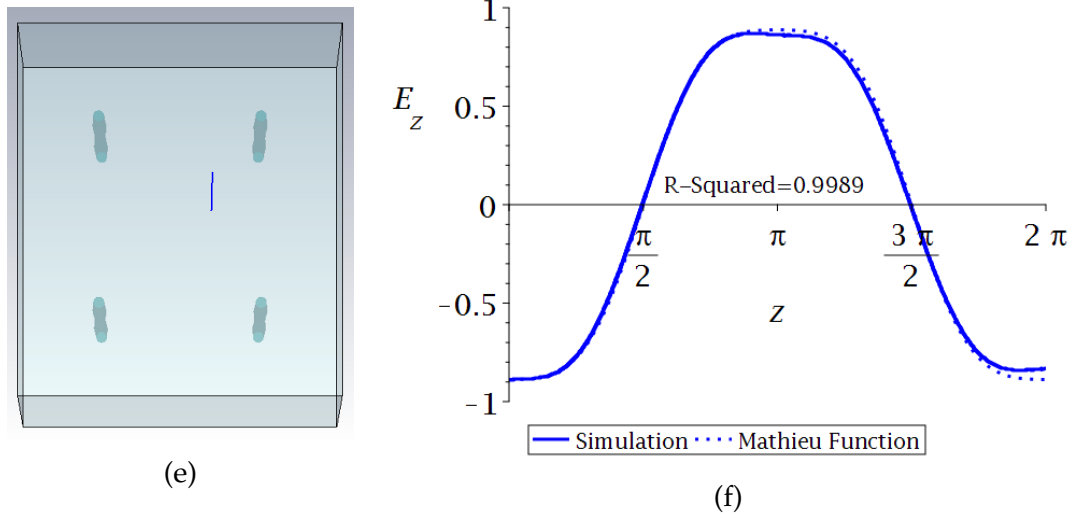
Figure 7.58: Images showing the positions in the partially finite wire medium (2×2, $\varepsilon_r = 100$, $a_x = 13.06$ mm and $a_y = 15.00$ mm) at which the field profile of the longitudinal mode ($f = 10.98$ GHz), which results from the implementation of the calculated radius function for a flattened profile ($q = 0.8$) based on the parameter choice of $f_d = 11$ GHz, $R_c = 0.5$ mm and $\lambda_C = 10.7$ GHz, is examined and the resulting field profiles. The coordinate system is centred at the bottom left of the structure as seen in (a) with the wires situated at the (x, y) positions of $(0.5a_x, 0.5a_y)$, $(0.5a_x, 1.5a_y)$, $(1.5a_x, 0.5a_y)$ and $(1.5a_x, 1.5a_y)$. (a) shows an evaluation position of (a_x, a_y), and (b) shows the resulting field profile scaled to compare with the desired profile along with the $\mathfrak{R}^2$ value of 0.9984 (black). (c) shows an evaluation position of $(1.1a_x, 1.1a_y)$, and (d) shows the resulting field profile scaled to compare with the desired profile along with the $\mathfrak{R}^2$ value of 0.9983 (crimson). (e) shows an evaluation position of $(1.2a_x, 1.2a_y)$, and (d) shows the resulting field profile scaled to compare with the desired profile along with the $\mathfrak{R}^2$ value of 0.9989 (blue).
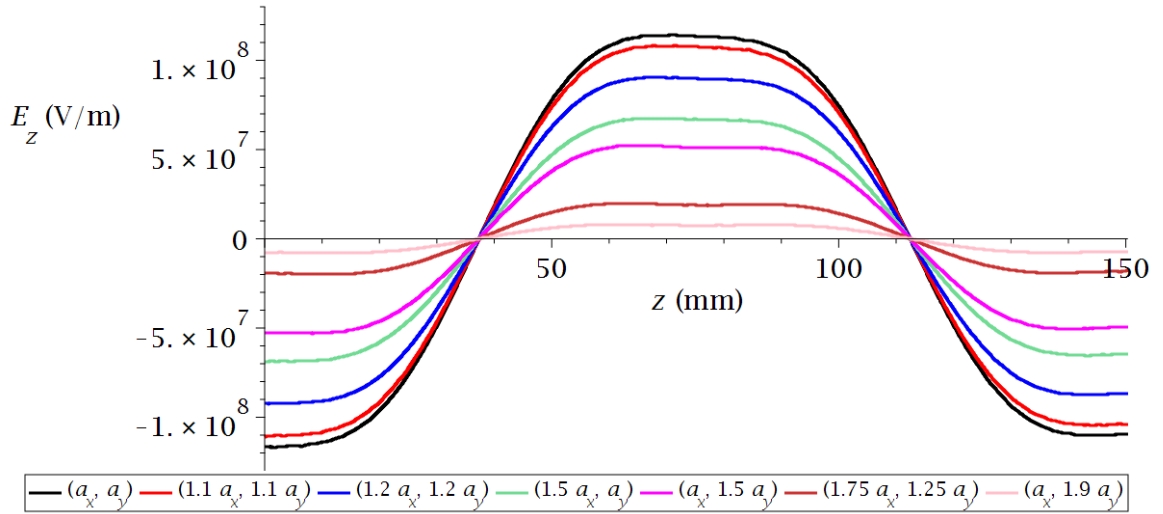
Figure 7.59: A plot of the field profiles (longitudinal, z, spatial variation of the electric field strength, E_z) of the longitudinal mode ($f = 10.98$ GHz) in a partially finite dielectric wire medium (2×2, $\varepsilon_r = 100$, $a_x = 13.06$ mm and $a_y = 15.00$ mm) for our attempt to produce a flattened profile ($q = 0.8$) with a radius function based on the parameter choice of $f_d = 11$ GHz, $R_c = 0.5$ mm and $\lambda_C = 10.7$ GHz for a variety of different evaluation positions. The field profiles shown are for the evaluation position of (a_x, a_y) in black, ($1.1a_x$, $1.1a_y$) in red, ($1.2a_x$, $1.2a_y$) in blue, ($1.5a_x$, a_y) in green, (a_x, $1.5a_y$) in green, ($1.75a_x$, $1.25a_y$) in brown and (a_x, $1.9a_y$) in pink.

channel, but even those evaluated outside this region showed great similarity to our desired profile.

The stability of the success of the mode profiling calls into question what position we should use as our standard position of evaluation. There are several positions where the mode profiling is very successful. We have chosen to use the central line with the coordinates of (a_x, a_y). Although there are positions where the mode profiling is marginally more successful, as judged by changes in the $\mathfrak{R}^2$ value of approximately 0.0007, this is where the field strength is at its peak, as shown in Fig. 7.59.
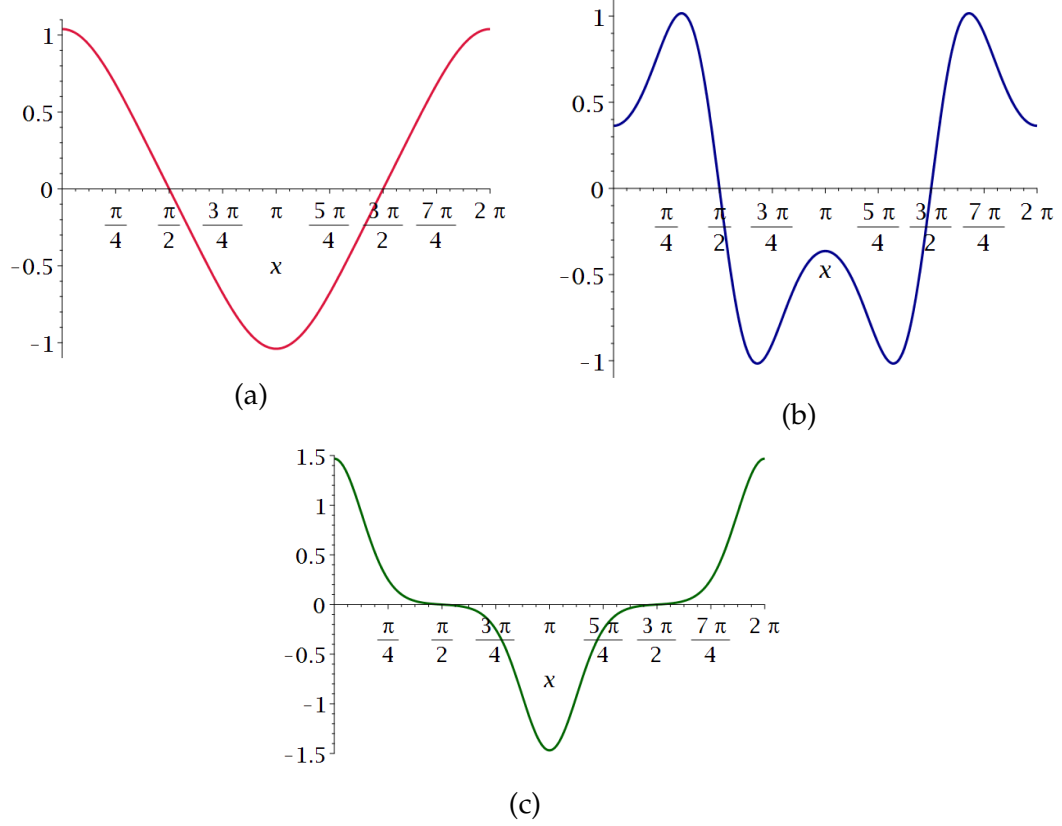
Figure 7.60: A series of plots of different Mathieu functions that we have attempted to replicate using our field shaping method with partially finite dielectric wire media comprising a two by two lattice. (a) is a triangular profile $q = -0.329$ (crimson), (b) is a profile with multiple turning points $q = 4.0$ (dark blue) and (c) is a profile with a pronounced peak $q = -10.0$ (dark green).

q	f_d (GHz)	R_C (mm)	λ_C (GHz)	Γ_1 (μm)	$\Gamma_2 \cdot 10^{-2}$	$\Gamma_3 \cdot 10^{-2}$	Γ_4 (m^{-1})	L (m)
0.8	11	0.5	10.7	153	3.81	-1.27	83.6	0.150
-0.329	11.3	0.5	10.7	153	3.81	-2.81	194	0.0649
4	10.8	0.5	10.7	153	3.81	1.43	39.7	0.316
-10	10.5	0.5	10.7	153	3.81	-1.39	24.7	0.509

Table 7.7: A table summarising some of the key parameters related to the implemented radius functions for a variety of profiles in partially finite dielectric wire media (2×2, $\varepsilon_r = 100$, $a_x = 13.06$ mm and $a_y = 15.00$ mm). The first set of parameters listed are design parameters we chose: the Mathieu parameter characterising the profile (q), design frequency (f_d), central radius (R_C) and the corresponding central plasma frequency (λ_c). The rest are the resulting structural parameters: the parameters specifying the corresponding radius function (Γ_{1-4}) and the length of our unit cell (L). The profiles considered are a triangular profile ($q = -0.329$), a profile with multiple turning points ($q = 4.0$) and a profile with a pronounced peak ($q = -10.0$).

We have shown that our field profiling method is still successful for a two by two lattice of infinitely long dielectric wires for a flattened mode profile. Given that one of the proposed strengths of our method is that it allows us to produce a wide range of desired profile without the need for iteration, we attempted to show that the method could be applied for a variety of profiles. The profiles we attempted to replicate were: a triangular profile (Mathieu parameter $q = -0.329$), a profile with a large number of turning points (Mathieu parameter $q = 4$) and a profile with a pronounced peak (Mathieu parameter $q = -10$). These are the same profiles that have been replicated in the case of an infinite lattice of dielectric wires. Fig. 7.60 is a reproduction of a previous figure which shows the Mathieu profiles we are attempting to replicate with our field profiles. The parameters for the calculated radius function of these profiles, along with those required for the flat profile, are listed in Table 7.7. These radius functions have also been plotted in Fig. 7.61.

(a)

(b)

(c)
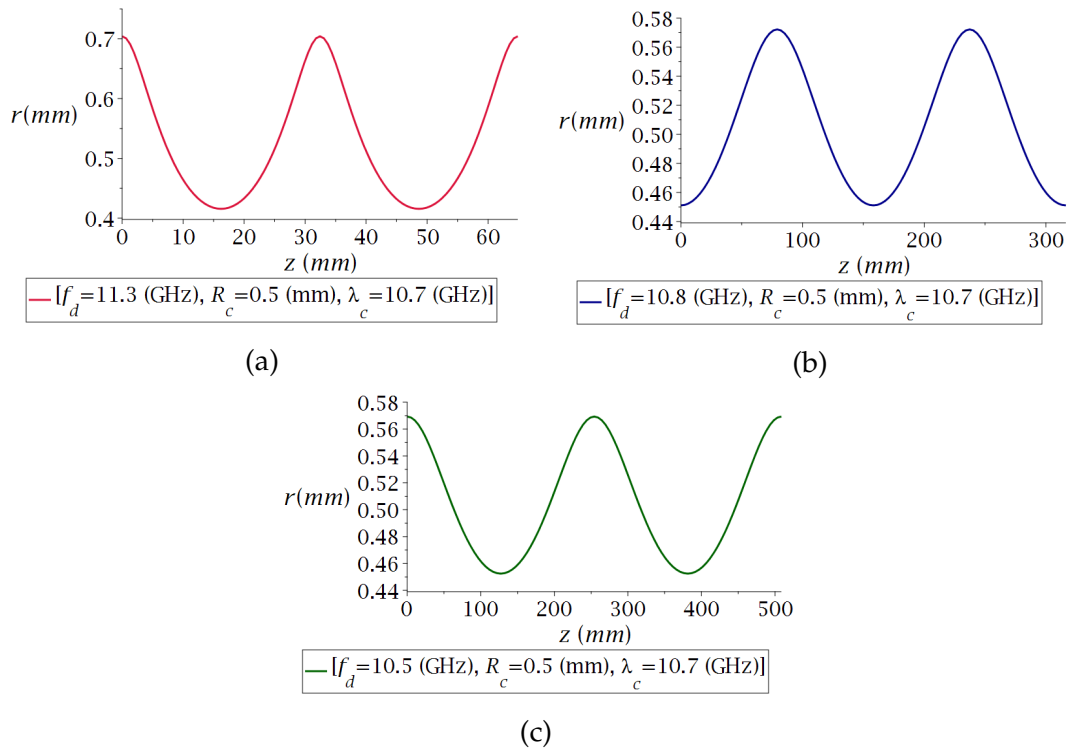
Figure 7.61: A series of plots of radius functions calculated for a variety of desired profiles in partially finite dielectric wire media (2×2, $\varepsilon_r = 100$, $a_x = 13.06$ mm and $a_y = 15.00$ mm). (a) shows the radius function for a triangular profile with a parameter choice of $f_d = 11.3$ GHz, $R_c = 0.5$ mm and $\lambda_C = 10.7$ GHz (crimson); (b), for a profile with multiple turning points with a parameter choice of $f_d = 10.8$ GHz, $R_c = 0.5$ mm and $\lambda_C = 10.7$ GHz (dark blue); and (c), for a profile with a pronounced peak with a parameter choice of $f_d = 10.5$ GHz, $R_c = 0.5$ mm and $\lambda_C = 10.7$ GHz (dark green).

Having calculated the required radius functions, we can implement them into CST and examine the field profiles that are produced. The modes found when implementing these radius functions are shown in Figs. 7.62, 7.63 and 7.64. This process was very successful, as can be seen from the mode profiles plotted in Fig. 7.65, with all the mode profiles being very similar to the desired profiles. As usual with our efforts at achieving mode profiling for the pronounced peak profile, two modes were found. The frequencies of these modes were 10.5295 and 10.5302 GHz, a separation of 0.0007 GHz, and the profile in Fig. 7.65c represents a superposition of the mode profiles of these two modes. For a quantitative measure of the success of the mode profiling for each mode profile, we have listed the $\mathfrak{R}^2$ value for each profile in Table 7.8. These results clearly show that our method retains its ability to provide accurate mode profiling for a variety of profiles when applied to partially finite structures.

(a)

(b)

(c)
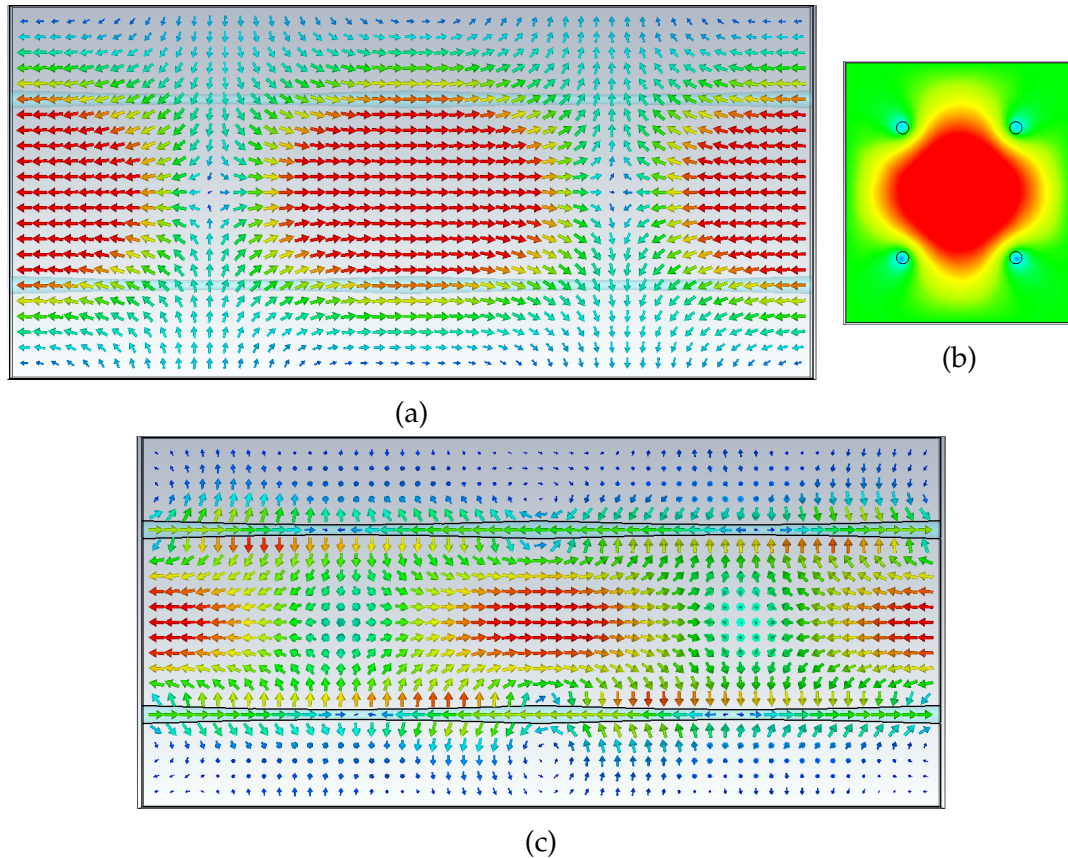
Figure 7.62: Images showing the resulting longitudinal mode ($f = 11.36$ GHz) after the implementation of the calculated radius function for a triangular profile ($q = -0.329$) in a partially finite dielectric wire medium (2×2, $\varepsilon_r = 100$, $a_x = 13.06$ mm and $a_y = 15.00$ mm) for the parameter choice of $f_d = 11.3$ GHz, $R_c = 0.5$ mm and $\lambda_C = 10.7$ GHz. The fields are either represented using arrow plots where the arrow direction represents field direction and colour represents the magnitude of the field strength, or colour plots where the direction and magnitude of the longitudinal field is represented by colour. (a) shows a y-z slice through the centre of the structure, (b) an x-y slice and (c) a y-z slice through two of the wires.

(a)

(b)

(c)

Figure 7.63: Images showing the resulting longitudinal mode (f = 10.81 GHz) after the implementation of the calculated radius function for a profile with multiple turning points (q = 4.0) in a partially finite dielectric wire medium (2×2, ε_r = 100, a_x = 13.06 mm and a_y = 15.00 mm) for the parameter choice of f_d = 10.8 GHz, R_c = 0.5 mm and λ_C = 10.7 GHz. The fields are either represented using arrow plots where the arrow direction represents field direction and colour represents the magnitude of the field strength, or colour plots where the direction and magnitude of the longitudinal field is represented by colour. (a) shows a y-z slice through the centre of the structure, (b) an x-y slice and (c) a y-z slice through two of the wires.

(a)

(b)

Figure 7.64: Images showing the resulting longitudinal modes after the implementation of the calculated radius function for a profile with a pronounced peak (q = −10.0) in a partially finite dielectric wire medium (2×2, ε_r = 100, a_x = 13.06 mm and a_y = 15.00 mm) for the parameter choice of f_d = 10.5 GHz, R_c = 0.5 mm and λ_C = 10.7 GHz. The fields are represented using arrow plots on an y-z slice of the structure where the arrow direction represents field direction and colour represents the magnitude of the field strength. (a) shows one of the resulting longitudinal modes (f = 10.5295 GHz); and (b), the other (f = 10.5302 GHz).

q	f_d (GHz)	λ_C (GHz)	L (mm)	f (GHz)	$\mathfrak{R}^2$
0.8	11	10.7	150	10.98	0.9984
-0.329	11.3	10.7	64.9	11.36	0.9982
4	10.8	10.7	316	10.81	0.9769
-10	10.5	10.7	509	10.53	0.7517

Table 7.8: A table summarising some of the key parameters related to the results of our implemented radius functions for a variety of profiles in partially finite dielectric wire media (2×2, $\varepsilon_r = 100$, $a_x = 13.06$ mm and $a_y = 15.00$ mm). The parameters listed are: the Mathieu parameter characterising the profile (q), design frequency (f_d), the central plasma frequency (λ_c), the length of our unit cell (L), longitudinal mode frequency (f) and a figure of merit for the agreement between our field profile and the desired profile ($\mathfrak{R}^2$). The profiles considered are a triangular profile ($q = -0.329$), a profile with multiple turning points ($q = 4.0$) and a profile with a pronounced peak ($q = -10.0$).

(a)

(b)

(c)

Figure 7.65: Plots of the field profiles (longitudinal, z, spatial variation of the electric field strength, E_z) of the longitudinal modes in partially finite dielectric wire media (2×2, $\varepsilon_r = 100$, $a_x = 13.06$ mm and $a_y = 15.00$ mm) for our attempts to produce a triangular profile ($q = -0.329$), a profile with multiple turning points ($q = 4.0$) and a profile with a pronounced peak ($q = -10.0$). The plots include the field profile observed in our numerical simulation (solid) and the desired profile (dotted). In order to compare these the field profile and z coordinate have been normalised. (a) shows the field profile of the longitudinal mode ($f = 11.36$ GHz) for the attempt to demonstrate a triangular profile by the implementation of a radius function based on the choice of $f_d = 11.3$ GHz, $R_c = 0.5$ mm and $\lambda_C = 10.7$ GHz (crimson); (b), the field profile of the longitudinal mode ($f = 10.8$ GHz) for the attempt to achieve a profile with multiple turning points by the implementation of a radius function based on the choice of $f_d = 10.5$ GHz, $R_c = 0.5$ mm and $\lambda_C = 10.7$ GHz (dark blue); and (c), the field profile of the longitudinal mode ($f = 10.8$ GHz) for the attempt to achieve a profile with multiple turning points by the implementation of a radius function based on the choice of $f_d = 10.8$ GHz, $R_c = 0.5$ mm and $\lambda_C = 10.7$ GHz (dark green).

This was very promising as a first step towards demonstrating that our results could be achieved in a realistic structure. The next step to take was to attempt to simulate a completely finite structure.

VI. Extending our method to finite wire media

To go from partially finite to completely finite structures, we introduced more metallic boundary conditions. This means the longitudinal dimension is now bounded by metallic boundaries, as shown in Fig. 7.66. This will force the transverse component of the E field at these boundaries to be zero, but this is not a problem as we are interested in longitudinal modes. Therefore, we should not expect the introduction of these boundaries to cause a significant change to the results we have found in our partially finite structures. As such, when attempting to extend our work to finite simulations, we have taken the varying radius structures from Section V and applied new boundary conditions. These structures are formed from dielectric wires with a relative permittivity of $\varepsilon_r = 100$ and are arranged in a two by two lattice, with the transverse boundaries placed at a distance of half of the relevant lattice parameter away.
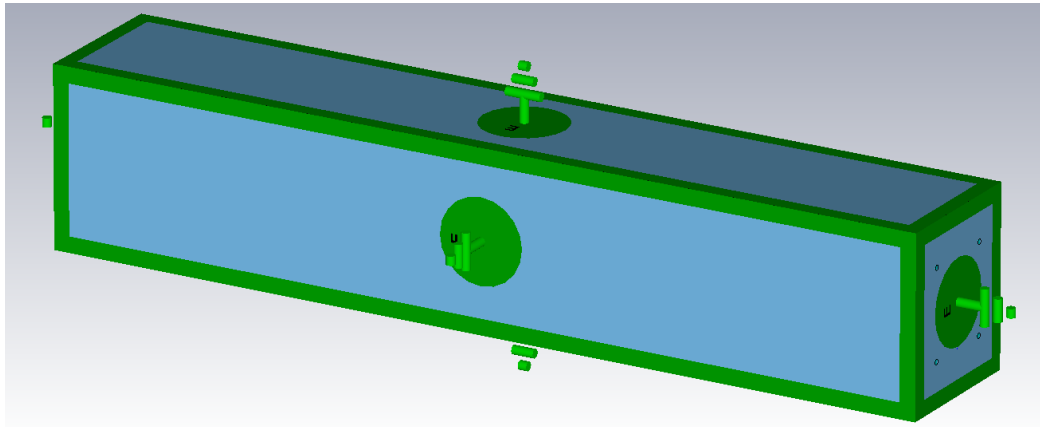
Figure 7.66: A representation of a finite wire medium in CST, consisting of a two by two lattice of dielectric wires in a unit cell with metallic boundary conditions ($\varepsilon_r = 100$, $a_x = 13.06$ mm and $a_y = 15.00$ mm). The dielectric wire has a radius variation based on a function generated using data from partially finite structures for the attempt to demonstrate a flattened profile based on the choice of $f_d = 11$ GHz, $R_c = 0.5$ mm and $\lambda_C = 10.7$ GHz. The image shows the boundaries of the structure with green representing metallic boundary conditions.

As we have already stated, our attempts at mode profile shaping in a completely finite structure are an extension of our work with partially finite structures. We have attempted to replicate all the same profiles as previously, starting with a flattened mode profile (Mathieu parameter q=0.8). Our desired flattened mode
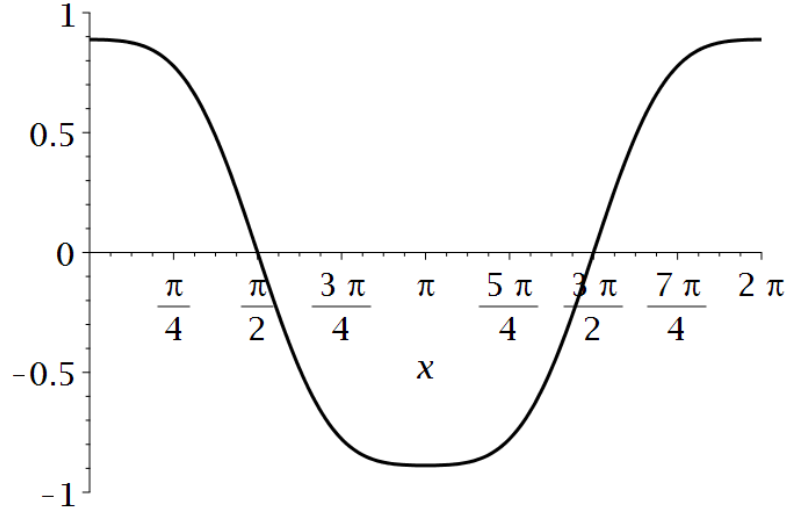
Figure 7.67: A solution to Mathieu's equations ($q = 0.8$) that can be loosely described as a flattened sinusoidal curve.

profile is shown in Fig. 7.67. The radius function we have used for this mode profile is identical to the one used for our partially finite structure, as is the case with the radius functions implemented for the other profiles attempted. A plot of this radius function is shown in Fig. 7.68.

q	f_d (GHz)	R_C (mm)	λ_C (GHz)	Γ_1 (μm)	$\Gamma_2 \cdot 10^{-2}$	$\Gamma_3 \cdot 10^{-2}$	Γ_4 (m^{-1})	L (m)
0.8	11	0.5	10.7	153	3.81	-1.27	83.6	0.150
-0.329	11.3	0.5	10.7	153	3.81	-2.81	194	0.0649
4	10.8	0.5	10.7	153	3.81	1.43	39.7	0.316
-10	10.5	0.5	10.7	153	3.81	-1.39	24.7	0.509

Table 7.9: A table summarising some of the key parameters related to the implemented radius functions for a variety of profiles in finite dielectric wire media (2×2, $\varepsilon_r = 100$, $a_x = 13.06$ mm and $a_y = 15.00$ mm). It should be noted that these radius functions were generated using data from partially finite dielectric wire media. The first set of parameters listed are design parameters we chose: the Mathieu parameter characterising the profile (q), design frequency (f_d), central radius (R_C) and the corresponding central plasma frequency (λ_c). The rest are the resulting structural parameters: the parameters specifying the corresponding radius function (Γ_{1-4}) and the length of our unit cell (L). The profiles considered are a triangular profile ($q = -0.329$), a profile with multiple turning points ($q = 4.0$) and a profile with a pronounced peak ($q = -10.0$).
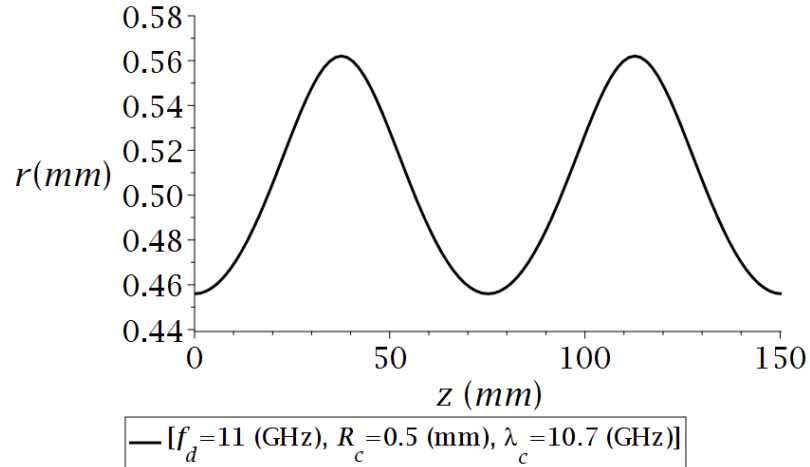
Figure 7.68: Radius function calculated for a flattened profile ($q = 0.8$) in a finite dielectric wire medium (2×2, $\varepsilon_r = 100$, $a_x = 13.06$ mm and $a_y = 15.00$ mm) for the parameter choice of $f_d = 11$ GHz, $R_c = 0.5$ mm and $\lambda_C = 10.7$ GHz.

(a)

(b)

(c)
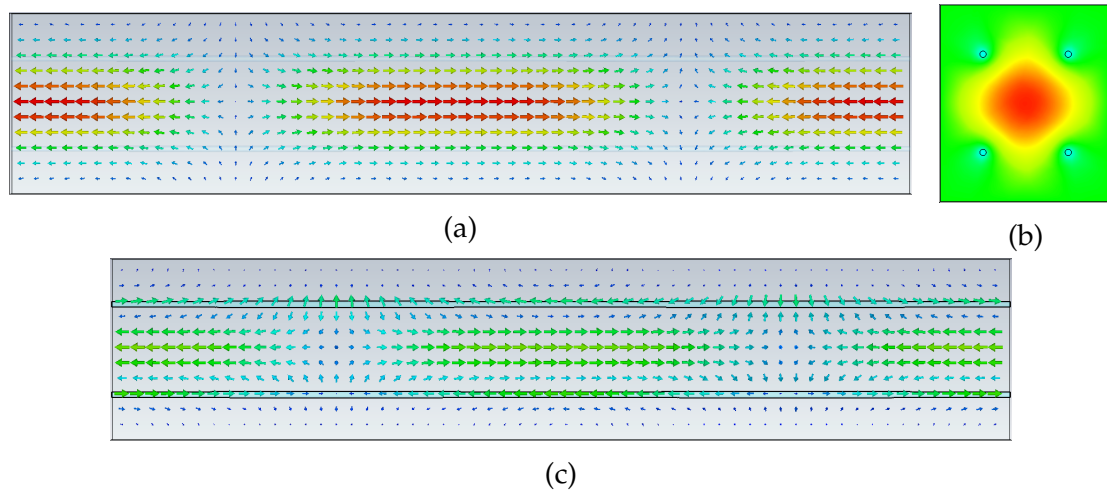
Figure 7.69: Images showing the resulting longitudinal mode ($f = 10.99$ GHz) after the implementation of the calculated radius function for a flattened profile ($q = 0.8$) in a finite dielectric wire medium (2×2, $\varepsilon_r = 100$, $a_x = 13.06$ mm and $a_y = 15.00$ mm) for the parameter choice of $f_d = 11$ GHz, $R_c = 0.5$ mm and $\lambda_C = 10.7$ GHz. The fields are either represented using arrow plots where the arrow direction represents field direction and colour represents the magnitude of the field strength, or colour plots where the direction and magnitude of the longitudinal field is represented by colour. (a) shows a y-z slice through the centre of the structure, (b) an x-y slice and (c) a y-z slice through two of the wires.

This radius function has already been implemented in a two by two structure of infinite length in Section V. We can now take this structure and apply metallic boundaries conditions to all the boundaries, as shown in Fig. 7.66, to get our

160

desired finite structure. Having done this, we ran an eigenmode simulation to find our longitudinal mode, shown in Fig. 7.69, and evaluated its profile, shown in Fig. 7.70. As can be seen from Fig. 7.70 the mode profiling success we have previously experienced is replicated with our new structure. This is reaffirmed by calculating the $\mathfrak{R}^2$ value for this comparison which is 0.9997. This is a promising result as it shows that we can achieve mode profiling in a finite structure by simply enclosing one unit of our partially finite structure in metallic boundaries.
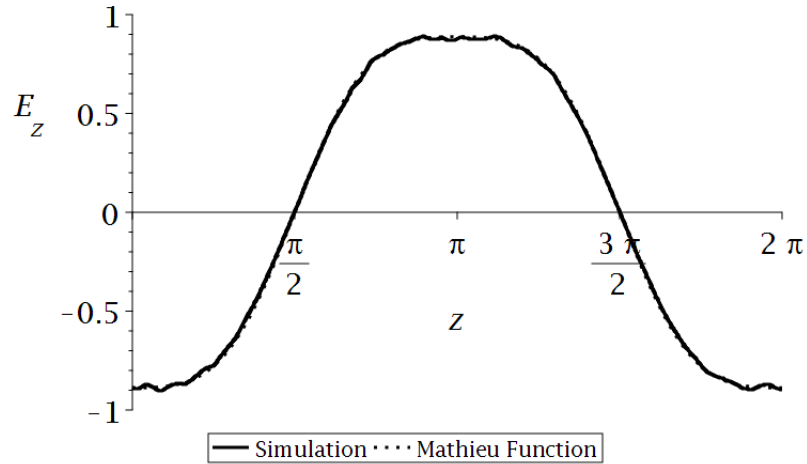
Figure 7.70: Plot of the field profile (longitudinal, z, spatial variation of the electric field strength, E_z) of the longitudinal mode (10.99 GHz) in a finite dielectric wire medium (2×2, $\varepsilon_r = 100$, $a_x = 13.06$ mm and $a_y = 15.00$ mm) for our attempt to produce a flattened profile ($q = 0.8$) by the implementation of a radius function based on the choice of $f_d = 11$ GHz, $R_c = 0.5$ mm and $\lambda_C = 10.7$ GHz (black). The plot includes the field profile observed in our numerical simulation (solid) and the desired profile (dotted). In order to compare these the field profile and z coordinate have been normalised.

Given our success in achieving the replication of a flattened mode profile, we then moved onto attempts to replicate other profiles. The profiles we attempted to replicate were a triangular profile ($q = -0.329$), a profile with more turning points ($q = 4$) and a profile with a pronounced peak ($q = -10$). These are the same profiles we have previously replicated for our partially finite structure. As with the case of the flattened mode, we are using the radius functions previously used for our partially finite structures. These radius functions have been plotted in Fig. 7.71.
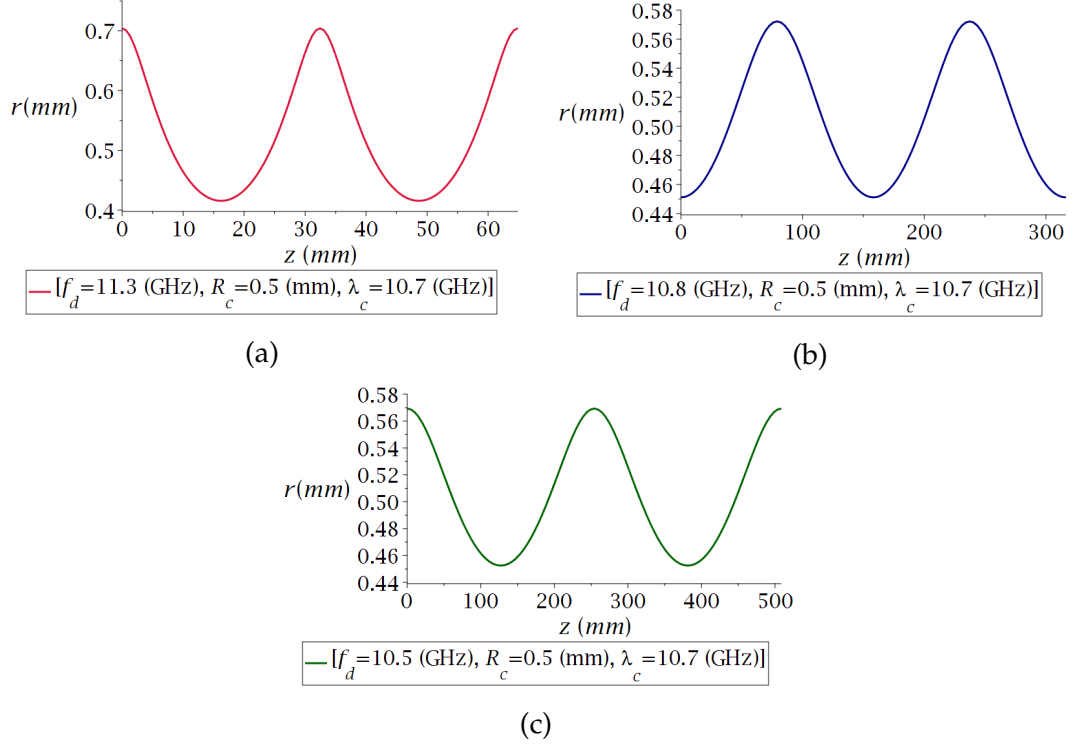
Figure 7.71: A series of plots of radius functions calculated for a variety of desired profiles in finite dielectric wire media (2×2, $\varepsilon_r = 100$, $a_x = 13.06$ mm and $a_y = 15.00$ mm). (a) shows the radius function for a triangular profile with a parameter choice of $f_d = 11.3$ GHz, $R_c = 0.5$ mm and $\lambda_C = 10.7$ GHz (crimson); (b), for a profile with multiple turning points with a parameter choice of $f_d = 10.8$ GHz, $R_c = 0.5$ mm and $\lambda_C = 10.7$ GHz (dark blue); and (c), for a profile with a pronounced peak with a parameter choice of $f_d = 10.5$ GHz, $R_c = 0.5$ mm and $\lambda_C = 10.7$ GHz (dark green).

Implementing these radius functions into our CST structures and running eigenmode simulations allows us to find our desired longitudinal modes. The longitudinal modes found in our simulations for the triangular profile and the profile with more turning points are shown in Figs. 7.72 and 7.73. The profiles for these two modes are shown in Fig. 7.74. We can see from Fig. 7.74 that the mode profiling has been successful, which is reflected in their $\mathfrak{R}^2$ value of 0.9987 for the triangular profile and 0.9772 for the profile with more turning points.

As usual, our attempt to replicate the profile with a pronounced peak was more complicated. We have previously experienced CST splitting our desired longitudinal into two modes, but on this occasion the mode seems to have been split into three modes. Longitudinal modes were found at frequencies of 10.5303, 10.5306 and 10.5318 GHz. These modes, which span a 0.0015 GHz band, are shown in Fig. 7.75. We can see that they all have significant longitudinal fields in separate parts of the structure and resemble our desired mode split across three modes. In Fig. 7.76 we show the combined profile of these three modes compared

(a)

(b)

(c)
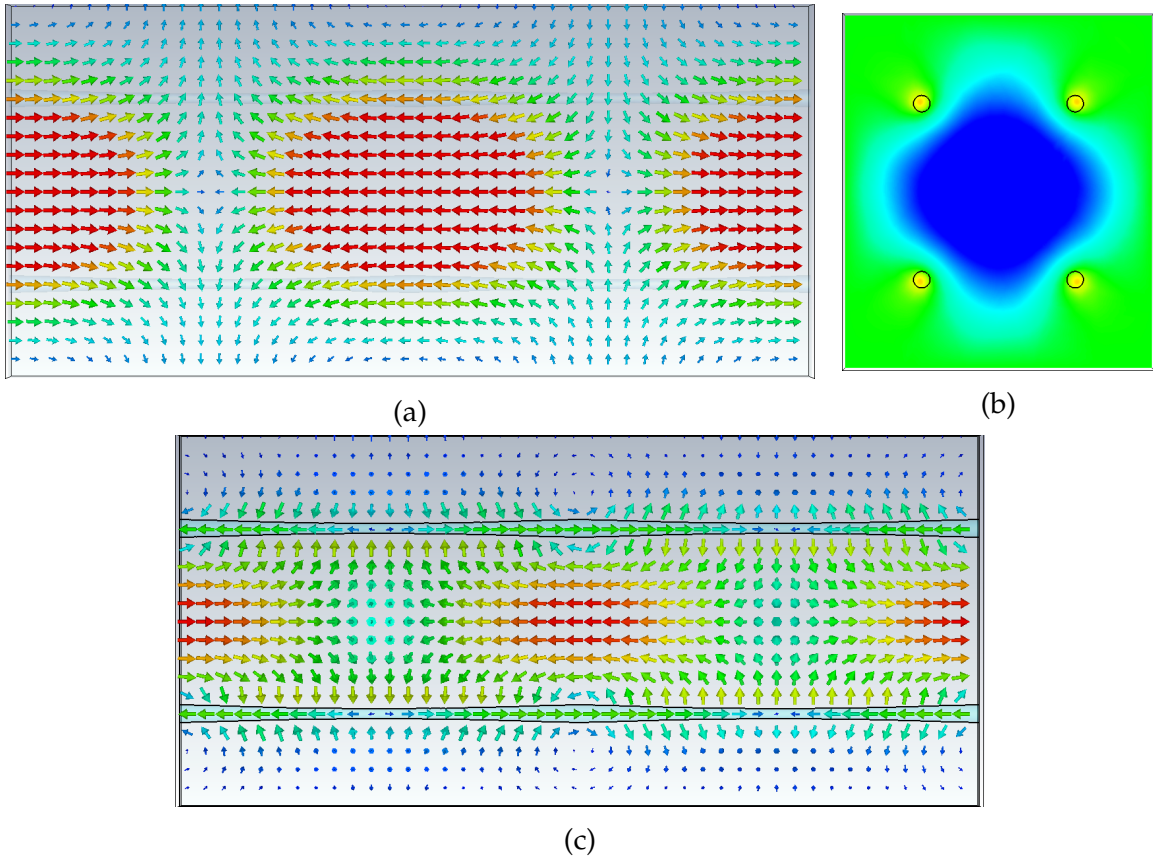
Figure 7.72: Images showing the resulting longitudinal mode ($f = 11.36$ GHz) after the implementation of the calculated radius function for a triangular profile ($q = -0.329$) in a finite dielectric wire medium (2×2, $\varepsilon_r = 100$, $a_x = 13.06$ mm and $a_y = 15.00$ mm) for the parameter choice of $f_\mathrm{d} = 11.3$ GHz, $R_c = 0.5$ mm and $\lambda_C = 10.7$ GHz. The fields are either represented using arrow plots where the arrow direction represents field direction and colour represents the magnitude of the field strength, or colour plots where the direction and magnitude of the longitudinal field is represented by colour. (a) shows a y-z slice through the centre of the structure, (b) an x-y slice and (c) a y-z slice through two of the wires.

163

(a)

(b)

(c)
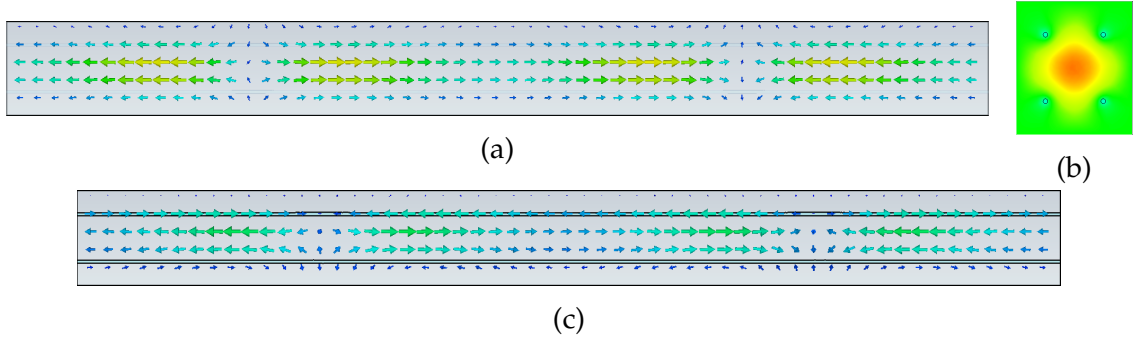
Figure 7.73: Images showing the resulting longitudinal mode ($f = 10.81$ GHz) after the implementation of the calculated radius function for a profile with multiple turning points ($q = 4.0$) in a finite dielectric wire medium (2×2, $\varepsilon_r = 100$, $a_x = 13.06$ mm and $a_y = 15.00$ mm) for the parameter choice of $f_d = 10.8$ GHz, $R_c = 0.5$ mm and $\lambda_C = 10.7$ GHz. The fields are either represented using arrow plots where the arrow direction represents field direction and colour represents the magnitude of the field strength, or colour plots where the direction and magnitude of the longitudinal field is represented by colour. (a) shows a y-z slice through the centre of the structure, (b) an x-y slice and (c) a y-z slice through two of the wires.

against the desired profile. Fig. 7.76 clearly shows that the combined profile is very close to our desired profile, as reflected by the calculated $\mathfrak{R}^2$ value of 0.9458.

The results of our mode profiling attempts for completely finite structures are summarised in Table 7.10. It is clear from Table 7.10 that our method continues to be extremely successful at replicating a variety of profiles. This is especially pleasing as we were able to obtain these results by simply applying new boundary conditions to our existing partially finite structures. These results confirm that our method for mode profiling can be extended to finite structures, which had been a potential area of concern.
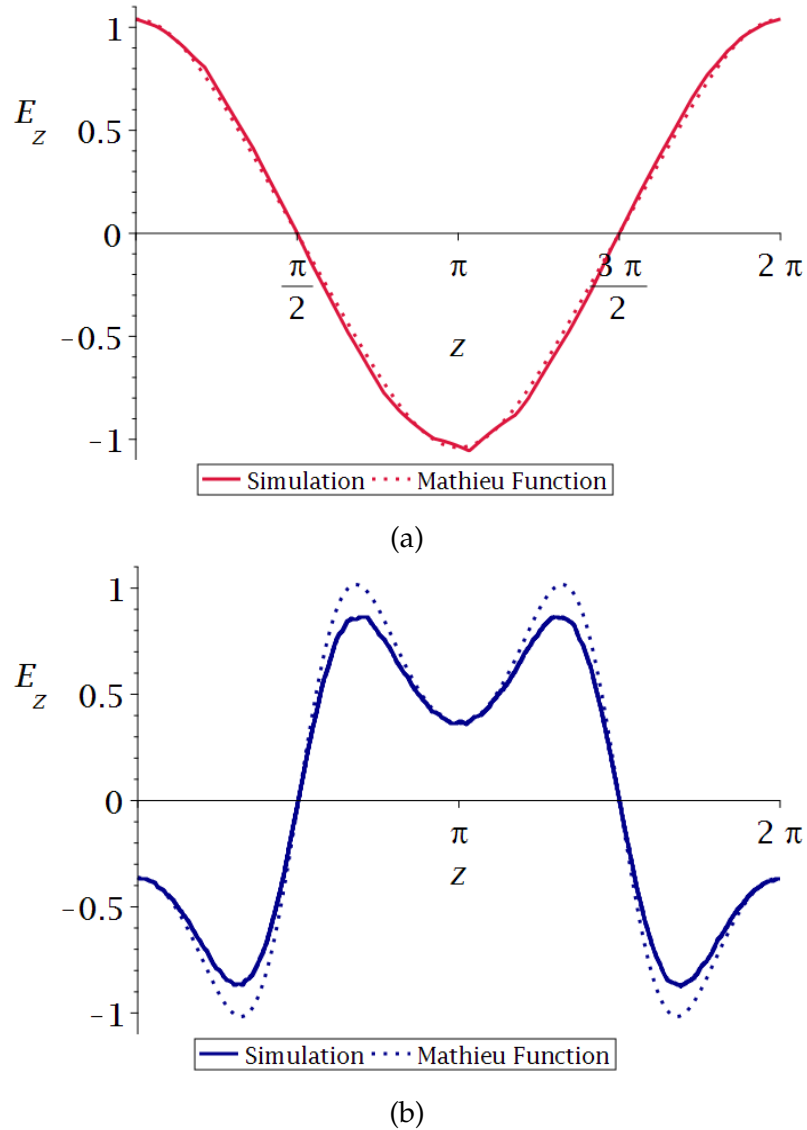
Figure 7.74: Plots of the field profiles (longitudinal, z, spatial variation of the electric field strength, E_z) of the longitudinal modes in finite dielectric wire media (2×2, $\varepsilon_r = 100$, $a_x = 13.06$ mm and $a_y = 15.00$ mm) for our attempts to produce a triangular profile ($q = -0.329$) and a profile with multiple turning points ($q = 4.0$). The plots include the field profile observed in our numerical simulation (solid) and the desired profile (dotted). In order to compare these the field profile and z coordinate have been normalised. (a) shows the field profile of the longitudinal mode ($f = 11.36$ GHz) for the attempt to demonstrate a triangular profile by the implementation of a radius function based on the choice of $f_d = 11.3$ GHz, $R_c = 0.5$ mm and $\lambda_C = 10.7$ GHz (crimson); and (b), the field profile of the longitudinal mode ($f = 10.8$ GHz) for the attempt to achieve a profile with multiple turning points by the implementation of a radius function based on the choice of $f_d = 10.8$ GHz, $R_c = 0.5$ mm and $\lambda_C = 10.7$ GHz (dark blue).

(a)

(b)

(c)

Figure 7.75: Images showing the resulting longitudinal modes after the imple-
mentation of the calculated radius function for a profile with a pronounced peak
($q = -10.0$) in a finite dielectric wire medium (2×2, $\varepsilon_r = 100$, $a_x = 13.06$ mm
and $a_y = 15.00$ mm) for the parameter choice of $f_d = 10.5$ GHz, $R_c = 0.5$ mm
and $\lambda_C = 10.7$ GHz. The fields are represented using arrow plots on an x-z slice
of the structure where the arrow direction represents field direction and colour
represents the magnitude of the field strength. (a) shows one of the resulting lon-
gitudinal modes ($f = 10.5303$ GHz); (b), another ($f = 10.5306$ GHz); and (c), the
mode with the highest frequency ($f = 10.5318$ GHz).
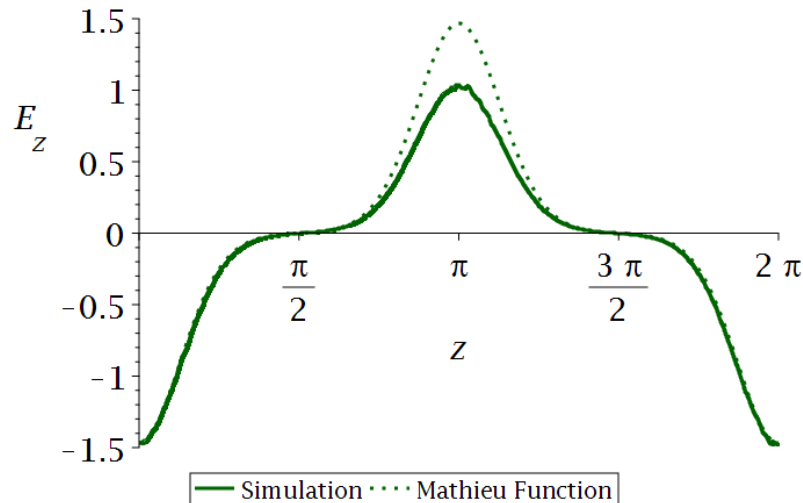
Figure 7.76: Plot of the combined field profile (longitudinal, z, spatial variation
of the electric field strength, E_z) of the longitudinal modes ($f = 10.5303$ GHz,
$f = 10.5306$ GHz and $f = 10.5318$ GHz) in finite dielectric wire media (2×2,
$\varepsilon_r = 100$, $a_x = 13.06$ mm and $a_y = 15.00$ mm) for our attempt to produce a profile
with a pronounced peak ($q = -10.0$) by the implementation of a radius function
based on the choice of $f_d = 10.5$ GHz, $R_c = 0.5$ mm and $\lambda_C = 10.7$ GHz (dark
green). The plot includes the field profile observed in our numerical simulation
(solid) and the desired profile (dotted).

q	f_d (GHz)	λ_C (GHz)	L (mm)	f (GHz)	$\mathfrak{R}^2$
0.8	11	10.7	150	10.98	0.9997
-0.329	11.3	10.7	64.9	11.36	0.9989
4	10.8	10.7	316	10.81	0.9772
-10	10.5	10.7	509	10.53	0.9458

Table 7.10: A table summarising some of the key parameters related to the results of our implemented radius functions for a variety of profiles in finite dielectric wire media (2×2, $\varepsilon_r = 100$, $a_x = 13.06$ mm and $a_y = 15.00$ mm). It should be noted that these radius functions were generated using data from partially finite dielectric wire media. The parameters listed are: the Mathieu parameter characterising the profile (q), design frequency (f_d), the central plasma frequency (λ_c), the length of our unit cell (L), longitudinal mode frequency (f) and a figure of merit for the agreement between our field profile and the desired profile ($\mathfrak{R}^2$). The profiles considered are a triangular profile ($q = -0.329$), a profile with multiple turning points ($q = 4.0$) and a profile with a pronounced peak ($q = -10.0$).

VII. Using a finite wire medium with a four by four lattice

(a)   (b)
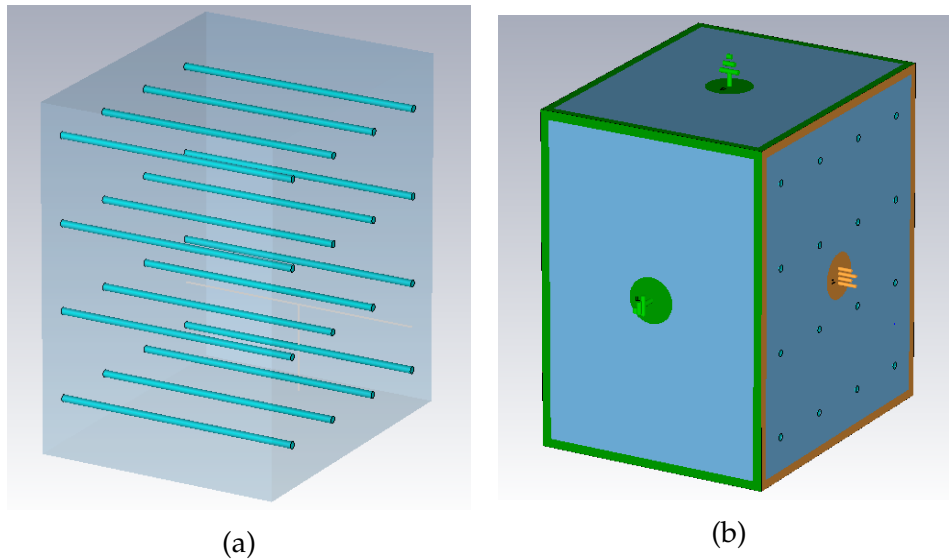
Figure 7.77: A representation of a partially finite wire medium in CST, consisting of a four by four lattice of dielectric wires in a unit cell with transverse metallic boundary conditions and longitudinal periodic boundary conditions ($a_x = 13.06$ mm and $a_y = 15.00$ mm). This is effectively a finite lattice of infinitely long wires in an infinite metallic waveguide. The dielectric wires have a radius (r) of 0.6 mm and a relative permittivity (ε) of 100. (a) shows the unit cell used in CST, and (b) shows the boundaries of the structure with green representing metallic boundaries and orange, periodic boundary conditions.

We have shown that our mode profiling method can be extended to completely finite structures. This has been done by replicating chosen mode profiles in a finite two by two lattice of dielectric wires. We will now explore the ability of four by four lattices, shown in Fig. 7.77, to do the same. Exploring multiple different lattice sizes proved useful in our later work in time domain simulations where we attempted to simulate the excitation of our structure.

We will first consider a structure made up of a four by four lattice of infinitely long dielectric wires in an infinitely long metallic waveguide. This is represented in CST by a unit cell containing our lattice of wires with the transverse boundaries given metallic boundary conditions and the longitudinal boundaries given periodic boundary conditions. The placement of the boundaries is half a lattice constant from the nearest row or column of wires, identical to the boundary placements for our infinite lattices. The dielectric wires used have a permittivity of $\varepsilon_r = 100$.
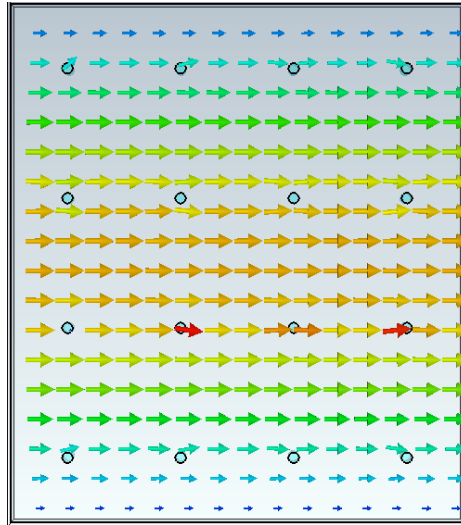
Figure 7.78: Numerical results showing a transverse electric mode, with a frequency of 4.30 GHz, in a representation of a partially finite four by four array of dielectric wires ($\varepsilon_r = 100$) of radius 0.5mm, and wire spacings $a_x = 13.06$ mm and $a_y = 15.00$ mm. The electric field is represented using a vector plot of an x-y slice of the structure where the arrow direction represents field direction and colour represents the magnitude of the field strength.

The modes in this structure can be found by running an eigenmode simulation. A large number of modes in our structures are transverse modes, such as the one shown in Fig. 7.78. We also can find our desired longitudinal modes, such as the one shown in Fig. 7.79 for a wire radius of 0.6 mm. These modes have the same characteristics as the modes we have found in the infinite case: a significant longitudinal component in the regions of free space, and the longitudinal field in the wire has the opposite orientation to the field in free space.

(a)

(b)

(c)
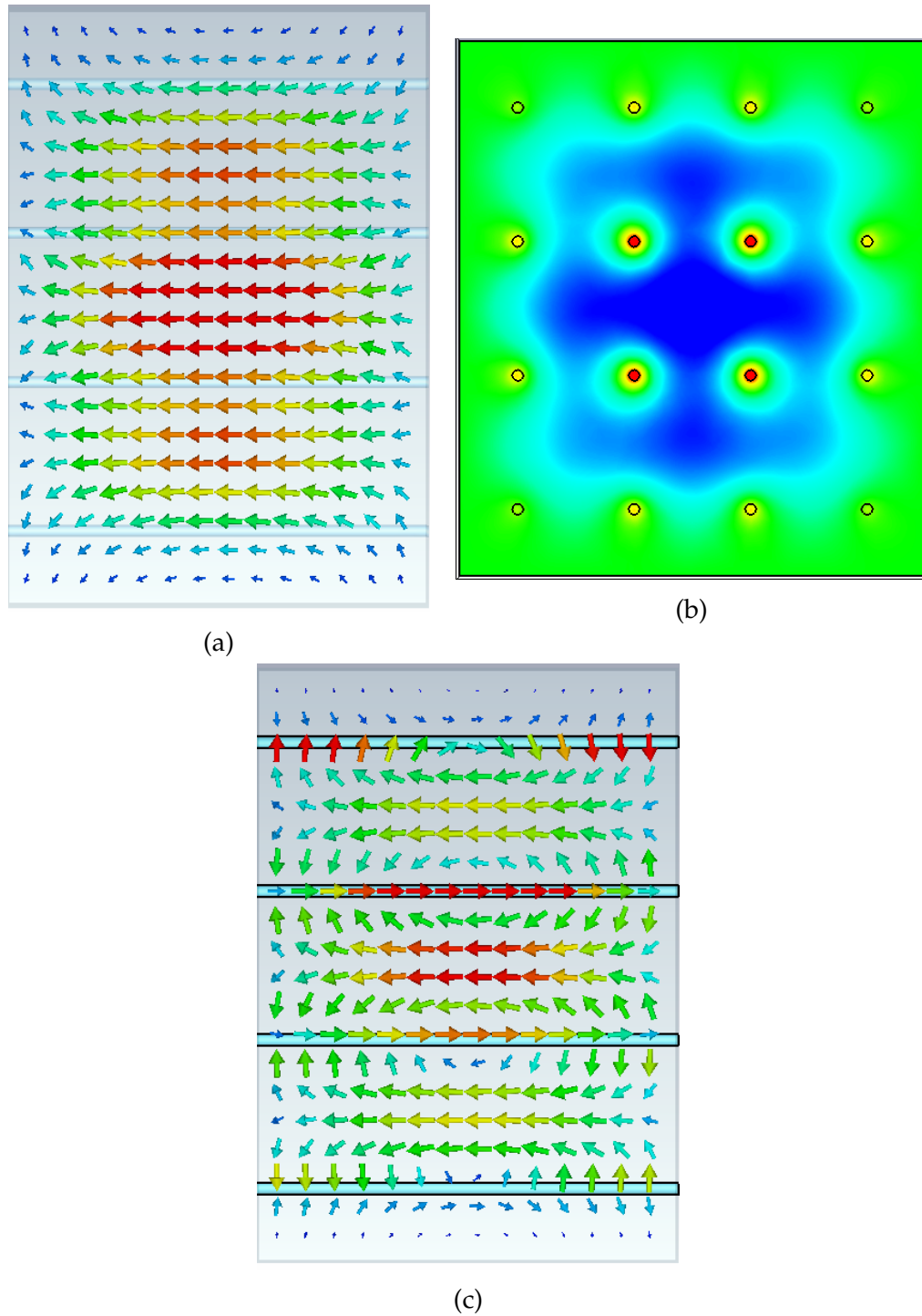
Figure 7.79: Images from numerical simulations in CST showing the longitudinal mode ($f = 10.05$ GHz) found in a partially finite dielectric wire medium (4×4, $\varepsilon_r = 100$, $r = 0.6$ mm, $a_x = 13.06$ mm and $a_y = 15.00$ mm). The fields are either represented using arrow plots where the arrow direction represents field direction and colour represents the magnitude of the field strength, or colour plots where the strength and magnitude of the longitudinal field is represented by colour. (a) shows a y-z slice through the centre of the structure, (b) an x-y slice and (c) a y-z slice through two of the wires.

169

Confirming the existence of modes which resemble our desired modes is important, but it is also important that these modes have the expected dispersion relation. The squared dispersion relation of the mode found for a wire radius of 0.6 mm is shown in Fig. 7.80. This does appear to be a plasma-like dispersion relation, but we can confirm this by plotting f^2 vs κ^2. We have confirmed that this dispersion relation is plasma-like and have also found the associated plasma frequency.
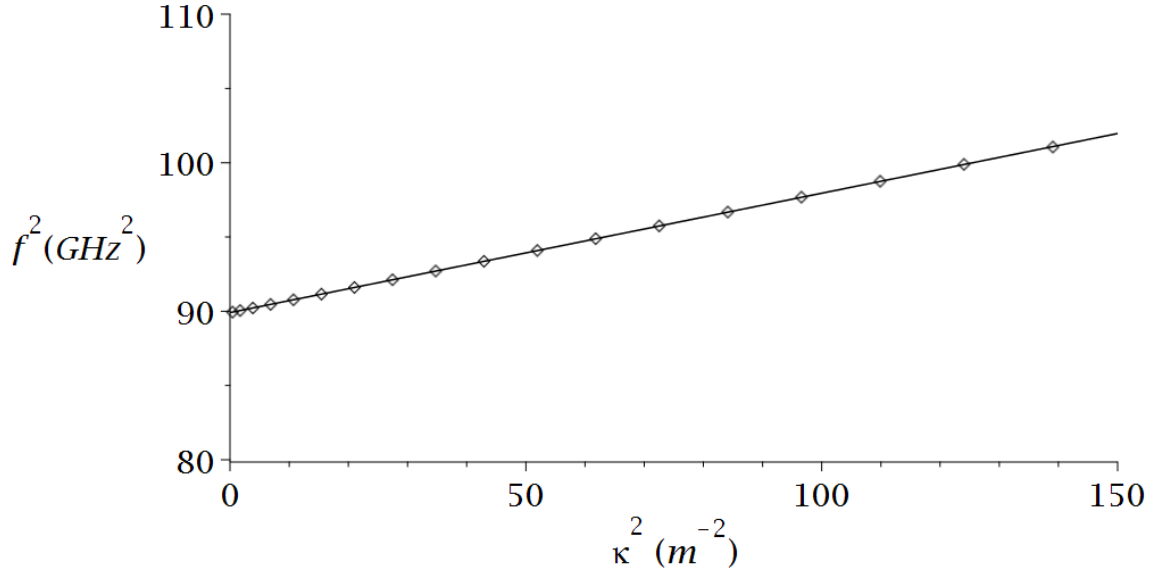
Figure 7.80: A plot of the squared dispersion relation, frequency squared (f^2) against our wavenumber squared (κ^2), of the longitudinal mode in a partially finite dielectric wire medium (4×4, $\varepsilon_r = 100$, $r = 0.6$ mm, $a_x = 13.06$ mm and $a_y = 15.00$ mm) that demonstrates the mode's plasma-like dispersion relation.

Having an analytic expression to link the plasma frequency and the wire radius is vital to our method for mode profile shaping. By repeating the process of finding longitudinal modes and their plasma frequencies for a variety of wire radii we can attempt to find a fit for this data. The data for the relationship between the plasma frequency squared and the wire radius has been plotted in Fig. 7.81. As with our other dielectric wire structures, this relationship is well described by an exponential decay curve. The fitting parameters for this data are $\delta = 72.3$ (GHz^2), $\sigma = 565$ (GHz^2) and $\rho = 0.171$ (mm^{-1}). This fitting curve, like the previous fits, is successful at describing the relationship of the data with an $\mathfrak{R}^2$ value of 0.9998.
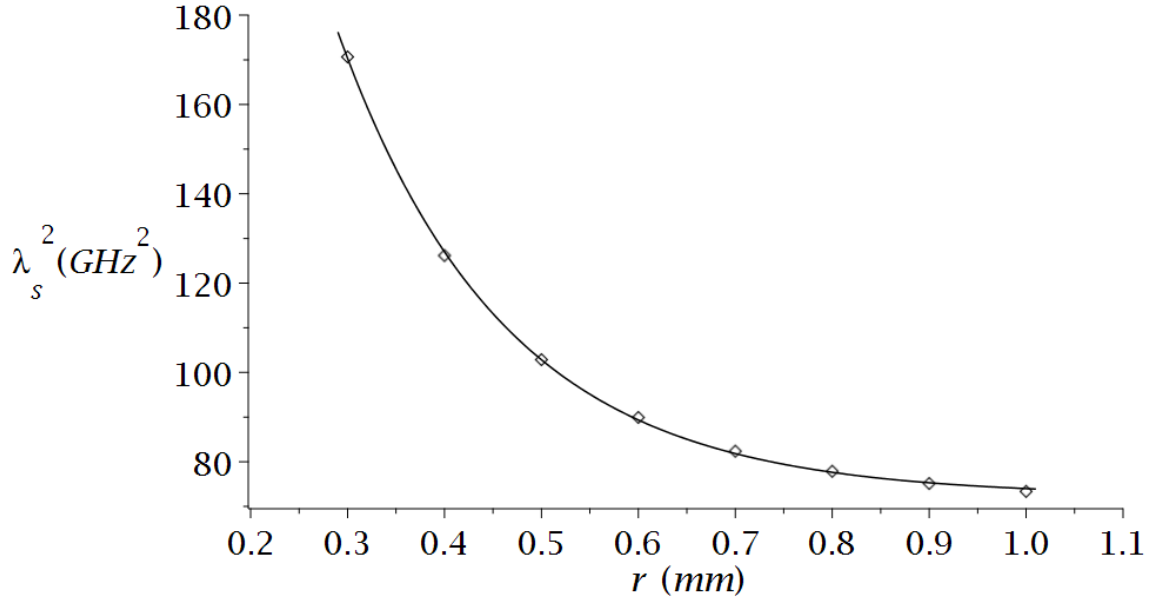
Figure 7.81: A plot of the plasma frequency squared, λ_s^2, of partially finite dielectric wire media (4×4, $\varepsilon_r = 100$, $a_x = 13.06$ mm and $a_y = 15.00$ mm) against wire radius, r, with an exponential decay fitting curve.
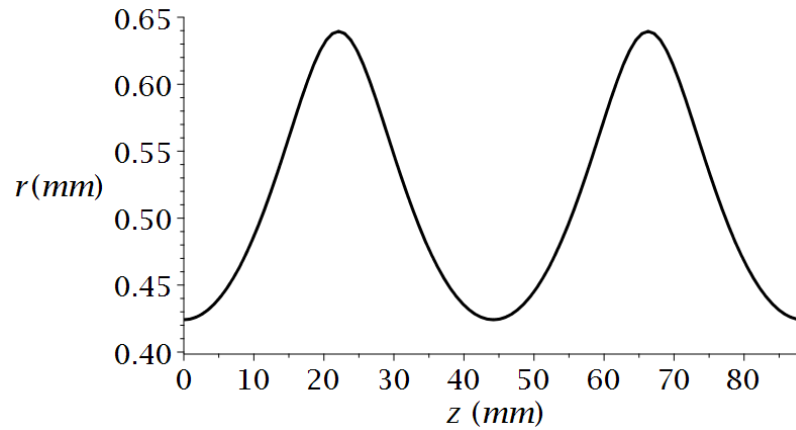
Figure 7.82: Radius function calculated for a flattened profile ($q = 0.8$) in a partially finite dielectric wire medium (4×4, $\varepsilon_r = 100$, $a_x = 13.06$ mm and $a_y = 15.00$ mm) for the parameter choice of $f_d = 11$ GHz, $R_c = 0.5$ mm and $\lambda_C = 10.1$ GHz.

Now that we have an approximate expression relating the plasma frequency and wire radius, we can use our established method to produce a radius function that if implemented, will give us our desired mode profile. Usually, we would attempt to replicate a variety of profiles, but as we have already shown that our mode profiling works for partially finite lattices, it should be sufficient to demonstrate mode profiling for one profile. The profile we have attempted to replicate is the flatter mode profile (Mathieu parameter q=0.8). We have chosen to fix the

parameters $R_C = 0.5$ mm and $f_d = 11$ GHz. Given this choice of profile and fixed parameters, the resulting radius function is plotted in Fig. 7.82, with the following parameter values $\Gamma_1 = 1.71 \cdot 10^{-1}$ (mm), $\Gamma_2 = 5.40 \cdot 10^{-2}$, $\Gamma_3 = 3.01 \cdot 10^{-2}$ and $\Gamma_4 = 1.42 \cdot 10^{-1}$ (mm^{-1}).

By implementing the radius function shown above, we should be able to replicate our desired field profile. We implemented the radius function using a series of conical frustums. Around the frequency range of our design frequency, we observed the longitudinal mode in Fig. 7.83. As we have done previously, we judged this mode to be longitudinal due to our observation in these images of the significant longitudinal component of the electric field at the centre of the structure an the minimal transverse components.

(a)

(b)

(c)
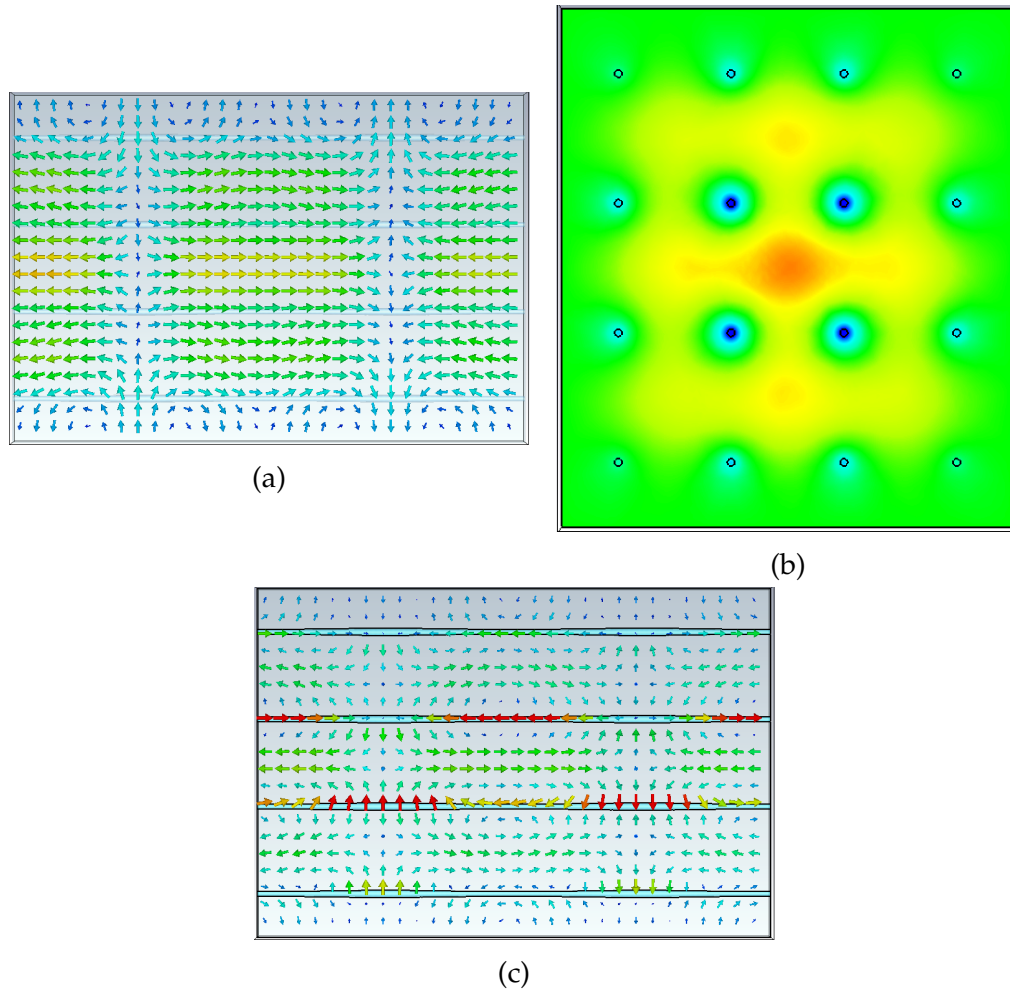
Figure 7.83: Images showing the resulting longitudinal mode ($f = 10.98$ GHz) after the implementation of the calculated radius function for a flattened profile ($q = 0.8$) in a partially finite dielectric wire medium (4×4, $\varepsilon_r = 100$, $a_x = 13.06$ mm and $a_y = 15.00$ mm) for the parameter choice of $f_d = 11$ GHz, $R_c = 0.5$ mm and $\lambda_C = 10.1$ GHz. The fields are either represented using arrow plots where the arrow direction represents field direction and colour represents the magnitude of the field strength, or colour plots where the direction and magnitude of the longitudinal field is represented by colour. (a) shows a y-z slice through the centre of the structure, (b) an x-y slice and (c) a y-z slice through two of the wires.

We evaluated the field along a line through the centre of the structure. Evaluating the field profile along this line gives the profile shown in Fig. 7.84. Our mode profiling attempt has been successful with an $\mathfrak{R}^2$ value of 0.9915.
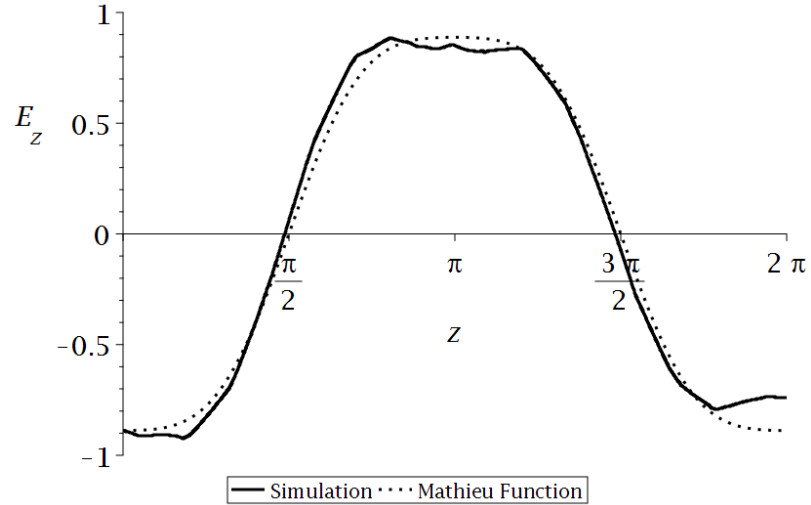
Figure 7.84: Plot of the field profile (longitudinal, z, spatial variation of the electric field strength, E_z) of the longitudinal mode (10.98 GHz) in a partially finite dielectric wire medium (4×4, $\varepsilon_r = 100$, $a_x = 13.06$ mm and $a_y = 15.00$ mm) for our attempt to produce a flattened profile ($q = 0.8$) by the implementation of a radius function based on the choice of $f_d = 11$ GHz, $R_c = 0.5$ mm and $\lambda_C = 10.1$ GHz (black). The plot includes the field profile observed in our numerical simulation (solid) and the desired profile (dotted). In order to compare these the field profile and z coordinate have been normalised.

Having extended our results to a four by four lattice of infinitely long wires in a metallic waveguide, the next step was to attempt to extend our results to a four by four lattice of finite wires in a metallic cavity. This only requires the introduction of metallic boundary conditions on the longitudinal boundaries of our previous unit cells. We can also reuse our plasma frequency data from the previous infinitely long structures and, thus, reuse the required radius functions. We introduced the new boundaries to the structure we have previously used to achieve mode profiling success. After doing this, we were able to find the longitudinal mode shown in Fig. 7.85.

(a)

(b)

(c)
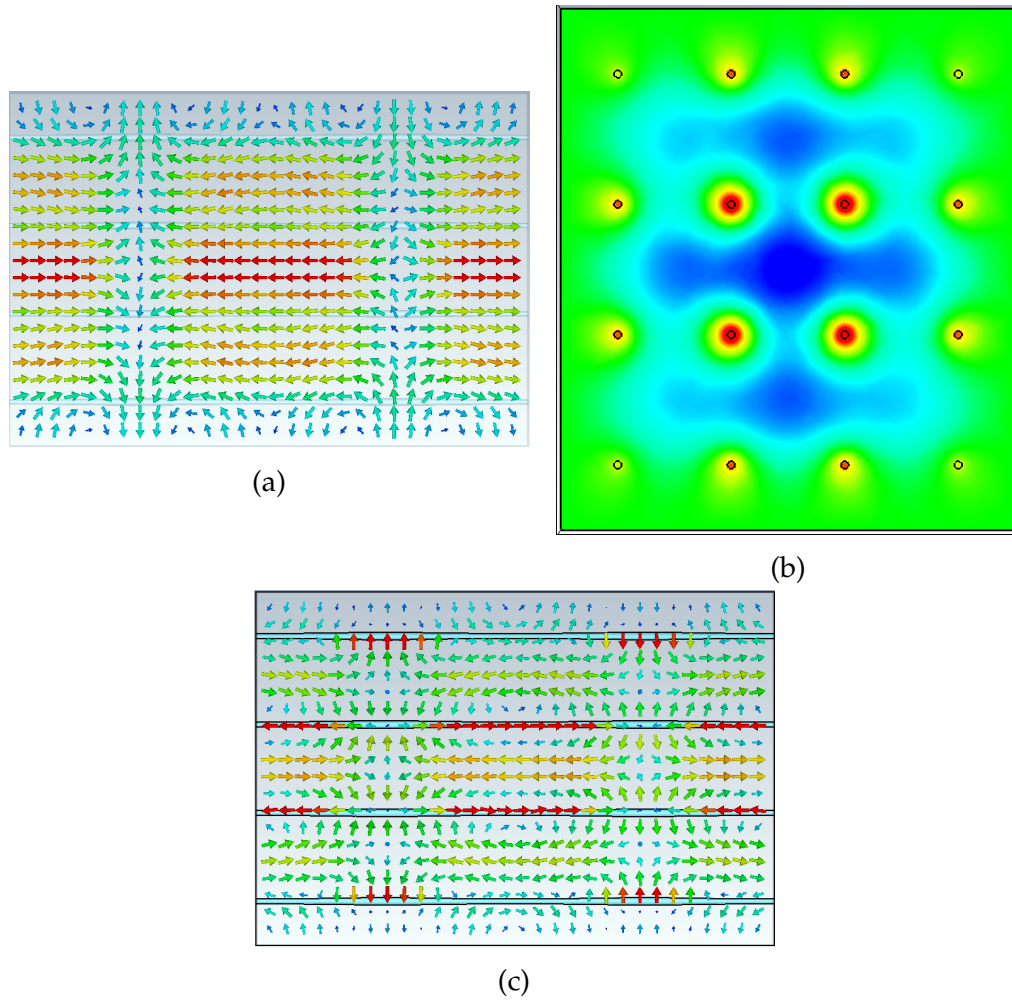
Figure 7.85: Images showing the resulting longitudinal mode ($f = 10.98$ GHz) after the implementation of the calculated radius function for a flattened profile ($q = 0.8$) in a finite dielectric wire medium (4×4, $\varepsilon_r = 100$, $a_x = 13.06$ mm and $a_y = 15.00$ mm) for the parameter choice of $f_d = 11$ GHz, $R_c = 0.5$ mm and $\lambda_C = 10.1$ GHz. The fields are either represented using arrow plots where the arrow direction represents field direction and colour represents the magnitude of the field strength, or colour plots where the direction and magnitude of the longitudinal field is represented by colour. (a) shows a y-z slice through the centre of the structure, (b) an x-y slice and (c) a y-z slice through two of the wires.

Evaluating the field profile in the same way as previously, we find the profile shown in Fig. 7.86. Again, we have been successful in our mode profiling efforts, with an $\mathfrak{R}^2$ value of 0.9935.
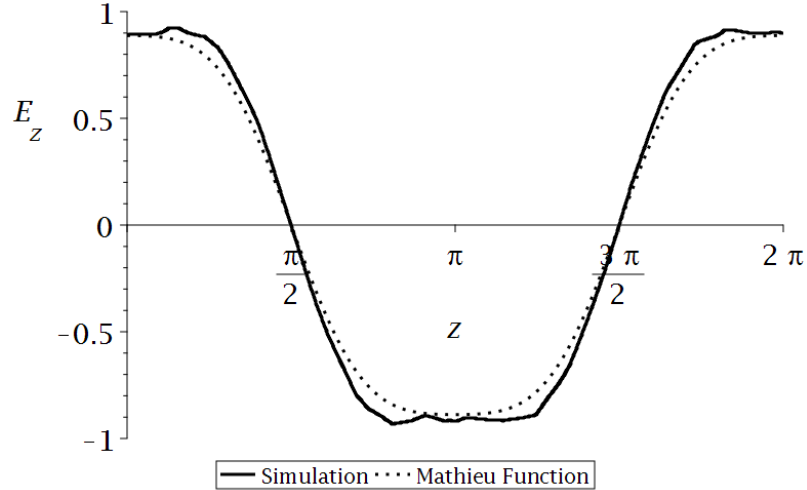
Figure 7.86: Plot of the field profile (longitudinal, z, spatial variation of the electric field strength, E_z) of the longitudinal mode (10.98 GHz) in a finite dielectric wire medium (4×4, $\varepsilon_r = 100$, $a_x = 13.06$ mm and $a_y = 15.00$ mm) for our attempt to produce a flattened profile ($q = 0.8$) by the implementation of a radius function based on the choice of $f_d = 11$ GHz, $R_c = 0.5$ mm and $\lambda_C = 10.1$ GHz (black). The plot includes the field profile observed in our numerical simulation (solid) and the desired profile (dotted). In order to compare these the field profile and z coordinate have been normalised.

The results contained in this section show that our mode profiling method is successful for a four by four lattice of infinite or finite length.

VIII. Introducing disorder into finite wire media

VIII.1 Random errors in the wire radius

Previously, we have studied the effect of introducing disorder to our infinite wire media structures. In that case, any disorder we introduce into a wire will be reproduced across all the wires due to the periodic boundary conditions used. A scenario where the exact same series of errors in the radius of a wire is replicated across all wires is not realistic. Now that we have extended our method to finite structures, we can perform an analysis of the introduction of radius errors to our finite structures.

In the case of a finite structure, we can introduce a different set of randomly generated radius errors for each wire. In all our studies in this section, we have used partially finite structures where the wires are infinitely long, but there are a finite number. The lattices used are all four by four lattices with the transverse boundaries given metallic boundary conditions. As for the case of the infinite structures, the randomly generated radius errors introduced into each segment of

the wire are generated by taking a randomly generated number between -1 and 1, then multiplying it by our tolerance. One of the tolerances we have chosen to use is 0.05 mm. The control structure we have decided to use is based on the choice of parameters $R_c = 0.5$ mm and $f = 11$ GHz. This structure has been shown to produce a flattened mode profile in previous simulations.
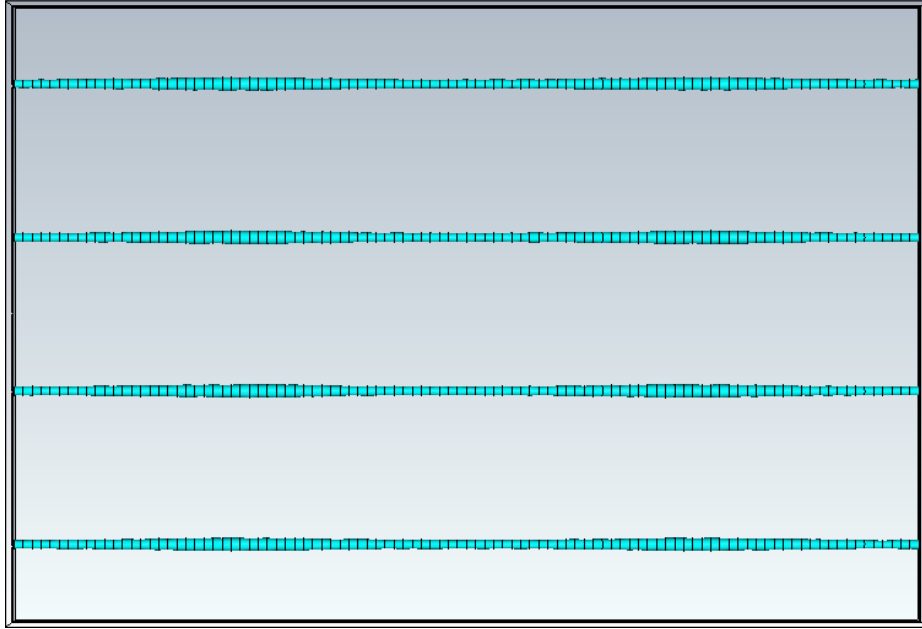
Figure 7.87: A view of the resulting dielectric wire structure for the inclusion of ± 0.05 mm disorder into the radius functions calculated for a flattened profile ($q = 0.8$) in a partially finite dielectric wire medium (4×4, $\varepsilon_r = 100$, $a_x = 13.06$ mm and $a_y = 15.00$ mm) for the parameter choice of $f_d = 11$ GHz, $R_c = 0.5$ mm and $\lambda_C = 10.1$ GHz.

We can get an idea of the effect of introducing this error on the structure from Fig. 7.87 where there are small but noticeable bumps in the wires with the random error introduced. In Fig. 7.88 two of the modified radius functions for the wires in the ± 0.05 mm analysis are shown along with a comparison with the unperturbed radius function from our control case. These plots demonstrate the impact of the introduction of the radius errors and the difference in the errors introduced for each wire.
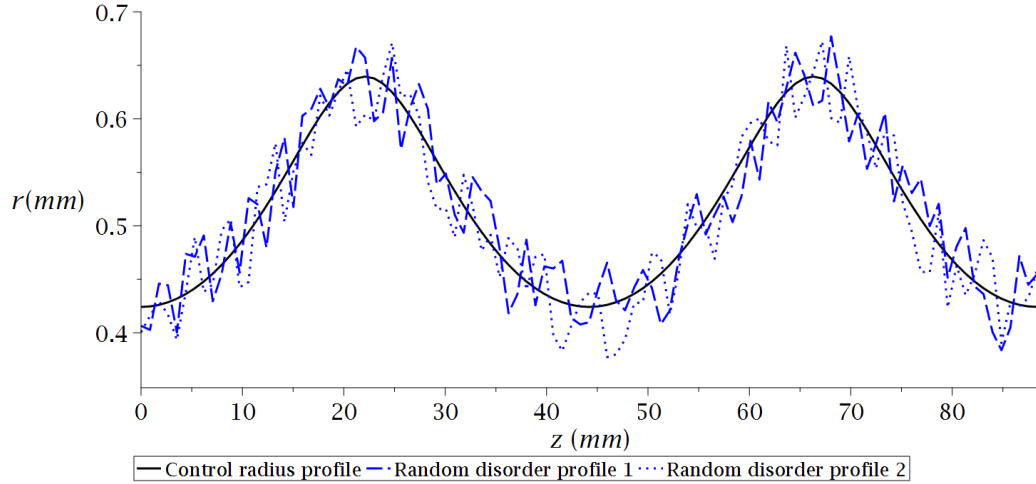
Figure 7.88: A plot of the resulting radius functions when disorder is introduced into our control radius function calculated for a flattened profile ($q = 0.8$) in a partially finite dielectric wire medium (4×4, $\varepsilon_r = 100$, $a_x = 13.06$ mm and $a_y = 15.00$ mm) for the parameter choice of $f_d = 11$ GHz, $R_c = 0.5$ mm and $\lambda_C = 10.1$ GHz. The level of disorder shown is ± 0.05 mm (blue), with two of the radius functions shown (dashed and dotted) to emphasise the different radius variations resulting from the introduction of random disorder in the radius. The original radius function is also shown (black).
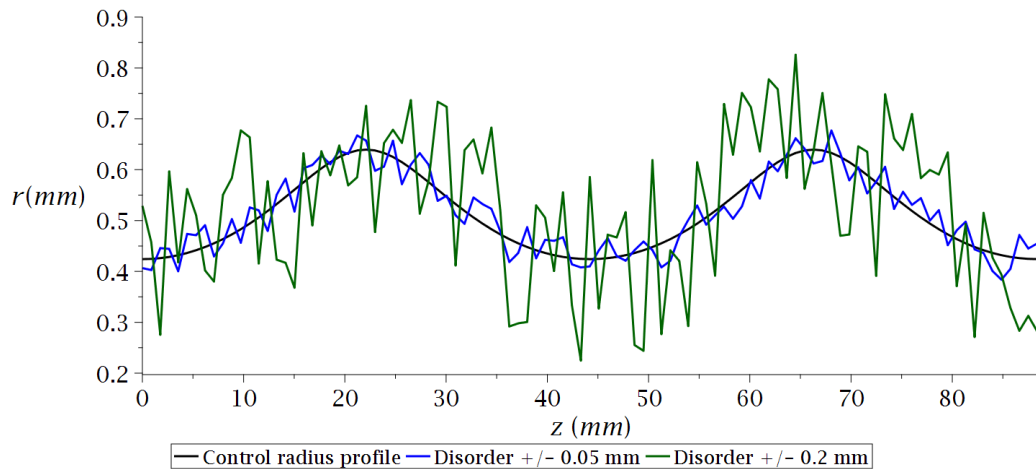
Figure 7.89: A plot of the resulting radius functions when different levels of disorder are introduced into our control radius function calculated for a flattened profile ($q = 0.8$) in a partially finite dielectric wire medium (4×4, $\varepsilon_r = 100$, $a_x = 13.06$ mm and $a_y = 15.00$ mm) for the parameter choice of $f_d = 11$ GHz, $R_c = 0.5$ mm and $\lambda_C = 10.1$ GHz (black). The levels of disorder shown are ± 0.05 mm (blue) and ± 0.2 mm (green).

We also investigated the introduction of radius error with a greater tolerance

of 0.2 mm. An example of a radius function after introducing this disorder is shown in Fig. 7.89 along with a radius function with 0.05 mm tolerance radius error and the original unperturbed radius function.

After producing these perturbed radius functions for each wire for each tolerance, we were able to run simulations to examine the effect of these changes. The field profiles found in these simulations are shown in Figs. 7.90 and 7.91. For the case of the smaller tolerance of 0.05 mm, we can see that the field profiling is still quite successful, with an $\mathfrak{R}^2$ value of 0.9677. As we might expect, when the error tolerance is increased to 0.2 mm, the field profiling attempt breaks down, as shown in Fig. 7.91.
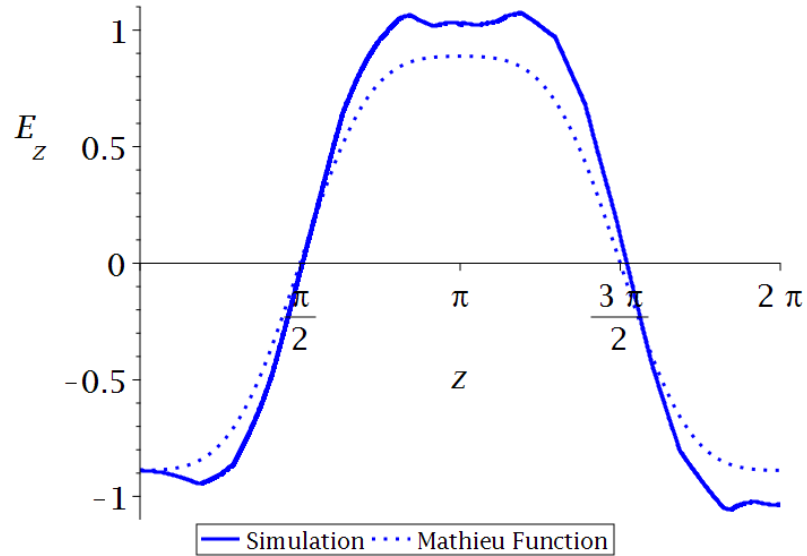
Figure 7.90: Plot showing the field profile of the longitudinal mode ($f = 11.01$ GHz) when disorder of the order ± 0.05 mm is introduced into our control radius function for a flattened profile ($q = 0.8$) in a partially finite dielectric wire medium (4×4, $\varepsilon_r = 100$, $a_x = 13.06$ mm and $a_y = 15.00$ mm) for the parameter choice of $f_d = 11$ GHz, $R_c = 0.5$ mm and $\lambda_C = 10.1$ GHz (blue).
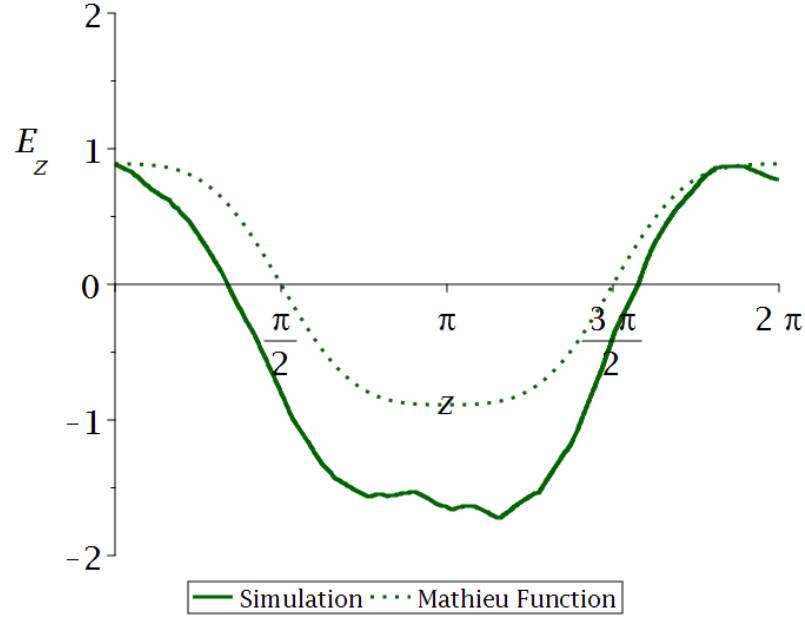
Figure 7.91: Plot showing the field profile of the longitudinal mode ($f = 11.13$ GHz) when disorder of the order ± 0.2 mm is introduced into our control radius function for a flattened profile ($q = 0.8$) in a partially finite dielectric wire medium (4×4, $\varepsilon_r = 100$, $a_x = 13.06$ mm and $a_y = 15.00$ mm) for the parameter choice of $f_d = 11$ GHz, $R_c = 0.5$ mm and $\lambda_C = 10.1$ GHz (blue).

We can conclude that based on our simulations, we would expect our method to be robust to fabrication errors on the order of 0.05 mm. This should be an acceptable level of tolerance. We have already discussed the advantages of this method of analysing the effect of radius errors, the fact that it is far more realistic, but it has the downside of being more time consuming to carry out and taxing for the software involved. In particular, the small variations in the segments of our wires proved to be especially challenging to mesh. These problems are the reason we have limited our analysis to just two different tolerances. Ideally, we would have explored in more detail at what level of error tolerance the field profiling breaks down. Also, it would have been useful to try many different ensembles of disordered radius functions for each tolerance rather than just one.

VIII.2 Random errors in the wire positions

Another area of potential disorder in our structure is the placement of the wires. It was not possible to properly study this in the infinite case. As we had purely periodic boundary conditions, a shift in the wire position would not change the relative positions of all the wires in the effective lattice. All that would be achieved is that if the position of field evaluation were kept constant it would effectively be observing the field at different positions as the wire shifted. We have already

180

studied the effect of evaluation position on field profiling, so it made no sense to carry out a further study on the same effect.

In the case of a partially finite lattice, if we randomly shift the position of each of the wires their relative positions will be changed. Similar to our exploration of radius errors, we have introduced random errors in the position of our wires by generating a series of random numbers between -1 and 1. In this case, we generate two numbers per wire. The first number is multiplied by $\frac{Ta_x}{\sqrt{2}}$ and the second by $\frac{Ta_y}{\sqrt{2}}$, with T being a tolerance parameter, to produce our shifts in the x and y dimensions respectively. In our study we have examined a variety of magnitudes of position error characterised by T values of $T = 0.01, 0.05, 0.1, 0.2$. The resulting structure caused by the introduction of the greatest level of disorder, $T = 0.2$, is shown in Fig. 7.92.
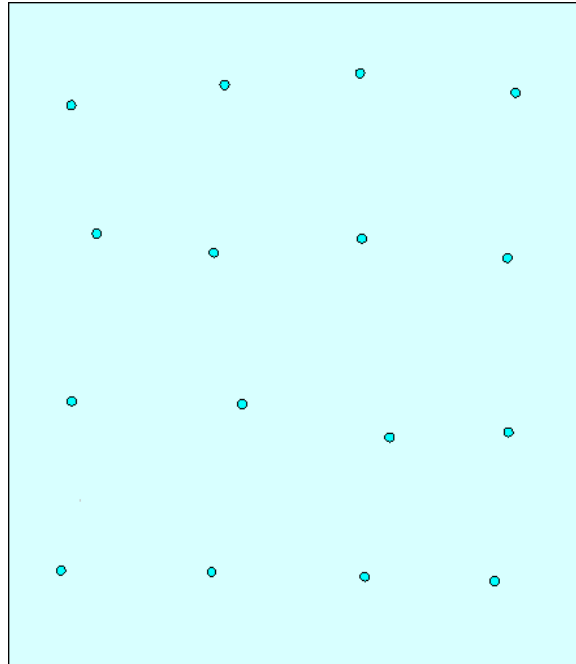
Figure 7.92: A view of the resulting dielectric wire structure for the inclusion of disorder of the order $\pm \frac{0.2}{\sqrt{2}} a_i$ mm ($i = x, y$) into the position of the dielectric wires with a radius function calculated for a flattened profile ($q = 0.8$) in a partially finite dielectric wire medium (4×4, $\varepsilon_r = 100$, $a_x = 13.06$ mm and $a_y = 15.00$ mm) for the parameter choice of $f_d = 11$ GHz, $R_c = 0.5$ mm and $\lambda_C = 10.1$ GHz.

The field profiles resulting from these structures are shown in Figs. 7.93-7.96.
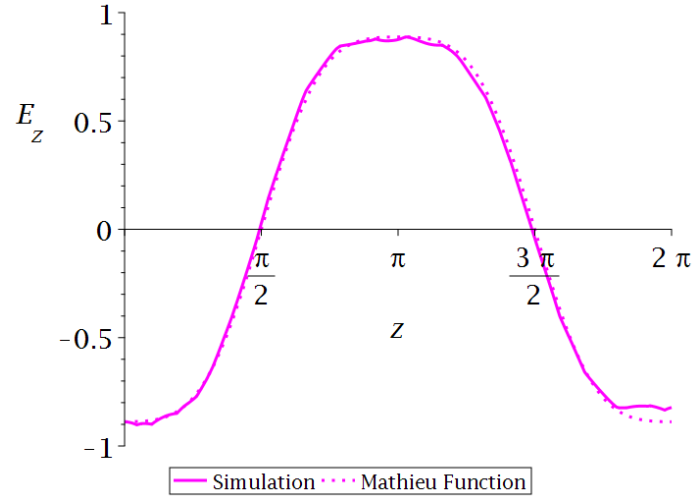
Figure 7.93: Plot showing the field profile of the longitudinal mode ($f = 10.99$ GHz) when disorder of the order $\pm\frac{0.01}{\sqrt{2}}a_i$ mm ($i = x, y$) is introduced into the position of the dielectric wires with a radius function for a flattened profile ($q = 0.8$) in a partially finite dielectric wire medium (4×4, $\varepsilon_r = 100$, $a_x = 13.06$ mm and $a_y = 15.00$ mm) for the parameter choice of $f_d = 11$ GHz, $R_c = 0.5$ mm and $\lambda_C = 10.1$ GHz (magenta).
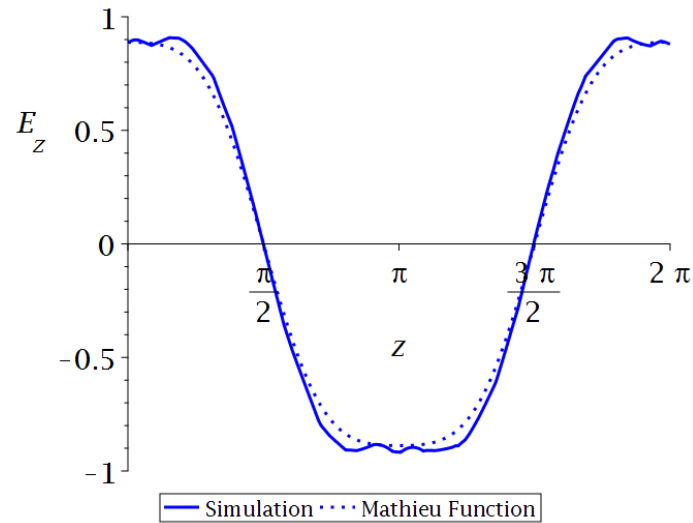
Figure 7.94: Plot showing the field profile of the longitudinal mode ($f = 10.97$ GHz) when disorder of the order $\pm\frac{0.05}{\sqrt{2}}a_i$ mm ($i = x, y$) is introduced into the position of the dielectric wires with a radius function for a flattened profile ($q = 0.8$) in a partially finite dielectric wire medium (4×4, $\varepsilon_r = 100$, $a_x = 13.06$ mm and $a_y = 15.00$ mm) for the parameter choice of $f_d = 11$ GHz, $R_c = 0.5$ mm and $\lambda_C = 10.1$ GHz (blue).

182
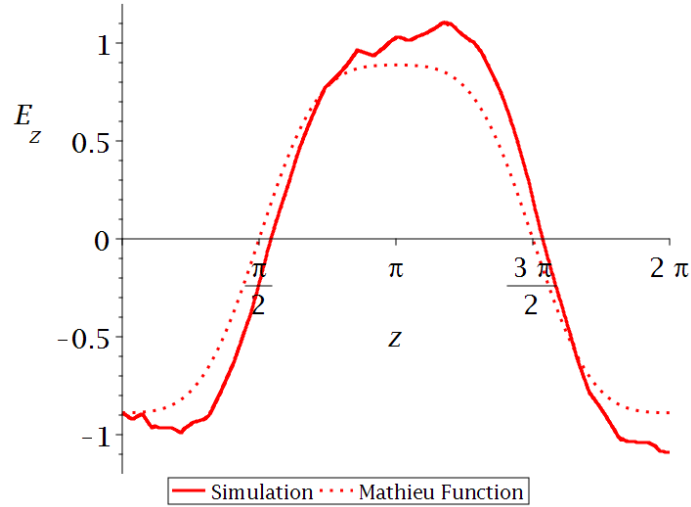
Figure 7.95: Plot showing the field profile of the longitudinal mode ($f = 10.92$ GHz) when disorder of the order $\pm \frac{0.1}{\sqrt{2}} a_i$ mm ($i = x, y$) is introduced into the position of the dielectric wires with a radius function for a flattened profile ($q = 0.8$) in a partially finite dielectric wire medium (4×4, $\varepsilon_r = 100$, $a_x = 13.06$ mm and $a_y = 15.00$ mm) for the parameter choice of $f_d = 11$ GHz, $R_c = 0.5$ mm and $\lambda_C = 10.1$ GHz (red).
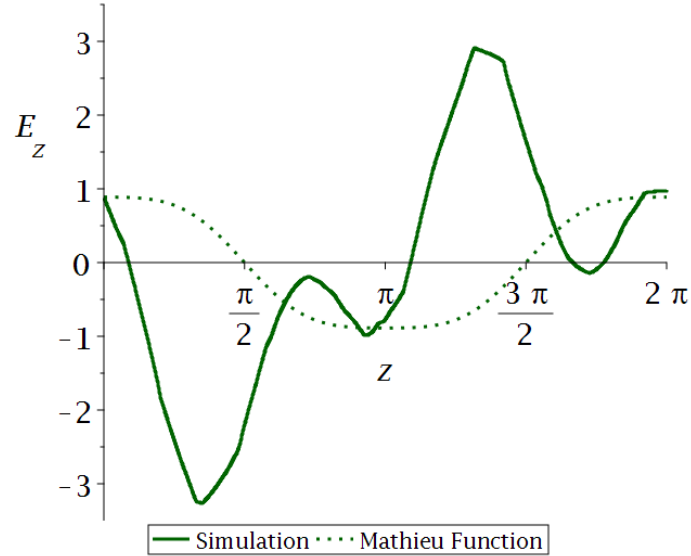
Figure 7.96: Plot showing the field profile of the longitudinal mode ($f = 10.92$ GHz) when disorder of the order $\pm \frac{0.2}{\sqrt{2}} a_i$ mm ($i = x, y$) is introduced into the position of the dielectric wires with a radius function for a flattened profile ($q = 0.8$) in a partially finite dielectric wire medium (4×4, $\varepsilon_r = 100$, $a_x = 13.06$ mm and $a_y = 15.00$ mm) for the parameter choice of $f_d = 11$ GHz, $R_c = 0.5$ mm and $\lambda_C = 10.1$ GHz (blue).

183

We can see from these profiles that the structures field profiling remains very consistent for $T = 0.01$ and $T = 0.05$. There is some noticeable deterioration at $T = 0.1$ and a complete collapse for $T = 0.2$. These results are summarised in Table 7.11 along with the $\mathfrak{R}^2$ value for each plot. We can conclude from this analysis that our results can cope with a position error of 5% of the lattice parameters in each dimension, with some clear deterioration when approaching a position error of 10%. Similar to our analysis of random radius, this analysis could have been improved by trying more ensembles of disorder for each tolerance.

T	f (GHz)	$\mathfrak{R}^2$
0	10.98	0.9806
0.01	10.99	0.9983
0.05	10.97	0.9960
0.1	10.92	0.9559
0.2	10.92	-0.4125

Table 7.11: Table summarising the results of the implementation of radius functions when different levels of disorder are introduced into the position of the dielectric wire with a radius function calculated for a flattened profile ($q = 0.8$) in a partially finite dielectric wire medium ($\varepsilon_r = 50$, $a_x = 13.06$ mm and $a_y = 15.00$ mm) for the parameter choice of $f_d = 11$ GHz, $R_c = 0.5$ mm and $\lambda_C = 10.1$ GHz. The parameters listed are: the level of disorder introduced (T), longitudinal mode frequency (f) and a figure of merit for the agreement between our field profile and the desired profile ($\mathfrak{R}^2$).

VIII.3   Coordinated shift in the wire positions

As well as considering random errors, we have examined a coordinated error in the position of the rods. We have considered a collective movement of all the wires either closer together or further away from each other. The lattice becomes either sparser or denser.

We have made these changes by introducing a scaling constant ξ, which is used to shift the position of each wire relative to the centre of the structure while the boundaries remain unchanged. This effectively represents a shifting in the lattice parameters of the wire medium and a change in the position of the boundaries. When the lattice is made denser it represents a wire medium with smaller lattice constants and boundaries that are placed further away.

We have run simulations for a variety of different ξ values. The frequency of the longitudinal modes for these values are shown in Fig. 7.98. The data shown fits an exponential decay curve well, although it should be noted that ξ values outside this range were simulated but it became difficult to identify comparable longitudinal modes.
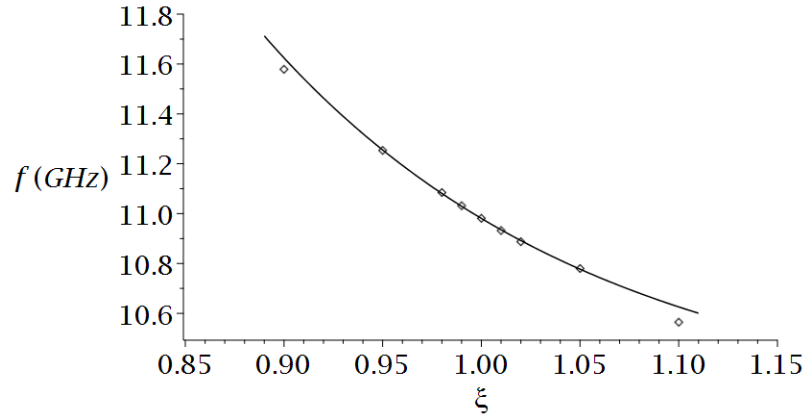
Figure 7.97: A plot of the longitudinal mode frequency, f, found in a modified partially finite dielectric wire medium (4×4, $\varepsilon_r = 100$, $a_x = 13.06$ mm and $a_y = 15.00$ mm) with a radius function calculated for a flattened profile ($q = 0.8$) for the parameter choice of $f_d = 11$ GHz, $R_c = 0.5$ mm and $\lambda_C = 10.1$ GHz, against the parameter ξ. The dielectric wire medium has been modified by scaling the position of the dielectric wires ($X \cdot a_x$, $Y \cdot a_y$), where X and Y are integers, relative to the centre of the structure by the factor ξ. An exponential fitting curve has also been included (black).
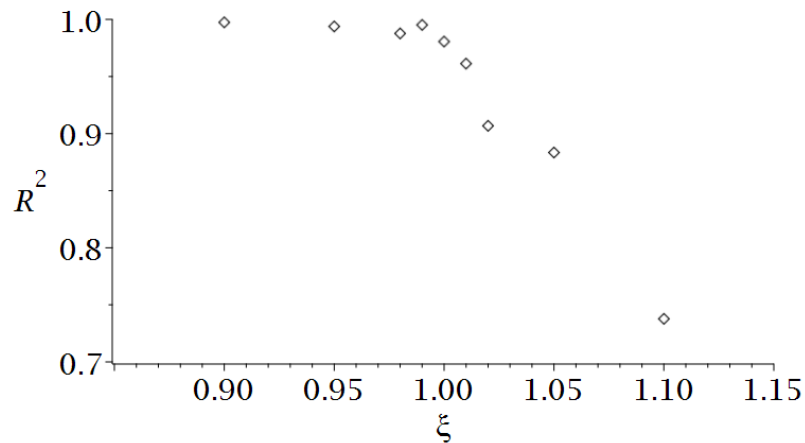
Figure 7.98: A plot of a figure of merit for the agreement between our desired profile and the longitudinal mode profile ($\mathfrak{R}^2$) found in a modified partially finite dielectric wire medium (4×4, $\varepsilon_r = 100$, $a_x = 13.06$ mm and $a_y = 15.00$ mm) with a radius function calculated for a flattened profile ($q = 0.8$) for the parameter choice of $f_d = 11$ GHz, $R_c = 0.5$ mm and $\lambda_C = 10.1$ GHz, against the parameter ξ. The dielectric wire medium has been modified by scaling the position of the dielectric wires ($X \cdot a_x$, $Y \cdot a_y$), where X and Y are integers, relative to the centre of the structure by the factor ξ.

The $\mathfrak{R}^2$ values for the longitudinal modes at these ξ values are shown in Fig.

185

7.98. The graph shows an asymmetric response to the introduction of our coordinated disorder. For $\tilde{\xi} < 1$, which leads to a denser lattice, the effects on the field profiling appears to be minimal, whereas shifts where $\tilde{\xi} > 1$ cause a serious deterioration in the quality of the field profiling. This is understandable as sparser lattices have rods which are closer to the distorting effects of the metallic boundaries. A sample of a few of the resulting field profiles from these coordinated shifts in wire position are shown in Figs. 7.99-7.101.
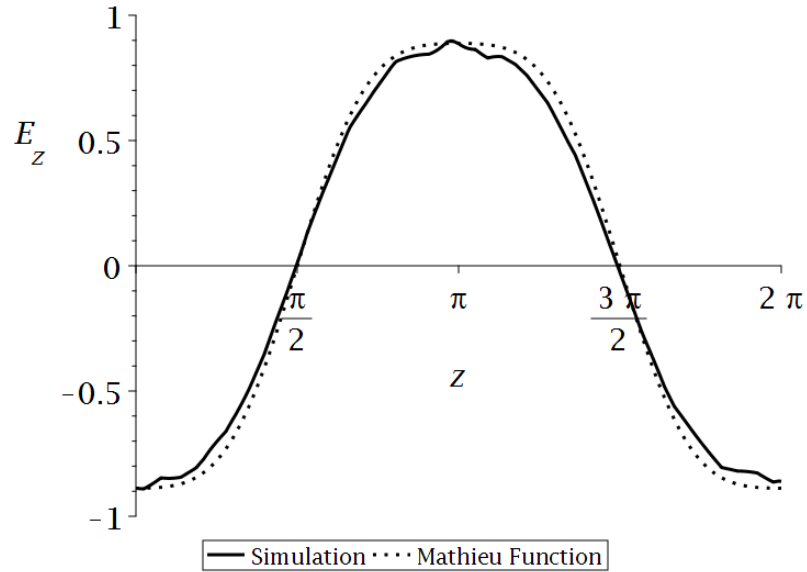
Figure 7.99: Plot showing the field profile of the longitudinal mode ($f = 11.25$ GHz) in a modified partially finite dielectric wire medium ($\tilde{\xi} = 0.95$, 4×4, $\varepsilon_r = 100$, $a_x = 13.06$ mm and $a_y = 15.00$ mm) with a radius function for a flattened profile ($q = 0.8$) for the parameter choice of $f_d = 11$ GHz, $R_c = 0.5$ mm and $\lambda_C = 10.1$ GHz.
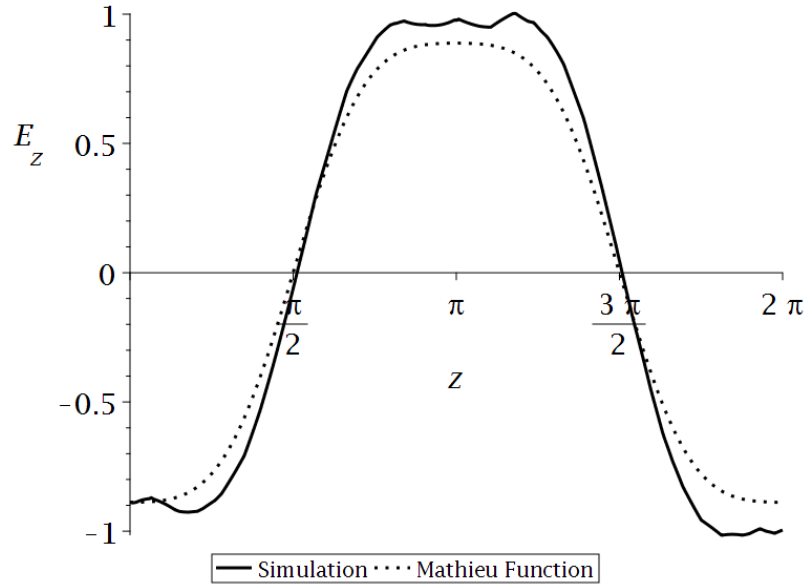
Figure 7.100: Plot showing the field profile of the longitudinal mode ($f = 10.98$ GHz) in an unmodified partially finite dielectric wire medium ($\xi = 1$, 4×4, $\varepsilon_r = 100$, $a_x = 13.06$ mm and $a_y = 15.00$ mm) with a radius function for a flattened profile ($q = 0.8$) for the parameter choice of $f_d = 11$ GHz, $R_c = 0.5$ mm and $\lambda_C = 10.1$ GHz.
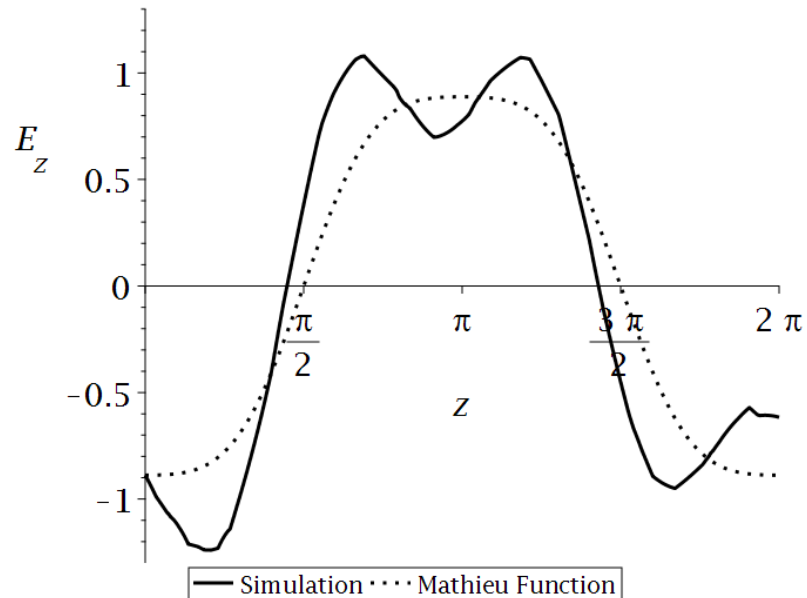
Figure 7.101: Plot showing the field profile of the longitudinal mode ($f = 10.77$ GHz) in a modified partially finite dielectric wire medium ($\xi = 1.05$, 4×4, $\varepsilon_r = 100$, $a_x = 13.06$ mm and $a_y = 15.00$ mm) with a radius function for a flattened profile ($q = 0.8$) for the parameter choice of $f_d = 11$ GHz, $R_c = 0.5$ mm and $\lambda_C = 10.1$ GHz.

187

IX.1   Observing field profiling in a time domain simulation

One more area in which we wanted to reassure ourselves is our ability to excite our structures. All our previous work has been based on eigenmode simulations which shows us that our modes are valid solutions. We will now investigate whether it is possible to excite our desired longitudinal electric modes in our structures.

The structure we are using in our time domain simulations is based on one of the finite structures that was able to achieve field profile shaping. This structure is a four by four lattice with the wire variation produced using the parameters $R_c = 0.5$ and $f_d = 11$ GHz for a flattened profile (q=0.8). This wire variation is plotted in Fig. 7.102. It should be noted that the radius variation shown contains only a single period. A full unit cell of our structures has two periods of the wire variation, but now we are only using a half structure. This was done in an attempt to increase the speed of our simulations. Accordingly, using a half structure, we would only expect to produce half a period of our desired profile.
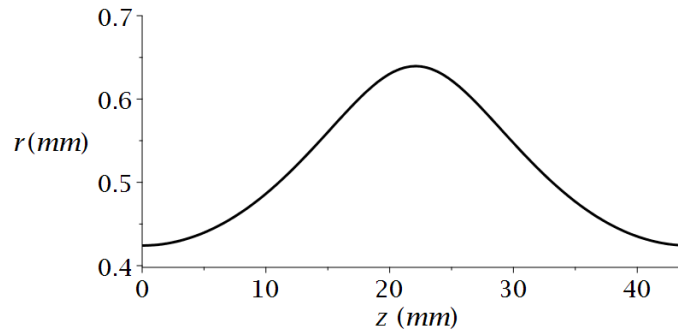
Figure 7.102: A single period of the radius function calculated for a flattened profile ($q = 0.8$) in a finite dielectric wire medium (4×4, $\varepsilon_r = 100$, $a_x = 13.06$ mm and $a_y = 15.00$ mm) for the parameter choice of $f_d = 11$ GHz, $R_c = 0.5$ mm and $\lambda_C = 10.1$ GHz. This is the wire radius variation used in the following time domain simulations, although the lattice configurations used differ from the basis of the calculated function.
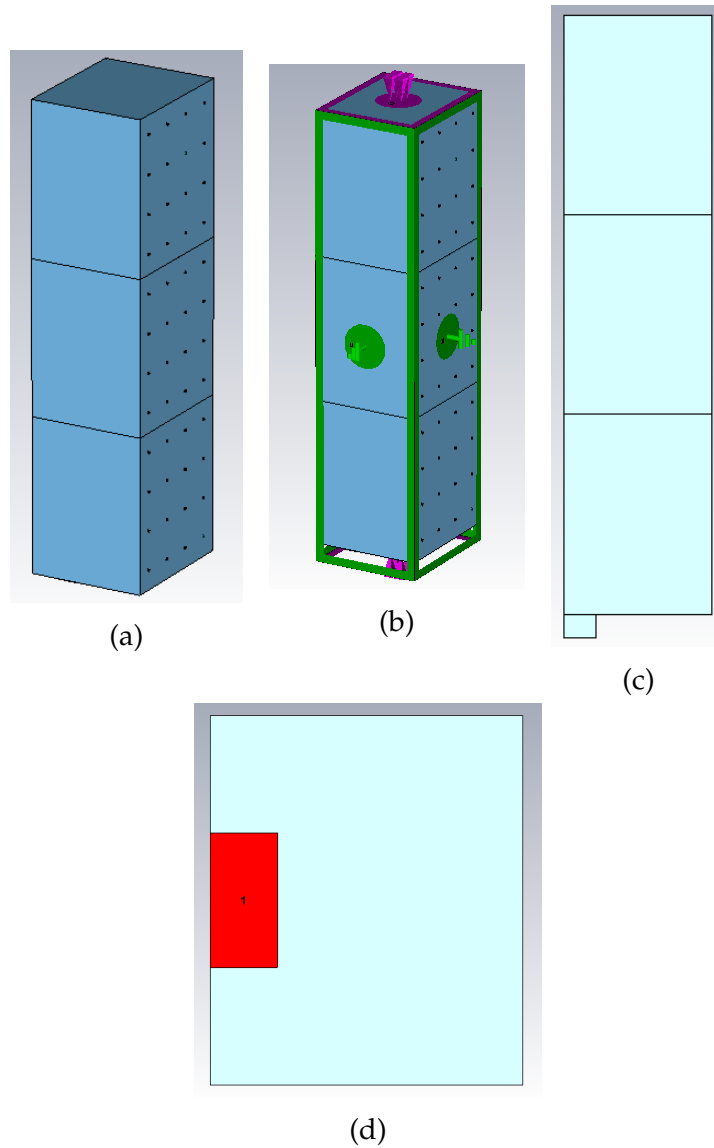
Figure 7.103: A representation of a finite wire medium in CST, consisting of three vertically stacked units of four by four lattices of dielectric wires. The unit cell has one set of metallic transverse boundary conditions, one set of open transverse boundary conditions and metallic longitudinal boundary conditions. The dielectric wires have a radius function calculated for a flattened profile ($q = 0.8$) in a partially finite dielectric wire medium (4×4, $\varepsilon_r = 100$, $a_x = 13.06$ mm and $a_y = 15.00$ mm) for the parameter choice of $f_d = 11$ GHz, $R_c = 0.5$ mm and $\lambda_C = 10.1$ GHz. A small section has been attached to the bottom of the structure with dimensions $x_{dim} = 19$ mm, $y_{dim} = 10$ mm and $z_{dim} = 9.5$ mm, where a waveguide port has been placed. (a) shows a perspective the unit cell of the structure in CST; (b) shows the boundaries of the structure with green representing metallic boundaries and purple, open boundary conditions; (c) shows a side view of the structure in CST, where the extra section can be more clearly seen; and (d) a view of the structure from below with the waveguide port shown in red.

The structure we have used is formed by taking the unit cell from these finite simulations and introducing two transformed copies of the unit cell, to form a structure with three of these unit cells stacked on top of each other. This creates a four by twelve lattice of wires which can be seen in Fig 7.103a. The decision to use three unit cells was motivated by the experience we had with other periodic structures [216]. The boundaries of this structure are all metallic, apart from the top and the bottom of the structure which were given open boundaries as illustrated in 7.103b. In addition to our usual lattice structure, we included an extra section that with the set boundary conditions acts as a waveguide attached to the bottom of the structure. This section can be seen more clearly in Fig. 7.103c. Attached to the bottom of this section is the waveguide port through which CST allows us to excite our structure, which is shown in Fig. 7.103d.

Having set up our structure, we defined the excitation signal we will use. CST allows the user to define a frequency range that can be used to generate a default excitation signal. Given that the basis unit cells were designed to support field profiling for a mode at 11 GHz, we chose a frequency range of 10.5-11.5 GHz. The resulting excitation signal, which was used, is shown in Fig. 7.104.
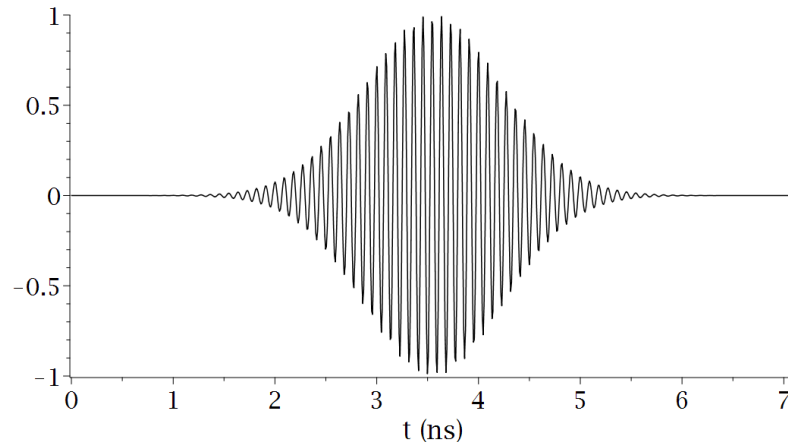
Figure 7.104: The default excitation signal generated by CST for a choice of frequency range of 10.5-11.5 GHz. This is the signal we will use to excite a finite dielectric wire medium structure (3 units of 4×4; $\varepsilon_r = 100$, $a_x = 13.06$ mm and $a_y = 15.00$ mm; $q = 0.8$, $f_d = 11$ GHz, $R_c = 0.5$ mm and $\lambda_C = 10.1$ GHz; open y boundaries, and metallic x and z boundaries; and a waveguide port, which is distanced 10 mm from the lattice, with dimension 19×9.5 mm).

At this stage, CST can be used to calculate port modes. These are the modes supported by our waveguide port which can be used to excite our structure. We used the fundamental mode shown in Fig. 7.105. It was important that the electric field of our port mode was directed along the wire. This meant choosing a waveguide port position which meant that the propagation of the excitation will be transverse to the wire direction.
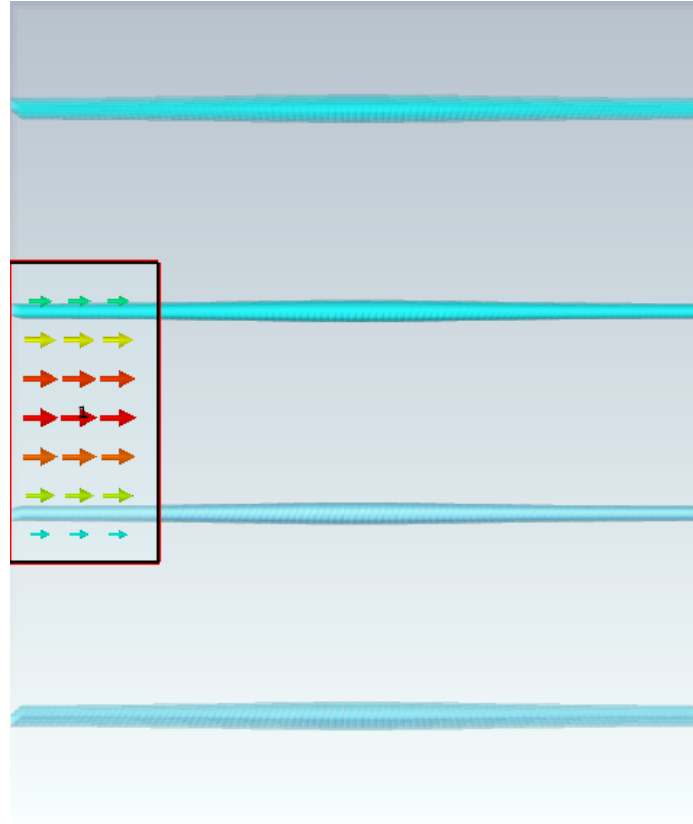
Figure 7.105: The fundamental port mode found for our chosen waveguide port (19×9.5 mm). The field is represented using an arrow plots on the surface of the waveguide port. This is the mode we will use to excite a finite dielectric wire medium structure (3 units of 4×4; $\varepsilon_r = 100$, $a_x = 13.06$ mm and $a_y = 15.00$ mm; $q = 0.8$, $f_d = 11$ GHz, $R_c = 0.5$ mm and $\lambda_C = 10.1$ GHz; open y boundaries, and metallic x and z boundaries; and a waveguide port, which is distanced 10 mm from the lattice, with dimension 19×9.5 mm).

With a chosen port mode it is possible to run a time domain simulation. Time domain simulations simulate the evolution of an excitation until an end point is reached which is set either in terms of the achievement of a minimum energy or a maximum time. This means that it will simulate the excitation of the structure until a set minimum energy level is hit after the initial increase of energy due to the excitation or until a maximum time has elapsed. Our energy limit was set at -30 dB, but usually the maximum time setting was the limiting factor. For these simulations, we set a time limit of t=200 ns. This is shown in Fig. 7.106 where the evolution of the system energy is plotted.
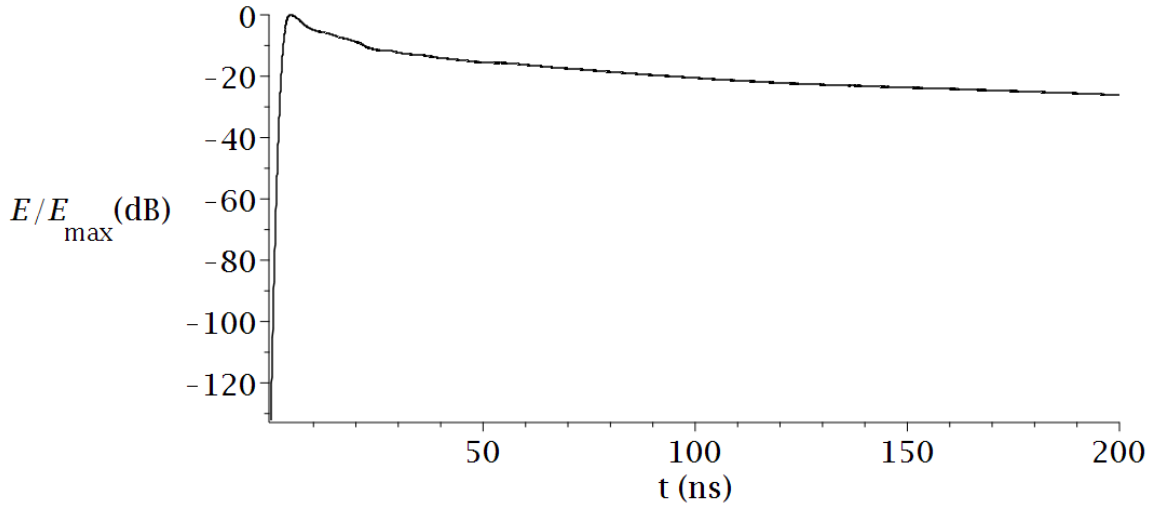
Figure 7.106: A plot of the energy (E) of a finite dielectric wire medium structure (3 units of 4×4; ε_r, $a_x = 13.06$ mm and $a_y = 15.00$ mm; $q = 0.8$, $f_d = 11$ GHz, $R_c = 0.5$ mm and $\lambda_C = 10.1$ GHz; open y boundaries, and metallic x and z boundaries; and a waveguide port, which is distanced 10 mm from the lattice, with dimension 19×9.5 mm) against time (t).

When these simulations have finished, CST produces s-parameter plots for the excitation. S-parameters communicate the reflection or transmittance of a field through a structure. We are interested in the S_{11} parameter which denotes the reflection of the excitation. In Fig. 7.107 the S parameter plot for the frequency range examined is shown, with coloured squares used to mark frequencies at which we have examined the fields produced. Despite producing this S_{11} plot, it became clear that due to various considerations we have not examined in detail, we cannot make a clear judgement on the quality of transmission at a given frequency. This is an area of improvement in our time domain analysis that we would have liked to address given more time. A more full analysis would consider the S_{21} parameter, the transmission parameter, and phases.
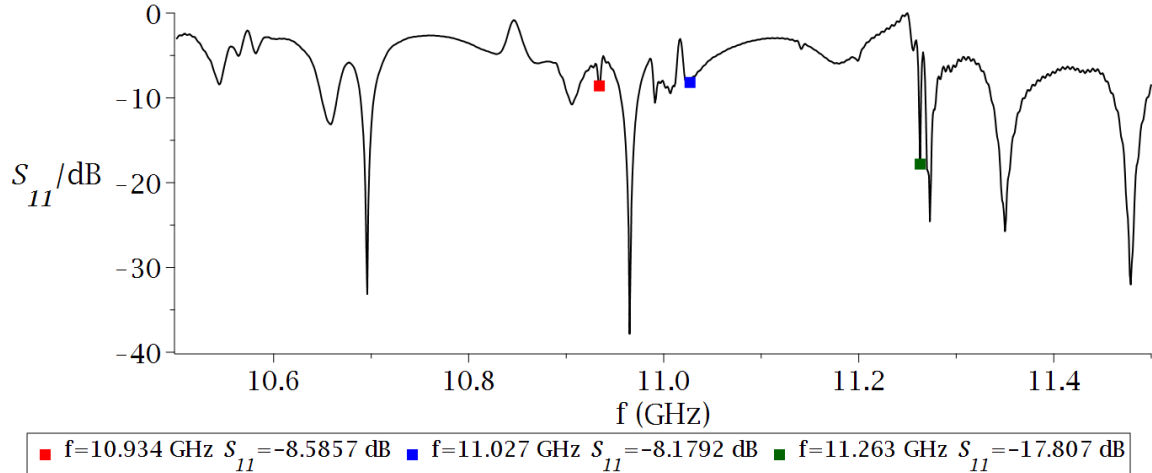
Figure 7.107: A plot of the S_{11} parameter, representing the energy remaining at the waveguide port, against the field frequency (f) for a finite dielectric wire medium structure (3 units of 4×4; $\varepsilon_r = 100$, $a_x = 13.06$ mm and $a_y = 15.00$ mm; $q = 0.8$, $f_d = 11$ GHz, $R_c = 0.5$ mm and $\lambda_C = 10.1$ GHz; open y boundaries, and metallic y and z boundaries; and a waveguide port, which is distanced 10 mm from the lattice, with dimension 19×9.5 mm) with $t = 200$ ns. Coloured squares have been included to represent some of the frequency monitors included in our simulation and the S_{11} parameter at that frequency: red ($f = 10.934$ GHz, $S_{11} = -8.5857$ dB), blue ($f = 11.027$ GHz, $S_{11} = -8.1792$ dB) and green ($f = 11.263$ GHz, $S_{11} = -17.807$ dB).

Field monitors introduced into our CST simulations allow us to look at the fields supported at particular frequencies. Fig. 7.108 shows logarithmic colour plots of some of the fields at frequencies we have examined. All of these fields show a significant longitudinal component and, qualitatively, have a longitudinal profile that we would expect. Given only half a period of the flattened profile should be supported, we would expect a variation from a high negative longitudinal field to a high positive longitudinal field or vice versa.
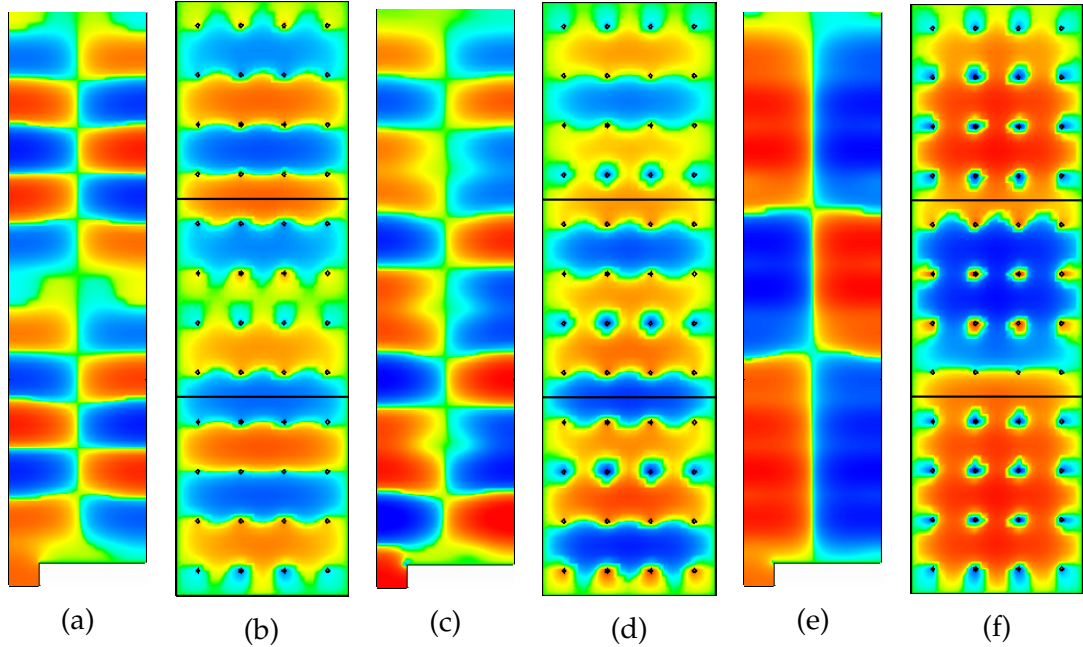
Figure 7.108: Images from numerical simulations in CST showing the fields found using different frequency monitors in a time domain simulation of a finite dielectric wire medium (3 units of 4×4; $\varepsilon_r = 100$, $a_x = 13.06$ mm and $a_y = 15.00$ mm; $q = 0.8$, $f_\mathrm{d} = 11$ GHz, $R_c = 0.5$ mm and $\lambda_C = 10.1$ GHz; open y boundaries, and metallic x and z boundaries; and a waveguide port, which is distanced 10 mm from the lattice, with dimension 19×9.5 mm) with $t = 200$ ns. The fields are represented using logarithmic colour plots where the longitudinal field direction and magnitude is represented by colour. (a) shows a y-z slice ($f = 10.934$ GHz); (b), an x-y slice ($f = 10.934$ GHz); (c), a y-z slice ($f = 11.027$ GHz); (d), an x-y slice ($f = 11.027$ GHz); (e), a y-z slice ($f = 11.263$ GHz); and (f), an x-y slice ($f = 11.263$ GHz).

The fields at 10.934 GHz and 11.027 GHz do not demonstrate the behaviour we expect around the wires, where the field should be strongly longitudinal in the wires but oriented in the opposite direction to the field surrounding the wires. This behaviour is shown in the field at 11.263 GHz. This was the reason that we decided to focus on examining the field profile of the field at 11.263 GHz, which was done in a similar way to our eigenmode simulations. Lines were defined spanning across the length of our structure and situated halfway between the lattice. These lines spanned from the bottom of the first lattice unit cell (none were placed within the waveguide section) to the top of the structure and were separated by $a_x/4$. Then, as we have previously done, the field was evaluated along the lines, and the $\mathfrak{R}^2$ value for the comparison with our desired profile were calculated. A plot of these $\mathfrak{R}^2$ values for our chosen field is shown in Fig. 7.109.

(a)

■ $y=16a_y/4$, $R^2=0.9991$	■ $y=18a_y/4$, $R^2=0.9757$
■ $y=19a_y/4$, $R^2=-2.059$ —— $R_c=0.5$ mm, $f_d=11$ GHz, 3 Units, t=200, $f=11.263$ GHz

(b)
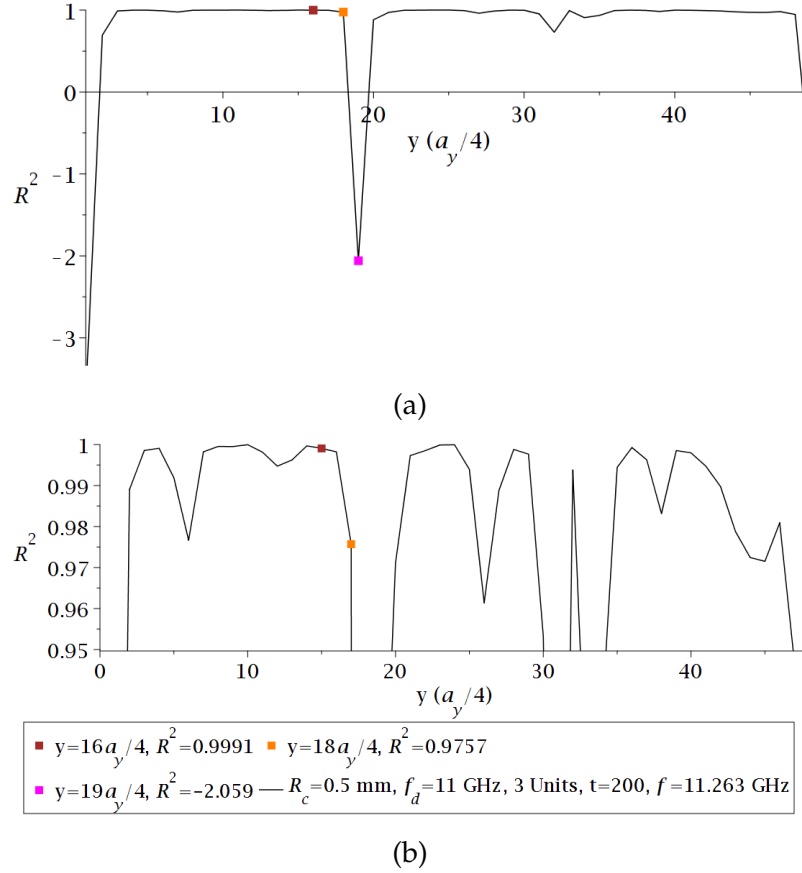
Figure 7.109: A plot of a figure of merit ($\mathfrak{R}^2$) for the comparison between the desired profile and the field profile (longitudinal, z, spatial variation of the electric field strength, E_z) of the field (11.263 GHz) in a finite dielectric wire medium ($t = 200$ ns; 3 units of 4×4; $\varepsilon_r = 100$, $a_x = 13.06$ mm and $a_y = 15.00$ mm; $q = 0.8$, $f_d = 11$ GHz, $R_c = 0.5$ mm and $\lambda_C = 10.1$ GHz; open y boundaries and, metallic x and z boundaries; and a waveguide port, which is distanced 10 mm from the lattice, with dimension 19×9.5 mm) at the evaluation position against the y position of the evaluation line given in terms of quarter lattice parameters from the bottom of the structure ($a_y/4$). Coloured squares are included to represent a few of the profiles we have plotted separately: maroon ($y = 16a_y/4$, $\mathfrak{R}^2 = 0.9991$), orange ($y = 18a_y/4$, $\mathfrak{R}^2 = 0.9757$) and magenta ($y = 19a_y/4$, $\mathfrak{R}^2 = -2.059$). (a) is a full plot and (b) only shows $\mathfrak{R}^2$ values above 0.95.

This plot shows that for large sections of the structure, the field profiles produced are a very good fit for our desired profile. In Fig. 7.109 there are a series of coloured squares that indicate a few evaluation positions, and their corresponding $\mathfrak{R}^2$ values, for which we have plotted the field profiles in Figs. 7.110-7.112. These plots help to give a qualitative view of our field profiling success. These results give us some confidence that our replicated field profiles can be excited in our structure, although as mentioned, we are unsure of whether these fields will

be transmitted well. We should also not that Fig. 7.112 clearly shows a significant difference between the field profile observed at this position and the desired field profile. We are not sure why this, although it does seem that the profiling is less successful in the regions where the electric field is weak in the gap between regions of high field with different directions.
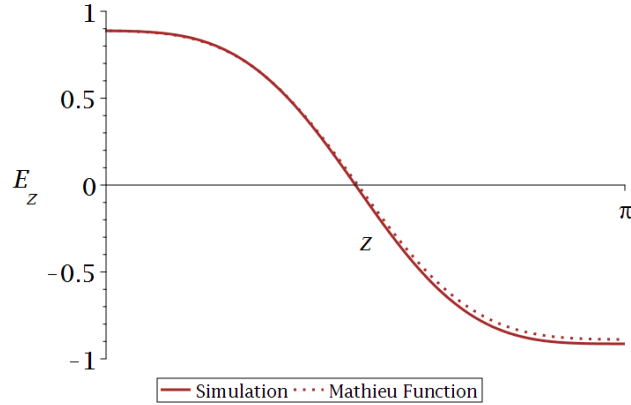
Figure 7.110: Plot of the field profile (longitudinal, z, spatial variation of the electric field strength, E_z) of the field (11.263 GHz) in a finite dielectric wire medium ($t = 200$ ns; 3 units of 4×4; $\varepsilon_r = 100$, $a_x = 13.06$ mm and $a_y = 15.00$ mm; $q = 0.8$, $f_d = 11$ GHz, $R_c = 0.5$ mm and $\lambda_C = 10.1$ GHz; open y boundaries, and metallic x and z boundaries; and a waveguide port, which is distanced 10 mm from the lattice, with dimension 19×9.5 mm) at the evaluation position $y = 16a_y/4$ (maroon). The plot includes the field profile observed in our numerical simulation (solid) and the desired profile (dotted). In order to compare these the field profile and z coordinate have been normalised.
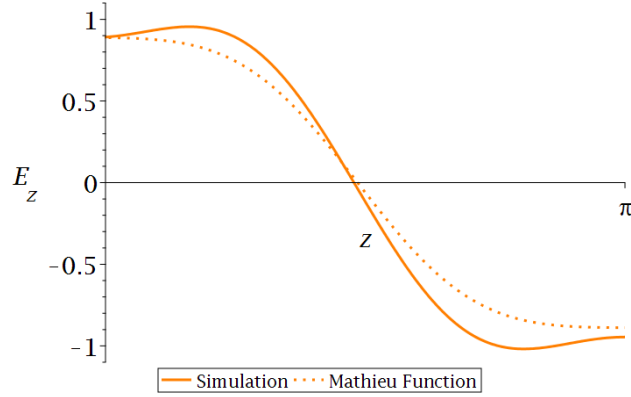
Figure 7.111: Plot of the field profile (longitudinal, z, spatial variation of the electric field strength, E_z) of the field (11.263 GHz) in a finite dielectric wire medium ($t = 200$ ns; 3 units of 4×4; $\varepsilon_r = 100$, $a_x = 13.06$ mm and $a_y = 15.00$ mm; $q = 0.8$, $f_d = 11$ GHz, $R_c = 0.5$ mm and $\lambda_C = 10.1$ GHz; open y boundaries, and metallic x and z boundaries; and a waveguide port, which is distanced 10 mm from the lattice, with dimension 19×9.5 mm) at the evaluation position $y = 18a_y/4$ (orange). The plot includes the field profile observed in our numerical simulation (solid) and the desired profile (dotted). In order to compare these the field profile and z coordinate have been normalised.
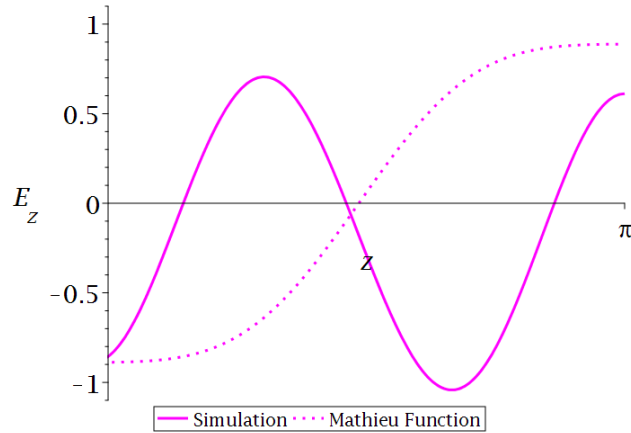
Figure 7.112: Plot of the field profile (longitudinal, z, spatial variation of the electric field strength, E_z) of the field (11.263 GHz) in time domain simulations of a finite dielectric wire medium ($t = 200$ ns; 3 units of 4×4; ε_r, $a_x = 13.06$ mm and $a_y = 15.00$ mm; $q = 0.8$, $f_d = 11$ GHz, $R_c = 0.5$ mm and $\lambda_C = 10.1$ GHz; open y boundaries and, metallic x and z boundaries; and a waveguide port, which is distanced 10 mm from the lattice, with dimension 19×9.5 mm) at the evaluation position $y = 19a_y/4$ (magenta). The plot includes the field profile observed in our numerical simulation (solid) and the desired profile (dotted). In order to compare these the field profile and z coordinate have been normalised.

IX.2 Examining the effect of simulation time

After achieving some qualified success with our time domain results, it was important to examine the choices made to determine which were vital to the replication of our field profiles. This should help with the reproducibility of our results. The first factor that we have studied is the choice of simulation time. We have repeated our previous simulation with an identical structure, but with a maximum simulation time of t=100 ns.

As we have previously discussed the limiting factor in our simulations run is the time limit; therefore, the excitation was now allowed to progress for 100 ns in the simulation. The fields found at some of our included frequency monitors are shown in Fig. 7.113. Both fields appear to show the features we would expect from our field.
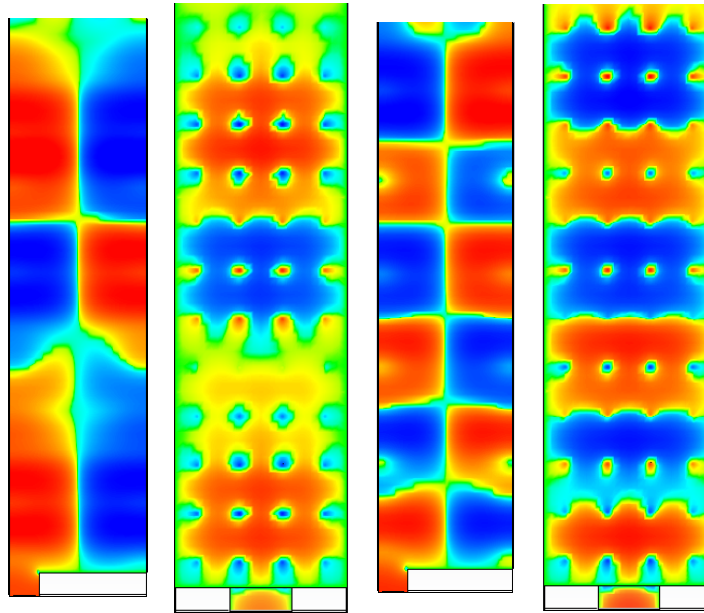
Figure 7.113: Images from numerical simulations in CST showing the fields found using different frequency monitors in a time domain simulation of a finite dielectric wire medium (3 units of 4×4; $\varepsilon_r = 100$, $a_x = 13.06$ mm and $a_y = 15.00$ mm; $q = 0.8$, $f_d = 11$ GHz, $R_c = 0.5$ mm and $\lambda_C = 10.1$ GHz; open y boundaries, and metallic x and z boundaries; and a waveguide port, which is distanced 10 mm from the lattice, with dimension 19×9.5 mm) with $t = 100$ ns. The fields are represented using logarithmic colour plots where the longitudinal field direction and magnitude is represented by colour. (a) shows a y-z slice ($f = 11.265$ GHz); (b), an x-y slice ($f = 11.265$ GHz); (c), a y-z slice ($f = 11.274$ GHz); and (d), an x-y slice ($f = 11.274$ GHz).

We have evaluated the profiles for both frequencies monitored. The $\mathfrak{R}^2$ plots for these two frequencies are shown in Figs. 7.114 and 7.115. These plots both

include a comparison with our successful t=200 ns plot. It is clear that allowing the excitation to progress for 100 ns has led to a severe reduction in field profiling success, with a high agreement with the desired profile only being shown sporadically.
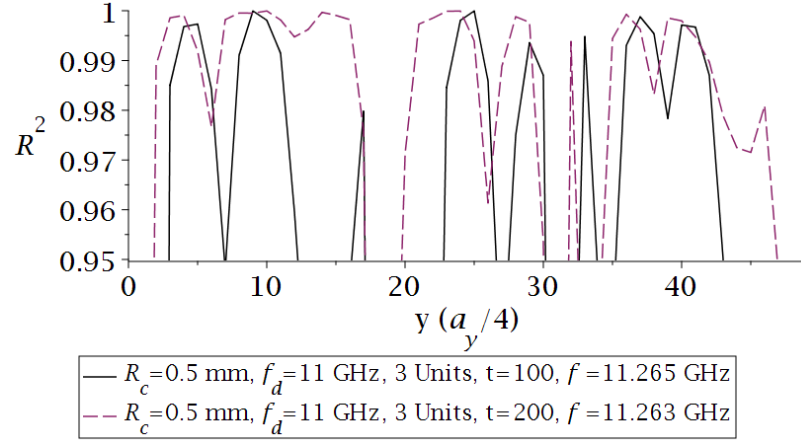
Figure 7.114: A plot of a figure of merit ($\mathfrak{R}^2$) for the comparison between the desired profile and the field profile (longitudinal, z, spatial variation of the electric field strength, E_z) of the field (11.265 GHz) in time domain simulations of a finite dielectric wire medium ($t = 100$ ns; 3 units of 4×4; $\varepsilon_r = 100$, $a_x = 13.06$ mm and $a_y = 15.00$ mm; $q = 0.8$, $f_d = 11$ GHz, $R_c = 0.5$ mm and $\lambda_C = 10.1$ GHz; open y boundaries and, metallic x and z boundaries; and a waveguide port, which is distanced 10 mm from the lattice, with dimension 19×9.5 mm) at the evaluation position against the y position of the evaluation line given in terms of quarter lattice parameters from the bottom of the structure ($a_y/4$). A comparison is included with the plot resulting from a field (11.263 GHz) in our original time domain simulations of a finite dielectric wire medium ($t = 200$ ns; 3 units of 4×4; $\varepsilon_r = 100$, $a_x = 13.06$ mm and $a_y = 15.00$ mm; $q = 0.8$, $f_d = 11$ GHz, $R_c = 0.5$ mm and $\lambda_C = 10.1$ GHz; open y boundaries and, metallic x and z boundaries; and a waveguide port, which is distanced 10 mm from the lattice, with dimension 19×9.5 mm)

Figure 7.115: A plot of a figure of merit ($\mathfrak{R}^2$) for the comparison between the desired profile and the field profile (longitudinal, z, spatial variation of the electric field strength, E_z) of the field (11.274 GHz) in time domain simulations of a finite dielectric wire medium ($t = 100$ ns; 3 units of 4×4; $\varepsilon_r = 100$, $a_x = 13.06$ mm and $a_y = 15.00$ mm; $q = 0.8$, $f_d = 11$ GHz, $R_c = 0.5$ mm and $\lambda_C = 10.1$ GHz; open y boundaries and, metallic x and z boundaries; and a waveguide port, which is distanced 10 mm from the lattice, with dimension 19×9.5 mm) at the evaluation position against the y position of the evaluation line given in terms of quarter lattice parameters from the bottom of the structure ($a_y/4$). A comparison is included with the plot resulting from a field (11.263 GHz) in our original time domain simulations of a finite dielectric wire medium ($t = 200$ ns; 3 units of 4×4; $\varepsilon_r = 100$, $a_x = 13.06$ mm and $a_y = 15.00$ mm; $q = 0.8$, $f_d = 11$ GHz, $R_c = 0.5$ mm and $\lambda_C = 10.1$ GHz; open y boundaries and, metallic x and z boundaries; and a waveguide port, which is distanced 10 mm from the lattice, with dimension 19×9.5 mm)

We have also repeated our simulation for a time limit of $t = 20$ ns. Given our experience with $t = 100$ ns, we would not expect these simulations to be successful. The fields resulting from the frequency monitors introduced are shown in Fig. 7.116.
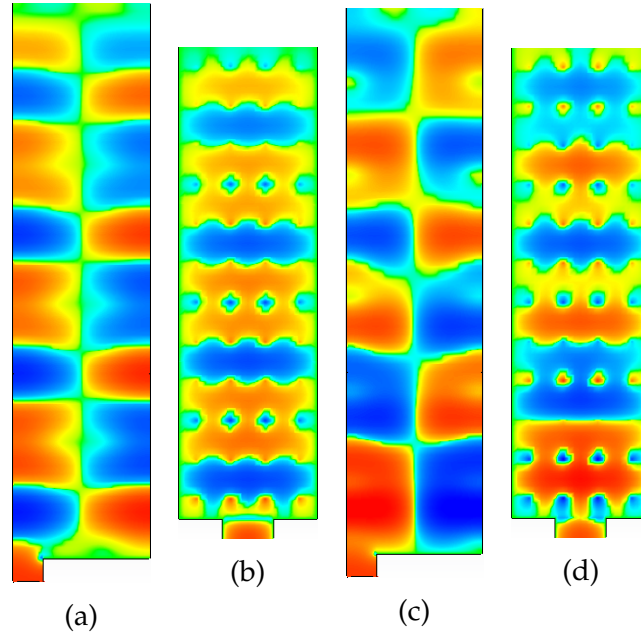
Figure 7.116: Images from numerical simulations in CST showing the fields found using different frequency monitors in a time domain simulation of a finite dielectric wire medium (3 units of 4×4; $\varepsilon_r = 100$, $a_x = 13.06$ mm and $a_y = 15.00$ mm; $q = 0.8$, $f_d = 11$ GHz, $R_c = 0.5$ mm and $\lambda_C = 10.1$ GHz; open y boundaries, and metallic x and z boundaries; and a waveguide port, which is distanced 10 mm from the lattice, with dimension 19×9.5 mm) with $t = 20$ ns. The fields are represented using logarithmic colour plots where the longitudinal field direction and magnitude is represented by colour. (a) shows a y-z slice ($f = 11.021$ GHz); (b), an x-y slice ($f = 11.021$ GHz); (c), a y-z slice ($f = 11.267$ GHz); and (d), an x-y slice ($f = 11.267$ GHz).

The resulting $\mathfrak{R}^2$ plots for the fields produced at our monitored frequencies are shown in Figs. 7.117 and 7.118. As we had expected, these plots show that with this amount of time elapsed there are only a few instances of successful field profile shaping.
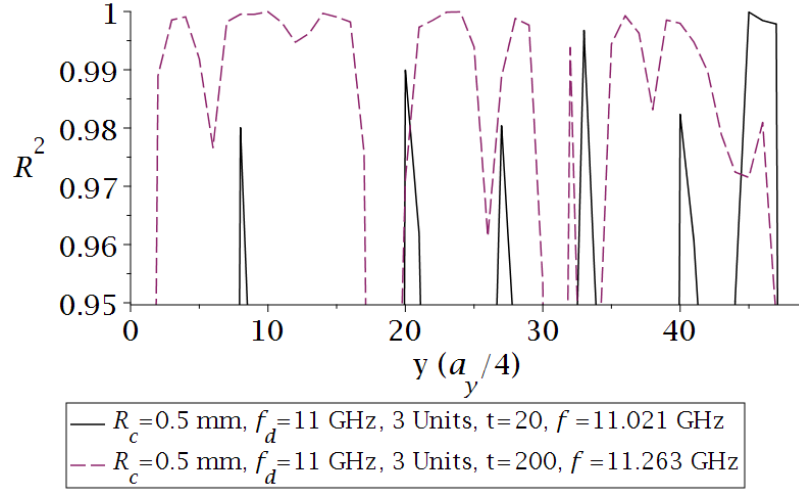
Figure 7.117: A plot of a figure of merit ($\mathfrak{R}^2$) for the comparison between the desired profile and the field profile (longitudinal, z, spatial variation of the electric field strength, E_z) of the field (11.021 GHz) in time domain simulations of a finite dielectric wire medium ($t = 20$ ns; 3 units of 4×4; $\varepsilon_r = 100$, $a_x = 13.06$ mm and $a_y = 15.00$ mm; $q = 0.8$, $f_d = 11$ GHz, $R_c = 0.5$ mm and $\lambda_C = 10.1$ GHz; open y boundaries, and metallic x and z boundaries; and a waveguide port, which is distanced 10 mm from the lattice, with dimension 19×9.5 mm) at the evaluation position against the y position of the evaluation line given in terms of quarter lattice parameters from the bottom of the structure ($a_y/4$). A comparison is included with the plot resulting from a field (11.263 GHz) in our original time domain simulations of a finite dielectric wire medium ($t = 200$ ns; 3 units of 4×4; $\varepsilon_r = 100$, $a_x = 13.06$ mm and $a_y = 15.00$ mm; $q = 0.8$, $f_d = 11$ GHz, $R_c = 0.5$ mm and $\lambda_C = 10.1$ GHz; open y boundaries and, metallic x and z boundaries; and a waveguide port, which is distanced 10 mm from the lattice, with dimension 19×9.5 mm)

(a)

Figure 7.118: A plot of a figure of merit ($\mathfrak{R}^2$) for the comparison between the desired profile and the field profile (longitudinal, z, spatial variation of the electric field strength, E_z) of the field (11.267 GHz) in time domain simulations of a finite dielectric wire medium ($t = 20$ ns; 3 units of 4×4; $\varepsilon_r = 100$, $a_x = 13.06$ mm and $a_y = 15.00$ mm; $q = 0.8$, $f_d = 11$ GHz, $R_c = 0.5$ mm and $\lambda_C = 10.1$ GHz; open y boundaries, and metallic x and z boundaries; and a waveguide port, which is distanced 10 mm from the lattice, with dimension 19×9.5 mm) at the evaluation position against the y position of the evaluation line given in terms of quarter lattice parameters from the bottom of the structure ($a_y/4$). A comparison is included with the plot resulting from a field (11.263 GHz) in our original time domain simulations of a finite dielectric wire medium ($t = 200$ ns; 3 units of 4×4; $\varepsilon_r = 100$, $a_x = 13.06$ mm and $a_y = 15.00$ mm; $q = 0.8$, $f_d = 11$ GHz, $R_c = 0.5$ mm and $\lambda_C = 10.1$ GHz; open y boundaries and, metallic x and z boundaries; and a waveguide port, which is distanced 10 mm from the lattice, with dimension 19×9.5 mm)

IX.3 Investigating the need for a waveguide section

Another important aspect to investigate is whether the inclusion of the waveguide section is necessary. This section of the structure was included because we had been struggling to observe field profiling without it. The dimensions of the waveguide, 9.5 by 19 mm, were chosen to support modes around our desired frequency. To investigate the importance of this inclusion, we have repeated our simulations with an identical structure bar the removal of the waveguide section. The resulting structure is shown in Fig. 7.119. The waveguide port is now situated over the entire bottom boundary of the structure.

(a)   (b)
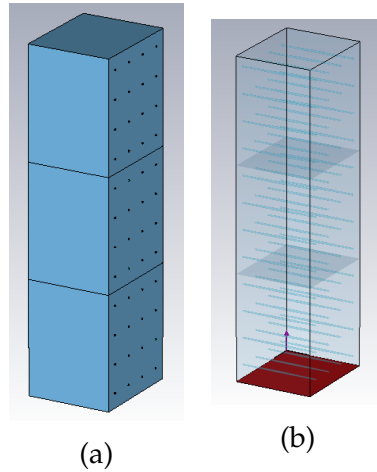
Figure 7.119: A representation of a finite wire medium in CST, consisting of three vertically stacked units of four by four lattices of dielectric wires. The unit cell has one set of metallic transverse boundary conditions, one set of open transverse boundary conditions and metallic longitudinal boundary conditions. The dielectric wires have a radius function calculated for a flattened profile ($q = 0.8$) in a partially finite dielectric wire medium (4×4, $\varepsilon_r = 100$, $a_x = 13.06$ mm and $a_y = 15.00$ mm) for the parameter choice of $f_d = 11$ GHz, $R_c = 0.5$ mm and $\lambda_C = 10.1$ GHz. This structure is identical to the one used in our initial time domain simulation except for the removal of the extra section upon which the waveguide port was placed. (a) shows the the unit cell of the structure in CST and (b) shows the unit cell with the waveguide port highlighted in red.

(a)   (b)   (c)   (d)
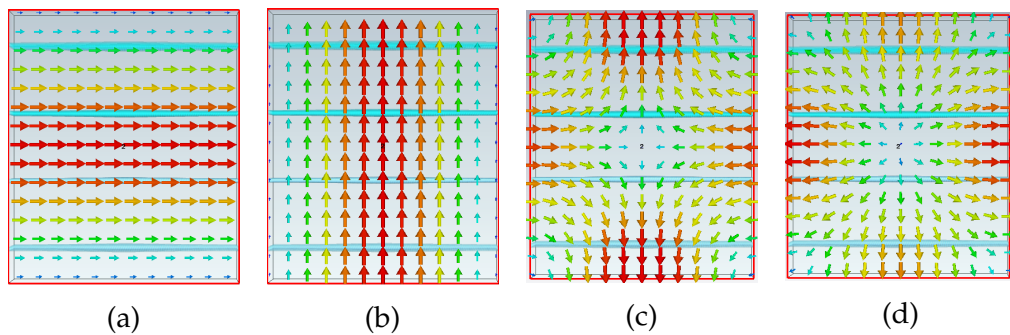
Figure 7.120: The fundamental port modes in a finite dielectric wire medium structure (3 units of 4×4; $\varepsilon_r = 100$, $a_x = 13.06$ mm and $a_y = 15.00$ mm; $q = 0.8$, $f_d = 11$ GHz, $R_c = 0.5$ mm and $\lambda_C = 10.1$ GHz; and open y boundaries, and metallic x and z boundaries). The field is represented using arrow plots on the surface of the waveguide port. (a) shows the first mode; (b), the second mode; (c), the third mode; and (d), the fourth mode, which we have found the most suitable for exciting our structure.

A selection of the modes supported by this new port are shown in Fig. 7.120.

The port mode that we have found to be most successful at achieving field profile shaping is the fourth port mode shown in Fig. 7.120d.

We have modified the simulation to run for a lesser amount of time, $t = 100$ ns, due to concerns about the energy of the system diverging. The modes found at our frequency monitors are shown in Fig. 7.121.
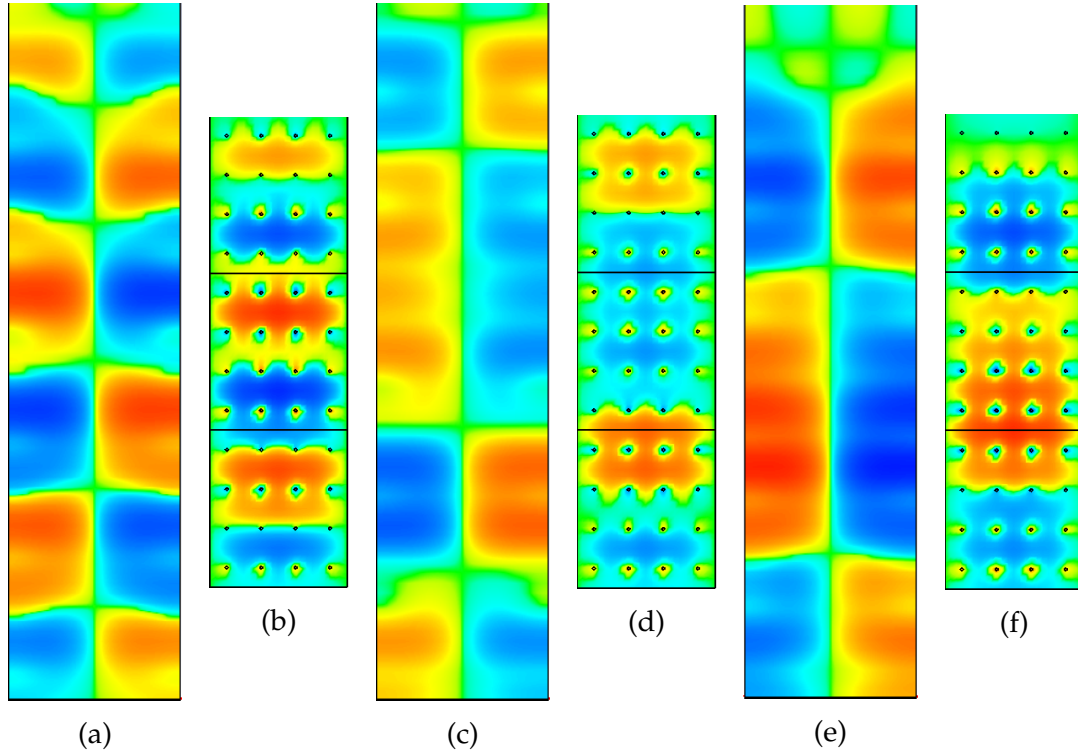

Figure 7.121: Images from numerical simulations in CST showing the fields found using different frequency monitors in a time domain simulation of a finite dielectric wire medium (3 units of 4×4; $\varepsilon_r = 100$, $a_x = 13.06$ mm and $a_y = 15.00$ mm; $q = 0.8$, $f_d = 11$ GHz, $R_c = 0.5$ mm and $\lambda_C = 10.1$ GHz; and open y boundaries, and metallic x and z boundaries) with $t = 100$ ns. The fields are represented using logarithmic colour plots where the longitudinal field direction and magnitude is represented by colour. (a) shows a y-z slice ($f = 11.309$ GHz); (b), an x-y slice ($f = 11.309$ GHz); (c), a y-z slice ($f = 11.324$ GHz); (d), an x-y slice ($f = 11.324$ GHz); (e), a y-z slice ($f = 11.338$ GHz); and (f), an x-y slice ($f = 11.338$ GHz).

The field produced by the monitor at the frequency of 11.338 GHz looks promising as an example of field profiling. The $\mathfrak{R}^2$ plot for this frequency is shown in Fig. 7.122.
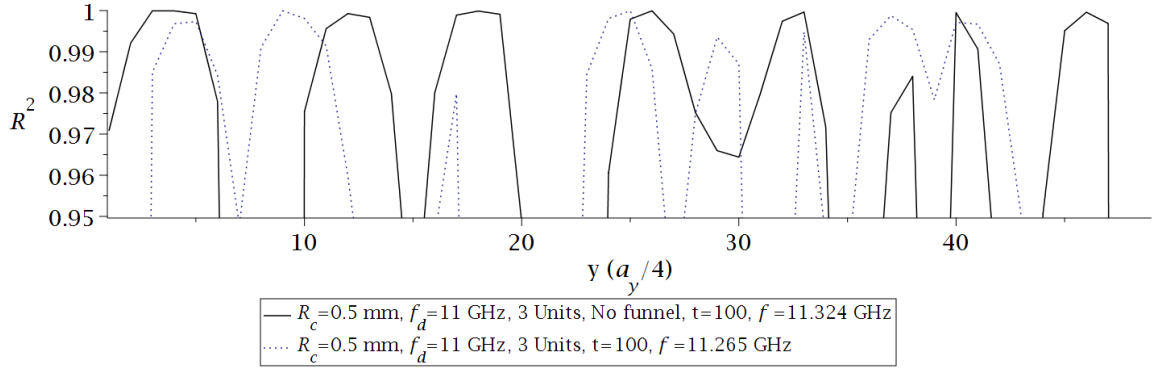
(a)
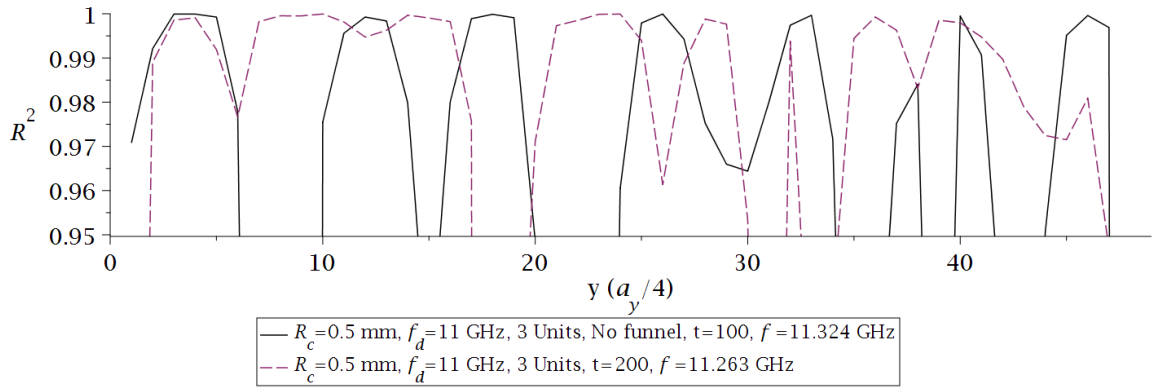
(b)

Figure 7.122: Plots (black) of a figure of merit ($\mathfrak{R}^2$) for the comparison between the desired profile and the field profile (longitudinal, z, spatial variation of the electric field strength, E_z) of the field (11.338 GHz) in time domain simulations of a finite dielectric wire medium ($t = 100$ ns; 3 units of 4×4; $\varepsilon_r = 100$, $a_x = 13.06$ mm and $a_y = 15.00$ mm; $q = 0.8$, $f_d = 11$ GHz, $R_c = 0.5$ mm and $\lambda_C = 10.1$ GHz; and open y boundaries, and metallic x and z boundaries) at the evaluation position against the y position of the evaluation line given in terms of quarter lattice parameters from the bottom of the structure ($a_y/4$). (a) is the plot with a comparison included with the plot (dotted blue) resulting from a field (11.265 GHz) in time domain simulations of a finite dielectric wire medium ($t = 100$ ns; 3 units of 4×4; $\varepsilon_r = 100$, $a_x = 13.06$ mm and $a_y = 15.00$ mm; $q = 0.8$, $f_d = 11$ GHz, $R_c = 0.5$ mm and $\lambda_C = 10.1$ GHz; open y boundaries and, metallic x and z boundaries; and a waveguide port, which is distanced 10 mm from the lattice, with dimension 19×9.5 mm), and (b) is the plot with a comparison included with the plot (dashed magenta) resulting from a field (11.263 GHz) in time domain simulations of a finite dielectric wire medium ($t = 200$ ns; 3 units of 4×4; $\varepsilon_r = 100$, $a_x = 13.06$ mm and $a_y = 15.00$ mm; $q = 0.8$, $f_d = 11$ GHz, $R_c = 0.5$ mm and $\lambda_C = 10.1$ GHz; open y boundaries and, metallic x and z boundaries; and a waveguide port, which is distanced 10 mm from the lattice, with dimension 19×9.5 mm)

The comparison of the $\mathfrak{R}^2$ plot for the case with no funnel and our original control case progressed by t=100 ns shows a greater performance for the structure with no funnel. Meanwhile, the comparison with the original structure allowed to progress for t=200 ns shows the no-funnel case being noticeably worse. Given the added complications of exciting with a higher order mode and the inability to excite the structure for longer times where better field profiling can be achieved, we conclude that the inclusion of the waveguide section has helped the performance of the structure.

IX.4 The effect of multiple units
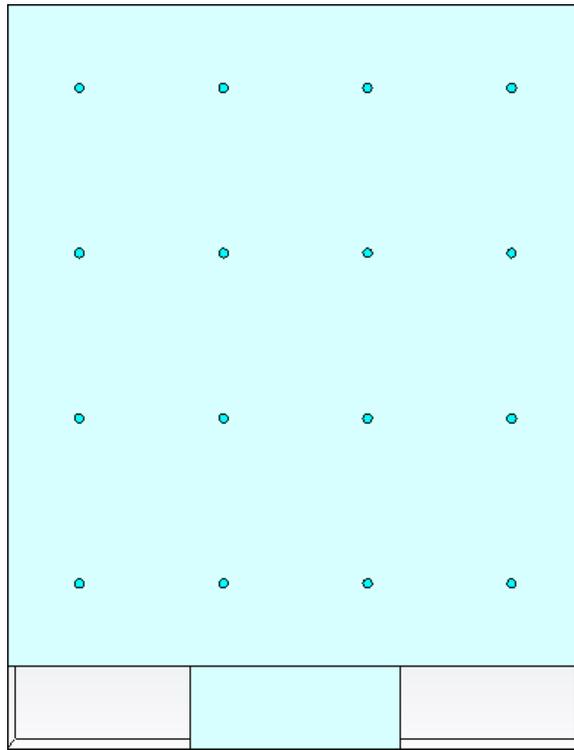
Figure 7.123: A representation of a finite wire medium in CST, consisting of a four by four lattices of dielectric wires. The unit cell has one set of metallic transverse boundary conditions, one set of open transverse boundary conditions and metallic longitudinal boundary conditions. The dielectric wires have a radius function calculated for a flattened profile ($q = 0.8$) in a partially finite dielectric wire medium (4×4, $\varepsilon_r = 100$, $a_x = 13.06$ mm and $a_y = 15.00$ mm) for the parameter choice of $f_d = 11$ GHz, $R_c = 0.5$ mm and $\lambda_C = 10.1$ GHz. A small section has been attached to the bottom of the structure with dimensions $x_{dim} = 19$ mm, $y_{dim} = 10$ mm and $z_{dim} = 9.5$ mm, where a waveguide port has been placed.

As mentioned previously, the structure used to find field profiling in our time domain simulations was formed by three unit cells of a four by four lattice which

had previously been successful. We were unsure whether this inclusion was necessary. Therefore, we ran simulations where only one unit of the lattice was used. This new structure is shown in Fig. 7.123.

We simulated this structure for a simulation time of $t = 200$ ns, but the system became unstable. Re-running the simulation for t=100 ns avoided this problem. The field produced by the field monitors introduced into our simulation is shown in Fig. 7.124.


(a)

(b)
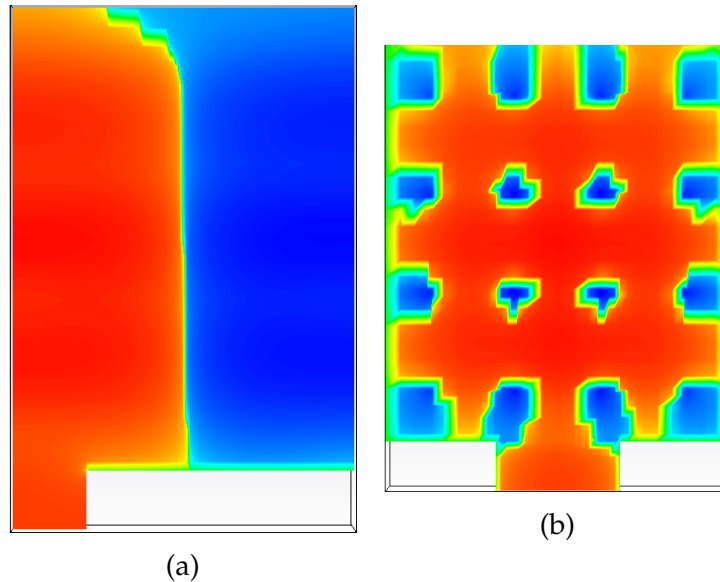
Figure 7.124: Images from numerical simulations in CST showing the field found using a frequency monitor ($f = 11.263$ GHz) in a time domain simulation of a finite dielectric wire medium (4×4; $\varepsilon_r = 100$, $a_x = 13.06$ mm and $a_y = 15.00$ mm; $q = 0.8$, $f_d = 11$ GHz, $R_c = 0.5$ mm and $\lambda_C = 10.1$ GHz; open y boundaries, and metallic x and z boundaries; and a waveguide port, which is distanced 10 mm from the lattice, with dimension 19×9.5 mm) with $t = 100$ ns. The fields are represented using logarithmic colour plots where the longitudinal field direction and magnitude is represented by colour. (a) shows a y-z slice; and (b), an x-y slice.

We can see the $\Re^2$ plot for this frequency in Fig. 7.125. Looking at the comparison with our successful control structure, we see that they are remarkably similar apart from at positions near the top of our single-unit structure. This discrepancy could be explained by the fact that it is an unfair comparison. The field shape at the top of the single-unit structure will be affected by the fact that it is nearing the edge of the structure, whereas it is being compared to a position in the three-unit structure that is two full lattice units away from reaching the area where it would be distorted by edge effects. It seems safe to conclude that there is minimal distortion in the quality of the results by using just one unit cell of our four by four base structure. There are significant advantages to using a smaller structure due to it being less computationally intensive.

(a)

(b)
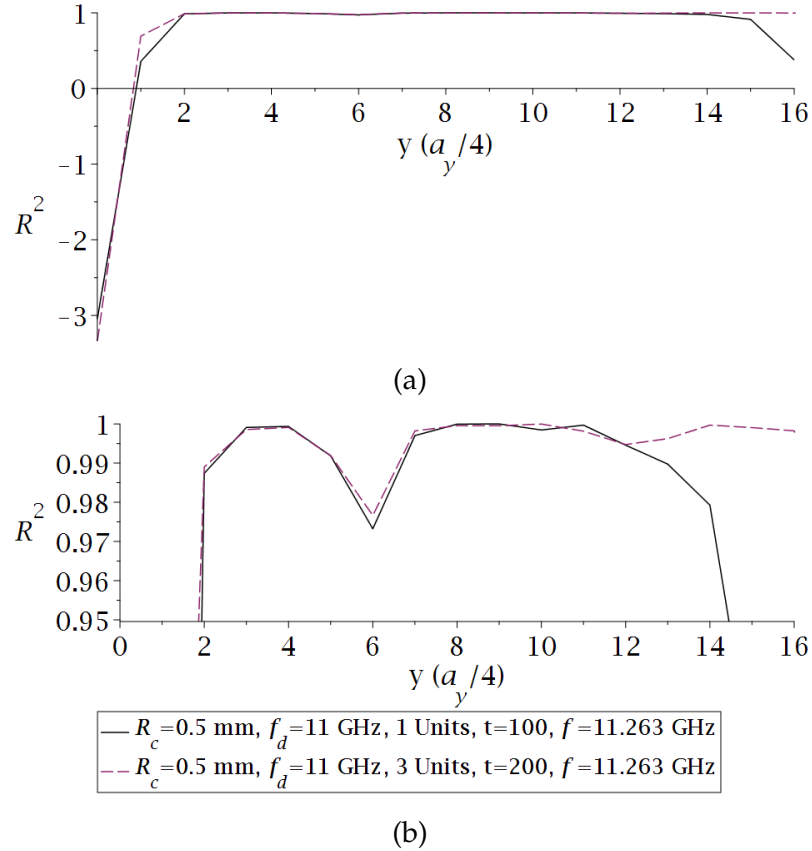
Figure 7.125: A plot of a figure of merit ($\mathfrak{R}^2$) for the comparison between the desired profile and the field profile (longitudinal, z, spatial variation of the electric field strength, E_z) of the field (11.263 GHz) in a finite dielectric wire medium ($t = 100$ ns; 3 units of 4×4; $\varepsilon_r = 100$, $a_x = 13.06$ mm and $a_y = 15.00$ mm; $q = 0.8$, $f_d = 11$ GHz, $R_c = 0.5$ mm and $\lambda_C = 10.1$ GHz; open y boundaries and, metallic x and z boundaries; and a waveguide port, which is distanced 10 mm from the lattice, with dimension 19×9.5 mm) at the evaluation position against the y position of the evaluation line given in terms of quarter lattice parameters from the bottom of the structure ($a_y/4$). (a) is a full plot with a comparison included with the plot (dashed magenta) resulting from a field (11.263 GHz) in time domain simulations of a finite dielectric wire medium ($t = 200$ ns; 3 units of 4×4; $\varepsilon_r = 100$, $a_x = 13.06$ mm and $a_y = 15.00$ mm; $q = 0.8$, $f_d = 11$ GHz, $R_c = 0.5$ mm and $\lambda_C = 10.1$ GHz; open y boundaries and, metallic x and z boundaries; and a waveguide port, which is distanced 10 mm from the lattice, with dimension 19×9.5 mm), and (b) only shows $\mathfrak{R}^2$ values above 0.95.

IX.5 The importance of the choice of base structure

We would expect the choice of the base structure to have little role in the field profiling success in our time domain simulations assuming the base structure was found to be able to support field profile shaping in eigenmode simulations.

Despite this, we have seen the opposite, with certain choices of base structure performing much worse than others. Due to the time required to run these simulations, we have not been able to run a detailed analysis of this problem to determine what factors in the choice of a base structure are important.

We will illustrate this effect by detailing an example simulation where the base lattice unit used leads to poor field profile shaping. We have created a model with a setup identical to our control case except the wire radius variation for the four by four lattice base was based on a parameter choice of $R_c = 0.7$ mm and $f = 9.4$ GHz for a flattened profile. This radius variation is plotted in Fig. 7.126 and the resulting structure is shown in Fig. 7.127.
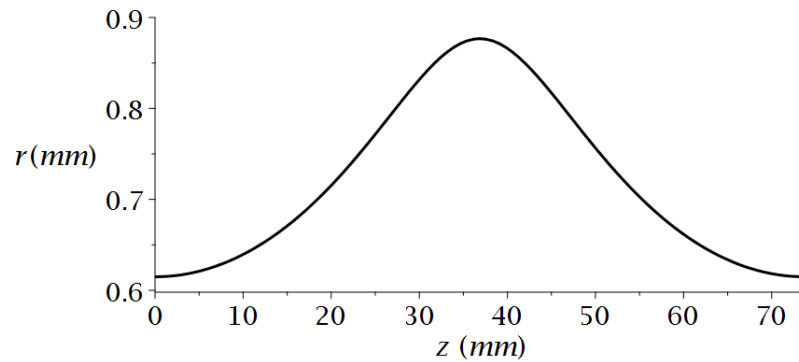
Figure 7.126: Half a period of the radius function calculated for a flattened profile ($q = 0.8$) in a partially finite dielectric wire medium (4×4, $\varepsilon_r = 100$, $a_x = 13.06$ mm and $a_y = 15.00$ mm) for the parameter choice of $f_d = 9.4$ GHz, $R_c = 0.7$ mm and $\lambda_C = 9.05$ GHz. This is the wire radius variation used in the following time domain simulations, although the lattice configurations used differ from the basis of the calculated function.
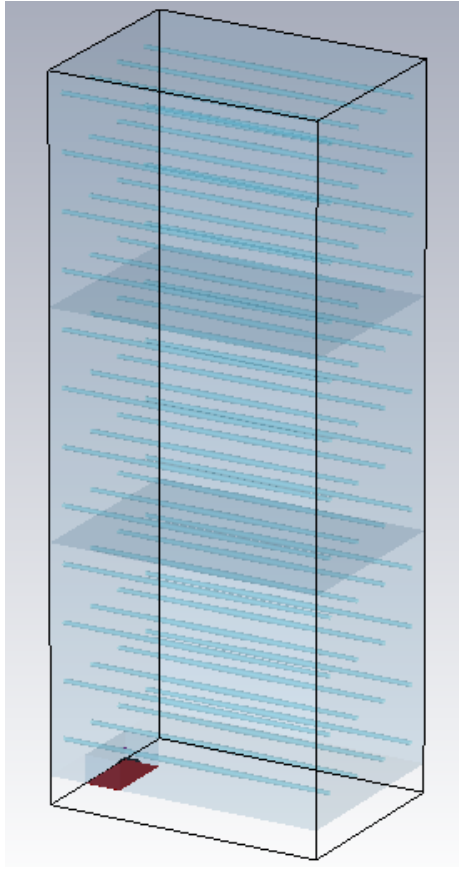
Figure 7.127: A representation of a finite wire medium in CST, consisting of three vertically stacked units of four by four lattices of dielectric wires. The unit cell has one set of metallic transverse boundary conditions, one set of open transverse boundary conditions and metallic longitudinal boundary conditions. The dielectric wires have a radius function calculated for a flattened profile ($q = 0.8$) in a partially finite dielectric wire medium (4×4, $\varepsilon_r = 100$, $a_x = 13.06$ mm and $a_y = 15.00$ mm) for the parameter choice of $f_d = 9.4$ GHz, $R_c = 0.7$ mm and $\lambda_C = 9.05$ GHz. A small section has been attached to the bottom of the structure with dimensions $x_{dim} = 19$ mm, $y_{dim} = 10$ mm and $z_{dim} = 9.5$ mm, where a waveguide port (red) has been placed.

As with our control case, we chose a frequency range for our excitation signal that spanned 2 GHz with our design frequency at the centre of this range. The resulting excitation signal is shown in Fig. 7.128.
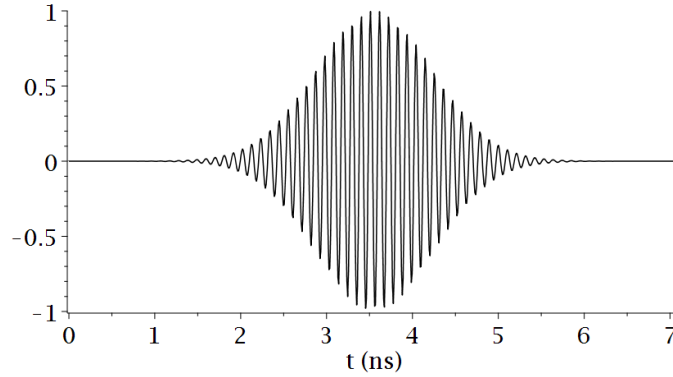
Figure 7.128: The default excitation signal generated by CST for a choice of frequency range of 8.4-10.4 GHz. This is the signal we will use to excite a finite dielectric wire medium structure (3 units of 4×4; $\varepsilon_r = 100$, $a_x = 13.06$ mm and $a_y = 15.00$ mm; $q = 0.8$, $f_d = 9.4$ GHz, $R_c = 0.7$ mm and $\lambda_C = 9.05$ GHz; open y boundaries, and metallic x and z boundaries; and a waveguide port, which is distanced 10 mm from the lattice, with dimension 19×9.5 mm).

(a)   (b)   (c)   (d)   (e)   (f)
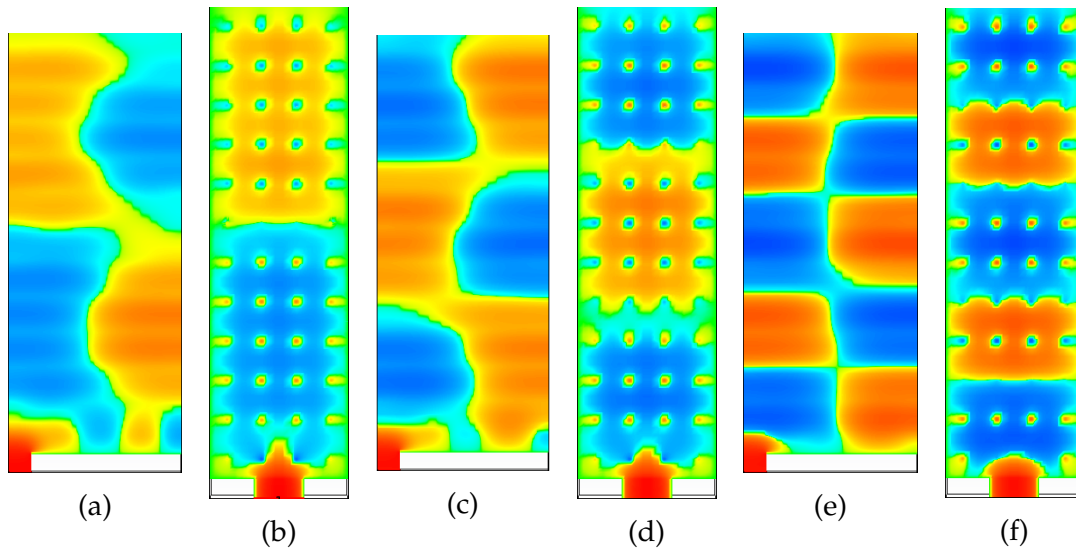
Figure 7.129: Images from numerical simulations in CST showing the fields found using different frequency monitors in a time domain simulation of a finite dielectric wire medium (3 units of 4×4; $\varepsilon_r = 100$, $a_x = 13.06$ mm and $a_y = 15.00$ mm; $q = 0.8$, $f_d = 9.4$ GHz, $R_c = 0.7$ mm and $\lambda_C = 9.05$ GHz; open y boundaries, and metallic x and z boundaries; and a waveguide port, which is distanced 10 mm from the lattice, with dimension 19×9.5 mm) with $t = 70$ ns. The fields are represented using logarithmic colour plots where the longitudinal field direction and magnitude is represented by colour. (a) shows a y-z slice ($f = 9.614$ GHz); (b), an x-y slice ($f = 9.614$ GHz); (c), a y-z slice ($f = 9.661$ GHz); (d), an x-y slice ($f = 9.661$ GHz); (e), a y-z slice ($f = 9.78$ GHz); and (f), an x-y slice ($f = 9.78$ GHz).

212

As we have seen in other cases, our original time setting of $t = 100$ ns results in a system which became unstable. We, therefore, chose a shorter simulation time which avoids this problem, t=70 ns. The fields found at our frequency monitors are shown in Fig. 7.129. These fields seem promising, with all of them displaying the features expected from our field and having the expected variation.

When we look at the $\mathfrak{R}^2$ plots for these frequencies, their field profiling is significantly worse than our control case. Some successful field profiling does occur, but it is more sporadic. This may be due to the inability to progress the simulation for a longer time. We have not established why some choices of four by four unit cells become unstable before others.
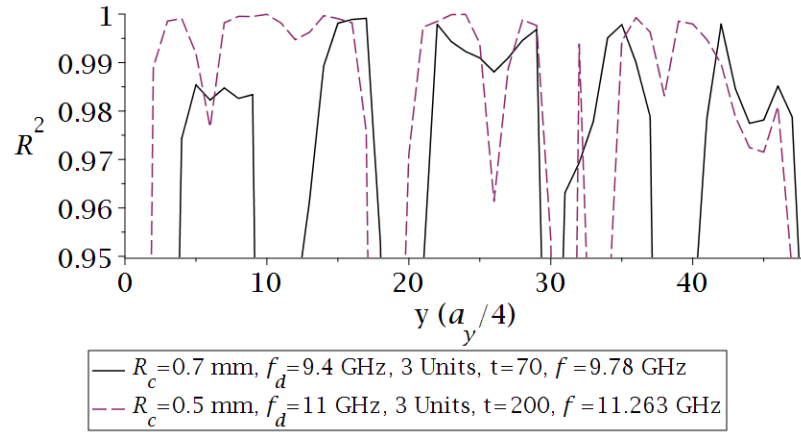
Figure 7.130: A plot of a figure of merit ($\mathfrak{R}^2$) for the comparison between the desired profile and the field profile (longitudinal, z, spatial variation of the electric field strength, E_z) of the field (9.78 GHz) in time domain simulations of a finite dielectric wire medium ($t = 70$ ns; 3 units of 4×4; $\varepsilon_r = 100$, $a_x = 13.06$ mm and $a_y = 15.00$ mm; $q = 0.8$, $f_d = 9.4$ GHz, $R_c = 0.7$ mm and $\lambda_C = 9.05$ GHz; open y boundaries and, metallic x and z boundaries; and a waveguide port, which is distanced 10 mm from the lattice, with dimension 19×9.5 mm) at the evaluation position against the y position of the evaluation line given in terms of quarter lattice parameters from the bottom of the structure ($a_y/4$). A comparison is included with the plot resulting from a field (11.263 GHz) in our original time domain simulations of a finite dielectric wire medium ($t = 200$ ns; 3 units of 4×4; $\varepsilon_r = 100$, $a_x = 13.06$ mm and $a_y = 15.00$ mm; $q = 0.8$, $f_d = 11$ GHz, $R_c = 0.5$ mm and $\lambda_C = 10.1$ GHz; open y boundaries and, metallic x and z boundaries; and a waveguide port, which is distanced 10 mm from the lattice, with dimension 19×9.5 mm)

IX.6 Full structure

We have attempted to run a simulation identical to our control case, but with two periods of the wire variation, as is usually done in our eigenmode simula-

tions. The full wire radius variation used is shown in Fig. 7.131 and the resulting structure is shown in Fig. 7.132.
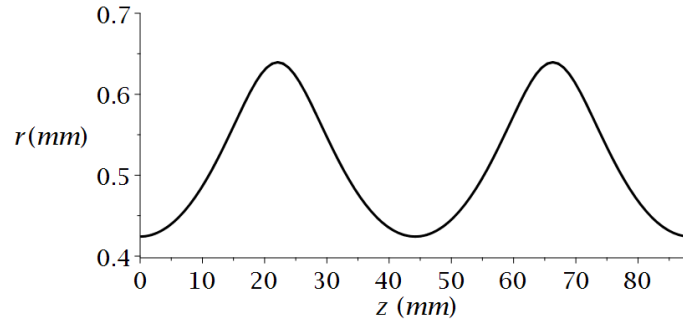
Figure 7.131: Two periods of the radius function calculated for a flattened profile ($q = 0.8$) in a partially finite dielectric wire medium (4×4, $\varepsilon_r = 100$, $a_x = 13.06$ mm and $a_y = 15.00$ mm) for the parameter choice of $f_d = 11$ GHz, $R_c = 0.5$ mm and $\lambda_C = 10.1$ GHz. This is the wire radius variation used in the following time domain simulations, although the lattice configurations used differ from the basis of the calculated function.
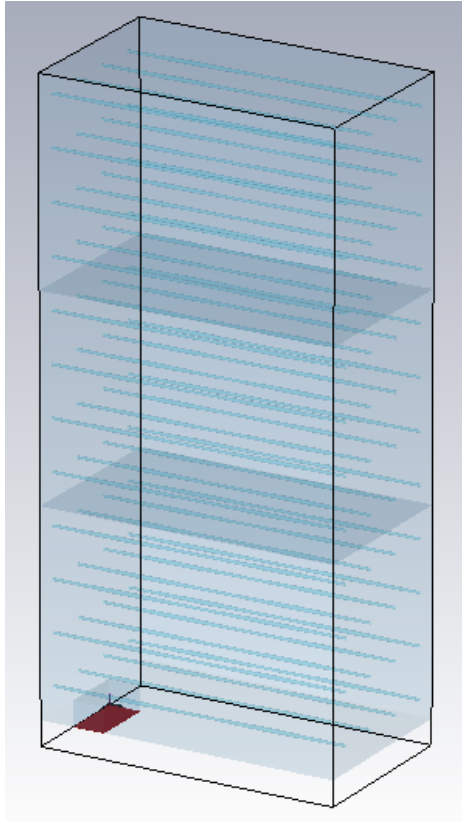
Figure 7.132: A representation of a finite wire medium in CST, consisting of three vertically stacked units of four by four lattices of dielectric wires. The unit cell has one set of metallic transverse boundary conditions, one set of open transverse boundary conditions and metallic longitudinal boundary conditions. The dielectric wires have a radius function calculated for a flattened profile ($q = 0.8$) in a partially finite dielectric wire medium (4×4, $\varepsilon_r = 100$, $a_x = 13.06$ mm and $a_y = 15.00$ mm) for the parameter choice of $f_d = 11$ GHz, $R_c = 0.5$ mm and $\lambda_C = 10.1$ GHz. A small section has been attached to the bottom of the structure with dimensions $x_{dim} = 19$ mm, $y_{dim} = 10$ mm and $z_{dim} = 9.5$ mm, where a waveguide port has been placed. This structure has dielectric wires with two periods of the radius variation.

We have initially used the same time setting as our control case, t=200 ns. The fields produced by our frequency monitors are shown in Fig. 7.133.
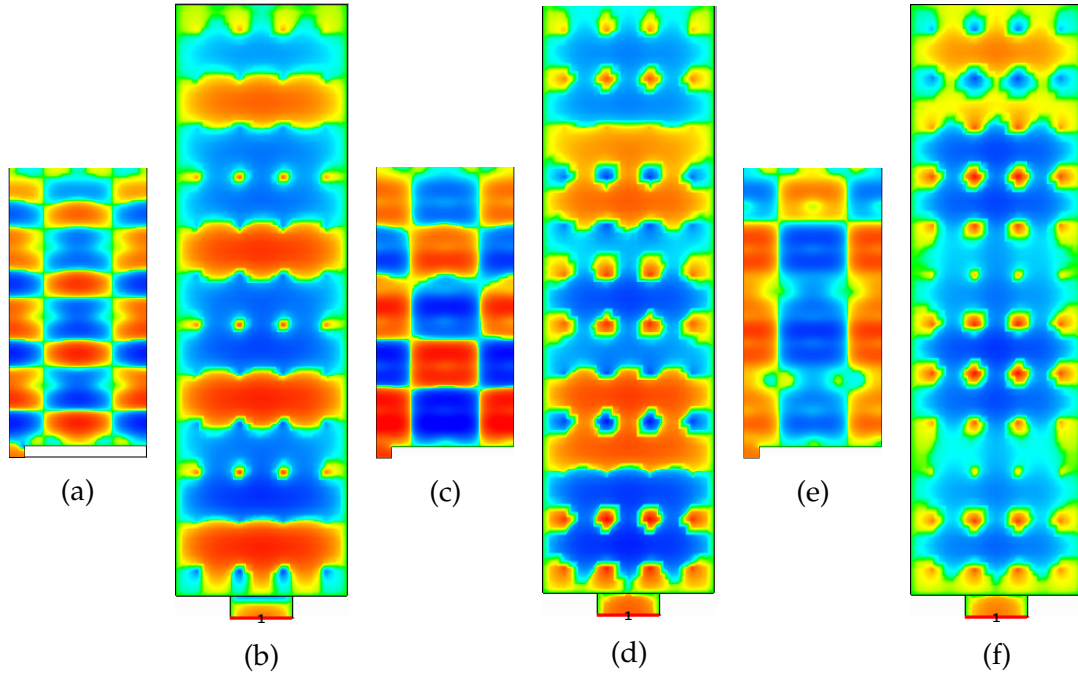
Figure 7.133: Images from numerical simulations in CST showing the fields found using different frequency monitors in a time domain simulation of a finite dielectric wire medium (3 units of 4×4; $\varepsilon_r = 100$, $a_x = 13.06$ mm and $a_y = 15.00$ mm; two periods, $q = 0.8$, $f_d = 11$ GHz, $R_c = 0.5$ mm and $\lambda_C = 10.1$ GHz; open y boundaries, and metallic x and z boundaries; and a waveguide port, which is distanced 10 mm from the lattice, with dimension 19×9.5 mm) with $t = 200$ ns. The fields are represented using logarithmic colour plots where the longitudinal field direction and magnitude is represented by colour. (a) shows a y-z slice ($f = 11.017$ GHz); (b), an x-y slice ($f = 11.017$ GHz); (c), a y-z slice ($f = 11.252$ GHz); (d), an x-y slice ($f = 11.252$ GHz); (e), a y-z slice ($f = 11.269$ GHz); and (f), an x-y slice ($f = 11.269$ GHz).

The $\mathfrak{R}^2$ plot for the field produced by the frequency monitor at 11.269 GHz is shown in Fig. 7.130. This plot shows a significantly worse performance compared to the single period structure.
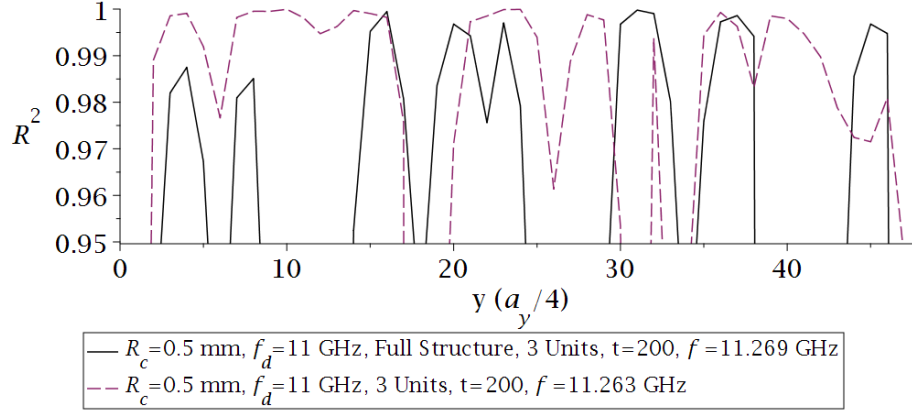
Figure 7.134: A plot of a figure of merit ($\mathcal{R}^2$) for the comparison between the desired profile and the field profile (longitudinal, z, spatial variation of the electric field strength, E_z) of the field (11.269 GHz) in time domain simulations of a finite dielectric wire medium ($t = 200$ ns; 3 units of 4×4; $\varepsilon_r = 100$, $a_x = 13.06$ mm and $a_y = 15.00$ mm; two periods, $q = 0.8$, $f_d = 11$ GHz, $R_c = 0.5$ mm and $\lambda_C = 10.1$ GHz; open y boundaries and, metallic x and z boundaries; and a waveguide port, which is distanced 10 mm from the lattice, with dimension 19×9.5 mm) at the evaluation position against the y position of the evaluation line given in terms of quarter lattice parameters from the bottom of the structure ($a_y/4$). A comparison is included with the plot resulting from a field (11.263 GHz) in our original time domain simulations of a finite dielectric wire medium ($t = 200$ ns; 3 units of 4×4; $\varepsilon_r = 100$, $a_x = 13.06$ mm and $a_y = 15.00$ mm; $q = 0.8$, $f_d = 11$ GHz, $R_c = 0.5$ mm and $\lambda_C = 10.1$ GHz; open y boundaries and, metallic x and z boundaries; and a waveguide port, which is distanced 10 mm from the lattice, with dimension 19×9.5 mm)

One possible reason for this deterioration in performance is that despite running for the same time, the situations are not equivalent, as the full structure is twice as long and therefore it will take more time for the excitation to progress. It would make sense to simulate for 400 ns, but we have done this, and the structure becomes unstable. Instead, we ran the simulation for 300 ns. The field produced by the frequency monitor in this new simulation is shown in Fig. 7.135.

(a)

(b)
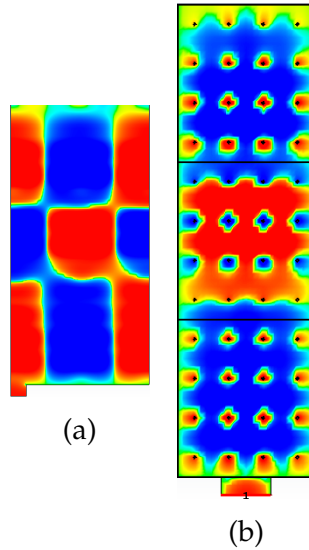
Figure 7.135: Images from numerical simulations in CST showing the field found using a frequency monitor in a time domain simulation of a finite dielectric wire medium (3 units of 4×4; $\varepsilon_r = 100$, $a_x = 13.06$ mm and $a_y = 15.00$ mm; two periods, $q = 0.8$, $f_d = 11$ GHz, $R_c = 0.5$ mm and $\lambda_C = 10.1$ GHz; open y boundaries, and metallic x and z boundaries; and a waveguide port, which is distanced 10 mm from the lattice, with dimension 19×9.5 mm) with $t = 300$ ns. The fields are represented using logarithmic colour plots where the longitudinal field direction and magnitude is represented by colour. (a) shows a y-z slice ($f = 11.262$ GHz); and (b), an x-y slice ($f = 11.262$ GHz).

The $\mathfrak{R}^2$ plot for the field observed by this frequency monitor is shown in Fig. 7.136. This plot shows a significant improvement, although the performance is still slightly weaker than for our original structure. One clear conclusion is that we were right to think that it would be easier to observe field profiling with a single period structure.
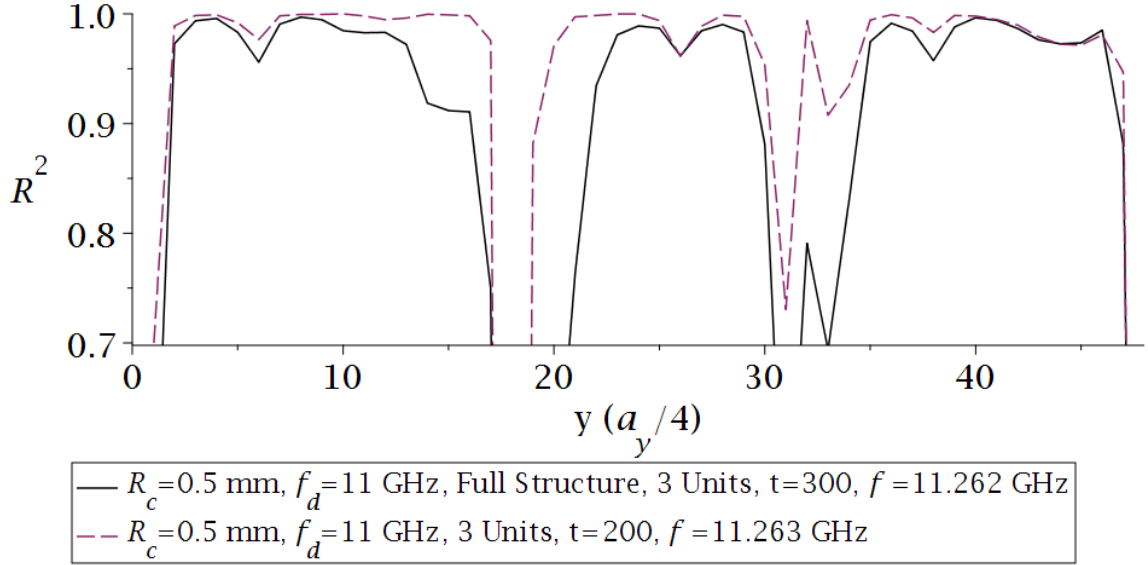
Figure 7.136: A plot of a figure of merit ($\mathfrak{R}^2$) for the comparison between the desired profile and the field profile (longitudinal, z, spatial variation of the electric field strength, E_z) of the field (11.262 GHz) in time domain simulations of a finite dielectric wire medium ($t = 300$ ns; 3 units of 4×4; $\varepsilon_r = 100$, $a_x = 13.06$ mm and $a_y = 15.00$ mm; two periods, $q = 0.8$, $f_d = 11$ GHz, $R_c = 0.5$ mm and $\lambda_C = 10.1$ GHz; open y boundaries and, metallic x and z boundaries; and a waveguide port, which is distanced 10 mm from the lattice, with dimension 19×9.5 mm) at the evaluation position against the y position of the evaluation line given in terms of quarter lattice parameters from the bottom of the structure ($a_y/4$). A comparison is included with the plot resulting from a field (11.263 GHz) in our original time domain simulations of a finite dielectric wire medium ($t = 200$ ns; 3 units of 4×4; $\varepsilon_r = 100$, $a_x = 13.06$ mm and $a_y = 15.00$ mm; $q = 0.8$, $f_d = 11$ GHz, $R_c = 0.5$ mm and $\lambda_C = 10.1$ GHz; open y boundaries and, metallic x and z boundaries; and a waveguide port, which is distanced 10 mm from the lattice, with dimension 19×9.5 mm)

X. CONCLUSIONS

In this chapter, we have verified that our method can be extended to a variety of different realisations of dielectric wire media while also examining several other factors which impact on the practicality of our method. We started by confirming that our method could be applied with wire media with a variety of permittivities as low as $\varepsilon_r = 3$. By considering several different lattice parameters, we showed that our longitudinal modes can be supported in a wide range of lattices with different frequencies. We have considered the introduction of disorder into our infinite wire media, in the form of random and systematic errors in the radii of our wires, and the presence of cladding around our wires. Our method proved

to be stable to these perturbations. We have shown that our method is applicable for both partially finite and finite wire media, with a variety of lattice sizes. This allowed us to also consider the effect of the introduction of a variety of disorders into partially finite wire media, with our method again proving to be quite stable. Finally, we have shown some success in observing field profile shaping in finite wire media in time domain simulations, although we have not fully considered the transmission of these fields.

Chapter 8

Mode profile shaping method with metallic wire media

We have developed a method for mode profile shaping using dielectric wires that has proved to be very successful. We wanted to see if we could extend this method to metallic wires. This seemed a reasonable step to take as the theoretical work underpinning our method was based on an analysis of metal wires. If we could confirm that our method can be extended to metal wires, then it would allow for greater flexibility when attempting to achieve a physical realisation of our structures and the mode profiling they facilitate.

I. ESTABLISHING OUR METHOD WITH WIRES MADE OF A PERFECT ELECTRICAL CONDUCTOR (PEC)
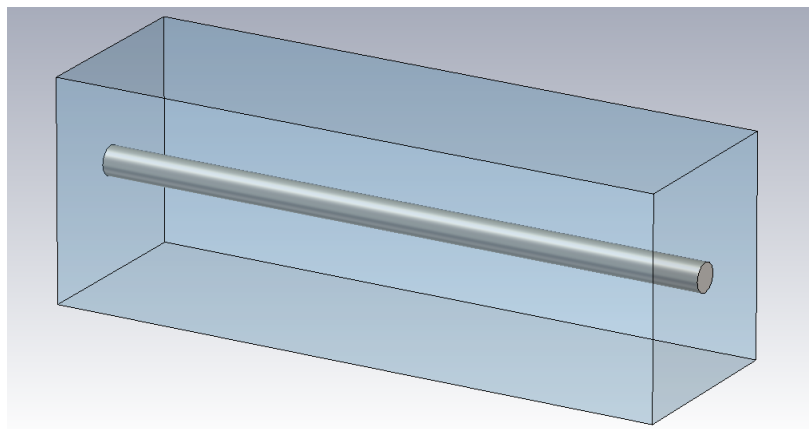
Figure 8.1: A typical representation of a wire medium in CST, consisting of a section of a wire made of a perfect electrical conductor (PEC) in a unit cell with periodic boundary conditions. This effectively represents an infinite PEC wire medium.

To start our exploration of metal wire media, we had to pick what material to use. We first chose the idealised material available in CST that is defined to be a perfect electrical conductor (PEC). This material is an idealised version of a metal. With the material chosen, we then started with an infinite lattice of wires. This is achieved in CST by using a unit cell centred on our PEC wire, with periodic boundary conditions applied to all boundaries. The transverse dimensions of the unit cell define the lattice parameters of the lattice. Throughout all the simulations in this section, the lattice parameters are set as $a_x = 13.06$ mm and $a_y = 15$ mm. This set-up can be seen in Fig. 8.1.
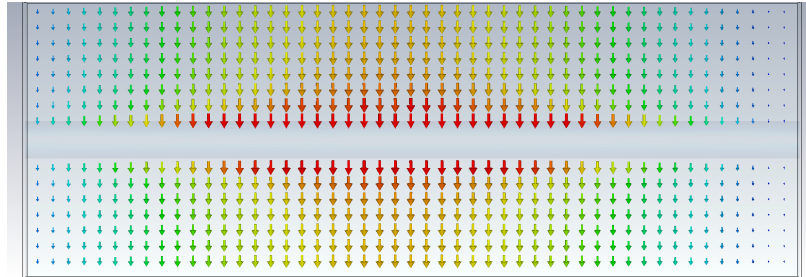
Figure 8.2: Numerical results showing a transverse electric mode, with a frequency of 3.53 GHz, in a representation of an infinite array of PEC wires of radius 0.3mm, with wire spacings $a_x = 13.06$ mm and $a_y = 15.00$ mm. The electric field is represented using a vector plot of a y-z slice of the structure where the arrow direction represents field direction and colour represents the magnitude of the field strength.

Having settled on an initial structure to explore, we ran eigenmode simulations to explore the modes supported by our structure and find our longitudinal electric modes. The majority of the modes found in these structures are transverse modes, such as the mode shown in Fig. 8.2. For structures with radii in an appropriate range, we can also find our desired longitudinal modes, as shown in Fig. 8.3 for a radius of 1 mm. As can be seen from Fig. 8.3 these modes have a significant longitudinal component outside of the wire near the boundaries of the unit cell, but, unlike the longitudinal modes found in our dielectric wire medium, the field in the wire is zero. This is to be expected from a metal wire.

<div align="center">(a)   (b)</div>
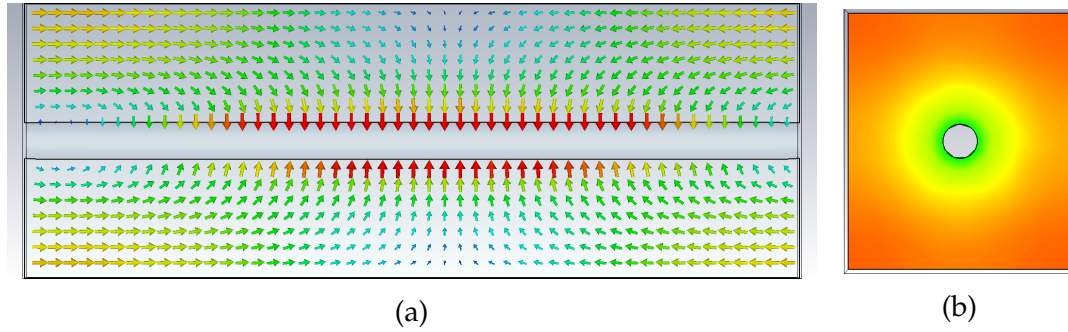
Figure 8.3: Images from numerical simulations in CST showing the longitudinal mode ($f = 7.94$ GHz) found in an infinite PEC wire medium ($r = 1$ mm, $a_x = 13.06$ mm and $a_y = 15.00$ mm). The fields are either represented using arrow plots where the arrow direction represents field direction and colour represents the magnitude of the field strength, or colour plots where the direction and magnitude of the longitudinal field is represented by colour. (a) shows a y-z slice of the structure and (b) an x-y slice.

One of the key predictions made about these modes is the form of their dispersion relation. The expected dispersion relation is a plasma-like dispersion relation given by $f^2 = \beta^2 c^2 \kappa^2 + \lambda_s^2$. Where f is the frequency, c is the speed of light in a vacuum, κ is the wavenumber divided by 2π and λ_s is the plasma frequency or cut-off frequency. By varying the phase associated with the longitudinal dimension in our simulations, we can vary κ and build up a plot of the dispersion relation. A dispersion plot of the longitudinal mode found with a wire radius of 1 mm was found. As in the dielectric case in Chapter 6, we can confirm whether this dispersion is plasma-like by plotting f^2 vs κ^2, as the curve should then obey the classic straight line formula—$y = mx + c$. We can see that this is true by looking at the predicted dispersion relation in equation 4.20. If we set f^2 as y and κ as x, then we will retrieve the straight line equation with $m = \beta^2 c^2$ and $C = \lambda_s^2$. The plot of f^2 vs κ^2 for the longitudinal mode found is shown in Fig. 8.4. Fig. 8.4 confirms that the longitudinal mode found does have the expected dispersion relation and by taking the intercept of the straight line fit in the figure we can find the value for the plasma frequency.

Our method for mode profiling relies on us being able to manipulate the plasma frequency and, in particular, make it vary longitudinally. As with the development of our method with dielectric wires, we will attempt to achieve this control by changing the radius of the wires. Before we can do this, we need to study the effect of the wire radius on the plasma frequency. To do this, we need to find our longitudinal modes for a variety of PEC wire radii. In Fig. 8.5 we show the longitudinal modes for wires of radius $r = 0.8, 1, 1.2$ mm. These modes have been found for the same κ value but are at different frequencies.

We can see that the change in radius has affected the dispersion relation of these modes. This is clear in Fig. 8.6 where the dispersion relation of modes

<div align="center">223</div>
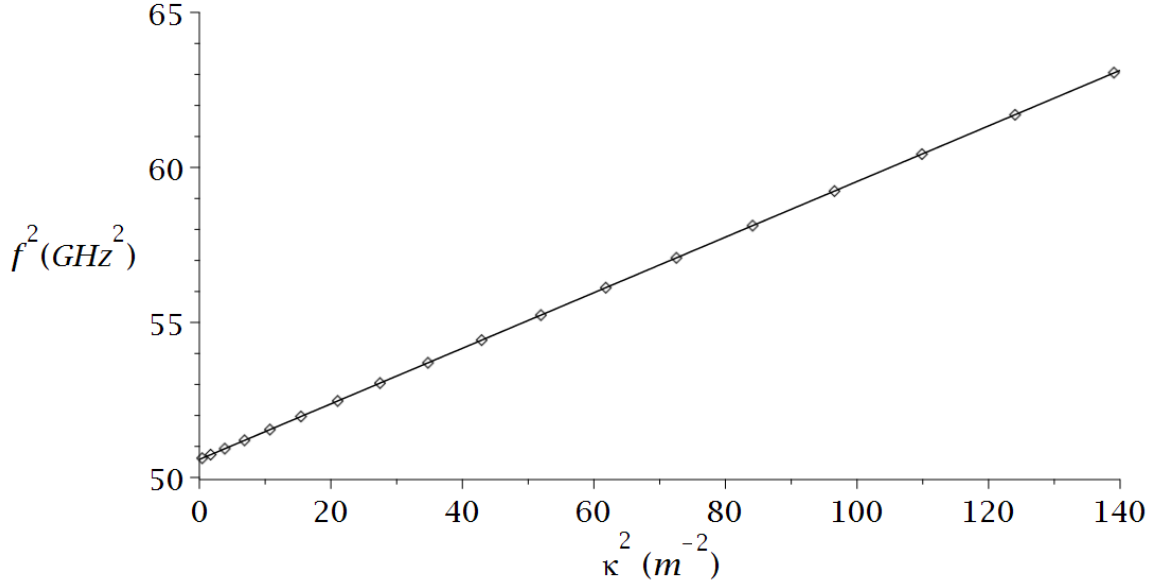
Figure 8.4: A plot of f^2 against κ^2 for a longitudinal mode found in an infinite PEC wire medium ($r = 1$ mm, $a_x = 13.06$ mm and $a_y = 15.00$ mm) along with a straight line fit which helps to demonstrate the plasma-like nature of the dispersion relation.

associated with different radii has been plotted. The change in radius produces a shift in the dispersion curve, which will result in a shift in the plasma frequency. This is shown in Fig. 8.7 where f^2 vs. κ^2 is plotted for different radii, and the cut-off of their straight line fits are shown. As we have discussed, the cut-off of these straight lines is directly related to the plasma frequency.

$$\lambda_s^2(r) \approx \Delta + \Theta r \qquad (8.1)$$

By plotting the dispersion relation for a variety of radii, we can determine the relationship between the plasma frequency, λ_s, and the wire radius, r. It is clear from Fig. 8.8 that the relationship can be extremely well described by a straight line. In this figure the data has been plotted with a straight line, of the form shown in equation 8.1 where Δ and Θ are the fitting parameters, fitted to the data. The fitting parameters for this line are $\Delta = 18.3$ (GHz^2) and $\Theta = 32.7$ (GHz^2/mm). This straight line fit clearly describes the data extremely well, which is confirmed quantitatively by the $\Re^2$ of 0.9992.

For our previous attempts at mode profile shaping the relationship between the plasma frequency and the wire radius has been well described by an exponential decay curve. As we have seen for a PEC wire this relationship is well described by a straight line fit.

This does not present any problems in implementing our previously established method, but it will change the form of our required radius functions. As
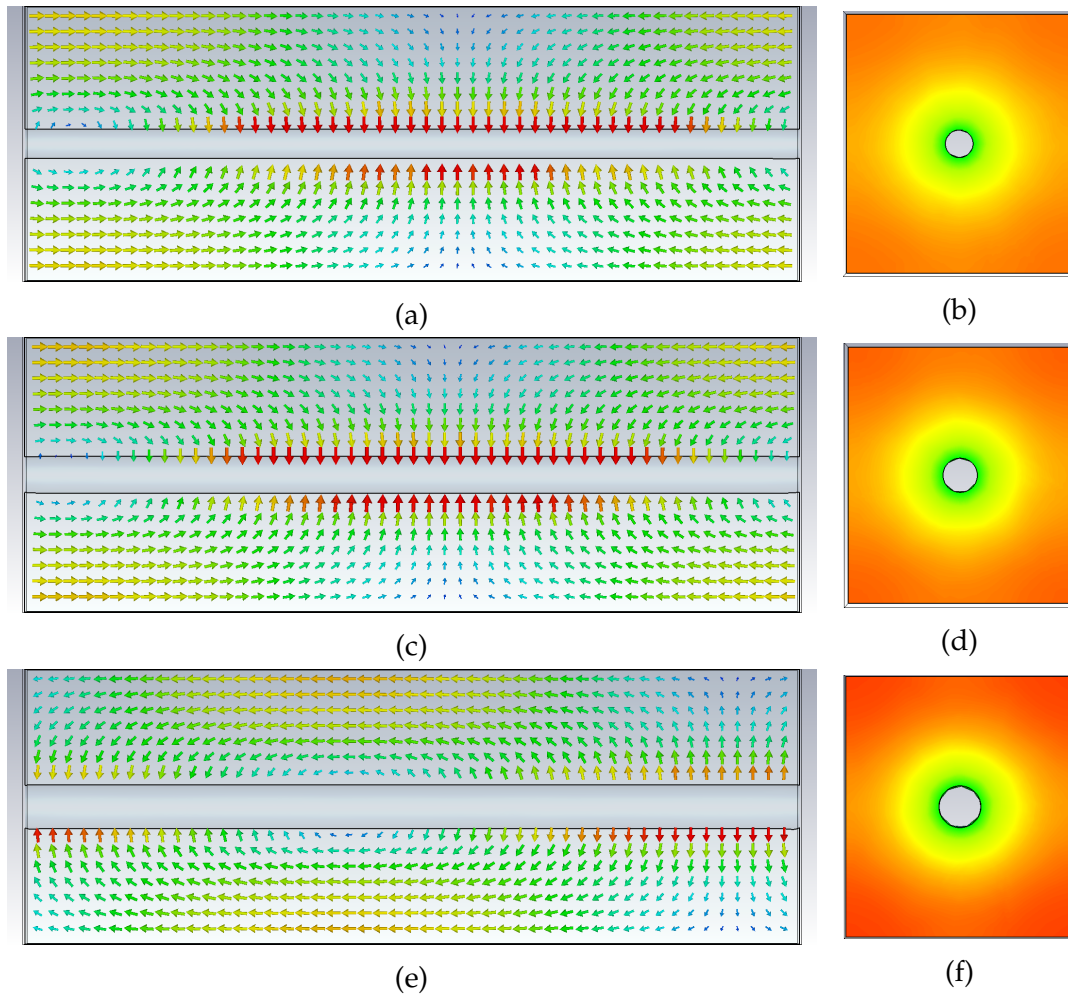
Figure 8.5: A series of images from numerical simulations in CST showing the longitudinal modes found in infinite PEC wire media ($a_x = 13.06$ mm and $a_y = 15.00$ mm) with a variety of radii. The fields are either represented using arrow plots where the arrow direction represents field direction and colour represents the magnitude of the field strength, or colour plots where the direction and magnitude of the longitudinal field is represented by colour. (a) and (b) show a longitudinal mode ($f = 7.53$ GHz) in a wire medium with $r = 0.8$ mm, with (a) showing a y-z slice and (b) an x-y slice. (c) and (d) show a longitudinal mode ($f = 7.94$ GHz) in a wire medium with $r = 1$ mm, with (c) showing a y-z slice and (d) an x-y slice. (e) and (f) show a longitudinal mode ($f = 8.35$ GHz) in a wire medium with $r = 1.2$ mm, with (e) showing a y-z slice and (f) an x-y slice.
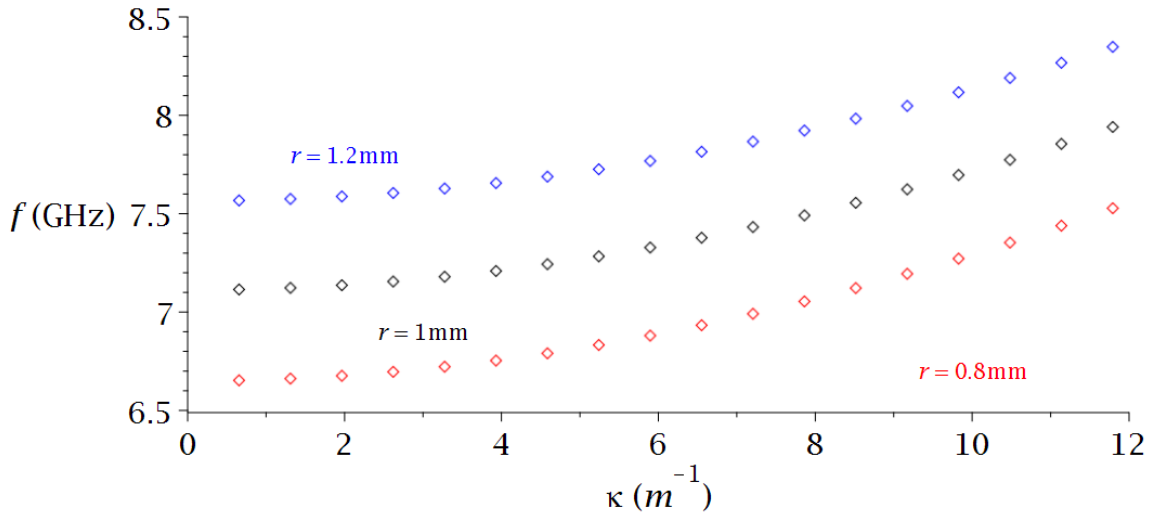
Figure 8.6: The dispersion plots, frequency (f) against wavenumber (κ), of the longitudinal modes in infinite PEC wire media ($a_x = 13.06$ mm and $a_y = 15.00$ mm) with a variety of radii. The radii are 0.8 mm (red), 1 mm (black) and 1.2 mm (blue).
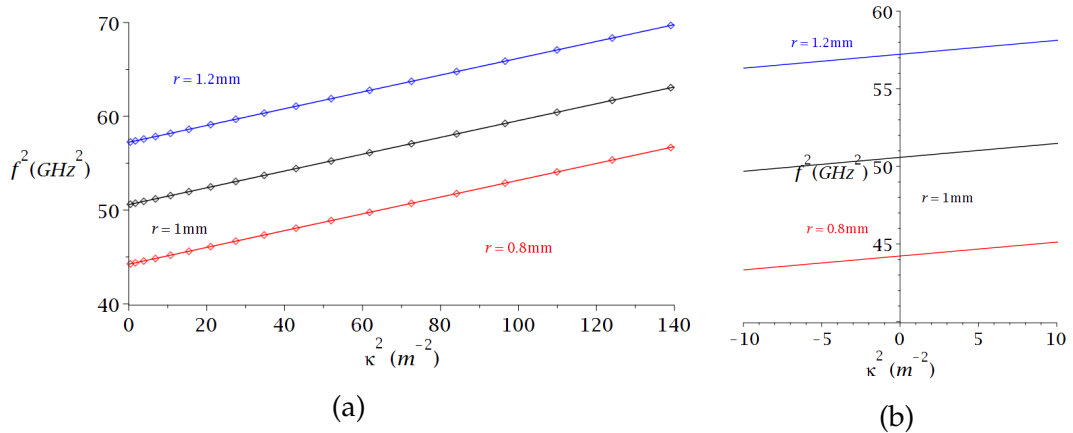
Figure 8.7: Plots of frequency squared, f^2, against wavenumber squared, κ^2, for the longitudinal modes in infinite PEC wire media ($a_x = 13.06$ mm and $a_y = 15.00$ mm) with a variety of radii. Straight line fitting curves have been included for each radii. The radii shown are 0.8 mm (red), 1 mm (black) and 1.2 mm (blue). (a) shows the plots and the fitting curves, whereas (b) shows only the fitting curves as they cross the y-axis to emphasise their different intercept values.
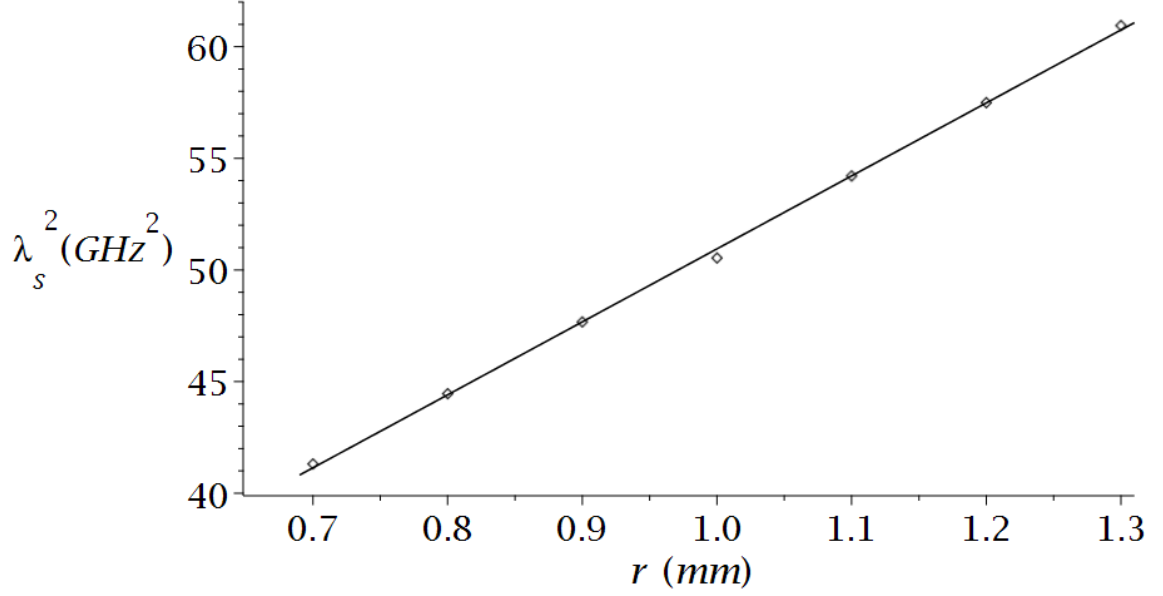
Figure 8.8: A plot of the plasma frequency squared, λ_s^2, of infinite PEC wire media ($a_x = 13.06$ mm and $a_y = 15.00$ mm) against wire radius, r, with a straight line fitting curve.

usual, to achieve mode profiling in our structure the condition set out in equations 8.2 and 8.3 must be satisfied.

$$\Lambda^2(z) = f^2 - \frac{\beta^2 c^2}{L^2}\left[a - 2q\cos\left(\frac{4\pi z}{L}\right)\right] \tag{8.2}$$

$$\lambda_s^2(R(z)) = \Lambda^2(z) \tag{8.3}$$

For the case of our PEC wires this condition will be satisfied if equation 8.4 is satisfied.

$$\Delta + \Theta R(z) = f^2 - \frac{\beta^2 c^2}{L^2}\left[a - 2q\cos\left(\frac{4\pi z}{L}\right)\right] \tag{8.4}$$

This condition for the support of our desired mode profile can be solved to give the following condition for the wire radius function required.

$$R(z) = \frac{f^2 - \Delta}{\Theta} - \frac{\beta^2 c^2}{\Theta L^2}\left[a - 2q\cos\left(\frac{4\pi z}{L}\right)\right] \tag{8.5}$$

Equation 8.5 has been rewritten in equation 8.6 in order to emphasise the form of the function.
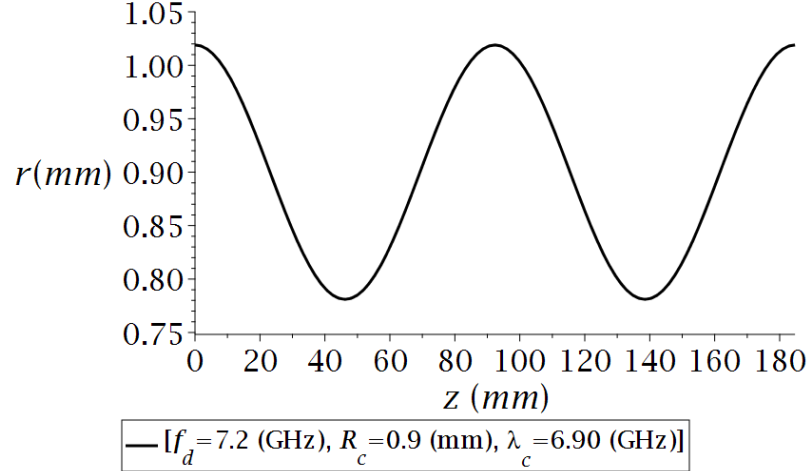
Figure 8.9: Radius function calculated for a flattened profile ($q = 0.8$) in an infinite PEC wire medium ($a_x = 13.06$ mm and $a_y = 15.00$ mm) for the parameter choice of $f_d = 7.2$ GHz, $R_c = 0.9$ mm and $\lambda_C = 6.90$ GHz.

$$R(z) = \eta_1 + \eta_2 \cos(\eta_3) \tag{8.6}$$

$$\eta_1 = \frac{f^2 L^2 - \Delta L^2 - \beta^2 c^2 a}{L^2 \Theta} \tag{8.7}$$

$$\eta_2 = \frac{2\beta^2 c^2 q}{L^2 \Theta} \tag{8.8}$$

$$\eta_4 = \frac{4\pi}{L} \tag{8.9}$$

We have been able to solve for a radius function which should allow our structure to support our desired longitudinal field profiles for a given choice of parameters. The value of a and q is specified by our choice of profile. We have to take care to fix the other parameters appropriately.

To test our method, we will implement a radius function into our CST models using a series of conical frustums. Our first attempt at validating our method for PEC wires was based on a flat Mathieu solution (Mathieu parameter $q = 0.8$). Having chosen our desired profile, we then fixed our parameters: $f_d = 7.2$ GHz and $R_C = 0.9$ mm. The required radius function given by our method is plotted in Fig. 8.9. The related parameters for this radius function are listed in Table 8.1.

Having implemented our required radius function into a CST model of an infinite PEC wire medium, we then ran an eigenmode simulation to examine the modes found. Extremely close to the design frequency of 7.2 GHz, we found a longitudinal mode, $f = 7.22$ GHz, which is shown in Fig. 8.10.

Using our usual method of evaluating the field strength of the field along a line along the top of the unit cell, we can examine the mode profile. This is shown in Fig. 8.11 along with a comparison with the desired Mathieu profile. We can see

(a)

(b)
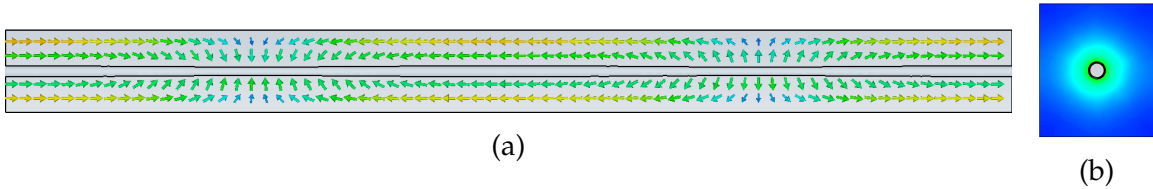
Figure 8.10: Images showing the resulting longitudinal mode ($f = 7.22$ GHz) after the implementation of the calculated radius function for a flattened profile ($q = 0.8$) in an infinite PEC wire medium ($a_x = 13.06$ mm and $a_y = 15.00$ mm) for the parameter choice of $f_d = 7.2$ GHz, $R_c = 0.9$ mm and $\lambda_C = 6.90$ GHz. The fields are either represented using arrow plots where the arrow direction represents field direction and colour represents the magnitude of the field strength, or colour plots where the direction and magnitude of the longitudinal field is represented by colour. (a) shows the field on a y-z slice of the structure, and (b) shows the field on an x-y slice.

from Fig. 8.11 that our mode profile shaping method has been very successful, which is confirmed by the $\mathfrak{R}^2$ value for these two curves of 0.9955.
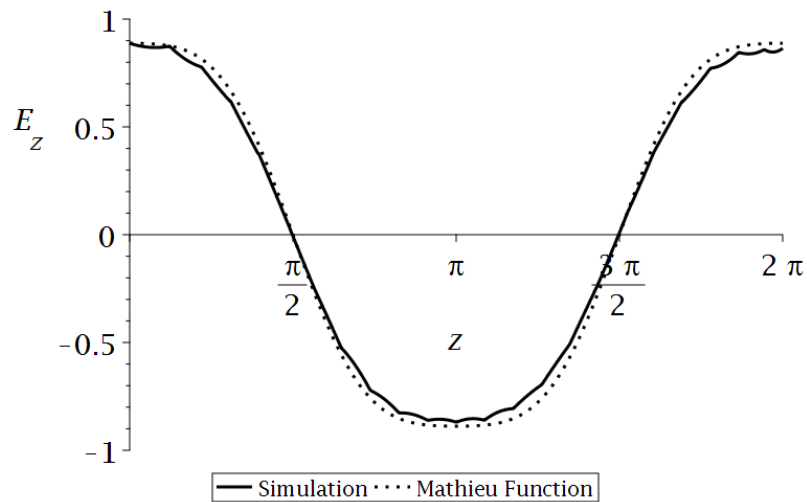
Figure 8.11: A plot of the field profile (longitudinal, z, spatial variation of the electric field strength, E_z) of the longitudinal mode ($f = 7.22$ GHz) in an infinite PEC wire medium ($a_x = 13.06$ mm and $a_y = 15.00$ mm) for our attempt to produce a flattened profile ($q = 0.8$) with a radius function based on the parameter choice of $f_d = 7.2$ GHz, $R_c = 0.9$ mm and $\lambda_C = 6.90$ GHz. The plot includes the field profile observed in our numerical simulation (solid black) and the desired profile (dotted black). In order to aid comparison the field profile from our simulation and the z coordinate have been normalised.

Following the success of our mode profiling method with one profile, we wanted to explore if the method could be used to support a variety of mode

profiles. The other profiles we attempted to replicate were a triangular profile (Mathieu parameter $q = -0.329$), a profile with an increased number of turning points (Mathieu parameter $q = 4$) and a profile with a pronounced peak (Mathieu parameter $q = -10$).

The choice of fixed parameters for each of these profiles, and the resulting parameters for the required radius function and structure are listed in Table 8.1. The required radius functions have also been plotted in Fig. 8.12.

q	f_d (GHz)	R_C (mm)	λ_C (GHz)	η_1 (mm)	η_2 (mm)	η_3 (mm^{-1})	L (mm)
0.8	7.2	0.9	6.9	0.9	0.119	0.0680	185
-0.329	7.2	0.9	6.9	0.9	-0.127	0.110	115
4	7	0.9	6.9	0.9	0.140	0.0329	381
-10	6.5	0.9	6.9	0.9	-0.238	0.0272	461

Table 8.1: A table summarising some of the key parameters related to the implemented radius functions for a variety of profiles in infinite PEC wire media ($a_x = 13.06$ mm and $a_y = 15.00$ mm). The first set of parameters listed are design parameters we chose: the Mathieu parameter characterising the profile (q), design frequency (f_d), central radius (R_C) and the corresponding central plasma frequency (λ_c). The rest are the resulting structural parameters: the parameters specifying the corresponding radius function (η_{1-3}) and the length of our unit cell (L). The profiles considered are a triangular profile ($q = -0.329$), a profile with multiple turning points ($q = 4.0$) and a profile with a pronounced peak ($q = -10.0$).

Figure 8.12: A series of plots of radius functions calculated for a variety of desired profiles in infinite PEC wire media ($a_x = 13.06$ mm and $a_y = 15.00$ mm). (a) shows the radius function for a triangular profile with a parameter choice of $f_d = 7.2$ GHz, $R_c = 0.9$ mm and $\lambda_C = 6.90$ GHz (crimson); (b), for a profile with multiple turning points with a parameter choice of $f_d = 7$ GHz, $R_c = 0.9$ mm and $\lambda_C = 6.90$ GHz (dark blue); and (c), for a profile with a pronounced peak with a parameter choice of $f_d = 6.5$ GHz, $R_c = 0.9$ mm and $\lambda_C = 6.90$ GHz (dark green).

We can now implement these radius functions to build a wire medium with the required radius variation. The modes found in eigenmode simulations for our attempts at replicating the triangular profile and profile with a larger number of turning points are shown in Fig. 8.13.

(a)

(b)

(c)

(d)
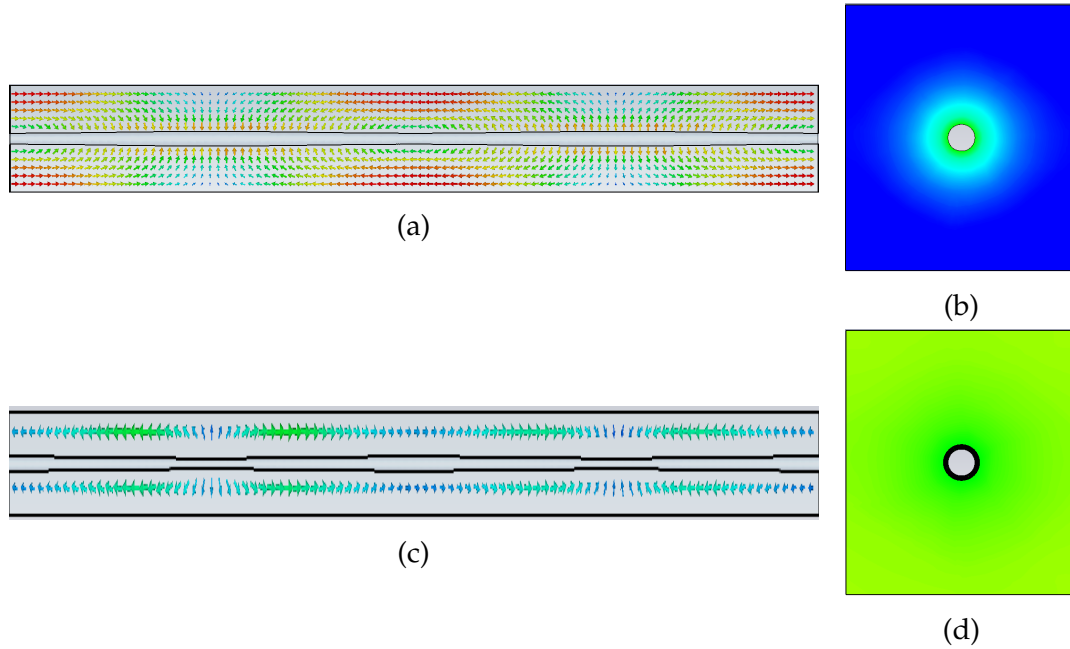
Figure 8.13: Images showing the resulting longitudinal modes after the implementation of the calculated radius function for a triangular profile ($q = -0.329$) and a profile with multiple turning points ($q = 4.0$) in infinite PEC wire media ($a_x = 13.06$ mm and $a_y = 15.00$ mm). The fields are represented using arrow plots on a y-z slice of the structure where the arrow direction represents field direction and colour represents the magnitude of the field strength, and colour plots on an x-y slice where the direction and magnitude of the longitudinal field is represented by colour. (a) and (b) shows the resulting longitudinal mode ($f = 7.17$ GHz) for the attempt to demonstrate a triangular profile by the implementation of a radius function based on the choice of $f_d = 7.2$ GHz, $R_c = 0.9$ mm and $\lambda_C = 6.90$ GHz; and (c) and (d), the resulting longitudinal mode ($f = 7.02$ GHz) for the attempt to achieve a profile with multiple turning points by the implementation of a radius function based on the choice of $f_d = 7$ GHz, $R_c = 0.9$ mm and $\lambda_C = 6.90$ GHz.

The profiles of these modes are shown in Fig. 8.14 along with the desired profiles. These plots show that our attempts at mode profiling have been successful. A quantitative measure of our mode profiling success is given by the $\mathfrak{R}^2$ values for the triangular profile and the turning point profile of 0.9992 and 0.9187 respectively. We should note, the performance of the turning point profiling is clearly not perfect, especially near the peaks, but it is still clearly closer to the desired profile than a sinusoidal profile.
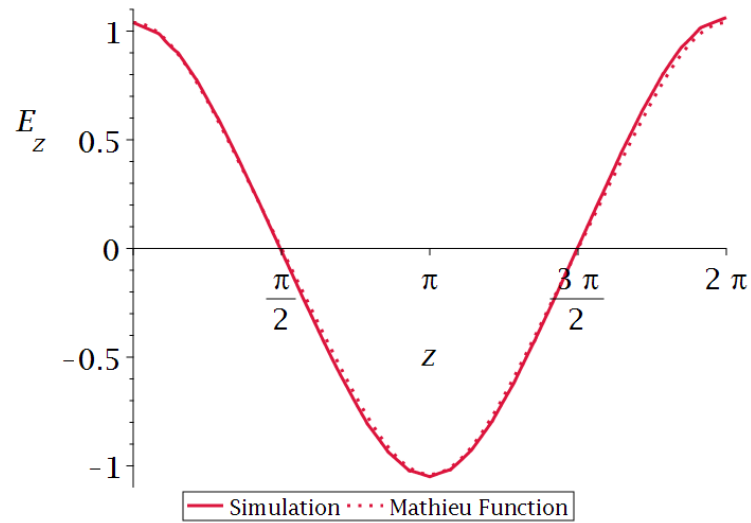
(a)
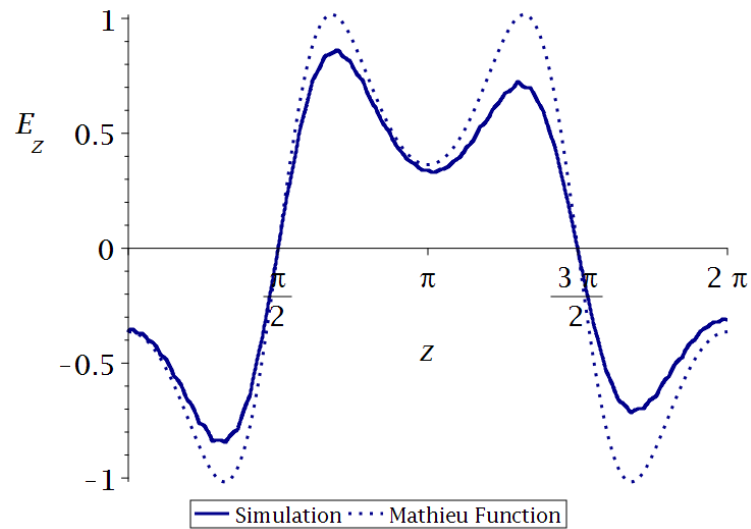
(b)

Figure 8.14: Plots of the field profiles (longitudinal, z, spatial variation of the electric field strength, E_z) of the longitudinal modes in infinite PEC wire media ($a_x = 13.06$ mm and $a_y = 15.00$ mm) for our attempts to produce a triangular profile ($q = -0.329$) and a profile with multiple turning points ($q = 4.0$). The plots include the field profile observed in our numerical simulation (solid) and the desired profile (dotted). In order to compare these the field profile and z coordinate have been normalised. (a) shows the field profile of the longitudinal mode ($f = 7.17$ GHz) for the attempt to demonstrate a triangular profile by the implementation of a radius function based on the choice of $f_d = 7.2$ GHz, $R_c = 0.9$ mm and $\lambda_C = 6.90$ GHz (crimson); and (b), the field profile of the longitudinal mode ($f = 7.02$ GHz) for the attempt to achieve a profile with multiple turning points by the implementation of a radius function based on the choice of $f_d = 7$ GHz, $R_c = 0.9$ mm and $\lambda_C = 6.90$ GHz (dark blue).

As we have previously found, assessing the mode profiling success for our attempts to replicate a profile with a pronounced peak is complicated. Instead of finding one longitudinal mode near our design frequency, we find two with very similar frequencies that have significant field strength only in certain, complementary areas of the structure. These modes are shown in Fig. 8.15. They were found around the design frequency of 6.5 GHz at 6.4960 GHz and 6.4968 GHz. This is a mode separation of just 0.0008 GHz.

(a)

(b)
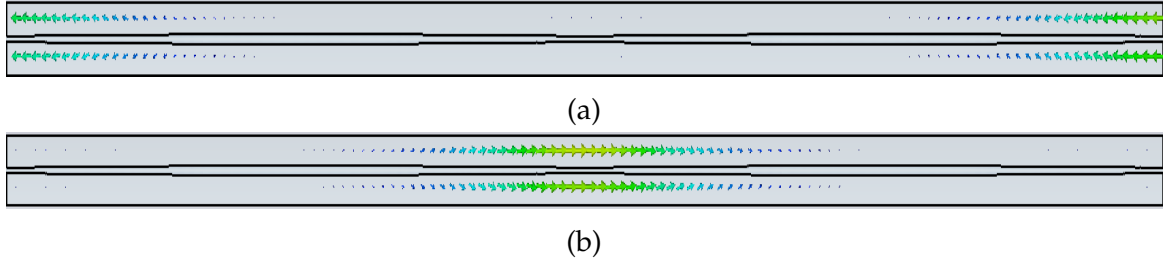
Figure 8.15: Images showing the resulting longitudinal modes after the implementation of the calculated radius function for a profile with a pronounced peak ($q = -10.0$) in an infinite PEC wire medium ($a_x = 13.06$ mm and $a_y = 15.00$ mm) with the parameter choice of $f_d = 6.5$ GHz, $R_c = 0.9$ mm and $\lambda_C = 6.90$ GHz. The fields are represented using arrow plots on a y-z slice of the structure where the arrow direction represents field direction and colour represents the magnitude of the field strength. (a) shows one of the resulting longitudinal modes ($f = 6.4960$ GHz); and (b), the other ($f = 6.4968$ GHz).

We can see from Fig. 8.15 that the fields in these modes are localised in different areas. In these areas, the fields resemble what we would expect from our desired mode. If we combine the profiles of these two modes, then we can see that the result is very similar to our desired profile, with an $\mathfrak{R}^2$ value of 0.9768. This is shown in Fig. 8.16. This seems to be an error with CST mislabelling our desired mode as two different modes.
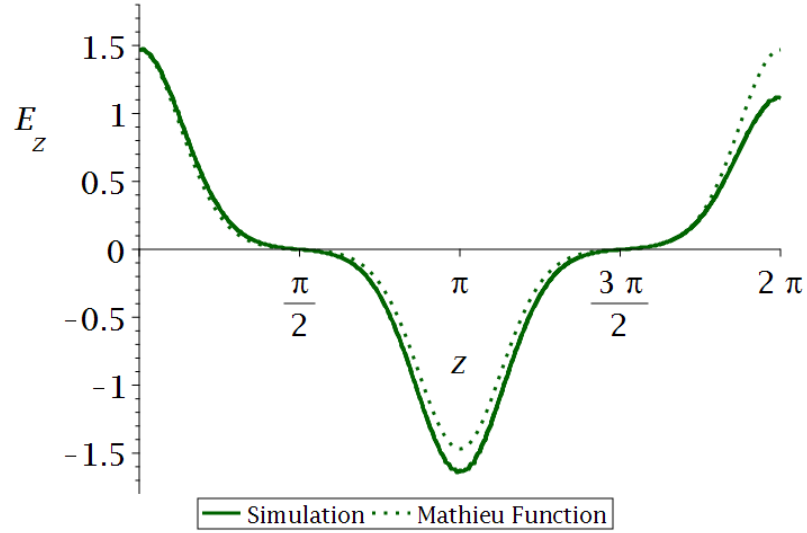
Figure 8.16: A plot of the combined field profile (longitudinal, z, spatial variation of the electric field strength, E_z) of the two longitudinal modes ($f = 6.4960$ GHz and $f = 6.4968$ GHz) in an infinite PEC wire medium ($a_x = 13.06$ mm and $a_y = 15.00$ mm) for our attempts to produce a profile with a pronounced peak ($q = -10.0$) with the parameter choice of $f_d = 6.5$ GHz, $R_c = 0.9$ mm and $\lambda_C = 6.90$ GHz (dark green).

The results of these simulations show that our mode profiling method has been successful for a variety of profiles with an infinite lattice of PEC wires. These results have been summarised in Table 8.2. This is a promising step in our efforts to extend our results to metallic wires. In our examination of dielectric wires, we moved from examining infinite lattices to finite lattices. In this case, we decided to investigate infinite lattices of actual metal before attempting to simulate partially or fully finite structures, as we wanted to confirm our results hold for more realistic material properties.

q	f_d (GHz)	λ_C (GHz)	L (mm)	f (GHz)	$\mathfrak{R}^2$
0.8	7.2	6.9	185	7.21	0.9955
-0.329	7.2	6.9	115	7.17	0.9992
4	7	6.9	381	7.02	0.9187
-10	6.5	6.9	461	6.50	0.9768

Table 8.2: A table summarising some of the key parameters related to the results of our implemented radius functions for a variety of profiles in infinite PEC wire media ($a_x = 13.06$ mm and $a_y = 15.00$ mm). The parameters listed are: the Mathieu parameter characterising the profile (q), design frequency (f_d), the central plasma frequency (λ_c), the length of our unit cell (L), longitudinal mode frequency (f) and a figure of merit for the agreement between our field profile and the desired profile ($\mathfrak{R}^2$). The profiles considered are a triangular profile ($q = -0.329$), a profile with multiple turning points ($q = 4.0$) and a profile with a pronounced peak ($q = -10.0$).

II. EXTENDING OUR METHOD TO INFINITE COPPER WIRE MEDIA

We have had success replicating our original method for mode profile shaping, which was developed using dielectric wire media, with wire media consisting of metal wires. In particular, we have been able to successfully shape mode profiles in simulations of PEC wire media. This is an idealised material that cannot be replicated in reality. We, therefore, extended this work to include the use of copper wires. In CST a material is defined for use in simulations which has the material properties of copper, such as the thermal and electrical conductivity, heat capacity, density and other properties.
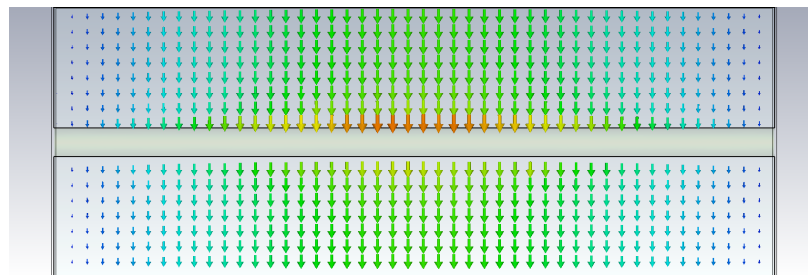
Figure 8.17: Numerical results showing a transverse electric mode, with a frequency of 3.73 GHz, in a representation of an infinite array of copper wires of radius 0.3 mm, and wire spacings $a_x = 13.06$ mm and $a_y = 15.00$ mm. The electric field is represented using a vector plot of a y-z slice of the structure where the arrow direction represents field direction and colour represents the magnitude of the field strength.

With a representation of copper available to us, we can then attempt to repli-

cate our previous results. The most simple case to begin with is a unit cell with periodic boundary conditions. Our first step is to find the expected longitudinal modes for our choice of structure and wire material. As we would expect, the structure supports a large number of transverse modes, such as the one shown in Fig. 8.17. Fig. 8.18 shows a longitudinal mode, $f = 7.62$ GHz, found in a simulation of a copper wire lattice with lattice parameters $a_x = 15$ mm and $a_y = 13.01$ mm, and wire radius $r = 0.8$ mm. It can be seen that it has the expected characteristics of our longitudinal mode. Fig. 8.19 shows the squared dispersion relation for the longitudinal mode. It is clear from Fig. 8.19 that the dispersion relation has the correct behaviour.

(a) (b)
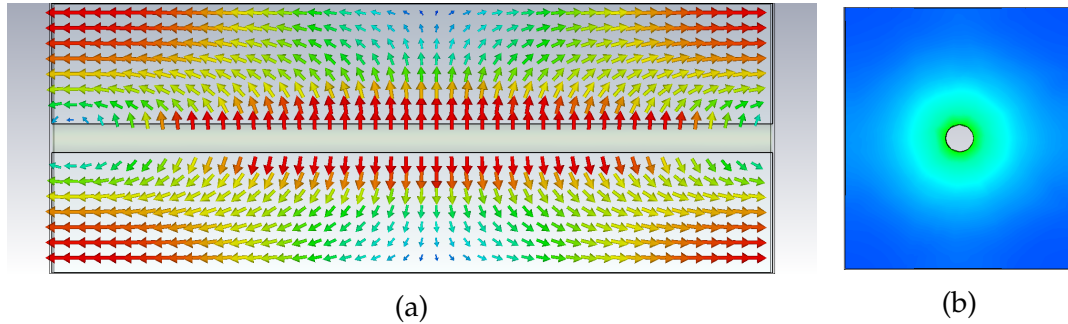
Figure 8.18: Images from numerical simulations in CST showing the longitudinal mode ($f = 7.62$ GHz) found in an infinite copper wire medium ($r = 0.8$ mm, $a_x = 13.06$ mm and $a_y = 15.00$ mm). The fields are either represented using arrow plots where the arrow direction represents field direction and colour represents the magnitude of the field strength, or colour plots where the direction and magnitude of the longitudinal field is represented by colour. (a) shows a y-z slice of the structure and (b) an x-y slice.

Having found the dispersion relation of a longitudinal mode for one wire radius, we can do the same for a variety of radii. The modes for a selection of different radii we examined are shown in Fig. 8.20. We can then build up the relationship between the plasma frequency, taken from the y-intercept of the dispersion curve, and the wire radius. The dispersion relations for the three longitudinal modes shown in Fig. 8.20 are shown in Fig. 8.21. The relationship between the square of the plasma frequency, λ_s^2, and wire radius, r, is shown in Fig. 8.22, this is the relationship that is most important for our mode profiling calculations. For a copper wire, this relationship takes the form of a simple linear relationship and, as such, can be well described by an appropriate straight line equation. This fit has the form shown in equation 8.1 with the following fitting parameters, $\Delta = 18.5$ (GHz^2) and $\Theta = 32.4$ (GHz^2/mm). The $\mathfrak{R}^2$ value for this straight line fit is 0.9995. We also plotted a version of Fig. 8.22 with the data from the PEC version included as well. On the scale of the plot the two lines overlapped so closely that showing them both is unhelpful.
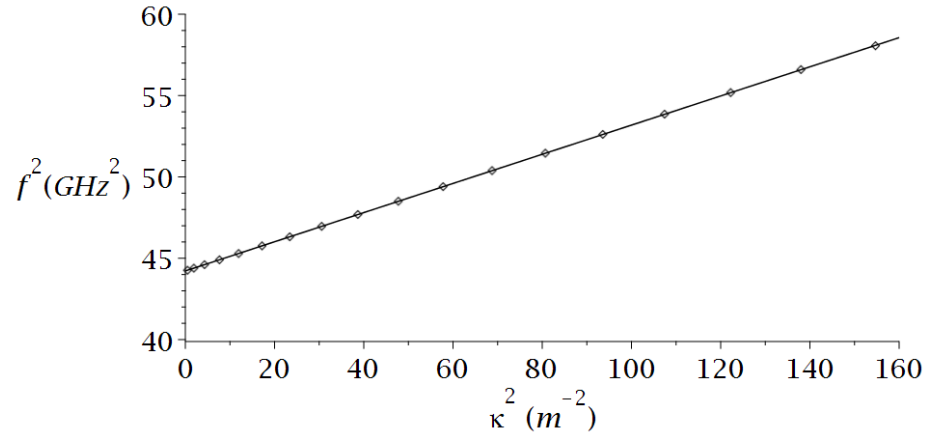
Figure 8.19: A plot of the squared dispersion relation, frequency squared (f^2) against our wavenumber squared (κ^2), of the longitudinal mode in an infinite copper wire medium ($r = 0.8$ mm, $a_x = 13.06$ mm and $a_y = 15.00$ mm) that demonstrates the mode's plasma-like dispersion relation along with a fitting curve.

(a)

(b)

(c)

(d)

(e) (f)
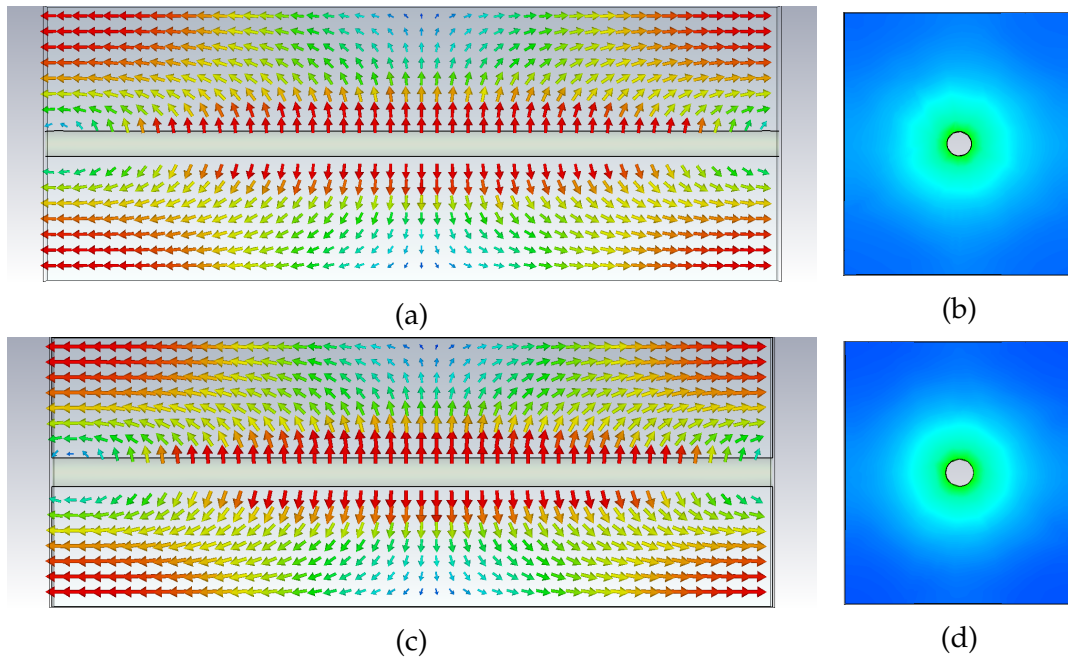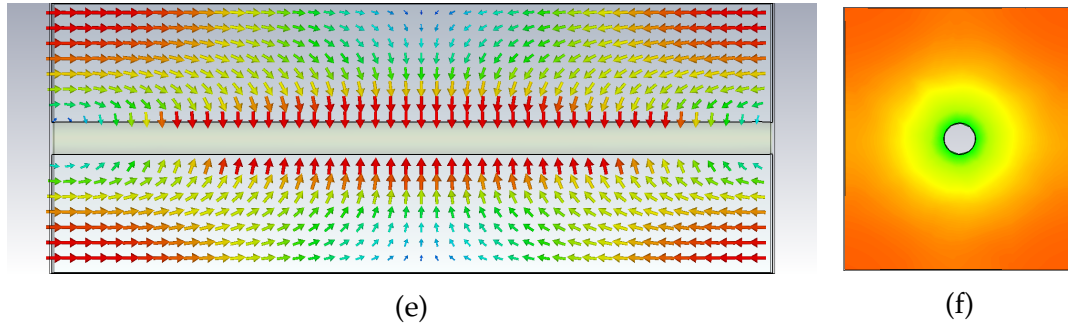
Figure 8.20: A series of images from numerical simulations in CST showing the longitudinal modes found in infinite copper wire media ($a_x = 13.06$ mm and $a_y = 15.00$ mm) with a variety of radii. The fields are either represented using arrow plots where the arrow direction represents field direction and colour represents the magnitude of the field strength, or colour plots where the direction and magnitude of the longitudinal field is represented by colour. (a) and (b) show a longitudinal mode ($f = 7.41$ GHz) in a wire medium with $r = 0.7$ mm, with (a) showing a y-z slice and (b) an x-y slice. (c) and (d) show a longitudinal mode ($f = 7.62$ GHz) in a wire medium with $r = 0.8$ mm, with (c) showing a y-z slice and (d) an x-y slice. (e) and (f) show a longitudinal mode ($f = 7.82$ GHz) in a wire medium with $r = 0.9$ mm, with (e) showing a y-z slice and (f) an x-y slice.
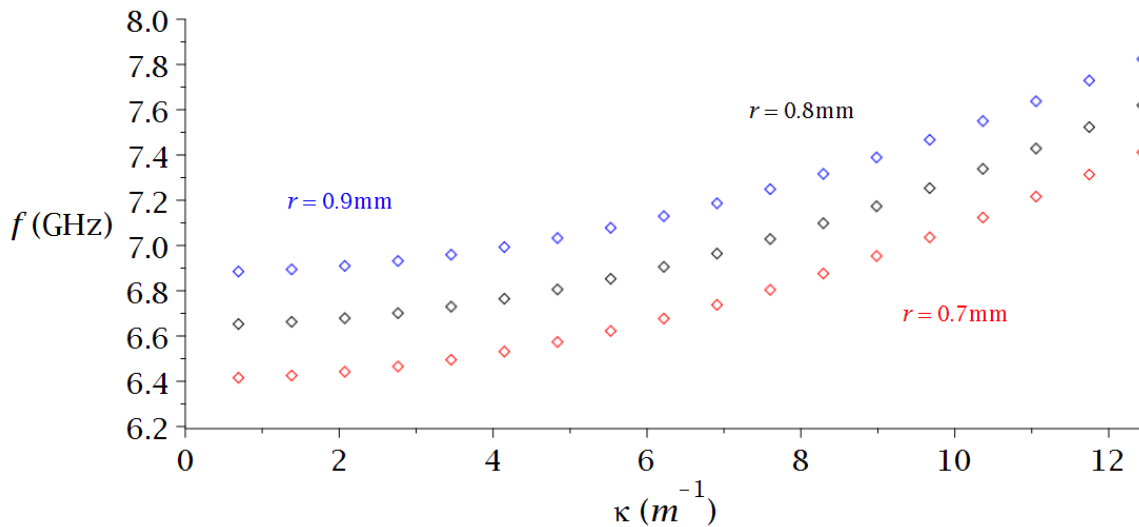
Figure 8.21: The dispersion plots, frequency (f) against wavenumber (κ), of the longitudinal modes in infinite copper wire media ($a_x = 13.06$ mm and $a_y = 15.00$ mm) with a variety of radii. The radii are 0.7 mm (red), 0.8 mm (black) and 0.9 mm (blue).

239
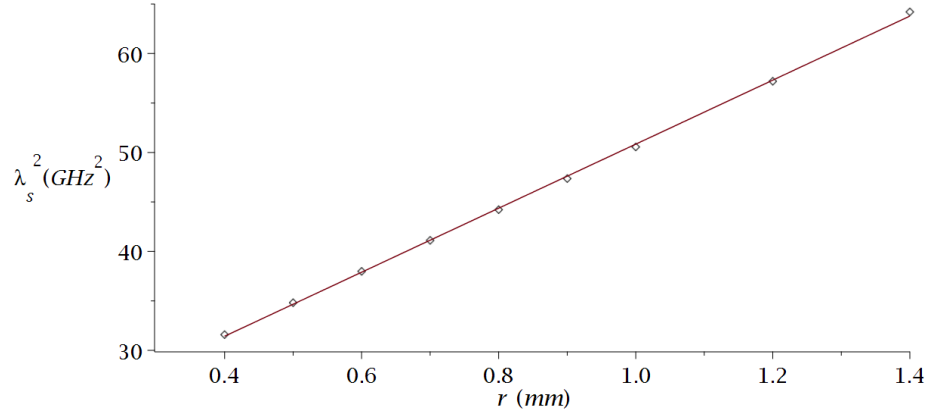
Figure 8.22: A plot of the plasma frequency squared, λ_s^2, of infinite copper wire media ($a_x = 13.06$ mm and $a_y = 15.00$ mm) against wire radius, r, with a straight line fitting curve.

Now that we have an analytic relationship for the relationship between λ_s^2 and r, we can use our previously established method to calculate a function for the radius variation of our copper wires which should give us a chosen mode profile. As we have done previously, we originally tested this method for a flat profile (Mathieu parameter $q = 0.8$). The free parameters we have chosen to fix are $R_c = 0.9$ mm and $f_d = 7.2$ GHz. The radius function resulting from this choice of parameters is shown in Fig. 8.23. Implementing this radius variation with copper wires in CST, we found a longitudinal mode at simulation frequency, f, 7.22 GHz, as shown in Fig. 8.24. The profile of this mode is shown in Fig. 8.25. The agreement with the desired profile is very good qualitatively, and the calculated $\mathcal{R}^2$ value of 0.9988 confirms the success of the mode profile shaping.
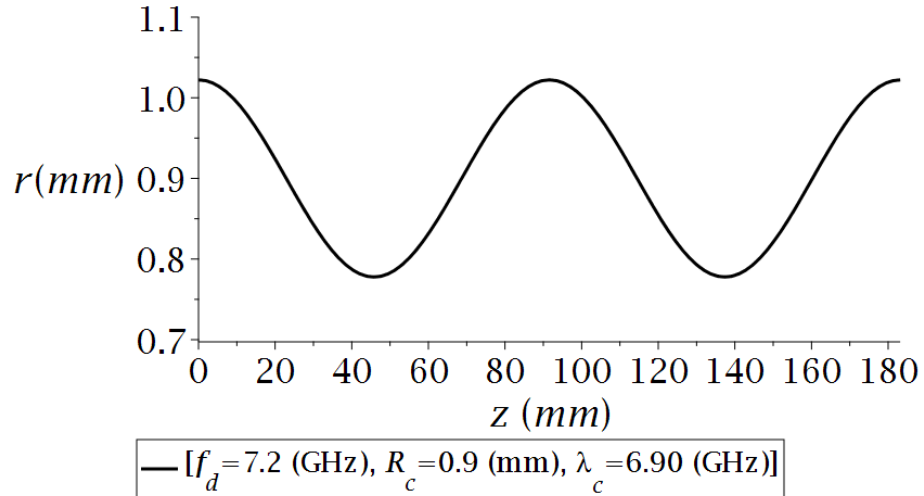
Figure 8.23: Radius function calculated for a flattened profile ($q = 0.8$) in an infinite copper wire medium ($a_x = 13.06$ mm and $a_y = 15.00$ mm) for the parameter choice of $f_d = 7.2$ GHz, $R_c = 0.9$ mm and $\lambda_C = 6.90$ GHz.


(a)

(b)
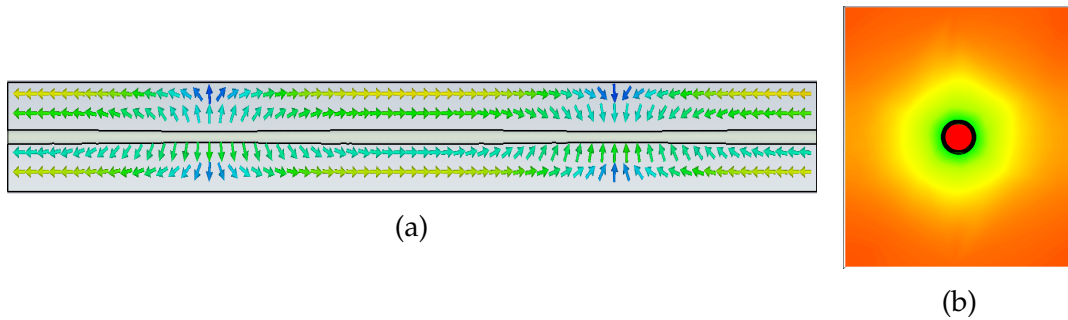
Figure 8.24: Images showing the resulting longitudinal mode ($f = 7.22$ GHz) after the implementation of the calculated radius function for a flattened profile ($q = 0.8$) in an infinite copper wire medium ($a_x = 13.06$ mm and $a_y = 15.00$ mm) for the parameter choice of $f_d = 7.2$ GHz, $R_c = 0.9$ mm and $\lambda_C = 6.90$ GHz. The fields are either represented using arrow plots where the arrow direction represents field direction and colour represents the magnitude of the field strength, or colour plots where the direction and magnitude of the longitudinal field is represented by colour. (a) shows the field on a y-z slice of the structure, and (b) shows the field on an x-y slice.

Figure 8.25: A plot of the field profile (longitudinal, z, spatial variation of the electric field strength, E_z) of the longitudinal mode ($f = 7.22$ GHz) in an infinite copper wire medium ($a_x = 13.06$ mm and $a_y = 15.00$ mm) for our attempt to produce a flattened profile ($q = 0.8$) with a radius function based on the parameter choice of $f_d = 7.2$ GHz, $R_c = 0.9$ mm and $\lambda_C = 6.90$ GHz. The plot includes the field profile observed in our numerical simulation (solid black) and the desired profile (dotted black). In order to aid comparison the field profile from our simulation and the z coordinate have been normalised.

Having demonstrated mode profile shaping with one profile, we wanted to show that our method works for other profiles. With this aim in mind, we attempted to achieve mode profiling with several profiles: a triangular profile (Mathieu parameter $q = -0.329$), a profile with an increased number of turning points (Mathieu parameter $q = 4.0$) and a profile with a pronounced peak (Mathieu parameter $q = -10.0$). This is the same method used in previous chapter for verifying that our method supports a variety of profiles. The free parameters we have chosen to fix are listed in Table 8.3 along with the resulting parameters for the required radius function and the structure. The radius functions resulting from these choices of parameters are shown in Fig. 8.26.

q	f_d (GHz)	R_C (mm)	λ_C (GHz)	η_1 (mm)	η_2 (mm)	η_3 (mm^{-1})	L (mm)
0.8	7.2	0.9	6.9	0.900	0.122	0.0686	183
-0.329	7.5	0.9	6.9	0.900	-0.267	0.158	79.5
4	7	0.9	6.9	0.900	0.149	0.0338	371
-10	6.2	0.9	6.9	0.900	-0.407	0.0354	355

Table 8.3: A table summarising some of the key parameters related to the implemented radius functions for a variety of profiles in infinite copper wire media ($a_x = 13.06$ mm and $a_y = 15.00$ mm). The first set of parameters listed are design parameters we chose: the Mathieu parameter characterising the profile (q), design frequency (f_d), central radius (R_C) and the corresponding central plasma frequency (λ_c). The rest are the resulting structural parameters: the parameters specifying the corresponding radius function (η_{1-3}) and the length of our unit cell (L). The profiles considered are a triangular profile ($q = -0.329$), a profile with multiple turning points ($q = 4.0$) and a profile with a pronounced peak ($q = -10.0$).

(a)

(b)

(c)

Figure 8.26: A series of plots of radius functions calculated for a variety of desired profiles in infinite copper wire media ($a_x = 13.06$ mm and $a_y = 15.00$ mm). (a) shows the radius function for a triangular profile with a parameter choice of $f_d = 7.5$ GHz, $R_c = 0.9$ mm and $\lambda_C = 6.90$ GHz (crimson); (b), for a profile with multiple turning points with a parameter choice of $f_d = 7$ GHz, $R_c = 0.9$ mm and $\lambda_C = 6.90$ GHz (dark blue); and (c), for a profile with a pronounced peak with a parameter choice of $f_d = 6.2$ GHz, $R_c = 0.9$ mm and $\lambda_C = 6.90$ GHz (dark green).

Now that we have calculated our required radius functions, we can implement them into CST and observe the mode profiles obtained. The modes found for the implementation of the radius functions for the triangular profile and the profile with a greater number of turning points are shown in Fig. 8.27. As usual, we can evaluate their profile using a line along the top of the unit cell. These profiles are plotted in Fig. 8.28 along with the desired profiles. These figures clearly show that our mode profiling has been very successful, which is reinforced by the $\mathfrak{R}^2$ values for these profiles of 0.9986 for the comparison between the simulated and desired triangular profiles, and 0.9556 for the comparison between the simulated and desired multiple turning point profiles.
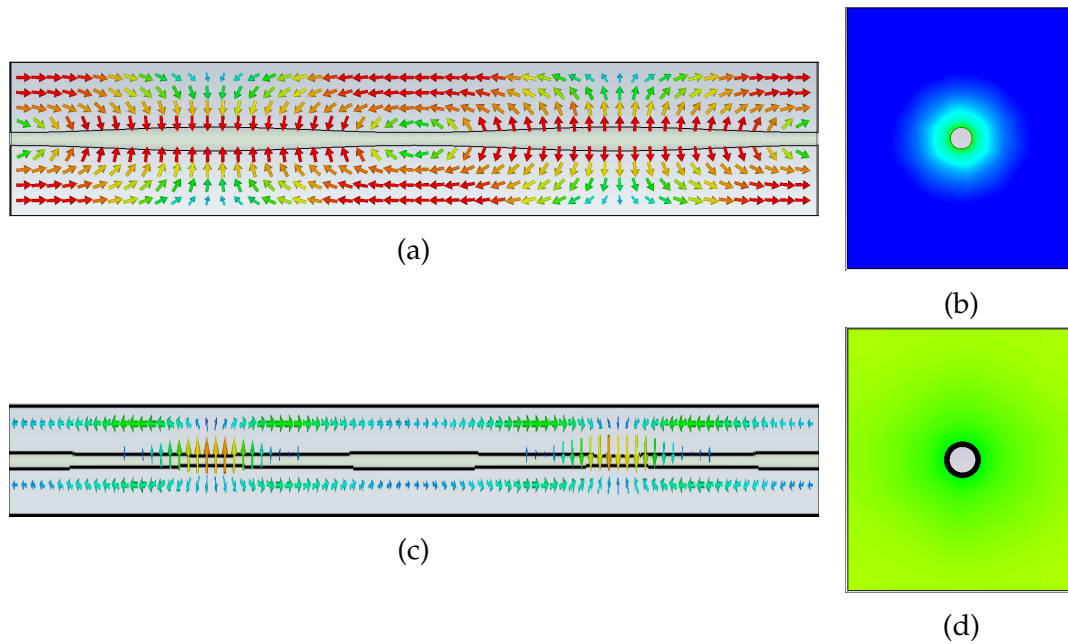
Figure 8.27: Images showing the resulting longitudinal modes after the implementation of the calculated radius function for a triangular profile ($q = -0.329$) and a profile with multiple turning points ($q = 4.0$) in infinite copper wire media ($a_x = 13.06$ mm and $a_y = 15.00$ mm). The fields are represented using arrow plots on a y-z slice of the structure where the arrow direction represents field direction and colour represents the magnitude of the field strength, and colour plots on an x-y slice where the direction and magnitude of the longitudinal field is represented by colour. (a) and (b) shows the resulting longitudinal mode ($f = 7.39$ GHz) for the attempt to demonstrate a triangular profile by the implementation of a radius function based on the choice of $f_d = 7.5$ GHz, $R_c = 0.9$ mm and $\lambda_C = 6.90$ GHz; and (c) and (d), the resulting longitudinal mode ($f = 7.02$ GHz) for the attempt to achieve a profile with multiple turning points by the implementation of a radius function based on the choice of $f_d = 7$ GHz, $R_c = 0.9$ mm and $\lambda_C = 6.90$ GHz.

Figure 8.28: Plots of the field profiles (longitudinal, z, spatial variation of the electric field strength, E_z) of the longitudinal modes in infinite copper wire media ($a_x = 13.06$ mm and $a_y = 15.00$ mm) for our attempts to produce a triangular profile ($q = -0.329$) and a profile with multiple turning points ($q = 4.0$). The plots include the field profile observed in our numerical simulation (solid) and the desired profile (dotted). In order to compare these the field profile and z coordinate have been normalised. (a) shows the field profile of the longitudinal mode ($f = 7.39$ GHz) for the attempt to demonstrate a triangular profile by the implementation of a radius function based on the choice of $f_d = 7.5$ GHz, $R_c = 0.9$ mm and $\lambda_C = 6.90$ GHz (crimson); and (b), the field profile of the longitudinal mode ($f = 7.02$ GHz) for the attempt to achieve a profile with multiple turning points by the implementation of a radius function based on the choice of $f_d = 7$ GHz, $R_c = 0.9$ mm and $\lambda_C = 6.90$ GHz (dark blue).

As with previous simulations of this kind, when we attempt to achieve a mode profile with a pronounced peak, there exist some complications. In the frequency range where we would expect to find our longitudinal mode, the simulation shows two longitudinal modes. These two longitudinal modes were found at simulation frequencies, f, of 6.204 GHz and 6.212 GHz, a separation of 0.008 GHz or a percentage difference of 0.13 % from the first mode to the second. These modes are shown in Fig. 8.29.

(a)

(b)
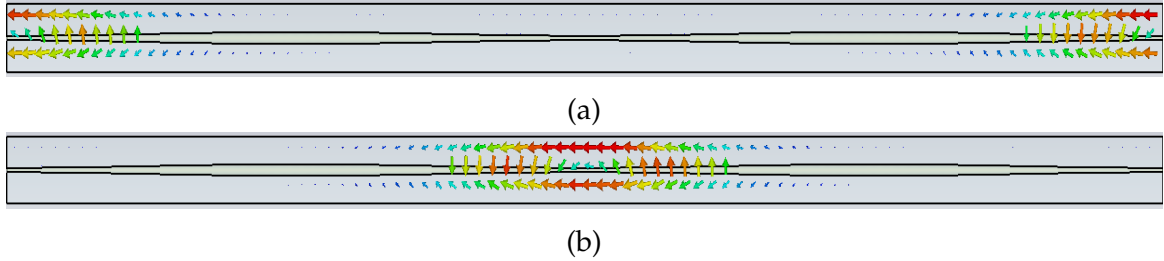
Figure 8.29: Images showing the resulting longitudinal modes after the implementation of the calculated radius function for a profile with a pronounced peak ($q = -10.0$) in an infinite copper wire medium ($a_x = 13.06$ mm and $a_y = 15.00$ mm) with the parameter choice of $f_d = 6.2$ GHz, $R_c = 0.9$ mm and $\lambda_C = 6.90$ GHz. The fields are represented using arrow plots on a y-z slice of the structure where the arrow direction represents field direction and colour represents the magnitude of the field strength. (a) shows one of the resulting longitudinal modes ($f = 6.204$ GHz); and (b), the other ($f = 6.212$ GHz).

We believe that due to confusion caused by the similarity of different Mathieu solutions at high negative q values CST has misinterpreted our desired mode as two separate modes. If we manually superimpose the profile of these modes appropriately, then we can compare with the desired profile, as shown in Fig. 8.30. Fig. 8.30 shows that this combined profile does agree well with our desired profile as confirmed by calculating its $\mathfrak{R}^2$ value of 0.9762.
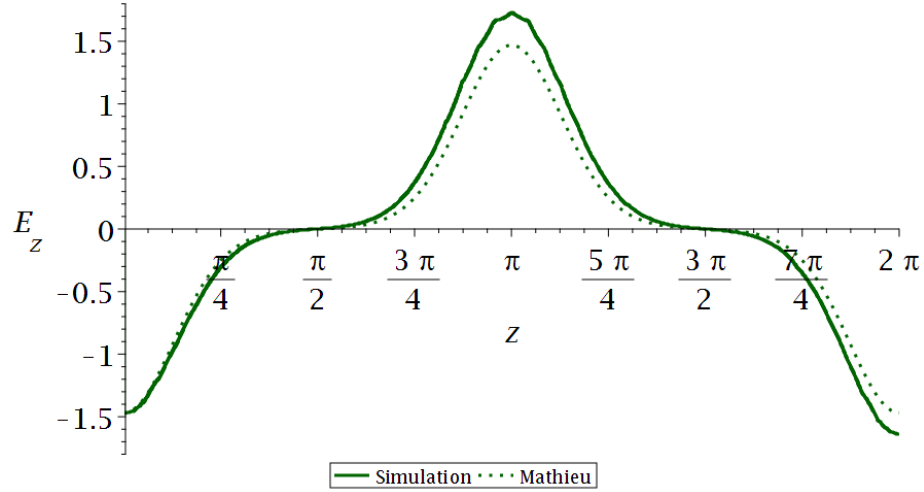
Figure 8.30: A plot of the combined field profile (longitudinal, z, spatial variation of the electric field strength, E_z) of the two longitudinal modes ($f = 6.204$ GHz and $f = 6.212$ GHz) in an infinite copper wire medium ($a_x = 13.06$ mm and $a_y = 15.00$ mm) for our attempts to produce a profile with a pronounced peak ($q = -10.0$) with the parameter choice of $f_d = 6.2$ GHz, $R_c = 0.9$ mm and $\lambda_C = 6.90$ GHz (dark green).

The results of our attempts to replicate a variety of profiles are summarised in Table 8.4. These results, obtained by varying the radius of the copper wires in an infinite wire medium, are promising. They confirm our ability to replicate a desired profile using infinite copper wire media. This is an essential step in our aim to investigate whether copper wire media could realistically be used to control field profiles. Our next step will be to examine whether these results will hold for finite structures.

q	f_d (GHz)	λ_C (GHz)	L (mm)	f (GHz)	$\mathfrak{R}^2$
0.8	7.2	6.9	183	7.22	0.9988
-0.329	7.5	6.9	79.5	7.39	0.9986
4	7	6.9	371	7.02	0.9556
-10	6.2	6.9	355	6.21	0.9762

Table 8.4: A table summarising some of the key parameters related to the results of our implemented radius functions for a variety of profiles in infinite copper wire media ($a_x = 13.06$ mm and $a_y = 15.00$ mm). The parameters listed are: the Mathieu parameter characterising the profile (q), design frequency (f_d), the central plasma frequency (λ_c), the length of our unit cell (L), longitudinal mode frequency (f) and a figure of merit for the agreement between our field profile and the desired profile ($\mathfrak{R}^2$). The profiles considered are a triangular profile ($q = -0.329$), a profile with multiple turning points ($q = 4.0$) and a profile with a pronounced peak ($q = -10.0$).

III. Demonstrating mode profile shaping with partially and fully finite copper wire media

We have now successfully applied our mode profiling to a structure containing an infinite lattice of infinitely long copper wires. The next step is to explore whether these results will hold for finite structures. As we have done previously with dielectric wire media, we first study a structure that is finite in the transverse dimensions but infinitely long. In this case, we have used a two by two lattice with boundaries placed as usual, but in the case of the transverse boundaries, they now have metallic boundary conditions. The structure is essentially a two by two lattice of infinitely long copper wires surrounded by an infinitely long waveguide. The unit cell used is shown in Fig. 8.31 along with a view of the different boundary conditions applied, where green represents a metallic boundary and orange a periodic boundary.

(a)   (b)
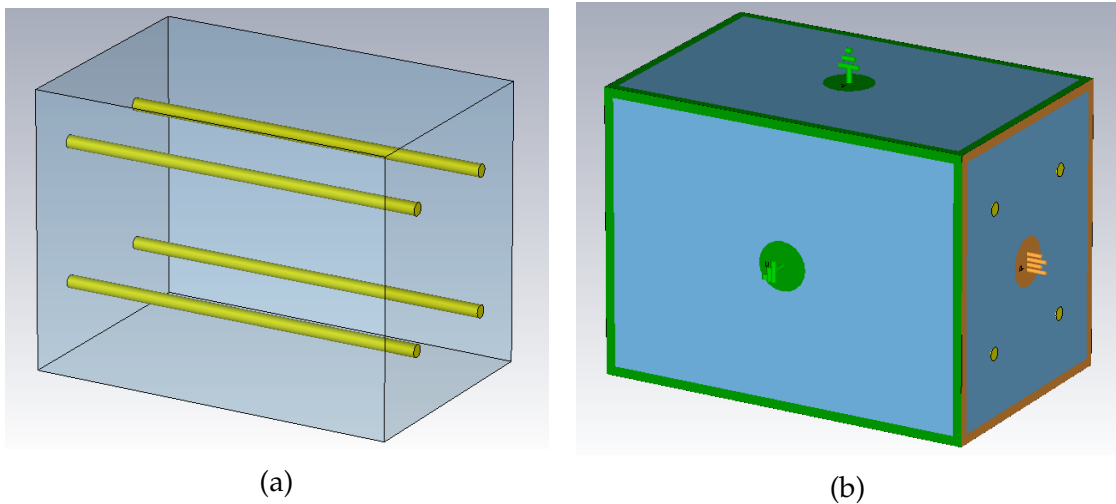
Figure 8.31: A representation of a partially finite wire medium in CST, consisting of a two by two lattice of copper wires in a unit cell with transverse metallic boundary conditions and longitudinal periodic boundary conditions (a_x = 13.06 mm and a_y = 15.00 mm). This is effectively a finite lattice of infinitely long wires in an infinite metallic waveguide. The copper wires have a radius (r) of 0.7 mm. (a) shows the unit cell used in CST, and (b) shows the boundaries of the structure with green representing metallic boundaries and orange, periodic boundary conditions.
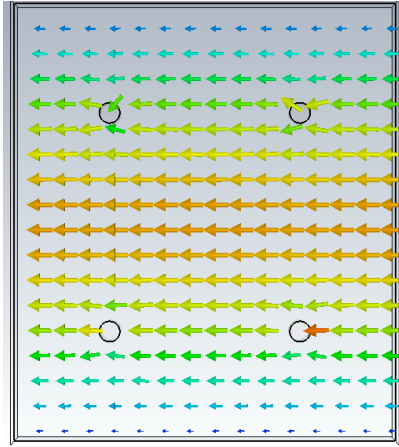
Figure 8.32: Numerical results showing a transverse electric mode, with a frequency of 6.22 GHz, in a representation of a partially finite two by two array of copper wires of radius 0.7mm, and wire spacings $a_x = 13.06$ mm and $a_y = 15.00$ mm. The electric field is represented using a vector plot of an x-y slice of the structure where the arrow direction represents field direction and colour represents the magnitude of the field strength.

Having defined our structure, we studied the modes present. As usual, we find many transverse modes, as shown in Fig. 8.32 for a wire medium with a radius of 0.7 mm. In the same structure, we can find our expected longitudinal modes, shown in Fig. 8.33.

After finding our longitudinal mode, we must confirm that it has the plasma-like dispersion relation that we expect. We have confirmed this, with the squared dispersion relation for a mode in the 0.7 mm structure shown in Fig. 8.34.
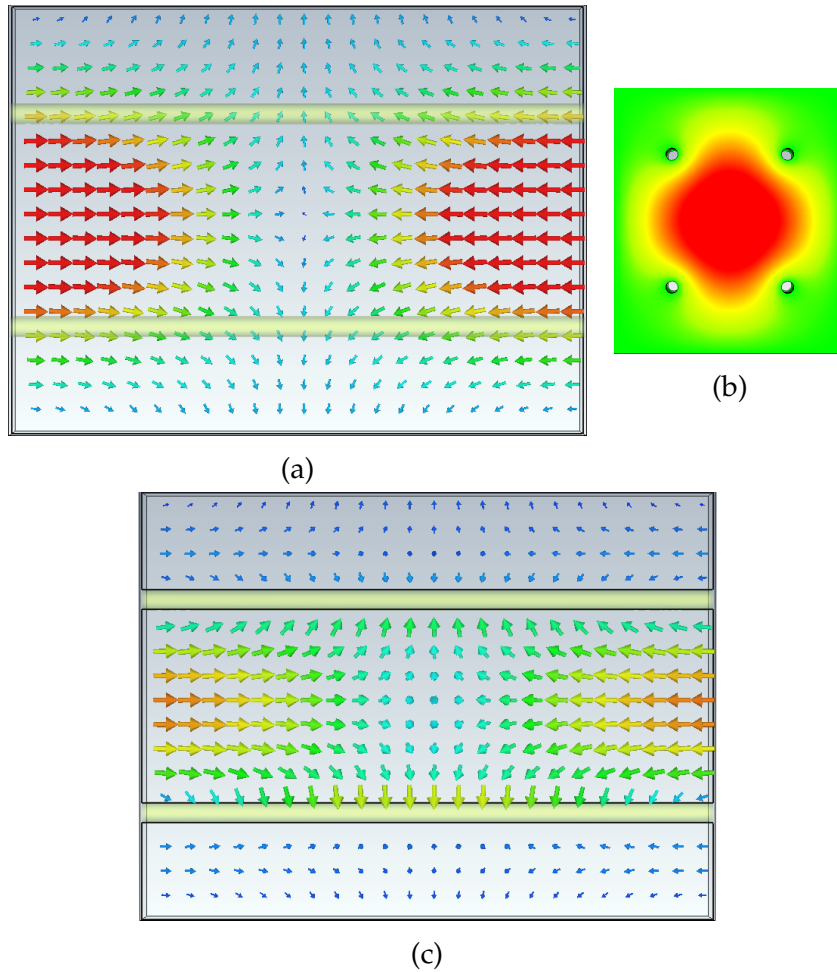
Figure 8.33: Images from numerical simulations in CST showing the longitudinal mode ($f = 10.35$ GHz) found in a partially finite copper wire medium (2×2, $r = 0.7$ mm, $a_x = 13.06$ mm and $a_y = 15.00$ mm). The fields are either represented using arrow plots where the arrow direction represents field direction and colour represents the magnitude of the field strength, or colour plots where the direction and magnitude of the longitudinal field is represented by colour. (a) shows a y-z slice through the centre of the structure, (b) an x-y slice and (c) a y-z slice through two of the wires.
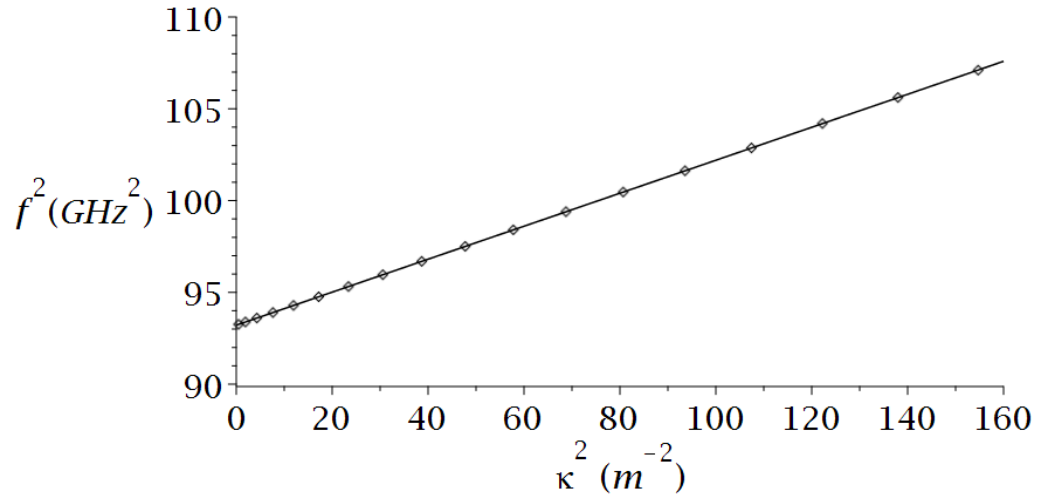
Figure 8.34: A plot of the squared dispersion relation, frequency squared (f^2) against our wavenumber squared (κ^2), of the longitudinal mode in a partially finite copper wire medium (2×2, $r = 0.7$ mm, $a_x = 13.06$ mm and $a_y = 15.00$ mm) that demonstrates the mode's plasma-like dispersion relation.

Our method relies on manipulating the dispersion relation of our structure by varying a structural parameter such as the wire radius. To do this, we need to know how a change in radius affects our longitudinal mode. Therefore we have run simulations for a variety of wire radii. In Figs. 8.35 and 8.36 the longitudinal modes in structures with wire radii of 0.6 and 0.8 mm are shown.
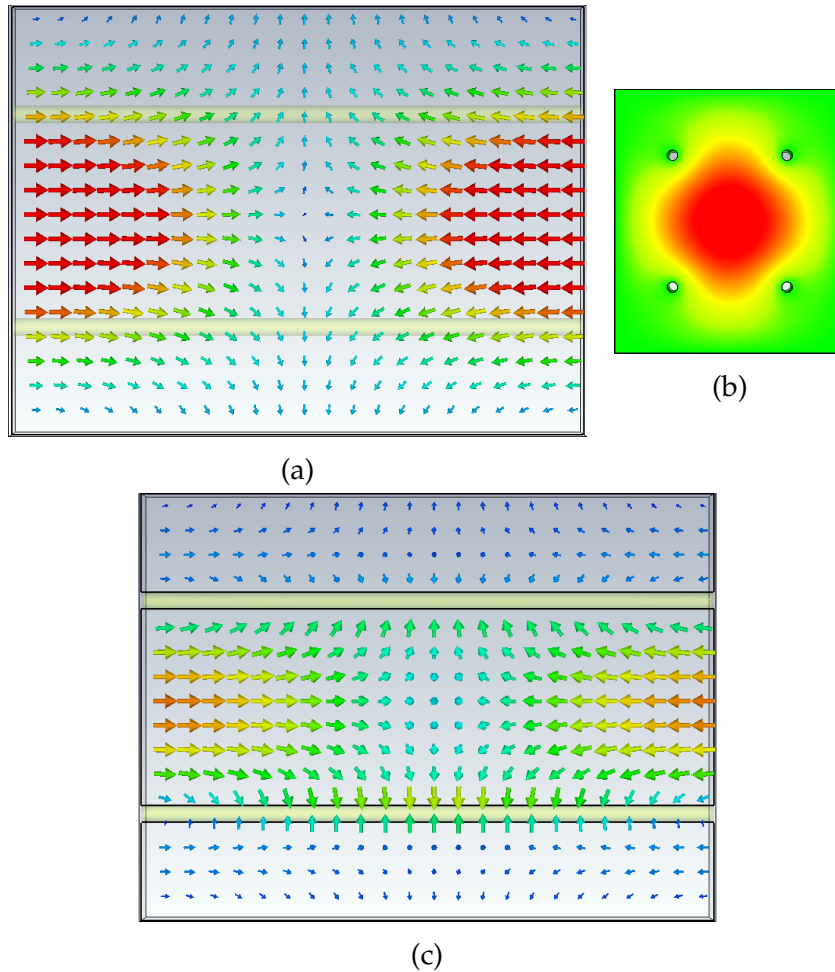
Figure 8.35: Images from numerical simulations in CST showing the longitudinal mode ($f = 10.23$ GHz) found in a partially finite copper wire medium (2×2, $r = 0.6$ mm, $a_x = 13.06$ mm and $a_y = 15.00$ mm). The fields are either represented using arrow plots where the arrow direction represents field direction and colour represents the magnitude of the field strength, or colour plots where the direction and magnitude of the longitudinal field is represented by colour. (a) shows a y-z slice through the centre of the structure, (b) an x-y slice and (c) a y-z slice through two of the wires.

(a)

(b)

(c)
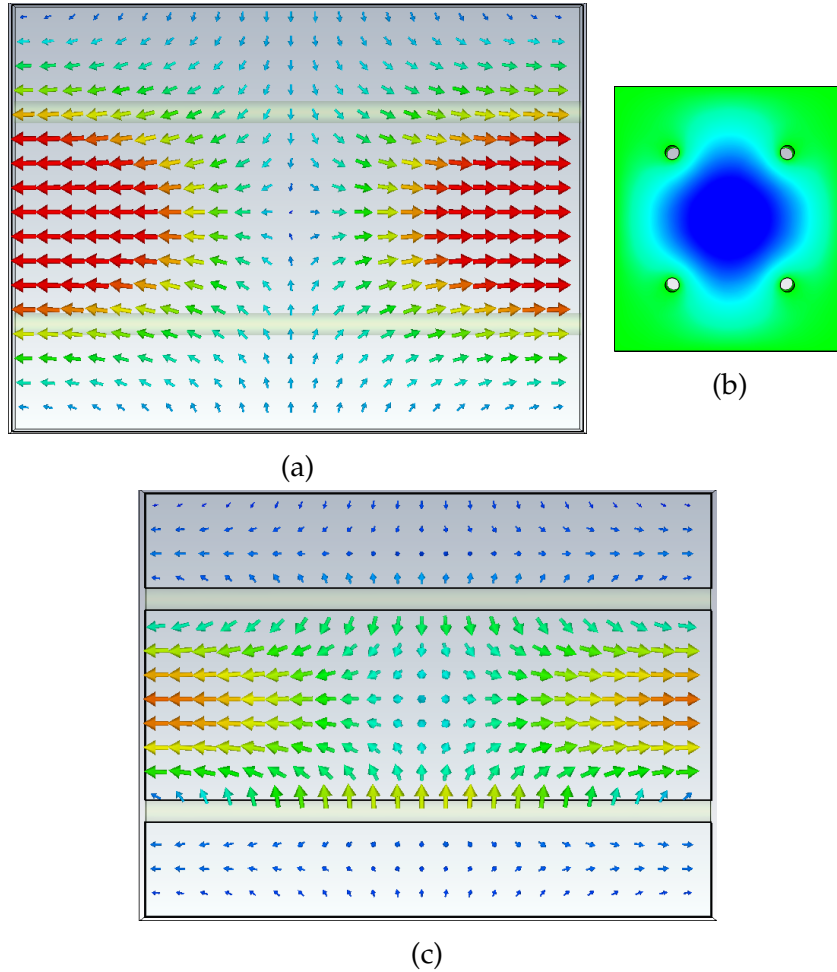
Figure 8.36: Images from numerical simulations in CST showing the longitudinal mode ($f = 10.47$ GHz) found in a partially finite copper wire medium (2×2, $r = 0.8$ mm, $a_x = 13.06$ mm and $a_y = 15.00$ mm). The fields are either represented using arrow plots where the arrow direction represents field direction and colour represents the magnitude of the field strength, or colour plots where the direction and magnitude of the longitudinal field is represented by colour. (a) shows a y-z slice through the centre of the structure, (b) an x-y slice and (c) a y-z slice through two of the wires.

By examining the dispersion relation of these modes we can find their plasma frequency. The dispersion relations for the three modes previously shown are plotted together in Fig. 8.37. As the plasma frequency of the modes is related to the cut-off frequency of their dispersion, we can see that the radius affects the plasma frequency.
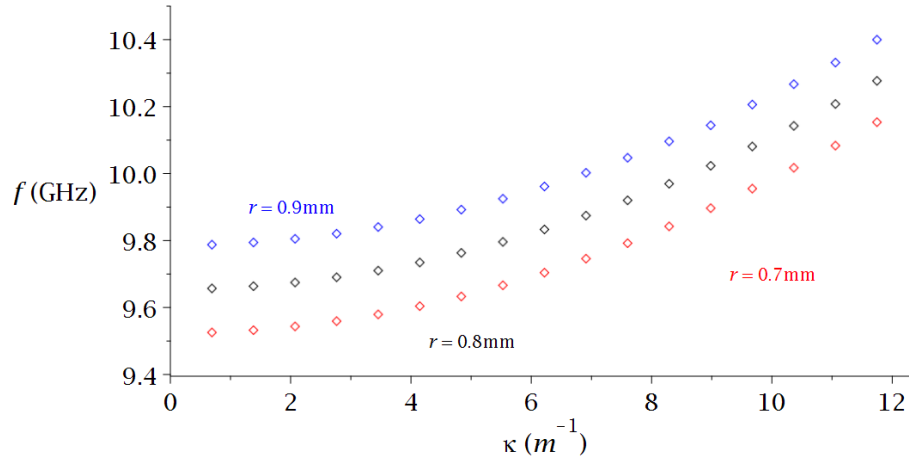
Figure 8.37: The dispersion plots, frequency (f) against wavenumber (κ), of the longitudinal modes in partially finite copper wire media (2×2, $a_x = 13.06$ mm and $a_y = 15.00$ mm) with a variety of radii. The radii are 0.7 mm (red), 0.8 mm (black) and 0.9 mm (blue).

By calculating the plasma frequency of these modes and for the modes found at different radii, we can build up the data plotted in Fig. 8.38. This is a plot of the plasma frequency squared against the wire radius of the structure. As with the infinite case, this relationship is well described by a straight line fit, with an $\mathfrak{R}^2$ value of 0.9995. This fit has the form shown in equation 8.1 with the following fitting parameters, $\Delta = 18.5$ (GHz^2) and $\Theta = 32.4$ (GHz^2/mm).
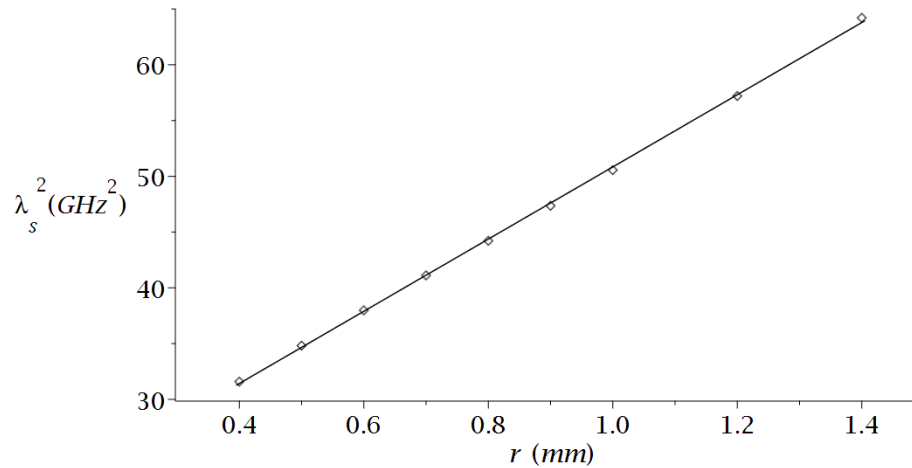
Figure 8.38: A plot of the plasma frequency squared, λ_s^2, of partially finite copper wire media (2×2, $a_x = 13.06$ mm and $a_y = 15.00$ mm) against wire radius, r, with a straight line fitting curve.

Now that we have an accurate function to describe the relationship between plasma frequency and radius, we can implement the mode profiling method we

have developed. As the form of this relationship is the same as the one found for infinite copper wire media, there is no need to alter the method used. We can now choose a mode profile, as defined by its Mathieu parameters and produce a required radius function.

Our first attempt at mode profiling with our partially finite copper structure was an attempt to replicate a flat mode profile (q=0.8). After fixing parameters, $f_d = 10$ GHz and $R_c = 0.8$ mm, we can produce a required radius function that if implemented in our structure, will support a longitudinal mode that replicates our desired profile. This radius function is plotted in Fig. 8.39 and the parameters of the function are shown in Table 8.5.
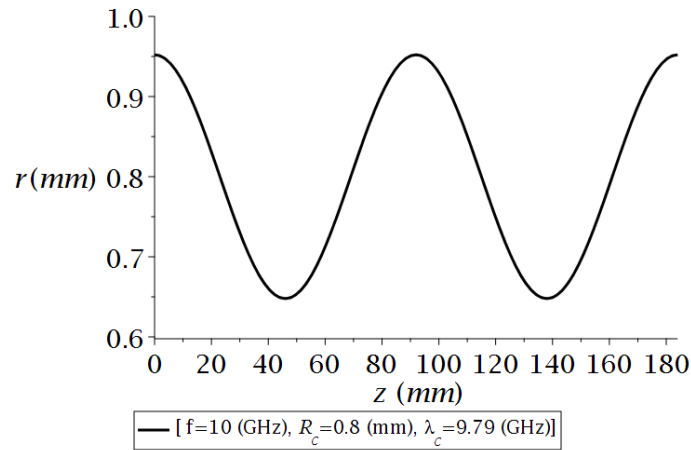
Figure 8.39: Radius function calculated for a flattened profile ($q = 0.8$) in a partially finite copper wire medium (2×2, $a_x = 13.06$ mm and $a_y = 15.00$ mm) for the parameter choice of $f_d = 10$ GHz, $R_c = 0.8$ mm and $\lambda_C = 9.79$ GHz.

We can implement this radius function in our structure by using a series of differing conical frustums. After doing this, we can examine the longitudinal modes supported, shown in Fig. 8.40.

(a)

(b)

(c)
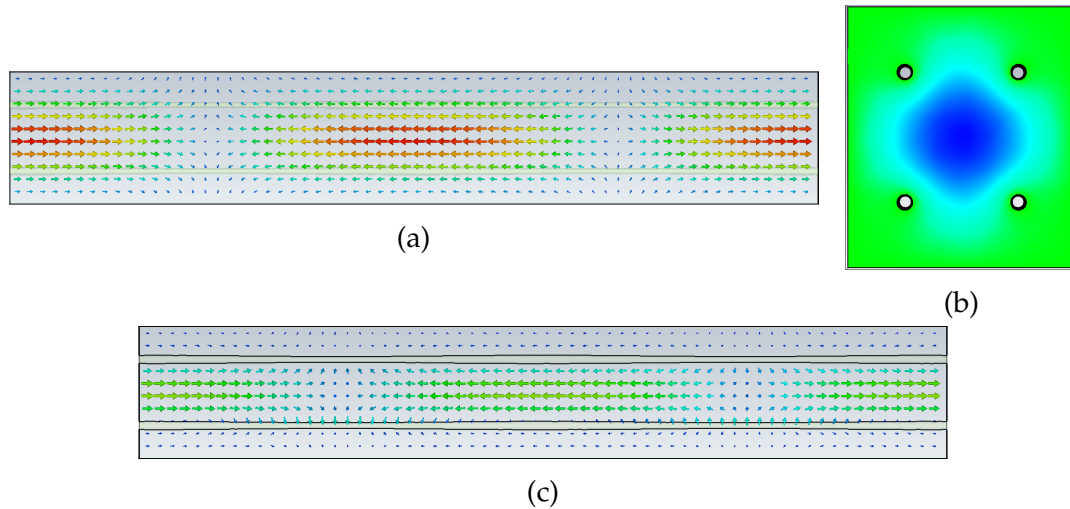
Figure 8.40: Images showing the resulting longitudinal mode ($f = 10.02$ GHz) after the implementation of the calculated radius function for a flattened profile ($q = 0.8$) in a partially finite copper wire medium (2×2, $a_x = 13.06$ mm and $a_y = 15.00$ mm) for the parameter choice of $f_{\mathrm{d}} = 10$ GHz, $R_c = 0.8$ mm and $\lambda_C = 9.79$ GHz. The fields are either represented using arrow plots where the arrow direction represents field direction and colour represents the magnitude of the field strength, or colour plots where the direction and magnitude of the longitudinal field is represented by colour. (a) shows a y-z slice through the centre of the structure, (b) an x-y slice and (c) a y-z slice through two of the wires.

We can better evaluate the profile of these modes by plotting the field strength along a line through the centre of the structure. This is shown in Fig. 8.41 along with the desired profile. This comparison clearly shows that our mode profiling has been very successful, as reinforced by the $\mathfrak{R}^2$ value of 0.9980.
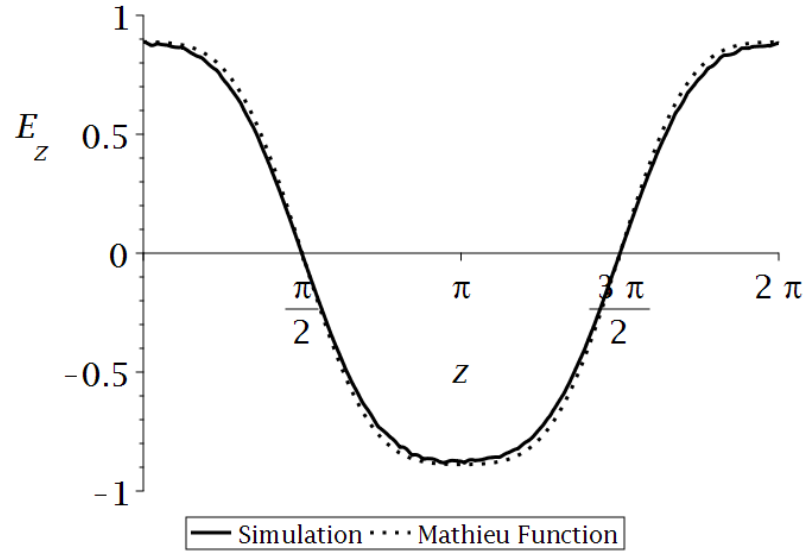
Figure 8.41: Plot of the field profile (longitudinal, z, spatial variation of the electric field strength, E_z) of the longitudinal mode (10.02 GHz) in a partially finite copper wire medium (2×2, $a_x = 13.06$ mm and $a_y = 15.00$ mm) for our attempts to produce a flattened profile ($q = 0.8$) by the implementation of a radius function based on the choice of $f_d = 10$ GHz, $R_c = 0.8$ mm and $\lambda_C = 9.79$ GHz (black). The plot includes the field profile observed in our numerical simulation (solid) and the desired profile (dotted). In order to compare these the field profile and z coordinate have been normalised.

Having demonstrated mode profile shaping with one profile, we now want to show that the method works for other profiles. With this aim in mind, we attempted to achieve mode profiling with several profiles: a triangular profile (Mathieu parameter $q = -0.329$), a profile with an increased number of turning points (Mathieu parameter $q = 4.0$) and a profile with a pronounced peak (Mathieu parameter $q = -10.0$). The free parameters we have chosen to fix are listed in Table 8.5 along with the resulting parameters for the required radius function and the structure. The radius functions resulting from these choices of parameters are shown in Fig. 8.42.

q	f_d (GHz)	R_C (mm)	λ_C (GHz)	η_1 (mm)	η_2 (mm)	η_3 (mm^{-1})	L (mm)
0.8	10	0.8	9.79	0.800	0.152	0.0683	184
-0.329	9.8	0.6	9.52	0.600	-0.209	0.125	101
4	9.6	0.6	9.52	0.600	0.202	0.0351	358
-10	9.3	0.6	9.52	0.600	-0.232	0.0239	527

Table 8.5: A table summarising some of the key parameters related to the implemented radius functions for a variety of profiles in partially finite copper wire media ($a_x = 13.06$ mm and $a_y = 15.00$ mm). The first set of parameters listed are design parameters we chose: the Mathieu parameter characterising the profile (q), design frequency (f_d), central radius (R_C) and the corresponding central plasma frequency (λ_c). The rest are the resulting structural parameters: the parameters specifying the corresponding radius function (η_{1-3}) and the length of our unit cell (L). The profiles considered are a triangular profile ($q = -0.329$), a profile with multiple turning points ($q = 4.0$) and a profile with a pronounced peak ($q = -10.0$).

(a)

(b)

(c)

Figure 8.42: A series of plots of radius functions calculated for a variety of desired profiles in partially finite copper wire media ($a_x = 13.06$ mm and $a_y = 15.00$ mm). (a) shows the radius function for a triangular profile with a parameter choice of $f_d = 9.8$ GHz, $R_c = 0.6$ mm and $\lambda_C = 9.52$ GHz (crimson); (b), for a profile with multiple turning points with a parameter choice of $f_d = 9.6$ GHz, $R_c = 0.6$ mm and $\lambda_C = 9.52$ GHz (dark blue); and (c), for a profile with a pronounced peak with a parameter choice of $f_d = 9.3$ GHz, $R_c = 0.6$ mm and $\lambda_C = 9.52$ GHz (dark green).

The modes resulting from the implementation of the required radius functions for the triangle profile and the profile with more turning points are shown in Figs. 8.43 and 8.44.

(a)

(b)

(c)
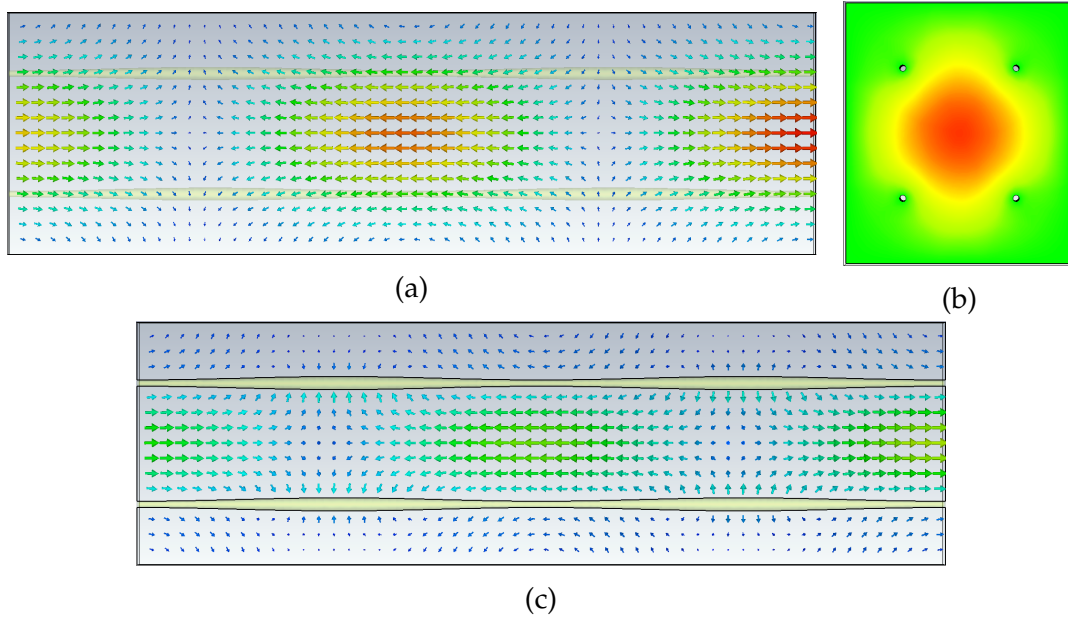
Figure 8.43: Images showing the resulting longitudinal mode (f = 9.83 GHz) after the implementation of the calculated radius function for a triangular profile ($q = -0.329$) in a partially finite copper wire medium (2×2, $a_x = 13.06$ mm and $a_y = 15.00$ mm) for the parameter choice of $f_{\mathrm{d}} = 9.8$ GHz, $R_c = 0.6$ mm and $\lambda_C = 9.52$ GHz. The fields are either represented using arrow plots where the arrow direction represents field direction and colour represents the magnitude of the field strength, or colour plots where the direction and magnitude of the longitudinal field is represented by colour. (a) shows a y-z slice through the centre of the structure, (b) an x-y slice and (c) a y-z slice through two of the wires.

(a)

(b)

(c)

Figure 8.44: Images showing the resulting longitudinal mode ($f = 9.61$ GHz) after the implementation of the calculated radius function for a profile with multiple turning points ($q = 4.0$) in a partially finite copper wire medium (2×2, $a_x = 13.06$ mm and $a_y = 15.00$ mm) for the parameter choice of $f_d = 9.6$ GHz, $R_c = 0.6$ mm and $\lambda_C = 9.52$ GHz. The fields are either represented using arrow plots where the arrow direction represents field direction and colour represents the magnitude of the field strength, or colour plots where the direction and magnitude of the longitudinal field is represented by colour. (a) shows an y-z slice through the centre of the structure, (b) an x-y slice and (c) a y-z slice through two of the wires.

The profiles for these two modes are shown in Figs. 8.45 and 8.46. These mode profiling attempts have been successful as can be seen from these plots and their $\mathfrak{R}^2$ values of 0.9771 for the triangular profile and 0.9403 for the profile with extra turning points.
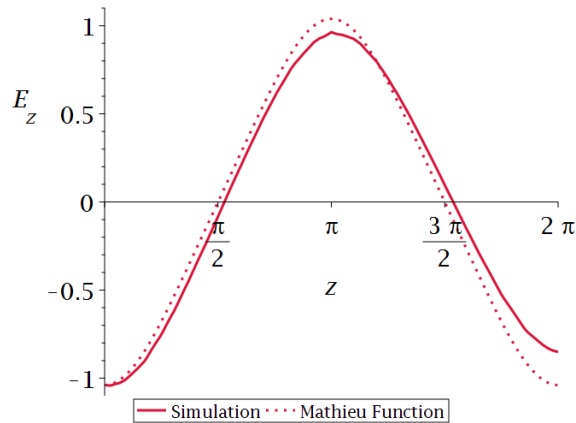
Figure 8.45: Plot of the field profile (longitudinal, z, spatial variation of the electric field strength, E_z) of the longitudinal mode ($f = 9.83$ GHz) in a partially finite copper wire medium (2×2, $a_x = 13.06$ mm and $a_y = 15.00$ mm) for our attempts to produce a triangular profile ($q = -0.329$) with a radius function based on the choice of $f_d = 11.3$ GHz, $R_c = 0.5$ mm and $\lambda_C = 10.7$ GHz (crimson). The plot includes the field profile observed in our numerical simulation (solid) and the desired profile (dotted). In order to compare these the field profile and z coordinate have been normalised.
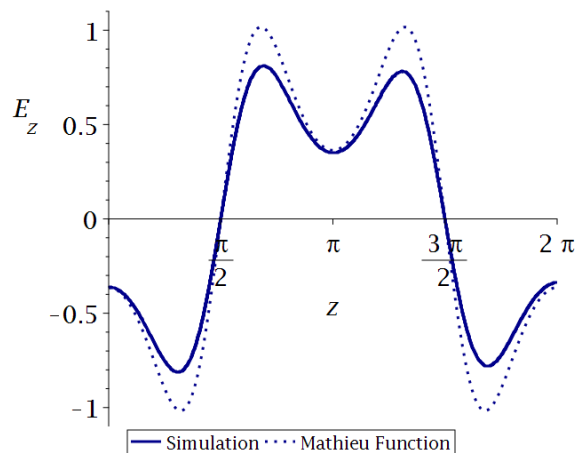
Figure 8.46: Plot of the field profile (longitudinal, z, spatial variation of the electric field strength, E_z) of the longitudinal mode ($f = 9.61$ GHz) in a partially finite copper wire medium (2×2, $a_x = 13.06$ mm and $a_y = 15.00$ mm) for our attempts to produce a profile with multiple turning points ($q = 4.0$) with a radius function based on the choice of $f_d = 9.6$ GHz, $R_c = 0.6$ mm and $\lambda_C = 9.52$ GHz (dark blue). The plot includes the field profile observed in our numerical simulation (solid) and the desired profile (dotted). In order to compare these the field profile and z coordinate have been normalised.

As with previous simulations of this kind, when we are attempting to achieve

a mode profile with a pronounced peak, there exist some complications. In the frequency range where we would expect to find our longitudinal mode the simulation finds two longitudinal modes, which are shown in Fig. 8.47. These two longitudinal modes were found at simulation frequencies, f, of 9.309 GHz and 9.311 GHz, a separation of 0.002 GHz or a percentage difference of 0.02 % from the first mode to the second.

(a)

(b)
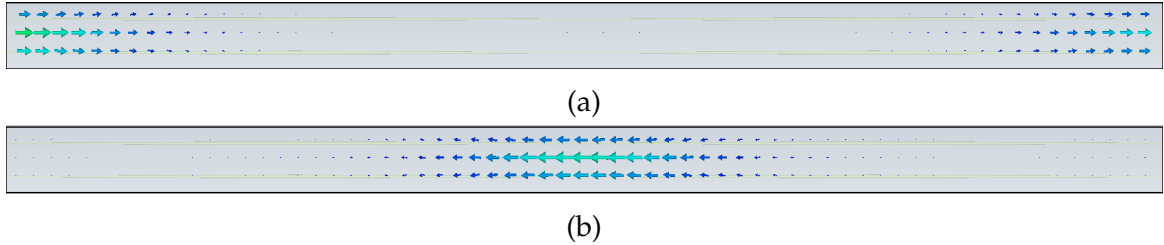
Figure 8.47: Images showing the resulting longitudinal modes after the implementation of the calculated radius function for a profile with a pronounced peak ($q = -10.0$) in a partially finite copper wire medium (2×2, $a_x = 13.06$ mm and $a_y = 15.00$ mm) for the parameter choice of $f_d = 9.3$ GHz, $R_c = 0.6$ mm and $\lambda_C = 9.52$ GHz. The fields are represented using arrow plots on a y-z slice of the structure where the arrow direction represents field direction and colour represents the magnitude of the field strength. (a) shows one of the resulting longitudinal modes ($f = 9.309$ GHz); and (b), the other ($f = 9.311$ GHz).

As we have done previously, we consider the superposition of these two modes. By doing this, we can find the mode profile shown in Fig. 8.48. This profile is somewhat similar to our desired profile with an $\Re^2$ value of 0.7972. Although we can see from the graph that there is some clear similarity between the desired and achieved profile, the significant differences in the peak values make the actual agreement between the profiles quite poor. This is potentially due to the use of a partially finite lattice and the effect of the metallic boundaries, but we cannot say for sure.
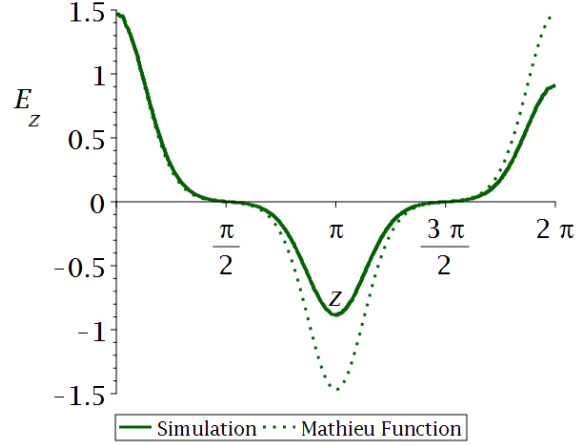
Figure 8.48: Plot of the combined field profile (longitudinal, z, spatial variation of the electric field strength, E_z) of the longitudinal modes (9.309 GHz and 9.311 GHz) in a partially finite copper wire medium (2×2, $a_x = 13.06$ mm and $a_y = 15.00$ mm) for our attempts to produce a profile with a pronounced peak ($q = -10.0$) with a radius function based on the choice of $f_d = 9.3$ GHz, $R_c = 0.6$ mm and $\lambda_C = 9.52$ GHz (dark green). The plot includes the field profile observed in our numerical simulation (solid) and the desired profile (dotted). In order to compare these the field profile and z coordinate have been normalised.

The results of our mode profiling attempts with a partially finite copper wire medium are summarised in Table 8.6. These results clearly show that our mode profiling continues to be successful in this new domain.

The obvious next step is to attempt to realise mode profiling results in a completely finite structure. As we have done previously, the easiest way to extend

q	f_d (GHz)	λ_C (GHz)	L (mm)	f (GHz)	$\mathfrak{R}^2$
0.8	10	9.79	184	10.02	0.9980
-0.329	9.8	9.52	101	9.83	0.9771
4	9.6	9.52	358	9.61	0.9403
-10	9.3	9.52	527	9.31	0.7972

Table 8.6: A table summarising some of the key parameters related to the results of our implemented radius functions for a variety of profiles in partially finite copper wire media ($a_x = 13.06$ mm and $a_y = 15.00$ mm). The parameters listed are: the Mathieu parameter characterising the profile (q), design frequency (f_d), the central plasma frequency (λ_c), the length of our unit cell (L), longitudinal mode frequency (f) and a figure of merit for the agreement between our field profile and the desired profile ($\mathfrak{R}^2$). The profiles considered are a triangular profile ($q = -0.329$), a profile with multiple turning points ($q = 4.0$) and a profile with a pronounced peak ($q = -10.0$).

our results from a partially finite structure to a finite structure is to apply metallic boundaries to the longitudinal boundaries of our successful partially finite structures. This is shown in Fig. 8.49 where the new boundaries are shown for the structure that we used to replicate a flat mode profile.
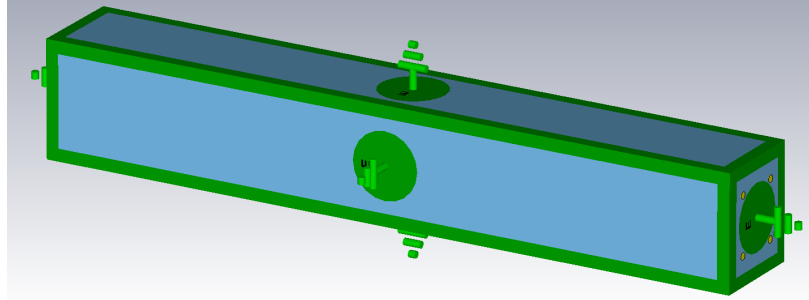
Figure 8.49: A representation of a finite wire medium in CST, consisting of a two by two lattice of copper wires in a unit cell with metallic boundary conditions ($a_x = 13.06$ mm and $a_y = 15.00$ mm). The copper wire has a variation based on a function generated using data from partially finite structures for the attempt to demonstrate a flattened profile based on the choice of $f_d = 10$ GHz, $R_c = 0.8$ mm and $\lambda_C = 9.79$ GHz. The image shows the boundaries of the structure with green representing metallic boundary conditions.

As our extension only involves the application of new boundary conditions to our structure, we can reuse the choice of parameters and the resulting radius functions from the partially finite case. The first profile we have attempted to replicate is the flattened profile ($q = 0.8$). The resulting radius function has previously been shown in Fig. 8.39.

(a)

(b)

(c)
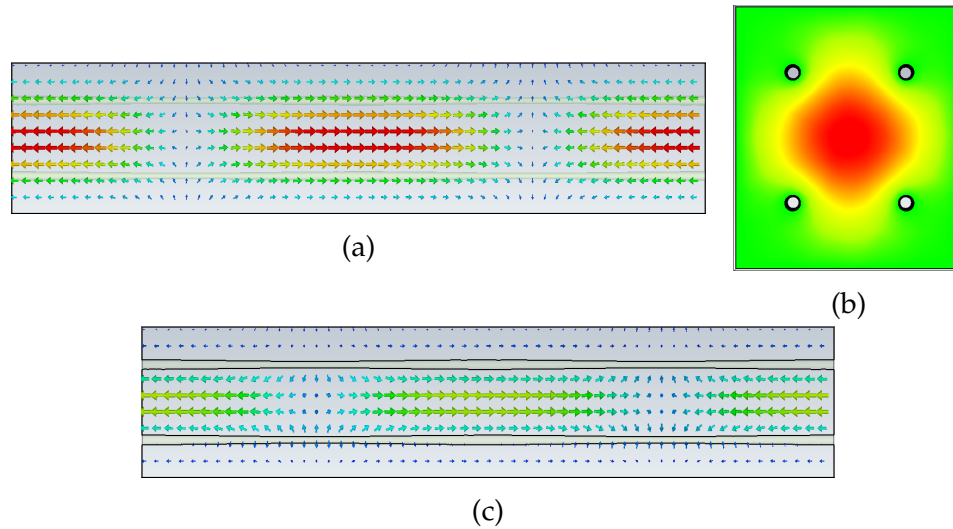
Figure 8.50: Images showing the resulting longitudinal mode ($f = 10.02$ GHz) after the implementation of the calculated radius function for a flattened profile ($q = 0.8$) in a finite copper wire medium (2×2, $a_x = 13.06$ mm and $a_y = 15.00$ mm) for the parameter choice of $f_d = 10$ GHz, $R_c = 0.8$ mm and $\lambda_C = 9.79$ GHz. The fields are either represented using arrow plots where the arrow direction represents field direction and colour represents the magnitude of the field strength, or colour plots where the direction and magnitude of the longitudinal field is represented by colour. (a) shows a y-z slice through the centre of the structure, (b) an x-y slice and (c) a y-z slice through two of the wires.

The longitudinal mode, found at 10.02 GHz, in the finite structure is shown in Fig. 8.50. The profile of this mode is shown in Fig. 8.51. This comparison clearly shows that our mode profiling method has continued to be successful, with an $\mathfrak{R}^2$ value of 0.9987.
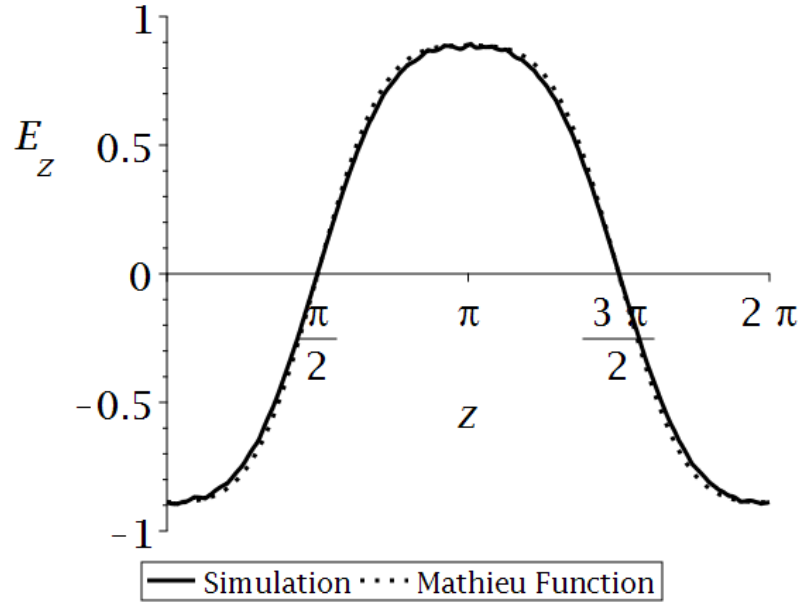
Figure 8.51: Plot of the field profile (longitudinal, z, spatial variation of the electric field strength, E_z) of the longitudinal mode (10.02 GHz) in a finite copper wire medium (2×2, $a_x = 13.06$ mm and $a_y = 15.00$ mm) for our attempts to produce a flattened profile ($q = 0.8$) by the implementation of a radius function based on the choice of $f_d = 10$ GHz, $R_c = 0.8$ mm and $\lambda_C = 9.79$ GHz (black). The plot includes the field profile observed in our numerical simulation (solid) and the desired profile (dotted). In order to compare these the field profile and z coordinate have been normalised.

As with the partially finite case, we also want to test our ability to replicate a variety of profiles. We are attempting to replicate the usual selection of profiles. Using the previously calculated radius functions, we have attempted to replicate the triangular profile and the profile with more turning points. The modes we have found in these simulations are shown in Figs. 8.52 and 8.53. The profiles of these modes have been plotted in Figs. 8.54 and 8.55. These attempts have been successful, as emphasised by the $\mathfrak{R}^2$ values of 0.9992 for the triangular profile and 0.9601 for the profile with more turning points.

(a)

(b)

(c)
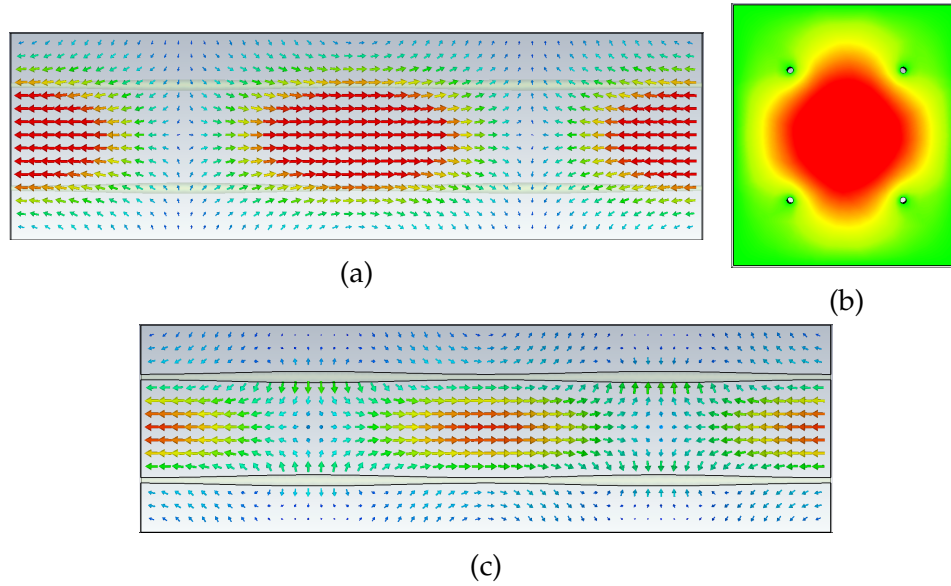
Figure 8.52: Images showing the resulting longitudinal mode ($f = 9.83$ GHz) after the implementation of the calculated radius function for a triangular profile ($q = -0.329$) in a finite copper wire medium (2×2, $a_x = 13.06$ mm and $a_y = 15.00$ mm) for the parameter choice of $f_d = 9.8$ GHz, $R_c = 0.6$ mm and $\lambda_C = 9.52$ GHz. The fields are either represented using arrow plots where the arrow direction represents field direction and colour represents the magnitude of the field strength, or colour plots where the direction and magnitude of the longitudinal field is represented by colour. (a) shows a y-z slice through the centre of the structure, (b) an x-y slice and (c) a y-z slice through two of the wires.

(a)

(b)

(c)
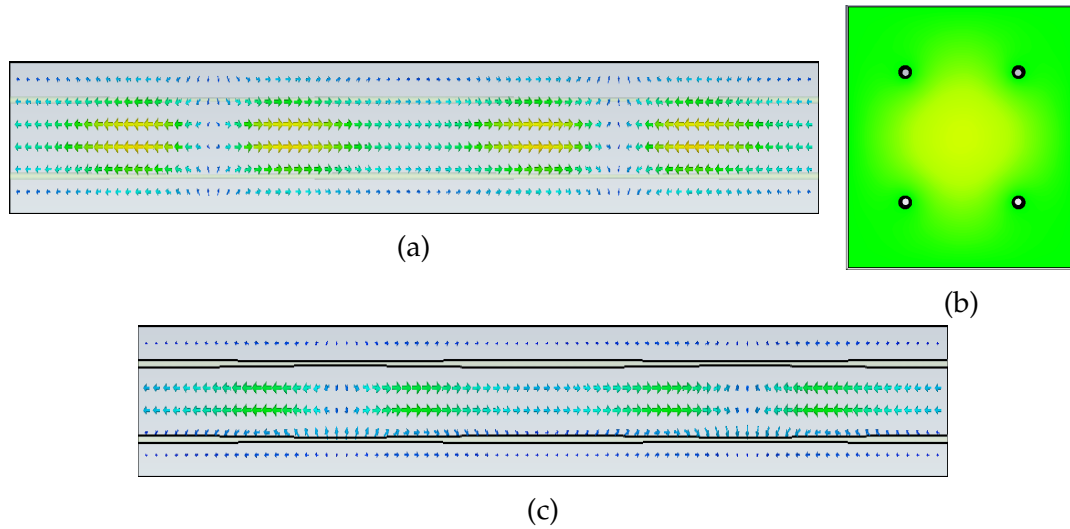
Figure 8.53: Images showing the resulting longitudinal mode ($f = 9.61$ GHz) after the implementation of the calculated radius function for a profile with multiple turning points ($q = 4.0$) in a finite copper wire medium (2×2, $a_x = 13.06$ mm and $a_y = 15.00$ mm) for the parameter choice of $f_d = 9.6$ GHz, $R_c = 0.6$ mm and $\lambda_C = 9.52$ GHz. The fields are either represented using arrow plots where the arrow direction represents field direction and colour represents the magnitude of the field strength, or colour plots where the direction and magnitude of the longitudinal field is represented by colour. (a) shows a y-z slice through the centre of the structure, (b) an x-y slice and (c) a y-z slice through two of the wires.


Figure 8.54: Plots of the field profile (longitudinal, z, spatial variation of the electric field strength, E_z) of the longitudinal mode ($f = 9.83$ GHz) in a finite copper wire medium (2×2, $a_x = 13.06$ mm and $a_y = 15.00$ mm) for our attempts to produce a triangular profile ($q = -0.329$) with a radius function based on the choice of $f_d = 11.3$ GHz, $R_c = 0.5$ mm and $\lambda_C = 10.7$ GHz (crimson). The plot includes the field profile observed in our numerical simulation (solid) and the desired profile (dotted). In order to compare these the field profile and z coordinate have been normalised.
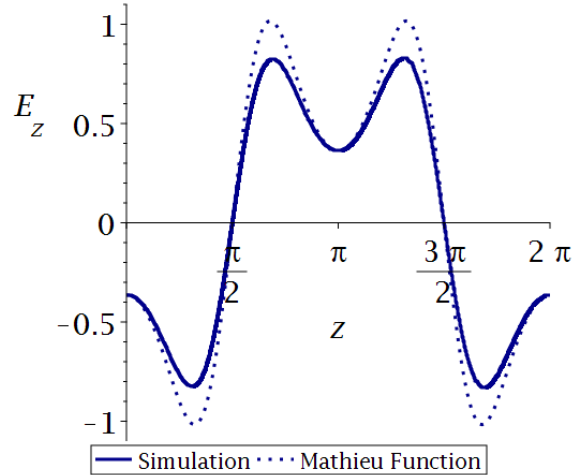
Figure 8.55: Plot of the field profile (longitudinal, z, spatial variation of the electric field strength, E_z) of the longitudinal mode ($f = 9.61$ GHz) in a finite copper wire medium (2×2, $a_x = 13.06$ mm and $a_y = 15.00$ mm) for our attempts to produce a profile with multiple turning points ($q = 4.0$) with a radius function based on the choice of $f_d = 9.6$ GHz, $R_c = 0.6$ mm and $\lambda_C = 9.52$ GHz (dark blue). The plot includes the field profile observed in our numerical simulation (solid) and the desired profile (dotted). In order to compare these the field profile and z coordinate have been normalised.


(a)

(b)

(c)
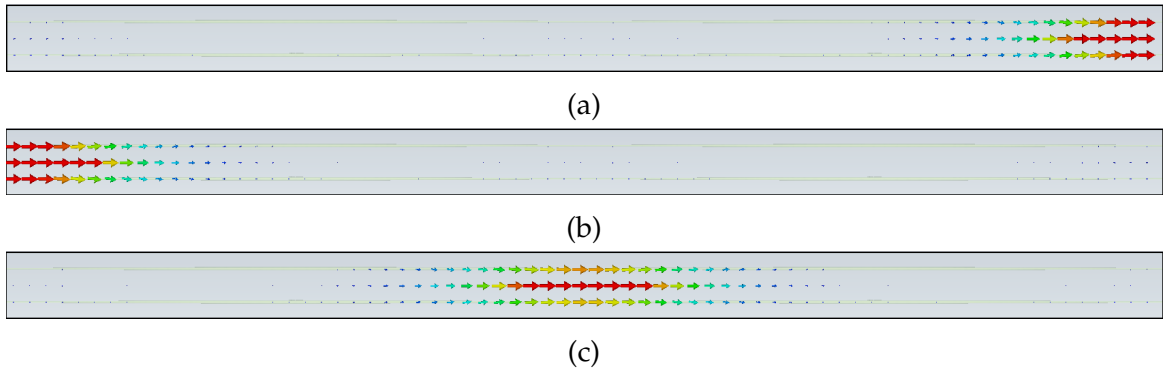
Figure 8.56: Images showing the resulting longitudinal modes after the implementation of the calculated radius function for a profile with a pronounced peak ($q = -10.0$) in a finite copper wire medium (2×2, $a_x = 13.06$ mm and $a_y = 15.00$ mm) for the parameter choice of $f_d = 9.3$ GHz, $R_c = 0.6$ mm and $\lambda_C = 9.52$ GHz. The fields are represented using arrow plots on a y-z slice of the structure where the arrow direction represents field direction and colour represents the magnitude of the field strength. (a) shows one of the resulting longitudinal modes ($f = 9.30547$ GHz); (b), another ($f = 9.30550$ GHz); and (c), the mode with highest frequency ($f = 9.30613$ GHz).

Similar to other attempts at replicating the profile with a pronounced peak, we

experienced some complications. In this case, our eigenmode simulation found three longitudinal modes, which are shown in Fig. 8.56, in the frequency range around our design frequency, 9.3 GHz. These modes were found at 9.30547, 9.30550 and 9.30613 GHz. There is a frequency range of $6.6 \cdot 10^{-3}$ GHz, which represents 0.007% of the initial mode frequency. These modes all have longitudinal fields that are localised to different areas of the structure.

As usual, we treat the separation of these modes as an artefact of the simulation. When the superposition of these fields is considered, we can compare profile of the combined field with the desired profile. This is shown in Fig. 8.57 where it can be seen that there is an excellent agreement, with an $\mathfrak{R}^2$ value of 0.9442.
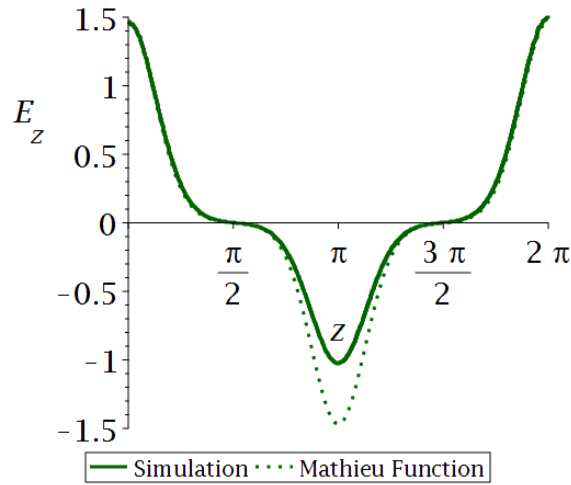

Figure 8.57: Plot of the combined field profile (longitudinal, z, spatial variation of the electric field strength, E_z) of the longitudinal modes ($f = 9.30547$ GHz, $f = 9.30550$ GHz and $f = 9.30613$ GHz) in a finite copper wire medium (2×2, $a_x = 13.06$ mm and $a_y = 15.00$ mm) for our attempts to produce a profile with a pronounced peak ($q = -10.0$) with a radius function based on the choice of $f_d = 9.3$ GHz, $R_c = 0.6$ mm and $\lambda_C = 9.52$ GHz (dark green). The plot includes the field profile observed in our numerical simulation (solid) and the desired profile (dotted). In order to compare these the field profile and z coordinate have been normalised.

The results of our attempts to achieve mode profiling in our finite copper structures are shown in Table 8.7. These results show that our method continues to be successful for finite copper structures. This is very promising as it gives us another route to take when attempting to realise our method experimentally. If dielectric materials prove to be troublesome, we have shown that metallic and, in particular, copper wires could potentially be used.

q	f_{d} (GHz)	λ_C (GHz)	L (mm)	$\mathfrak{R}^2$
0.8	10	9.79	184	0.9987
-0.329	9.8	9.52	101	0.9992
4	9.6	9.52	358	0.9601
-10	9.3	9.52	527	0.9442

Table 8.7: A table summarising some of the key parameters related to the results of our implemented radius functions for a variety of profiles in finite copper wire media (a_x = 13.06 mm and a_y = 15.00 mm). The parameters listed are: the Mathieu parameter characterising the profile (q), design frequency (f_{d}), the central plasma frequency (λ_c), the length of our unit cell (L), longitudinal mode frequency (f) and a figure of merit for the agreement between our field profile and the desired profile ($\mathfrak{R}^2$). The profiles considered are a triangular profile ($q = -0.329$), a profile with multiple turning points ($q = 4.0$) and a profile with a pronounced peak ($q = -10.0$).

IV. Time domain simulations of finite copper wire media

Now that we have demonstrated field profile shaping in finite copper structures, we can move onto attempting to observe field profile shaping in time domain simulations of our structures. This will gives us some indication of how easy it is to excite our structure.

We first chose a finite copper wire medium that had already demonstrated field shaping in eigenmode simulations. In this case, it was a two by two lattice of copper wires with a radius variation based on a parameter choice of $R_c = 0.8$ mm and $f_{\mathrm{d}} = 10$ GHz, shown in Fig. 8.58. It should be noted that, as shown in Fig. 8.58, we are using two periods of the radius variation, so we should expect a full period of our field profile. We then formed our structure by stacking five unit cells of this lattice on top of each other, creating a ten by two lattice, and including an extra section where the waveguide port is placed, effectively creating an inlet waveguide. This structure is shown in Fig 8.59. The waveguide section was designed to support modes around our design frequency, with dimensions of 10 mm by 23 mm.
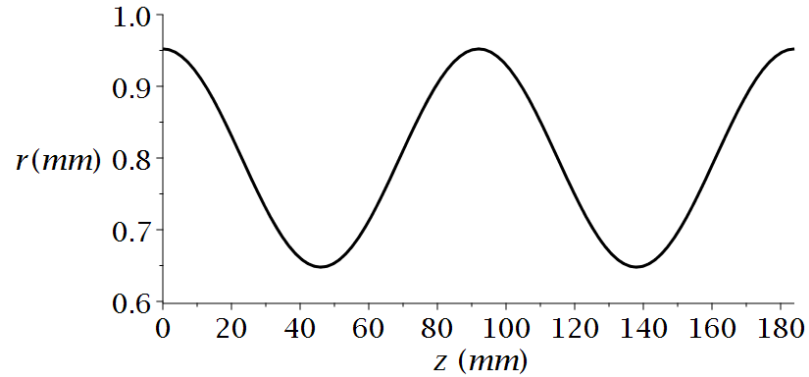
Figure 8.58: Two periods of the radius function calculated for a flattened profile ($q = 0.8$) in a finite copper wire medium (2×2, $a_x = 13.06$ mm and $a_y = 15.00$ mm) for the parameter choice of $f_d = 10$ GHz, $R_c = 0.8$ mm and $\lambda_C = 9.79$ GHz. This is the wire radius variation used in the following time domain simulations, although the lattice configurations used differ from the basis of the calculated function.
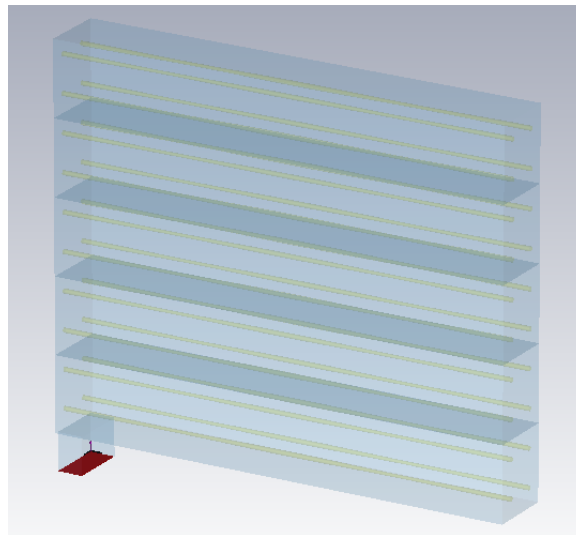
Figure 8.59: A representation of a finite wire medium in CST, consisting of five vertically stacked units of two by two lattices of copper wires. The unit cell has one set of metallic transverse boundary conditions, one set of open transverse boundary conditions and metallic longitudinal boundary conditions. The copper wires have a radius function calculated for a flattened profile ($q = 0.8$) in a finite copper wire medium (2×2, $a_x = 13.06$ mm and $a_y = 15.00$ mm) for the parameter choice of $f_d = 10$ GHz, $R_c = 0.8$ mm and $\lambda_C = 9.79$ GHz. A small section has been attached to the bottom of the structure with dimensions $x_{dim} = 23$ mm, $y_{dim} = 15$ mm and $z_{dim} = 10$ mm, where a waveguide port has been placed. This structure has copper wires with two periods of the radius variation.

We have chosen a frequency range of 9-11 GHz, which results in the excitation shown in Fig. 8.60.
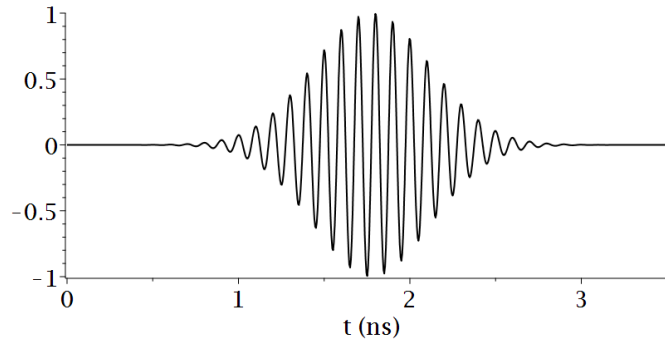
Figure 8.60: The default excitation signal generated by CST for a choice of frequency range of 9-11 GHz. This is the signal we will use to excite a finite copper wire medium structure (5 units of 2×2; $a_x = 13.06$ mm and $a_y = 15.00$ mm; $q = 0.8$, $f_d = 10$ GHz, $R_c = 0.8$ mm and $\lambda_C = 9.79$ GHz; open y boundaries, and metallic x and z boundaries; and a waveguide port, which is distanced 15 mm from the lattice, with dimension 23×10 mm).

As with the majority of our dielectric time domain simulations, we have used the fundamental port mode to excite our structure. The simulation time we have chosen is $t = 180$ ns. The field produced at the frequency monitor included is shown in Fig. 8.61. This field has significant longitudinal components and shows a full period variation in the field, which is promising.

(a)

(b)
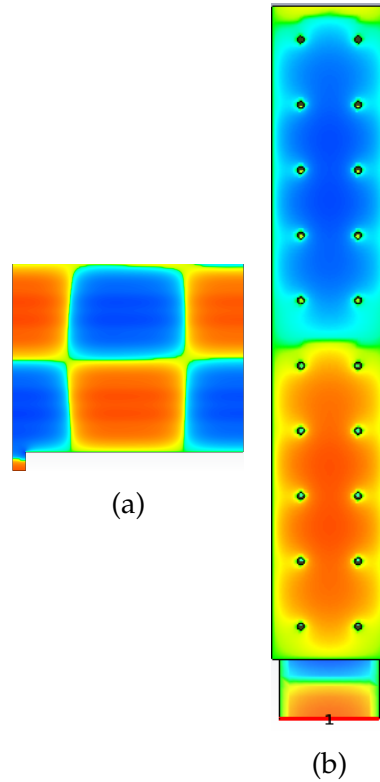
Figure 8.61: Images from numerical simulations in CST showing the field ($f = 9.08$ GHz) found using a frequency monitor in a time domain simulation of a finite copper wire medium (5 units of 2×2; $a_x = 13.06$ mm and $a_y = 15.00$ mm; $q = 0.8$, $f_d = 10$ GHz, $R_c = 0.8$ mm and $\lambda_C = 9.79$ GHz; open y boundaries, and metallic x and z boundaries; and a waveguide port, which is distanced 15 mm from the lattice, with dimension 23×10 mm) with $t = 180$ ns. The fields are represented using logarithmic colour plots where the longitudinal field strength and magnitude is represented by colour. (a) shows a y-z slice; and (b), an x-y slice.

A plot of the $\mathfrak{R}^2$ value of our field profiles comparison with our desired profile at various positions throughout the structure is shown in Fig. 8.62. This plot shows two extended regions of successful field profile shaping, although also some extended regions of poor profile shaping. This seems like a good achievement considering the difficulty we found observing prolonged regions of successful field profiling in two period structure with dielectric wire media. As with our time domain simulations of dielectric wire media, our success observing some regions of field profile shaping is qualified by the fact that we have not demonstrated that this field can achieve a significant transmission through the structure. It should also be noted that the field profiling is found at a frequency quite far from our design frequency, a difference of about 1 GHz.
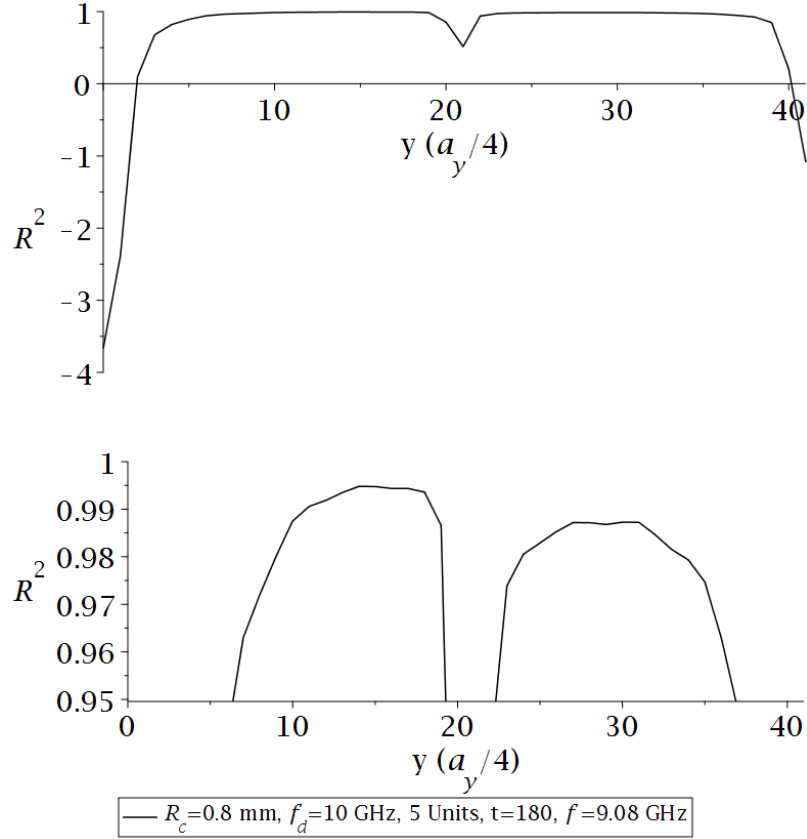
Figure 8.62: A plot of a figure of merit ($\mathfrak{R}^2$) for the comparison between the desired profile and the field profile (longitudinal, z, spatial variation of the electric field strength, E_z) of the field (9.08 GHz) in a finite copper wire medium ($t = 180$ ns; 5 units of 2×2; $a_x = 13.06$ mm and $a_y = 15.00$ mm; $q = 0.8$, $f_d = 10$ GHz, $R_c = 0.8$ mm and $\lambda_C = 9.79$ GHz; open y boundaries and, metallic x and z boundaries; and a waveguide port, which is distanced 15 mm from the lattice, with dimension 23×10 mm) at the evaluation position against the y position of the evaluation line given in terms of quarter lattice parameters from the bottom of the structure ($a_y/4$). (a) is a full plot and (b) only shows $\mathfrak{R}^2$ values above 0.95.

V.   Conclusions

In this chapter, we showed that our success with mode profile shaping could be extended to wire media formed from metallic wires. Similar to our work with dielectric wire media, we first showed that our longitudinal modes existed in infinite PEC wire media and that their plasma frequency is related to the wire radius. In this case, the relationship is well described by a straight line fit. We then developed our field profiling method with infinite PEC wire media and successfully replicated a variety of desired profiles. We then repeated this process with infi-

276

nite copper wire media with similar results. After this, we then showed that our method could be used with partially finite and finite copper wire media. Finally, we again explored the excitation of our structures by running time domain simulations; successful field profile shaping could be observed, but we did not confirm the transmission of these fields.

Chapter 9

Future Work

In this thesis, we have detailed the development of a method for field profile shaping that exploits the spatial dispersion in wire media. We have been successful in validating this method in eigenmode simulations for a wide variety of wire media realisations. In this section, we will consider some ways in which the work of this thesis could be extended further.

There are several areas already explored where it would be useful to extend our work before attempting experimental verification. It would be beneficial to confirm the quality of the transmission of the fields for which field profiling was observed in our time domain simulations. Further time domain simulations could have also focused on a complete structure including input and output funnels, supports and other practical features. More emphasis could also be used on the excitation used; different excitations such as very long pulses could be studied, which are closer to the continuous waves used in experiments.

Given more time, we would have attempted more ensembles of disorder in our simulations of partially finite structures. Trying just one ensemble of introduced imperfections risks accidentally using a configuration that has a collective effect that is not common to other ensembles. It is difficult to generate these ensembles in CST in an automated way, so this could necessitate a move to a different program. These simulations would reassure us that our method produces an effect that should be observable and that the effect is resistant to the sort of imperfections inherent in fabricated structures.

Another potential area of future work is further extending the lattice and material parameters used for our wire media. It would be interesting to simulate a dielectric wire made out of real dielectric material, as was done with copper for the metal wires. Demonstrating field profile shaping with a different set of lattice parameters that lead to fields in a different frequency regime would also have been interesting. The effect of using a lossy material could also be considered.

Other interesting approaches could involve modifying the field in a way focused on maximising figures of merit such as Q factor or shunt impedance. As briefly touched upon, it would be very useful to explore methods in which the

plasma frequency has a time dependence for acceleration applications. This could possibly be achieved using a material whose permittivity depends on an applied voltage. Another useful development would be to move from an ad hoc design process to an automated process which takes a set of initial parameters and outputs the necessary radius function, especially if this could be integrated into the simulation software.

One major area of development would be attempting to fabricate these structures and experimentally verify the work in this thesis. Many of our simulations were focused on extending our results to structures that could be more easily fabricated. Experimental verification of the field profile shaping would then lead to more consideration of how our method could be applied.

After experimental verification, attention could turn to wakefield simulations of the structure and simulations in which particles enter the structure and interact with the fields. We could also export the field profiles to tracking programs to see the effect of the field on a bunch of particles. These would potentially pave the way to possible applications of our structure in accelerator applications. This would require a large amount of work and development of the method as it currently exists.

Chapter 10

Conclusion

We have detailed the development of our method for the field profile shaping of longitudinal electric fields by exploiting the spatial dispersion of wire media. The ability to achieve the desired field profile, without the need for an iterative design, could open up a number of different applications. There could potentially be uses in the field of particle acceleration, although it would be preferable if we were controlling the temporal profile of the field. Other potential applications include improving the ionisation in high harmonic generation; producing fields with high gradients but reduced peak fields to reduce non-linear effects; and creating fields with a pronounced peak for use in signal processing. In this section, we will detail the conclusions of our work in the various results chapters of this thesis.

In Chapter 4, the first step in the development of our field profiling method for infinite dielectric wire media is laid out, which focuses on the theoretical analysis of the problem. We should note that the analysis in Chapter 4 can be applied to any spatially dispersive realisation of uniaxial wire media and is based on the existence of plasma-like longitudinal electric fields in wire media that have been predicted by others. We were able to find a condition for the required variation in the plasma frequency of our wire medium along the longitudinal direction to produce our desired field profile. These desired field profiles are taken from the solutions of Mathieu's equation. We also proposed how this condition could be met in the case of a plasma frequency with a radius dependence, where the requirements for the satisfaction of our field profiling condition could be found by solving for a required radius function.

Our first attempt to characterise the longitudinal fields in wire media is detailed in Chapter 5. For this exploration, we used numerical simulations of an effectively infinite uniaxial dielectric wire media. The dielectric permittivity of our wires, or rods, was $\varepsilon_r = 1600$, which could be achieved using barium-strontium-titanate (BST), and their radius was $r = 0.3$ mm. The lattice parameters were $a_x = 13.06$ mm and $a_y = 15$ mm. Given this realisation of wire media, we were able to confirm the existence of longitudinal modes in an eigenmode simulation at a frequency of 6.03 GHz. As well as confirming their existence, by plotting the

mode's dispersion relation, we were able to confirm that they were plasma-like. This was a crucial step in the development of our field profile shaping as our theoretical analysis of the problem was built on the existence of these plasma-like longitudinal fields. In Chapter 5, we also plotted the dispersion relation of a few transverse modes, emphasising their difference, and carried out a mesh study that reassured us that our results were stable with respect to an increase in the density of the mesh.

The initial development of our field profile shaping method and its successful testing is covered in Chapter 6. In an attempt to control the properties of our longitudinal field, we studied the effect of changing the wire radius of our wire media. We were able to find our desired longitudinal field for a variety of wire radii in the range 0.1 to 0.475 mm in otherwise identical infinite dielectric wire media. Having found these fields at different radii, we could see the effect on their plasma frequency by comparing their dispersion relations. By taking the plasma frequencies associated with each radius from their dispersion relation, we were able to plot a graph of plasma frequency against radius as shown in Section I. We used the data in this graph to find an approximate analytic relationship between these two quantities. After first trying a second order polynomial function, we found that an exponential decay function described our data exceptionally accurately in section II. We could now achieve the variation in the plasma frequency prescribed by our theoretical analysis. This involved substituting in the analytic function for the relationship between the plasma frequency and wire radius into our previously derived condition for the support of our desired field profile. We can then solve this condition for a required longitudinally varying radius function as showed in Section III.

This function contains several free parameters that need to be fixed. A discussion of how to sensibly fix these parameters to give valid solutions is included in Section IV. At this point, our field profiling method, which involved choosing the desired profile and producing a required radius function, was established, and we moved onto testing it in numerical simulations. Dielectric wires formed from a number of segments with differing radii were used to approximate our required radius function in the simulations. As covered extensively in Section V, we were able to achieve the replication of a flattened profile in our wire media in a variety of different realisations of wire media based on different choices for the fixed parameters. We then confirmed the stability of these results to variations in both the number of segments used for the varying wire and the density of mesh in Sections VI and VII. Finally, in Section VIII we confirmed that we could replicate not only a flattened profile but also several other profiles. In total, we replicated four different profiles, but the method should support profiles corresponding to any solution of Mathieu's equation.

After achieving our initial success with infinite dielectric wire media, which were formed from high permittivity rods, we wanted to extend our results to structures more suitable for fabrication as explored in Chapter 7. We first inves-

tigated the effect of using dielectric wires with lower permittivities in I. We confirmed that our longitudinal fields were still supported and had all the required properties. Importantly, we also found that although the relationship between the plasma frequency and radius was altered, it could still be described by an exponential decay function. This allowed us to implement our previous field profiling method without significant modifications. By doing this, we were able to show that our method was still hugely successful replicating a variety of profile even with dielectric wires with a permittivity as low as $\varepsilon_r = 3$. The effect of the lattice parameters of our dielectric wire media was studied in Section II. We found that longitudinal fields were supported even for shifts in either one or both of the lattice parameters, although their frequencies were shifted. This effect could be utilised in extending our results to different frequency ranges by changing the lattice parameters. In Section III, the addition of various types of disorder was studied to determine the stability of our results to the sort of errors that are unavoidable in fabrication. Random variations in the radius of our wire were considered with the results being quite stable up to variations on the order of 0.1 mm as compared to the central wire radius of 0.6 mm. Systematic shifts in the radius of the wire radii were also considered with the results being incredibly stable, although a shift in the frequency of the profiled field was observed. We also examined the effect of including a dielectric cladding over our wires, which could aid fabrication, in Section IV. We found that given a suitable cladding it could be introduced with minimal deterioration to our field profile shaping results.

The extension of our method to partially finite structures is described in Section V. By partially finite we mean a finite lattice (two by two) of infinitely long wires surrounded by transverse metallic boundary conditions. This effort started with the confirmation of the existence of longitudinal fields in these structures and that their dispersion relation is plasma-like. Again, we found the relationship between the plasma frequencies of these fields and the wire radius to be extremely well described by an exponential decay function. Given this, we repeated the method laid out previously and were able to replicate a variety of profiles using partially finite dielectric wire media. In Section VI, this work was then extended further to completely finite structures. In this case, the wire media is a finite lattice (two by two) of wires of finite length. We found that extending our results to this regime only required the application of metallic boundary conditions to the longitudinal dimension of structures already used in our simulations of partially finite structures. By doing this, we were able to replicate a variety of desired field profile in finite dielectric wire media. This process was repeated in Section VII for a finite four by four lattice with the same success. Having extended our field profile shaping to finite structures, we then studied the effect of introducing disorder into these structures in Section VIII. As with our previous study of disorder, we considered random variations in the wire radii, but in this case, each wire had their own unique set of random radius variations. We found that with a wire with a central radius value of 0.6 mm, errors on the order of 0.1 mm lead

to minimal deterioration in our results, but a significant deterioration was seen for errors on the order of 0.2 mm. A consideration of the effect of random variations in the wire positions found our results to be stable up to and including the introduction of errors on the order of 5% of the lattice parameters. The study of a coordinated shift of the wire positions to make a denser or more sparse lattice found that the existence of the longitudinal fields was stable for a 10 % shift, but that the quality of the field profile shaping was only maintained when making the lattice denser. We also attempted to explore the excitation of our structure using time domain simulations in Section IX. We had some success in this area. We were able to observe field profile shaping at some frequencies in the structure, but we did not establish that an adequate transmission was reached at those frequencies. This limitation was due to a lack of time and experience with these simulations and not necessarily a reflection on the ability of these structures to produce the required transmissions.

After developing a robust and successful method for field profile shaping with dielectric wire media, we extended this method to metallic wire media in Chapter 8. We first made progress by applying the process undertaken with dielectric wire to wires made of a perfect electrical conductor (PEC), as discussed in Section I. We confirmed the existence of plasma-like longitudinal electric fields in infinite PEC wire media. With this established, we could investigate the effect of varying the radius on the plasma frequency of these fields. In the case of PEC, there was a positive linear relationship between the quantities. This lead to the data being well described by a straight line function rather than an exponential decay function. This caused some minor differences in the calculation and solutions of the required radius function but otherwise affected our method minimally. With our method for mode profile shaping with infinite PEC wire media now developed, we confirmed that we were able to replicate several different profiles. After our success with PEC wire media, we switched our attention to copper wires in Section II. As before, we found our longitudinal plasma-like electric fields in infinite copper wire media and found that a straight line function well described the relationship between the plasma frequency and wire radius. Given this, we were able to develop and test our method; confirming that we could replicate several different profiles very accurately. In Section III we extended our work with copper wire media to include simulation of partially finite and finite lattices. We were able to show that for both of these regimes, our method was still able to achieve successful replication of desired field profiles. Finally, in Section IV we explore our attempts to simulate the excitation of finite copper structures. Similar to our experience with dielectric wire media, we found that we could observe field profile shaping, but we did not confirm whether the transmission of these fields was adequate.

The culmination of this work represents the establishment of a field profiling method for longitudinal electric field, which has proved to be very successful in numerical simulations and extremely flexible in its application, spanning various

realisations and materials. One clear area of improvement would be confirming the transmission of the fields found in our time domain simulations. Beyond this, a logical next step would be the possible fabrication of a structure and an attempt at experimental verification.

Bibliography

[1] Taylor Boyd, Jonathan Gratus, Paul Kinsler, and Rosa Letizia. Customizing longitudinal electric field profiles using spatial dispersion in dielectric wire arrays. *Optics express*, 26(3):2478–2494, 2018.

[2] Taylor Boyd, Jonathan Gratus, Paul Kinsler, Rosa Letizia, and Rebecca Seviour. Mode profile shaping in wire media: Towards an experimental verification. *Applied Sciences*, 8(8):1276, 2018.

[3] Jonathan Gratus and Robin W Tucker. Covariant constitutive relations and relativistic inhomogeneous plasmas. *Journal of Mathematical Physics*, 52(4):042901, 2011.

[4] GS Agarwal, DN Pattanayak, and E Wolf. Electromagnetic fields in spatially dispersive media. *Physical Review B*, 10(4):1447, 1974.

[5] SI Pekar. The theory of electromagnetic waves in a crystal in which excitons are produced. *Sov. Phys. JETP*, 6(4):785, 1958.

[6] JJ Hopfield and DG Thomas. Theoretical and experimental effects of spatial dispersion on the optical properties of crystals. *Physical Review*, 132(2):563, 1963.

[7] Constantin Simovski. *Composite Media with Weak Spatial Dispersion*. Jenny Stanford, 2018.

[8] PA Belov, R Marques, SI Maslovski, IS Nefedov, M Silveirinha, CR Simovski, and SA Tretyakov. Strong spatial dispersion in wire media in the very large wavelength limit. *Physical Review B*, 67(11):113103, 2003.

[9] Torben Skettrup and I Balslev. Boundary conditions in case of spatial resonance dispersion. *Physical Review B*, 3(4):1457, 1971.

[10] Roland Zeyher, Joseph L Birman, and Wilhelm Brenig. Spatial dispersion effects in resonant polariton scattering. I. Additional boundary conditions for polarization fields. *Physical Review B*, 6(12):4613, 1972.

[11] Joseph L Birman and John J Sein. Optics of polaritons in bounded media. *Physical Review B*, 6(6):2482, 1972.

[12] AA Maradudin and DL Mills. Effect of spatial dispersion on the properties of a semi-infinite dielectric. *Physical Review B*, 7(6):2787, 1973.

[13] C Alden Mead and Michael R Philpott. Reflectivity of a spatially dispersive crystal. *Physical Review B*, 17(2):914, 1978.

[14] B Chen and DF Nelson. Wave propagation of exciton polaritons by a wave-vector-space method. *Physical Review B*, 48(20):15372, 1993.

[15] K Henneberger. Additional boundary conditions: An historical mistake. *Physical review letters*, 80(13):2889, 1998.

[16] Mário G Silveirinha. Additional boundary condition for the wire medium. *IEEE transactions on antennas and propagation*, 54(6):1766–1780, 2006.

[17] Mário G Silveirinha, Carlos A Fernandes, and Jorge R Costa. Additional boundary condition for a wire medium connected to a metallic surface. *New Journal of Physics*, 10(5):053011, 2008.

[18] Mário G Silveirinha. Additional boundary conditions for nonconnected wire media. *New Journal of Physics*, 11(11):113016, 2009.

[19] Stanislav I Maslovski, Tiago A Morgado, Mário G Silveirinha, Chandra SR Kaipa, and Alexander B Yakovlev. Generalized additional boundary conditions for wire media. *New Journal of Physics*, 12(11):113047, 2010.

[20] Jonathan Gratus and Matthew McCormack. *Inhomogeneous spatially dispersive electromagnetic media*, pages 1007–1012. 9 2013.

[21] Andrey Aleksandrovich Golubkov and Vladimir A Makarov. Boundary conditions for electromagnetic field on the surface of media with weak spatial dispersion. *Physics-Uspekhi*, 38(3):325, 1995.

[22] SI Pekar. Dispersion of light in the exciton absorption region of crystals. *Sov. Phys. JETP*, 7:813–822, 1958.

[23] Vladimir M Agranovich and Vitalii L Ginzburg. Crystal optics with allowance for spatial dispersion; exciton theory. I. *Soviet Physics Uspekhi*, 5(2):323, 1962.

[24] DD Sell, R Dingle, SE Stokowski, and JV DiLorenzo. Observation of polaritons in gaas: a new interpretation of the free-exciton reflectance and luminescence. *Physical Review Letters*, 27(24):1644, 1971.

[25] C Alden Mead. Exactly soluble model for crystal with spatial dispersion. *Physical Review B*, 15(2):519, 1977.

[26] Michael R Philpott. Effect of spatial dispersion on the s-polarized optical properties of a slab dielectric. *The Journal of Chemical Physics*, 60(6):2520–2529, 1974.

[27] GS Agarwal, DN Pattanayak, and E Wolf. Structure of the electromagnetic field in a spatially dispersive medium. *Physical Review Letters*, 27(15):1022, 1971.

[28] W E Jones, KL Kliewer, and Ronald Fuchs. Nonlocal theory of the optical properties of thin metallic films. *Physical Review*, 178(3):1201, 1969.

[29] Wilhelm Brenig, Roland Zeyher, and Joseph L Birman. Spatial dispersion effects in resonant polariton scattering. II. Resonant Brillouin scattering. *Physical Review B*, 6(12):4617, 1972.

[30] R Ruppin. Reflectivity of a nonlocal dielectric with an excitonic surface potential. *Physical Review B*, 29(4):2232, 1984.

[31] Vassilios Yannopapas. Non-local optical response of two-dimensional arrays of metallic nanoparticles. *Journal of Physics: Condensed Matter*, 20(32):325211, 2008.

[32] Jeffrey M McMahon, Stephen K Gray, and George C Schatz. Nonlocal optical response of metal nanostructures with arbitrary shape. *Physical review letters*, 103(9):097403, 2009.

[33] N Guth, B Gallas, J Rivory, J Grand, A Ourir, G Guida, R Abdeddaim, C Jouvaud, and J De Rosny. Optical properties of metamaterials: Influence of electric multipoles, magnetoelectric coupling, and spatial dispersion. *Physical Review B*, 85(11):115138, 2012.

[34] Ruey-Lin Chern and Dezhuan Han. Nonlocal optical properties in periodic lattice of graphene layers. *Optics express*, 22(4):4817–4829, 2014.

[35] SI Pekar. Identification of excitons with light waves in a crystal and the macroscopic theory of excitons with and without account of retardation. *Sov. Phys. JETP*, 11:1286–1293, 1960.

[36] Craig W Deutsche and C Alden Mead. Use of retarded green's functions in exciton theory. *Physical Review*, 138(1A):A63, 1965.

[37] MF Bishop and AA Maradudin. Energy flow in a semi-infinite spatially dispersive absorbing dielectric. *Physical Review B*, 14(8):3384, 1976.

[38] Daniel C Mattis and Gerardo Beni. Eigenstates of excitons near a surface. *Physical Review B*, 18(8):3816, 1978.

[39] A Quattropani, LC Andreani, and F Bassani. Quantum theory of polaritons with spatial dispersion: Exact solutions. *Il Nuovo Cimento D*, 7(1):55–69, 1986.

[40] VN Tsytovich. Spatial dispersion in a relativistic plasma. *Sov. Phys. JETP*, 13(6):1249, 1961.

[41] Mikhail V Starodubtsev, Alexander V Kostrov, Vladimir V Nazarov, and German V Permitin. Excitation of quasielectrostatic waves in a laboratory magnetoplasma with weak spatial dispersion. *Physical Review E*, 72(2):026401, 2005.

[42] KL Kliewer and Ronald Fuchs. Anomalous skin effect for specular electron scattering and optical experiments at non-normal angles of incidence. *Physical Review*, 172(3):607, 1968.

[43] DF Nelson. Generalizing the poynting vector. *Physical review letters*, 76(25):4713, 1996.

[44] Vladimir M Agranovich and Yu N Gartstein. Spatial dispersion and negative refraction of light. *Physics-Uspekhi*, 49(10):1029, 2006.

[45] Chao Zhang and Tie Jun Cui. Spatial dispersion and energy in a strong chiral medium. *Optics Express*, 15(8):5114–5119, 2007.

[46] Bruno Gompf, Julia Braun, Thomas Weiss, Harald Giessen, Martin Dressel, and Uwe Hübner. Periodic nanostructures: spatial dispersion mimics chirality. *Physical review letters*, 106(18):185501, 2011.

[47] Massimo Moccia, Giuseppe Castaldi, Vincenzo Galdi, Andrea Alù, and Nader Engheta. Dispersion engineering via nonlocal transformation optics. *Optica*, 3(2):179–188, 2016.

[48] Jonathan Gratus, Paul Kinsler, Martin W McCall, and Robert T Thompson. On spacetime transformation optics: temporal and spatial dispersion. *arXiv preprint arXiv:1608.00496*, 2016.

[49] Jeffrey M McMahon, Stephen K Gray, and George C Schatz. Optical properties of nanowire dimers with a spatially nonlocal dielectric function. *Nano Letters*, 10(9):3473–3481, 2010.

[50] Søren Raza, Giuseppe Toscano, Antti-Pekka Jauho, Martijn Wubs, and N Asger Mortensen. Unusual resonances in nanoplasmonic structures due to nonlocal response. *Physical Review B*, 84(12):121412, 2011.

[51] Justin Elser, Viktor A Podolskiy, Ildar Salakhutdinov, and Ivan Avrutsky. Nonlocal effects in effective-medium response of nanolayered metamaterials. *Applied physics letters*, 90(19):191109, 2007.

[52] Mário G Silveirinha and Pavel A Belov. Spatial dispersion in lattices of split ring resonators with permeability near zero. *Physical Review B*, 77(23):233104, 2008.

[53] Alexey A Orlov, Pavel M Voroshilov, Pavel A Belov, and Yuri S Kivshar. Engineered optical nonlocality in nanostructured metamaterials. *Physical Review B*, 84(4):045424, 2011.

[54] AV Chebykin, AA Orlov, AV Vozianova, Stanislav I Maslovski, Yu S Kivshar, and Pavel A Belov. Nonlocal effective medium model for multilayered metal-dielectric metamaterials. *Physical Review B*, 84(11):115438, 2011.

[55] AV Chebykin, AA Orlov, CR Simovski, Yu S Kivshar, and Pavel A Belov. Nonlocal effective parameters of multilayered metal-dielectric metamaterials. *Physical Review B*, 86(11):115420, 2012.

[56] Ruey-Lin Chern. Spatial dispersion and nonlocal effective permittivity for periodic layered metamaterials. *Optics express*, 21(14):16514–16527, 2013.

[57] John Brown. Artificial dielectrics having refractive indices less than unity. *Proceedings of the IEE-Part IV: Institution Monographs*, 100(5):51–62, 1953.

[58] John Brown and Willis Jackson. The properties of artificial dielectrics at centimetre wavelengths. *Proceedings of the IEE-Part B: Radio and Electronic Engineering*, 102(1):11–16, 1955.

[59] A Carne and J Brown. Theory of reflections from the rodded-type artificial dielectric. *Proceedings of the IEE-Part B: Radio and Electronic Engineering*, 106(26):107–114, 1959.

[60] JS Seeley. The quarter-wave matching of dispersive materials. *Proceedings of the IEE-Part B: Radio and Electronic Engineering*, 106(26):103–106, 1959.

[61] JS Seeley and J Brown. The use of dispersive artificial dielectrics in a beam-scanning prism. *Proceedings of the IEE-Part B: Radio and Electronic Engineering*, 106(26):93–102, 1959.

[62] Walter Rotman. Plasma simulation by artificial dielectrics and parallel-plate media. *IRE Transactions on Antennas and Propagation*, 10(1):82–95, 1962.

[63] David R Smith, John B Pendry, and Mike CK Wiltshire. Metamaterials and negative refractive index. *Science*, 305(5685):788–792, 2004.

[64] John B Pendry, Anthony J Holden, David J Robbins, WJ Stewart, et al. Magnetism from conductors and enhanced nonlinear phenomena. *IEEE transactions on microwave theory and techniques*, 47(11):2075–2084, 1999.

[65] John Brian Pendry. Negative refraction makes a perfect lens. *Physical review letters*, 85(18):3966, 2000.

[66] Richard A Shelby, David R Smith, and Seldon Schultz. Experimental verification of a negative index of refraction. *science*, 292(5514):77–79, 2001.

[67] Costas M Soukoulis, Stefan Linden, and Martin Wegener. Negative refractive index at optical wavelengths. *Science*, 315(5808):47–49, 2007.

[68] Nicholas Fang, Hyesog Lee, Cheng Sun, and Xiang Zhang. Sub–diffraction-limited optical imaging with a silver superlens. *Science*, 308(5721):534–537, 2005.

[69] Pavel A Belov, Yang Hao, and Sunil Sudhakaran. Subwavelength microwave imaging using an array of parallel conducting wires as a lens. *Physical Review B*, 73(3):033108, 2006.

[70] Zhaowei Liu, Hyesog Lee, Yi Xiong, Cheng Sun, and Xiang Zhang. Far-field optical hyperlens magnifying sub-diffraction-limited objects. *Science*, 315(5819):1686–1686, 2007.

[71] N I Landy, S Sajuyigbe, Jack J Mock, David R Smith, and Willie J Padilla. Perfect metamaterial absorber. *Physical review letters*, 100(20):207402, 2008.

[72] Claire M Watts, Xianliang Liu, and Willie J Padilla. Metamaterial electromagnetic wave absorbers. *Advanced materials*, 24(23):OP98–OP120, 2012.

[73] David R Smith and John B Pendry. Homogenization of metamaterials by field averaging. *JOSA B*, 23(3):391–403, 2006.

[74] Mário G Silveirinha. Nonlocal homogenization model for a periodic array of ε-negative rods. *Physical Review E*, 73(4):046612, 2006.

[75] Constantin R Simovski. On electromagnetic characterization and homogenization of nanostructured metamaterials. *Journal of Optics*, 13(1):013001, 2010.

[76] Andrea Alu. First-principles homogenization theory for periodic metamaterials. *Physical Review B*, 84(7):075153, 2011.

[77] Mário G Silveirinha. Metamaterial homogenization approach with application to the characterization of microstructured composites with negative parameters. *Physical Review B*, 75(11):115104, 2007.

[78] CR Simovski and PA Belov. Low-frequency spatial dispersion in wire media. *Physical Review E*, 70(4):046616, 2004.

[79] Igor S Nefedov, Ari J Viitanen, and Sergei A Tretyakov. Propagating and evanescent modes in two-dimensional wire media. *Physical Review E*, 71(4):046612, 2005.

[80] Mário G Silveirinha and Carlos A Fernandes. Homogenization of 3-d-connected and nonconnected wire metamaterials. *IEEE transactions on microwave theory and techniques*, 53(4):1418–1430, 2005.

[81] Stanislav I Maslovski and Mário G Silveirinha. Nonlocal permittivity from a quasistatic model for a class of wire media. *Physical Review B*, 80(24):245101, 2009.

[82] SI Maslovski, MG Silveirinha, AB Yakovlev, CSR Kaipa, GW Hanson, PA Belov, O Luukkonen, IS Nefedov, CR Simovski, SA Tretyakov, et al. Recent advances in the analytical modeling of wire media based metamaterials with microwave and terahertz applications. In *2013 International Symposium on Electromagnetic Theory*, pages 384–387. IEEE, 2013.

[83] AL Pokrovsky and AL Efros. Nonlocal electrodynamics of two-dimensional wire mesh photonic crystals. *Physical Review B*, 65(4):045110, 2002.

[84] DF Sievenpiper, ME Sickmiller, and E Yablonovitch. 3D wire mesh photonic crystals. *Physical Review Letters*, 76(14):2480, 1996.

[85] John B Pendry, AJ Holden, DJ Robbins, and WJ Stewart. Low frequency plasmons in thin-wire structures. *Journal of Physics: Condensed Matter*, 10(22):4785, 1998.

[86] Philippe Gay-Balmaz, Claudio Maccio, and Olivier JF Martin. Microwire arrays with plasmonic response at microwave frequencies. *Applied Physics Letters*, 81(15):2896–2898, 2002.

[87] Jonghwa Shin, Jung-Tsung Shen, and Shanhui Fan. Three-dimensional electromagnetic metamaterials that homogenize to uniform non-maxwellian media. *Physical Review B*, 76(11):113101, 2007.

[88] Mário G Silveirinha and Carlos A Fernandes. Nonresonant structured material with extreme effective parameters. *Physical Review B*, 78(3):033108, 2008.

[89] Mário G Silveirinha, Carlos A Fernandes, Jorge R Costa, and Carla R Medeiros. Experimental demonstration of a structured material with extreme effective parameters at microwaves. *Applied Physics Letters*, 93(17):174103, 2008.

[90] Mário G Silveirinha, Carlos A Fernandes, and Jorge R Costa. Superlens made of a metamaterial with extreme effective parameters. *Physical Review B*, 78(19):195121, 2008.

[91] Mário G Silveirinha. Anomalous refraction of light colors by a metamaterial prism. *Physical review letters*, 102(19):193903, 2009.

[92] Mário G Silveirinha. Broadband negative refraction with a crossed wire mesh. *Physical Review B*, 79(15):153109, 2009.

[93] Tiago A Morgado and Mário G Silveirinha. Transport of an arbitrary near-field component with an array of tilted wires. *New Journal of Physics*, 11(8):083023, 2009.

[94] Mário G Silveirinha, Carla R Medeiros, Carlos A Fernandes, and Jorge R Costa. Experimental verification of broadband superlensing using a metamaterial with an extreme index of refraction. *Physical Review B*, 81(3):033101, 2010.

[95] Tiago A Morgado, João S Marcos, Mário G Silveirinha, and Stanislav I Maslovski. Experimental verification of full reconstruction of the near-field with a metamaterial lens. *Applied Physics Letters*, 97(14):144102, 2010.

[96] Tiago A Morgado, Joao S Marcos, Stanislav I Maslovski, and Mário G Silveirinha. Negative refraction and partial focusing with a crossed wire mesh: physical insights and experimental verification. *Applied Physics Letters*, 101(2):021104, 2012.

[97] Olli Luukkonen, Mário G Silveirinha, Alexander B Yakovlev, Constantin R Simovski, Igor S Nefedov, and Sergei A Tretyakov. Effects of spatial dispersion on reflection from mushroom-type artificial impedance surfaces. *IEEE Transactions on Microwave Theory and Techniques*, 57(11):2692–2699, 2009.

[98] Alexander B Yakovlev, Mário G Silveirinha, Olli Luukkonen, Constantin R Simovski, Igor S Nefedov, and Sergei A Tretyakov. Characterization of surface-wave and leaky-wave propagation on wire-medium slabs and mushroom structures based on local and nonlocal homogenization models. *IEEE Transactions on Microwave Theory and Techniques*, 57(11):2700–2714, 2009.

[99] Chandra SR Kaipa, Alexander B Yakovlev, and Mário G Silveirinha. Characterization of negative refraction with multilayered mushroom-type metamaterials at microwaves. *Journal of Applied Physics*, 109(4):044901–044901, 2011.

[100] Chandra SR Kaipa, Alexander B Yakovlev, Stanislav I Maslovski, and Màrio G Silveirinha. Mushroom-type high-impedance surface with loaded vias: Homogenization model and ultra-thin design. *IEEE Antennas and Wireless Propagation Letters*, 10:1503–1506, 2011.

[101] Chandra SR Kaipa, Alexander B Yakovlev, Stanislav I Maslovski, and Mário G Silveirinha. Near-field imaging with a loaded wire medium. *Physical Review B*, 86(15):155103, 2012.

[102] David R Smith, Willie J Padilla, DC Vier, Syrus C Nemat-Nasser, and Seldon Schultz. Composite medium with simultaneously negative permeability and permittivity. *Physical review letters*, 84(18):4184, 2000.

[103] David R Smith and Norman Kroll. Negative refractive index in left-handed materials. *Physical review letters*, 85(14):2933, 2000.

[104] Constantin R Simovski, Pavel A Belov, Alexander V Atrashchenko, and Yuri S Kivshar. Wire metamaterials: physics and applications. *Advanced Materials*, 24(31):4229–4248, 2012.

[105] John B Pendry, AJ Holden, WJ Stewart, and I Youngs. Extremely low frequency plasmons in metallic mesostructures. *Physical review letters*, 76(25):4773, 1996.

[106] W Dickson, GA Wurtz, P Evans, D O'Connor, R Atkinson, R Pollard, and AV Zayats. Dielectric-loaded plasmonic nanoantenna arrays: a metamaterial with tuneable optical properties. *Physical Review B*, 76(11):115411, 2007.

[107] GA Wurtz, W Dickson, D O'connor, R Atkinson, W Hendren, P Evans, R Pollard, and AV Zayats. Guided plasmonic modes in nanorod assemblies: strong electromagnetic coupling regime. *Optics express*, 16(10):7460–7470, 2008.

[108] Mário G Silveirinha. Artificial plasma formed by connected metallic wires at infrared frequencies. *Physical Review B*, 79(3):035118, 2009.

[109] Tiago A Morgado, João S Marcos, Mário G Silveirinha, and Stanislav I Maslovski. Ultraconfined interlaced plasmons. *Physical review letters*, 107(6):063903, 2011.

[110] NA Nicorovici, RC McPhedran, and LC Botten. Photonic band gaps for arrays of perfectly conducting cylinders. *Physical Review E*, 52(1):1135, 1995.

[111] JM Pitarke, FJ García-Vidal, and JB Pendry. Effective electronic response of a system of metallic cylinders. *Physical Review B*, 57(24):15261, 1998.

[112] PA Belov, SA Tretyakov, and AJ Viitanen. Dispersion and reflection properties of artificial media formed by regular lattices of ideally conducting wires. *Journal of electromagnetic waves and applications*, 16(8):1153–1170, 2002.

[113] SI Maslovski, SA Tretyakov, and PA Belov. Wire media with negative effective permittivity: A quasi-static model. *Microwave and Optical Technology Letters*, 35(1):47–51, 2002.

[114] Ron Atkinson, William R Hendren, Gregory A Wurtz, Wayne Dickson, Anatoly V Zayats, Paul Evans, and Robert J Pollard. Anisotropic optical properties of arrays of gold nanorods embedded in alumina. *Physical Review B*, 73(23):235402, 2006.

[115] Justin Elser, Robyn Wangberg, Viktor A Podolskiy, and Evgenii E Narimanov. Nanowire metamaterials with extreme optical anisotropy. *Applied physics letters*, 89(26):261102, 2006.

[116] Paolo Burghignoli, Giampiero Lovat, Filippo Capolino, David R Jackson, and Donald R Wilton. Modal propagation and excitation on a wire-medium slab. *IEEE Transactions on Microwave Theory and Techniques*, 56(5):1112–1124, 2008.

[117] Paolo Burghignoli, Giampiero Lovat, Filippo Capolino, David R Jackson, and Donald R Wilton. Directive leaky-wave radiation from a dipole source in a wire-medium slab. *IEEE Transactions on Antennas and Propagation*, 56(5):1329–1339, 2008.

[118] Mário G Silveirinha and Stanislav I Maslovski. Radiation from elementary sources in a uniaxial wire medium. *Physical Review B*, 85(15):155125, 2012.

[119] Ebrahim Forati and George W Hanson. Transport model for homogenized uniaxial wire media: Three-dimensional scattering problems and homogenized model limits. *Physical Review B*, 88(12):125125, 2013.

[120] Alexander B Yakovlev, Maziar Hedayati, Mário G Silveirinha, and George W Hanson. Local thickness-dependent permittivity model for nonlocal bounded wire-medium structures. *Physical Review B*, 94(15):155442, 2016.

[121] Atsushi Ono, Jun-ichi Kato, and Satoshi Kawata. Subwavelength optical imaging through a metallic nanorod array. *Physical review letters*, 95(26):267407, 2005.

[122] Pavel A Belov, Constantin R Simovski, and Pekka Ikonen. Canalization of subwavelength images by electromagnetic crystals. *Physical review B*, 71(19):193105, 2005.

[123] Pavel A Belov and Mario G Silveirinha. Resolution of subwavelength transmission devices formed by a wire medium. *Physical Review E*, 73(5):056607, 2006.

[124] Yan Zhao, Pavel A Belov, and Yang Hao. Spatially dispersive finite-difference time-domain analysis of sub-wavelength imaging by the wire medium slabs. *Optics express*, 14(12):5154–5167, 2006.

[125] Mário G Silveirinha, Pavel A Belov, and Constantin R Simovski. Subwavelength imaging at infrared frequencies using an array of metallic nanorods. *Physical Review B*, 75(3):035108, 2007.

[126] Gennady Shvets, S Trendafilov, JB Pendry, and A Sarychev. Guiding, focusing, and sensing on the subwavelength scale using metallic wire arrays. *Physical review letters*, 99(5):053903, 2007.

[127] Pavel A Belov, Yan Zhao, Sunil Sudhakaran, Akram Alomainy, and Yang Hao. Experimental study of the subwavelength imaging by a wire medium slab. *Applied physics letters*, 89(26):262109, 2006.

[128] Pavel A Belov, Yan Zhao, Simon Tse, Pekka Ikonen, Mário G Silveirinha, Constantin R Simovski, Sergei Tretyakov, Yang Hao, and Clive Parini. Transmission of images with subwavelength resolution to distances of several wavelengths in the microwave range. *Physical Review B*, 77(19):193108, 2008.

[129] Mário G Silveirinha, Pavel A Belov, and Constantin R Simovski. Ultimate limit of resolution of subwavelength imaging devices formed by metallic rods. *Optics letters*, 33(15):1726–1728, 2008.

[130] Yan Zhao, Pavel Belov, and Yang Hao. Subwavelength internal imaging by means of a wire medium. *Journal of Optics A: Pure and Applied Optics*, 11(7):075101, 2009.

[131] Atiqur Rahman, Pavel A Belov, and Yang Hao. Tailoring silver nanorod arrays for subwavelength imaging of arbitrary coherent sources. *Physical Review B*, 82(11):113408, 2010.

[132] Yan Zhao, George Palikaras, Pavel A Belov, Rostyslav F Dubrovka, Constantin R Simovski, Yang Hao, and Clive G Parini. Magnification of subwavelength field distributions using a tapered array of metallic wires with planar interfaces and an embedded dielectric phase compensator. *New Journal of Physics*, 12(10):103045, 2010.

[133] Yan Zhao. Investigation of image magnification properties of hyperlenses formed by a tapered array of metallic wires using a spatially dispersive finite-difference time-domain method in cylindrical coordinates. *Journal of Optics*, 14(3):035102, 2012.

[134] Ali Forouzmand, Hossein M Bernety, and Alexander B Yakovlev. Graphene-loaded wire medium for tunable broadband subwavelength imaging. *Physical Review B*, 92(8):085402, 2015.

[135] Ali Forouzmand and Alexander B Yakovlev. Tunable dual-band subwavelength imaging with a wire medium slab loaded with nanostructured graphene metasurfaces. *AIP Advances*, 5(7):077108, 2015.

[136] Pekka Ikonen, Constantin Simovski, Sergei Tretyakov, Pavel Belov, and Yang Hao. Magnification of subwavelength field distributions at microwave frequencies using a wire medium slab operating in the canalization regime. *Applied Physics Letters*, 91(10):104102, 2007.

[137] Jie Yao, Zhaowei Liu, Yongmin Liu, Yuan Wang, Cheng Sun, Guy Bartal, Angelica M Stacy, and Xiang Zhang. Optical negative refraction in bulk metamaterials of nanowires. *Science*, 321(5891):930–930, 2008.

[138] Yongmin Liu, Guy Bartal, and Xiang Zhang. All-angle negative refraction and imaging in a bulk medium made of metallic nanowires in the visible region. *Optics Express*, 16(20):15439–15448, 2008.

[139] Mário G Silveirinha and Alexander B Yakovlev. Negative refraction by a uniaxial wire medium with suppressed spatial dispersion. *Physical Review B*, 81(23):233105, 2010.

[140] Chandra SR Kaipa, Alexander B Yakovlev, Stanislav I Maslovski, and Mário G Silveirinha. Indefinite dielectric response and all-angle negative refraction in a structure with deeply-subwavelength inclusions. *Physical Review B*, 84(16):165135, 2011.

[141] Tiago A Morgado, Stanislav I Maslovski, and Mario G Silveirinha. Uniaxial indefinite material formed by helical-shaped wires. *New Journal of Physics*, 14(6):063002, 2012.

[142] Chandra SR Kaipa and Alexander B Yakovlev. Partial focusing by a bulk metamaterial formed by a periodically loaded wire medium with impedance insertions. *Journal of Applied Physics*, 112(12):124902, 2012.

[143] Marc Thevenot, Cyril Cheype, Alain Reineix, and Bernard Jecko. Directive photonic-bandgap antennas. *IEEE Transactions on microwave theory and techniques*, 47(11):2115–2122, 1999.

[144] Ebrahim Forati and George W Hanson. On the epsilon near zero condition for spatially dispersive materials. *New Journal of Physics*, 15(12):123027, 2013.

[145] Mário G Silveirinha, Carlos A Fernandes, and Jorge R Costa. Electromagnetic characterization of textured surfaces formed by metallic pins. *IEEE Transactions on Antennas and Propagation*, 56(2):405–415, 2008.

[146] Olli Luukkonen, Filippo Costa, Constantin R Simovski, Agostino Monorchio, and Sergei A Tretyakov. A thin electromagnetic absorber for wide incidence angles and both polarizations. *IEEE transactions on antennas and propagation*, 57(10):3119–3125, 2009.

[147] Atiqur Rahman, Pavel A Belov, Yang Hao, and Clive Parini. Periscope-like endoscope for transmission of a near field in the infrared range. *Optics letters*, 35(2):142–144, 2010.

[148] Atiqur Rahman, Yang Hao, and Clive Parini. Subwavelength image splitter with a metallic wire array. *Physical Review B*, 82(15):153102, 2010.

[149] Evgenya I Smirnova, Amit S Kesar, Ivan Mastovsky, Michael A Shapiro, and Richard J Temkin. Demonstration of a 17-GHz, high-gradient accelerator with a photonic-band-gap structure. *Physical review letters*, 95(7):074801, 2005.

[150] Ismo V Lindell, SA Tretyakov, KI Nikoskinen, and S Ilvonen. BW media—Media with negative parameters, capable of supporting backward waves. *Microwave and Optical Technology Letters*, 31(2):129–133, 2001.

[151] Yashwanth R Padooru, Alexander B Yakovlev, Chandra SR Kaipa, George W Hanson, Francisco Medina, Francisco Mesa, and Allen W Glisson. New absorbing boundary conditions and analytical model for multilayered mushroom-type metamaterials: Applications to wideband absorbers. *IEEE Transactions on Antennas and Propagation*, 60(12):5727–5742, 2012.

[152] AL Pokrovsky and AL Efros. Electrodynamics of metallic photonic crystals and the problem of left-handed materials. *Physical review letters*, 89(9):093901, 2002.

[153] Alexander B Yakovlev, Yashwanth R Padooru, George W Hanson, Arash Mafi, and Salman Karbasi. A generalized additional boundary condition for mushroom-type and bed-of-nails-type wire media. *IEEE Transactions on Microwave Theory and Techniques*, 59(3):527–532, 2010.

[154] Igor S Nefedov, Ari J Viitanen, and Sergei A Tretyakov. Electromagnetic wave refraction at an interface of a double wire medium. *Physical Review B*, 72(24):245113, 2005.

[155] George W Hanson, Ebrahim Forati, and Mário G Silveirinha. Modeling of spatially-dispersive wire media: transport representation, comparison with natural materials, and additional boundary conditions. *IEEE Transactions on Antennas and Propagation*, 60(9):4219–4232, 2012.

[156] Ebrahim Forati and George W Hanson. Scattering from isotropic connected wire medium metamaterials: Three-, two-, and one-dimensional cases. *IEEE Transactions on Antennas and Propagation*, 61(7):3564–3574, 2013.

[157] Yan Zhao, Pavel A Belov, and Yang Hao. Modelling of wave propagation in wire media using spatially dispersive finite-difference time-domain method:

numerical aspects. *IEEE transactions on antennas and propagation*, 55(6):1506–1513, 2007.

[158] MA Shapiro, G Shvets, JR Sirigiri, and RJ Temkin. Spatial dispersion in metamaterials with negative dielectric permittivity and its effect on surface waves. *Optics letters*, 31(13):2051–2053, 2006.

[159] Wei Song, Zhun Yang, Xin-Qing Sheng, and Yang Hao. Accurate modeling of high order spatial dispersion of wire medium. *Optics express*, 21(24):29836–29846, 2013.

[160] João T Costa and Mário G Silveirinha. Macroscopic electromagnetic response of arbitrarily shaped spatially dispersive bodies formed by metallic wires. *Physical Review B*, 86(7):075129, 2012.

[161] RJ Pollard, A Murphy, WR Hendren, PR Evans, R Atkinson, GA Wurtz, AV Zayats, and Viktor A Podolskiy. Optical nonlocalities and additional waves in epsilon-near-zero metamaterials. *Physical review letters*, 102(12):127405, 2009.

[162] A Demetriadou and JB Pendry. Taming spatial dispersion in wire metamaterial. *Journal of Physics: Condensed Matter*, 20(29):295222, 2008.

[163] Jonathan Gratus and Matthew McCormack. Spatially dispersive inhomogeneous electromagnetic media with periodic structure. *Journal of Optics*, 17(2):025105, 2015.

[164] Mikhail V Rybin, Dmitry S Filonov, Kirill B Samusev, Pavel A Belov, Yuri S Kivshar, and Mikhail F Limonov. Phase diagram for the transition from photonic crystals to dielectric metamaterials. *Nature communications*, 6:10102, 2015.

[165] Kevin Vynck, Didier Felbacq, Emmanuel Centeno, AI Căbuz, David Cassagne, and Brahim Guizal. All-dielectric rod-type metamaterials at optical frequencies. *Physical review letters*, 102(13):133901, 2009.

[166] Costas M Soukoulis, Thomas Koschny, Jiangfeng Zhou, Maria Kafesaki, and Eleftherios N Economou. Magnetic response of split ring resonators at terahertz frequencies. *Physica status solidi (b)*, 244(4):1181–1187, 2007.

[167] Stephen O'Brien and John B Pendry. Photonic band-gap effects and magnetic activity in dielectric composites. *Journal of Physics: Condensed Matter*, 14(15):4035, 2002.

[168] Qian Zhao, Ji Zhou, Fuli Zhang, and Didier Lippens. Mie resonance-based dielectric metamaterials. *Materials today*, 12(12):60–69, 2009.

[169] S Foteinopoulou, Eleftherios N Economou, and CM Soukoulis. Refraction in media with a negative refractive index. *Physical review letters*, 90(10):107402, 2003.

[170] Kerwyn Casey Huang, ML Povinelli, and John D Joannopoulos. Negative effective permeability in polaritonic photonic crystals. *Applied Physics Letters*, 85(4):543–545, 2004.

[171] Jon A Schuller, Rashid Zia, Thomas Taubner, and Mark L Brongersma. Dielectric metamaterials based on electric and magnetic resonances of silicon carbide particles. *Physical review letters*, 99(10):107401, 2007.

[172] Liang Peng, Lixin Ran, Hongsheng Chen, Haifei Zhang, Jin Au Kong, and Tomasz M Grzegorczyk. Experimental observation of left-handed behavior in an array of standard dielectric resonators. *Physical review letters*, 98(15):157403, 2007.

[173] Shiyang Liu, Weikang Chen, Junjie Du, Zhifang Lin, ST Chui, and CT Chan. Manipulating negative-refractive behavior with a magnetic field. *Physical review letters*, 101(15):157407, 2008.

[174] Lei Kang and Didier Lippens. Mie resonance based left-handed metamaterial in the visible frequency range. *Physical Review B*, 83(19):195125, 2011.

[175] E Özbay, A Abeyta, G Tuttle, M Tringides, R Biswas, CT Chan, CM Soukoulis, and KM Ho. Measurement of a three-dimensional photonic band gap in a crystal structure made of dielectric rods. *Physical Review B*, 50(3):1945, 1994.

[176] LC Botten, TP White, C Martijn de Sterke, and RC McPhedran. Wide-angle coupling into rod-type photonic crystals with ultralow reflectance. *Physical Review E*, 74(2):026603, 2006.

[177] Ruey-Lin Chern and Yu-Tang Chen. Effective parameters for photonic crystals with large dielectric contrast. *Physical Review B*, 80(7):075118, 2009.

[178] Liang Peng, Lixin Ran, and Niels Asger Mortensen. Achieving anisotropy in metamaterials made of dielectric cylindrical rods. *Applied Physics Letters*, 96(24):241108, 2010.

[179] Efthymios Kallos, Ioannis Chremmos, and Vassilios Yannopapas. Resonance properties of optical all-dielectric metamaterials using two-dimensional multipole expansion. *Physical Review B*, 86(24):245108, 2012.

[180] Parikshit Moitra, Yuanmu Yang, Zachary Anderson, Ivan I Kravchenko, Dayrl P Briggs, and Jason Valentine. Realization of an all-dielectric zero-index optical metamaterial. *Nature Photonics*, 7(10):791, 2013.

[181] Ekaterina E Maslova, Mikhail F Limonov, and Mikhail V Rybin. Dielectric metamaterials with electric response. *Optics letters*, 43(22):5516–5519, 2018.

[182] Saman Jahani and Zubin Jacob. All-dielectric metamaterials. *Nature nanotechnology*, 11(1):23, 2016.

[183] P St J Russell and TA Birks. Hamiltonian optics of nonuniform photonic crystals. *Journal of lightwave technology*, 17(11):1982, 1999.

[184] Philip St J Russell, Timothy A Birks, and F Dominic Lloyd-Lucas. Photonic bloch waves and photonic band gaps. In *Confined electrons and photons*, pages 585–633. Springer, 1995.

[185] M Turduev, IH Giden, and Hamza Kurt. Design of flat lens-like graded index medium by photonic crystals: Exploring both low and high frequency regimes. *Optics Communications*, 339:22–33, 2015.

[186] Alexander Baev, Paras N Prasad, Hans Ågren, Marek Samoć, and Martin Wegener. Metaphotonics: An emerging field with opportunities and challenges. *Physics Reports*, 594:1–60, 2015.

[187] Jonathan Gratus, Paul Kinsler, Rosa Letizia, and Taylor Boyd. Electromagnetic mode profile shaping in waveguides. *Applied Physics A*, 123(1):108, 2017.

[188] Silvia Verdú-Andrés, Sergey Belomestnykh, Ilan Ben-Zvi, Rama Calaga, Qiong Wu, and Binping Xiao. Crab cavities for colliders: past, present and future. *Nuclear and particle physics proceedings*, 273:193–197, 2016.

[189] M Larrañaga, R Enparantza, and C Plostinar. Design optimisation of the re-bunching cavities for the front end test stand at RAL. *Proc. of LINAC2010, Tsukuba, Japan*, 2010.

[190] SeungWook Shin and Jong-Seo Chai. Optimization of the RF cavity of the medical purpose electron linac by using genetic algorithm. 2014.

[191] Ph Piot, Y-E Sun, JG Power, and M Rihaoui. Generation of relativistic electron bunches with arbitrary current distribution via transverse-to-longitudinal phase space exchange. *Physical Review Special Topics-Accelerators and Beams*, 14(2):022801, 2011.

[192] F Albert, AGR Thomas, SPD Mangles, S Banerjee, Sébastien Corde, Alessandro Flacco, M Litos, D Neely, J Vieira, Z Najmudin, et al. Laser wakefield accelerator based light sources: potential applications and requirements. *Plasma Physics and Controlled Fusion*, 56(8):084015, 2014.

[193] Hélène Ward and Luc Bergé. Temporal shaping of femtosecond solitary pulses in photoionized media. *Physical review letters*, 90(5):053901, 2003.

[194] Emil Persson, Klaus Schiessl, Armin Scrinzi, and Joachim Burgdörfer. Generation of attosecond unidirectional half-cycle pulses: Inclusion of propagation effects. *Physical Review A*, 74(1):013818, 2006.

[195] P Kinsler, SBP Radnor, JCA Tyrrell, and GHC New. Optical carrier wave shocking: detection and dispersion. *Physical Review E*, 75(6):066603, 2007.

[196] SBP Radnor, LE Chipperfield, P Kinsler, and GHC New. Carrier-wave steepened pulses and gradient-gated high-order harmonic generation. *Physical Review A*, 77(3):033806, 2008.

[197] Markus C Kohler, Thomas Pfeifer, Karen Z Hatsagortsyan, and Christoph H Keitel. Frontiers of atomic high-harmonic generation. In *Advances in Atomic, Molecular, and Optical Physics*, volume 61, pages 159–208. Elsevier, 2012.

[198] Paris Panagiotopoulos, Patrick Whalen, Miroslav Kolesik, and Jerome V Moloney. Carrier field shock formation of long-wavelength femtosecond pulses in single-crystal diamond and air. *JOSA B*, 32(8):1718–1730, 2015.

[199] Viktor V Vorobev and Andrey V Tyukhtin. Nondivergent cherenkov radiation in a wire metamaterial. *Physical review letters*, 108(18):184801, 2012.

[200] David E Fernandes, Stanislav I Maslovski, and Mário G Silveirinha. Cherenkov emission in a nanowire material. *Physical Review B*, 85(15):155107, 2012.

[201] Andrey V Tyukhtin and Viktor V Vorobev. Cherenkov radiation in a metamaterial comprised of coated wires. *JOSA B*, 30(6):1524–1531, 2013.

[202] Andrey V Tyukhtin and Viktor V Vorobev. Radiation of charges moving along the boundary of a wire metamaterial. *Physical Review E*, 89(1):013202, 2014.

[203] Andrey V Tyukhtin, Viktor V Vorobev, and Sergey N Galyamin. Radiation excited by a charged-particle bunch on a planar periodic wire structure. *Physical Review Special Topics-Accelerators and Beams*, 17(12):122802, 2014.

[204] Andrey V Tyukhtin, Viktor V Vorobev, and Sergey N Galyamin. Radiation of charged-particle bunches passing perpendicularly by the edge of a semi-infinite planar wire structure. *Physical Review E*, 91(6):063202, 2015.

[205] Viktor V Vorobev, Andrey V Tyukhtin, and Sergey N Galyamin. Surface waves generated by charged particle bunch moving along the edge of semi-infinite planar wire grid. *Radiation Physics and Chemistry*, 133:91–97, 2017.

[206] PD Hoang, G Andonian, I Gadjev, B Naranjo, Y Sakai, N Sudar, O Williams, M Fedurin, K Kusche, C Swinson, et al. Experimental characterization of electron-beam-driven wakefield modes in a dielectric-woodpile cartesian symmetric structure. *Physical review letters*, 120(16):164801, 2018.

[207] Sergey N Galyamin, Viktor V Vorobev, and Andrei Benediktovitch. Radiation field of an ideal thin gaussian bunch moving in a periodic conducting wire structure. *Physical Review Accelerators and Beams*, 22(4):043001, 2019.

[208] A EL Haddad. Exact analytical solution for the electromagnetic wave propagation in a photonic band gaps material with sinusoidal periodicity of dielectric permittivity. *Optik-International Journal for Light and Electron Optics*, 127(4):1627–1629, 2016.

[209] John W Staples. RFQs−An Introduction. In *AIP Conference Proceedings*, volume 249, pages 1483–1532. AIP, 1992.

[210] PN Ostroumov, AA Kolomiets, DA Kashinsky, SA Minaev, VI Pershin, TE Tretyakova, and SG Yaramishev. Design of 57.5 MHz cw RFQ for medium energy heavy ion superconducting linac. *Physical Review Special Topics-Accelerators and Beams*, 5(6):060101, 2002.

[211] PN Ostroumov, B Mustapha, A Barcikowski, C Dickerson, AA Kolomiets, SA Kondrashev, Y Luo, D Paskvan, A Perry, D Schrage, et al. Development and beam test of a continuous wave radio frequency quadrupole accelerator. *Physical Review Special Topics-Accelerators and Beams*, 15(11):110101, 2012.

[212] SV Kutsaev, B Mustapha, PN Ostroumov, A Barcikowski, D Schrage, J Rodnizki, and D Berkovits. Design and multiphysics analysis of a 176 MHz continuous-wave radio-frequency quadrupole. *Physical Review Special Topics-Accelerators and Beams*, 17(7):072001, 2014.

[213] Xiaowen Zhu, Hu Wang, Yuanrong Lu, Zhi Wang, Kun Zhu, Yubin Zou, and Zhiyu Guo. 2.5 MeV CW 4-vane RFQ accelerator design for BNCT applications. *Nuclear Instruments and Methods in Physics Research Section A: Accelerators, Spectrometers, Detectors and Associated Equipment*, 883:57–74, 2018.

[214] Han-Sung Chan, Zhi-Ming Hsieh, Wei-Hong Liang, AH Kung, Chao-Kuei Lee, Chien-Jen Lai, Ru-Pin Pan, and Lung-Han Peng. Synthesis and measurement of ultrafast waveforms from five discrete optical harmonics. *Science*, 331(6021):1165–1168, 2011.

[215] Jonathan A Cox, William P Putnam, Alexander Sell, Alfred Leitenstorfer, and Franz X Kärtner. Pulse synthesis in the single-cycle regime from independent mode-locked lasers using attosecond-precision feedback. *Optics letters*, 37(17):3579–3581, 2012.

[216] Jonathan Gratus, Paul Kinsler, Rosa Letizia, and Taylor Boyd. Subwave-length mode profile customization using functional materials. *Journal of Physics Communications*, 1(2):025003, 2017.

[217] *CST Microwave Studio*. CST Computer Simulation Technology AG, Germany, 2018.

[218] Larry J Segerlind. *Applied finite element analysis*, volume 316. Wiley New York, 1976.

[219] *CST Microwave Studio Help*. CST Computer Simulation Technology AG, Germany, 2018.

[220] *CST White Paper: Understanding Time Domain Meshing in CST Microwave Studio*. CST Computer Simulation Technology AG, Germany, 2010.

[221] Darko Kajfez. Q-factor. *Encyclopedia of RF and Microwave Engineering*, 2005.

[222] V Svorčik, O Ekrt, V Rybka, J Lipták, and V Hnatowicz. Permittivity of polyethylene and polyethyleneterephtalate. *Journal of materials science letters*, 19(20):1843–1845, 2000.